

ELECTROWEAK PHYSICS

Conveners: *S. Haywood, P.R. Hobson, W. Hollik, Z. Kunszt*

Contributing authors: *G. Azuelos, U. Baur, J. van der Bij, D. Bourilkov, O. Brein, R. Casalbuoni, A. Deandrea, S. De Curtis, D. De Florian, A. Denner, S. Dittmaier, M. Dittmar, A. Dobado, M. Dobbs, D. Dominici, R. Gatto, A. Ghinculov, F. Gianotti, M. Grazzini, J.B. Hansen, R. Harper, S. Haywood, S. Heinemeyer, M.J. Herrero, P.R. Hobson, W. Hollik, M. Lefebvre, M. Krämer, Z. Kunszt, C.K. Mackay, R. Mazini, A. Miagkov, T. Muller, D. Neuberger, R. Orr, B. Osculati, J.R. Peláez, A. Pich, D. Rainwater, M. Redi, S. Riley, E. Ruiz Morales, C. Schappacher, A. Signer, K. Sliwa, H. Spiesberger, W.H. Thümmel, D. Wackeroth, G. Weiglein, D. Zeppenfeld, D. Zürcher*

Abstract

In this review, we consider four main topics:

1. The prospects for a significant improvement in the precise measurement of the electroweak parameters.
2. NLO QCD description of the production W^+W^- , $W^\pm Z$, ZZ , $W^\pm\gamma$ or $Z\gamma$ pairs with leptonic decays and with anomalous triple gauge-boson couplings.
3. The prospects for significant improvement in the direct measurement of the non-Abelian gauge-coupling, with direct limits on triple and quartic anomalous couplings.
4. Gauge-boson scattering at large centre of mass energy.

1. INTRODUCTION ¹

1.1 Electroweak parameters

At the LHC, substantial improvement in the precise determination of electroweak parameters, such as the W boson mass, the top-quark mass and the electroweak mixing angle, will become feasible, as well as an accurate measurement of the vector-boson self couplings and of the mass of the Higgs boson. This opens promising perspectives towards very comprehensive and challenging tests of the electroweak theory.

Electroweak precision observables provide the basis for important consistency tests of the Standard Model (SM) or its extensions, in particular the Minimal Supersymmetric Standard Model (MSSM). By comparing precision data with the predictions of specific models, it is possible to derive indirect constraints on the parameters of the model. In the case of the top-quark mass, m_t , the indirect determination from the precision observables in the framework of the SM turned out to be in remarkable agreement with the direct experimental measurement of m_t . Since the Higgs boson mass, M_H , enters the predictions for the precision observables only logarithmically in leading order, the indirect determination of M_H requires very accurate experimental data as well as high precision of the theoretical predictions. The uncertainties of the predictions arise from the following sources: a) the unknown higher-order corrections - since the perturbative evaluation is truncated at a certain order, and b) the parametric uncertainties induced by the experimental errors of the input parameters.

The most important universal top-quark contribution to the electroweak precision observables enters via the ρ parameter, which deviates from unity by a loop contribution $\Delta\rho$. At the one-loop level, the (t, b) doublet yields a term proportional to m_t^2 [1], namely $\Delta\rho = 3G_\mu m_t^2 / (8\pi^2 \sqrt{2})$ in the limit $m_b \rightarrow 0$. Therefore, it is to be expected that the precision measurement of the top-quark mass at the LHC (see Section 3.1) will significantly improve the theoretical prediction of the W mass, M_W – at

¹Section coordinators: W. Hollik, Z. Kunszt.

present, the experimental error on m_t is a limiting factor for the accuracy in the theoretical predictions of the precision observables. M_W itself will be measured at the LHC with a sizably improved accuracy.

The theoretical prediction for M_W is obtained from the relation between the vector-boson masses $M_{W,Z}$ and the Fermi constant G_μ , which is conventionally written in the form

$$M_W^2 \left(1 - \frac{M_W^2}{M_Z^2} \right) = \frac{\pi\alpha}{\sqrt{2}G_\mu} \frac{1}{1 - \Delta r}. \quad (1)$$

The quantity $\Delta r = \Delta r(\alpha, M_Z, M_W, m_t, M_H)$, first derived in [2, 3] in one-loop order, summarises the quantum corrections to the vector-boson mass correlation; it is obtained from the calculation of the muon lifetime in the SM beyond the tree-level approximation. At one-loop order, Δr can be written as

$$\Delta r = \Delta\alpha - \frac{c_W^2}{s_W^2} \Delta\rho + (\Delta r)_{\text{rem}}. \quad (2)$$

$\Delta\alpha$ contains the large logarithmic contributions from the light fermions, and $\Delta\rho$ the m_t^2 dependence; the non-leading terms are collected in $(\Delta r)_{\text{rem}}$ where also the dependence on M_H enters. In Equation 1, Δr is a quantity that accounts also for terms of higher order than just one-loop. Moreover, a partial resummation of large contributions from light fermions and from the ρ parameter is contained in the expression. For a discussion see for example the section on the Electroweak Working Group Report in [4]. Results for M_W that were not yet available at the time of the report [4] are the next-to-leading two-loop terms of $\mathcal{O}(G_\mu^2 m_t^2 M_Z^2)$ [5, 6] in an expansion for asymptotically large m_t and the result for the Higgs mass dependence of the fermionic two-loop contributions [7]. Recently, the complete result for the fermionic two-loop contributions has been obtained [8]. Furthermore, the QCD corrections to Δr of $\mathcal{O}(\alpha\alpha_s^2)$ have been derived [9].

The most recent theoretical prediction [8] for M_W within the SM is displayed in Figure 1 as a function of M_H . To illustrate the comparison between theory and experiment, the experimental result is included in the figure for the current uncertainty $\delta M_W = \pm 0.042$ GeV [10] and the estimated LHC uncertainty $\delta M_W = \pm 0.015$ GeV (see Section 3.1) (assuming the same central value). The uncertainty for the current status and for the case where the LHC will have measured the top-quark mass with much higher accuracy is also displayed, in combination with the theoretical uncertainty from unknown higher-order corrections. It is clear that both improvements, in M_W and in m_t , will lead to a substantial increase in the significance of Standard Model tests, with stringent bounds on the Higgs boson mass to be confronted with the directly measured value of M_H .

Besides the W boson mass, the improvement in m_t will also have an effect on the predictions of the Z pole observables. They are conveniently described in terms of effective couplings

$$g_V^f = \sqrt{\rho_f} (I_3^f - 2Q_f \sin^2 \theta_{\text{eff}}^f), \quad g_A^f = \sqrt{\rho_f} I_3^f \quad (3)$$

in the neutral-current vertex at the Z resonance for a given fermion species f , normalised according to $J_\mu^{\text{NC}} = (\sqrt{2}G_\mu M_Z^2)^{1/2} (g_V^f \gamma_\mu - g_A^f \gamma_\mu \gamma_5)$. Besides the overall normalisation factor $\rho_f = 1 + \Delta\rho + \dots$, we mention in particular the effective mixing angle, which is usually chosen as the on-resonance mixing angle for the leptons $f = e, \mu, \tau$ in Equation 3 and denoted as $\sin^2 \theta_{\text{eff}}^{\text{lept}}$. This quantity also depends sensitively on the top-quark mass, mainly through $\Delta\rho$. The theoretical prediction of $\sin^2 \theta_{\text{eff}}^{\text{lept}}$ will definitely be sharpened by the precise measurement of the top-quark mass; a sizable improvement concerning the internal consistency test can be anticipated. The on-resonance mixing angle for the light quarks $\neq b$ is numerically very close to the leptonic one. $\sin^2 \theta_{\text{eff}}^{\text{lept}}$ can therefore be measured at the LHC in the Drell-Yan production of charged-lepton pairs around the Z resonance, via $q\bar{q} \rightarrow l^+l^-$, where an accuracy of 1.4×10^{-4} on $\sin^2 \theta_{\text{eff}}^{\text{lept}}$ may be feasible (see Section 3.2).

Besides these internal consistency checks of the SM, the electroweak precision observables may be useful to distinguish between different models as candidates for the electroweak theory. In Figure 2,

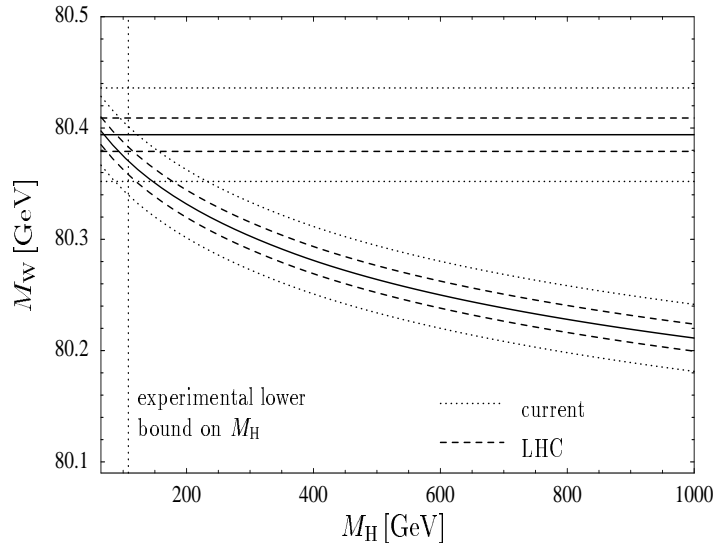


Fig. 1: The dependence of M_W , predicted by means of Equation 1, on M_H is shown for the SM. The uncertainty of the predictions corresponds to the present and expected parametric uncertainty owing to the top mass, in combination with the theoretical uncertainty. The central lines (solid) correspond to the present central values of $M_W = 80.394$ GeV and $m_t = 174.3$ GeV.

the SM prediction of M_W as a function of m_t is compared with the prediction within the MSSM, where the MSSM prediction is based on results up to $\mathcal{O}(\alpha\alpha_s)$ [11, 12]. The SM uncertainty arises from the only unknown parameter, the Higgs boson mass. On the other hand, within the MSSM, the Higgs boson mass is not a free parameter [13], and the uncertainty originates from the unknown SUSY mass scales. In the small overlap region, the MSSM behaves like the SM, *i.e.* all SUSY particles are heavy and decouple from the precision observables, and the M_H value of the SM stays below 130 GeV, the upper bound on the lightest MSSM Higgs boson mass for $m_t = 175$ GeV (see [14] and references therein). Figure 2 shows the clear improvement from the current status to the LHC era, where eventually, besides direct experimental evidence, a distinction between SM and MSSM might become feasible.

1.2 Vector-boson pair production and scattering

At the LHC, the precise measurement of the production of W^+W^- , $W^\pm Z$, ZZ , $W^\pm\gamma$ or $Z\gamma$ pairs is also an important physics goal. In the simplest studies, the gauge-bosons will be detected via their leptonic decays. Already a couple events have been obtained by CDF and D0 for WW and WZ production and D0 has seen about 100 $W\gamma$ and 30 $Z\gamma$ events. The data set at Run II will be about 20 times larger and about 1000 times larger at the LHC. For a summary of the experimental situation see [15, 16].

The production of gauge-boson pairs provide us with the best test of the non-Abelian gauge-symmetry of the Standard Model (SM). Deviation from the SM predictions may come either from the presence of anomalous couplings or the production of new heavy particles and their decays into vector-boson pairs. If the particle spectrum of the SM has to be enlarged with new particles (as in the Minimal Supersymmetric Standard Model (MSSM)) with mass values of $\geq 0.5 - 1$ TeV, small anomalous couplings are generated at low energy. If the Higgs boson is very heavy, it will decay mainly into W^+W^- and ZZ pairs. If the symmetry breaking mechanism is dynamical (technicolor models, BESS models), large anomalous couplings might be generated or new heavy particles may be produced. In both of these cases, vector-boson pair production will show deviations from the Standard Model predictions. At the same time, vector-boson pair production gives the most important background for a number of new physics signals. For example, one of the most important physics signal for supersymmetry at hadron

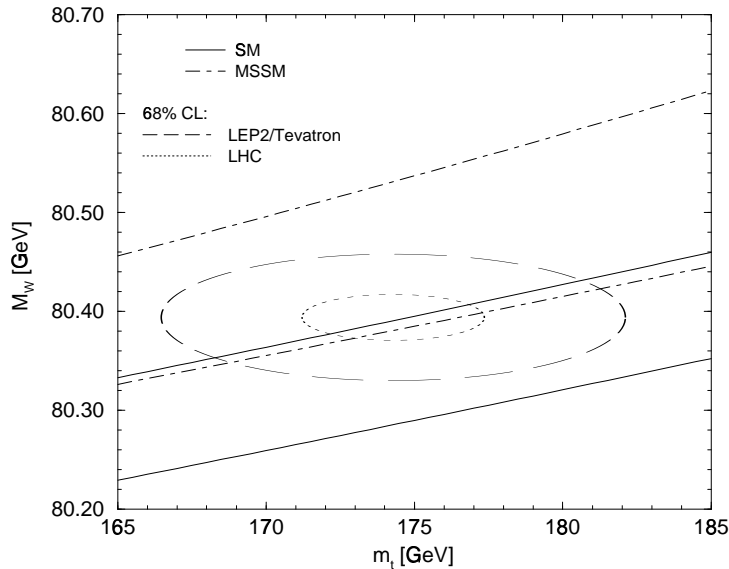


Fig. 2: The dependence of M_W on m_t is shown for the SM and the MSSM. It is compared to the current errors and to the errors expected from the LHC.

colliders is the production of three charged leptons and missing transverse momentum. The dominant background for this process is the production of W plus a Z (real or virtual) or γ .

The leading order production mechanism of gauge-boson pair production is $q\bar{q}$ annihilation. The precise calculation of the cross sections in the QCD improved parton model have received recently a lot of attention. The cross sections of the gauge-boson pair production and its decay into lepton pairs have been calculated in next-to-leading order (NLO) accuracy retaining the full spin correlations of the leptonic decay products. A significant achievement was that the theoretical results in NLO QCD for the production of W^+W^- , $W^\pm Z$, ZZ , $W^\pm\gamma$ or $Z\gamma$ pairs could be documented in short analytic formulae [17] allowing for independent numerical implementations. Subsequently, several so called NLO numerical Monte Carlo programs have been developed and the complete one loop corrections became available for the first time for W^+W^- , $W^\pm Z$, ZZ in [18, 19], and for $W^\pm\gamma$, or $Z\gamma$ pairs in [20]. These new results have superseded and confirmed previous NLO results on spin averaged production gauge-boson pair production [21, 22, 23, 24, 25, 26, 27, 28], as well the approximate results where spin correlation have been neglected in the virtual corrections [29, 30, 31, 32, 33]. The agreement between the well documented results in [19] and in [22, 24, 26] is within the precise integration error and the agreement between the results of [19] and the recent programs of [29, 30, 31, 32, 33] is about 3%. Therefore, previous experimental simulation studies based on these programs (see Section 6.5) should not be repeated.

Simple analytic NLO results exist also for the anomalous coupling contributions at NLO accuracy in [19, 20]. Again, the agreement with previous approximate NLO results [29, 30, 31, 32, 33] is also good (see Section 5.5). Future anomalous coupling studies may like to use the more accurate packages. At the LHC, contrary to LEP, the phenomenological studies of anomalous triple gauge-boson coupling constants cannot be treated as constant couplings since they lead to violation of $SU(2)$ gauge-symmetry and unitarity. The difficulty comes from truncation of the contribution of an infinite series of higher dimensional non-renormalisable gauge-invariant operators. In the case of $q\bar{q}$ annihilation to gauge-boson pairs, a suitable phenomenological approach is the introduction of form factors for the anomalous couplings (which in principle are calculable in the true underlying theory). As long as we do not obtain deviations from the Standard Model, for practical purposes, simple dipole form factors with various cut-

off parameters can be used. With better data, one can put limits on the form factor values in small \sqrt{s} intervals, assuming constant couplings for each interval. In the case of positive signals, such a form factor measurement will provide us with important information on the underlying theory (see Sections 3., 4. and 5.).

At higher energies, the higher order production processes of WW and ZZ scattering (the weak boson are emitted from the incoming quarks) will become more and more important. These interactions are the most sensitive to the mechanism of the electroweak symmetry breaking. In particular, if the breaking of the electroweak symmetry is due to new particles with strong interactions at the TeV scale, enhanced production of longitudinal gauge-boson pairs will be the most typical signal [34, 35]. The minimal model to describe this alternative is obtained by assuming that the new particles are too heavy to be produced at LHC and the linear σ -model Higgs-sector of the Standard Model is replaced by the non-renormalisable non-linear σ -model which can also be considered as an effective chiral vector-boson Lagrangian with non-linear realisation of the gauge-symmetry [36, 37]. The question is whether this more phenomenological approach is consistent with the precision data. In a recent analysis, a positive answer was obtained [38]. It has been found that due to the screening of the symmetry breaking sector [39], this alternative still has enough flexibility to be in perfect agreement with the precision data up to a cut-off scale of 3 TeV (see Sections 5. and 6.). In the chiral approach, the gauge-boson observables are obtained as truncated series in powers of the external momenta $p^n/(4\pi v)^n$ with $M_W^2 \approx gv^2/8$. The approximation is valid up to energy scales of $E = 4\pi v \approx 3$ TeV. At the LHC, the partonic centre of mass energy can be higher and the phenomenological implementation is confronted with the problem of unitarisation [40, 41, 42]. Although unitarisation is not unique, the use of the K-matrix formalism [40] or the $\mathcal{O}(p^4)$ Inverse Amplitude Method [42] appear to give reasonable model independent framework to explore the various possibilities. When extrapolating to higher energies in particular, the masses of resonances are rather sensitive to the actual value of additional chiral parameters. An alternative approach for the phenomenological formulation of the dynamical symmetry breaking consistent with the precision data is offered by the BESS model [43] with an extended strongly interacting gauge-sector with enhanced global symmetries and with important decoupling properties at low energies. The phenomenologically acceptable technicolor models [44] also require an enhanced global symmetry in the spectrum of the theory. In the most pessimistic parameter ranges, it is rather difficult to detect the signals of the strong WW and WZ scattering; therefore, one has to push the LHC analysis to its limits. In the future, further clever strategies have to be pursued for this case (see Section 6.).

2. ELECTROWEAK CORRECTIONS TO DRELL-YAN PROCESSES ²

The basic parton processes for single vector-boson production are $q\bar{q}' \rightarrow W \rightarrow l\nu_l$ and $q\bar{q} \rightarrow Z \rightarrow l^+l^-$, with charged leptons l in the final state. Investigations around the W and Z resonance allow a precise measurement of the W mass and of the electroweak mixing angle from the forward-backward asymmetry. At high invariant masses of the l^+l^- pair, deviations from the standard cross section and A_{FB} could indicate scales of new physics, *e.g.* associated with an extra heavy Z' or extra space dimensions. For the envisaged precision, a discussion of the electroweak higher-order contributions is necessary, on top of the QCD corrections. The electroweak corrections consist of the set of electroweak loop contributions, including virtual photons, and of the emission of real photons.

With respect to QCD, the cross sections in this section are all of lowest order, evaluated with parton distribution functions at factorisation scales M_W (for W production) and M_Z (for Z production). Hence, the numerical values are not yet directly the physical ones. They are given here to point out the structure and the size of the higher-order electroweak contributions. The QCD corrections are considered in the QCD chapter of this report, where a QCD-related uncertainty of $\sim 5\%$ is estimated. For illustration, we give the values (in nb) for $[\sigma(pp \rightarrow W^+) + \sigma(pp \rightarrow W^-)] \cdot BR(W \rightarrow e\nu)$ and

²Section coordinator: W. Hollik.

$\sigma(pp \rightarrow Z) \cdot BR(Z \rightarrow e^+e^-)$ in the purely electroweak calculation (EW) and with NNLO QCD [50]:

$$\begin{aligned} W &: 17.9 \text{ (EW)} \quad \text{and} \quad 20.3 \pm 1.0 \text{ (NNLO)}, \\ Z &: 1.71 \text{ (EW)} \quad \text{and} \quad 1.87 \pm 0.09 \text{ (NNLO)}. \end{aligned}$$

2.1 Universal initial-state QED corrections

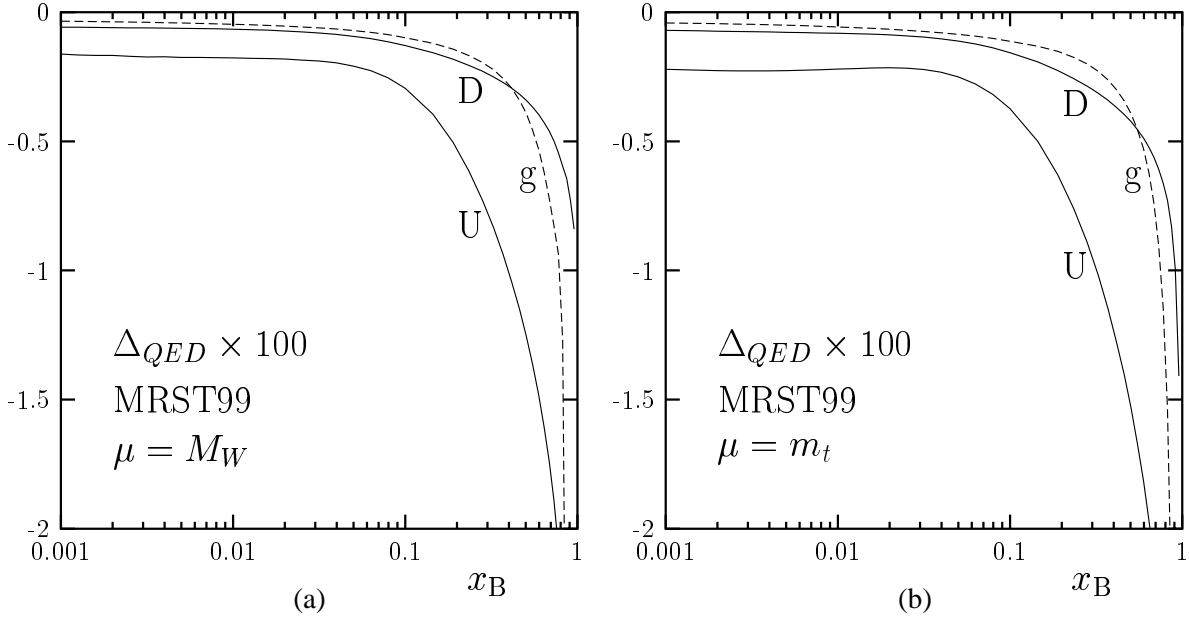


Fig. 3: QED corrections to the parton distribution functions for up -type quarks, $U(x, \mu^2) = \sum_{gen} (u + \bar{u})$, $down$ -type quarks, $D(x, \mu^2) = \sum_{gen} (d + \bar{d})$ and the gluon $g(x, \mu^2)$ in per cent for the scale $\mu = M_W$ (a) and $\mu = m_t$ (b).

QED corrections related to the emission of (real or virtual) photons from quarks contain mass singularities which factorise and therefore can be absorbed by a redefinition (*renormalisation*) of parton distribution functions [45]. This redefinition is well-known in the calculation of QCD radiative corrections where in complete analogy to photon radiation, the emission of gluons leads to mass singularities as well. By the redefinition, the mass singularities disappear from the observable cross section and the renormalised distribution functions become dependent on the factorisation scale μ which is controlled by the well-known Gribov-Lipatov-Altarelli-Parisi (GLAP) equations [46, 47]. The factorisation scale should be identified with a typical scale of the process, *i.e.* a large transverse momentum, or the mass of a produced particle.

Since mass singularities are universal, *i.e.* independent of the process under consideration, the definition of renormalised parton distributions is also universal. Therefore it is possible to discuss the bulk of initial-state QED radiative corrections in terms of parton distribution functions. This will be true if there is only one large scale in the process.

The treatment of mass singularities due to gluonic or photonic radiation is identical. Photonic corrections can therefore be taken into account by a straightforward modification [48, 49] of the standard GLAP equations which describe gluonic corrections only. The modification corresponds to the addition of a term of the order of the electromagnetic fine-structure constant, α . Apart from small non-singular contributions, the resulting modified scale dependence of parton distribution functions is the only observable effect of initial-state QED corrections in high-energy scattering of hadrons.

The modified evolution equation for the charged parton distribution functions, $q_f(x, \mu^2)$ for quarks with flavour f , can be written as:

$$\begin{aligned} \frac{d}{dt}q_f(x, t) = & \frac{\alpha_s(t)}{2\pi} \int_x^1 \frac{dz}{z} \left[P_{q/q}(z, t)q_f(x/z, t) + P_{q/g}(z, t)g(x/z, t) \right] \\ & + \frac{\alpha(t)}{2\pi} \int_x^1 \frac{dz}{z} P_{q/q}^\gamma(z, t)q_f(x/z, t) \end{aligned} \quad (4)$$

In the leading logarithmic approximation, the splitting functions $P_{i/j}$ are independent of the scale $t = \ln \mu^2/\Lambda^2$, and the QED splitting function is given by

$$P_{q/q}^\gamma(z) = Q_f^2 \left[\frac{1+z^2}{(1-z)_+} + \frac{3}{2}\delta(1-z) \right] = \frac{Q_f^2}{C_F} P_{q/q}. \quad (5)$$

Since quarks are coupled through the splitting function $P_{q/g}(z) = \frac{1}{2} [z^2 + (1-z)^2]$ to gluons, the gluon distribution $g(x, \mu^2)$ is affected by QED corrections as well, although only indirectly, by terms of the order of $\mathcal{O}(\alpha\alpha_s)$. $\alpha(t)$ is the running electromagnetic fine-structure constant and Q_f are the fermion charges in units of the positron charge.

The proper treatment of the mass-singular initial-state QED corrections would require not only the solution of the evolution equations with the QED term, but also to correct all data that are used to fit the parton distributions for those QED effects. Apart from a few exceptions, experimental data have not been corrected for photon emission from quarks. However, one can illustrate the QED radiative corrections by comparing the modification of the parton distributions relative to the distribution functions obtained from the evolution equations without the QED terms, which are used as an input.

The solution of the evolution equations corresponds to the resummation of terms containing factors $\alpha(\alpha_s \ln \mu^2)^n$ with arbitrary power n . In Figures 3a and 3b, we show numerical results for the corrections Δ_{QED} to the distribution functions $U(x, \mu^2)$ ($D(x, \mu^2)$) for the sum of all *up*-(*down*)-type quarks, and the gluon distribution $g(x, \mu^2)$. The figures show the QED corrections in per cent relative to the distribution functions obtained from the GLAP equations without the QED term. The input distributions were taken from [50]. One finds small, negative corrections at the per-mille level for all values of x and μ^2 relevant in the LHC experiments. Only at large $x \gtrsim 0.5$ and large $\mu^2 \gtrsim 10^3 \text{ GeV}^2$ do the corrections reach the magnitude of one per cent. The increase of corrections for $x \rightarrow 1$ is due to the $\ln(1-x)$ terms appearing in the evaluation of the “+” distributions.

The largest corrections are obtained for up-type quarks due to the larger charge factor 4/9 as compared to 1/9 for down-type quarks. The gluon distribution, being of order $\mathcal{O}(\alpha\alpha_s)$, is corrected by less than 0.1% up to values of x of about 0.2.

The corrections vanish for $\mu^2 \rightarrow \mu_0^2$ since it was assumed that the input distributions $q_f(x, \mu_0^2)$ and $g(x, \mu_0^2)$ have been extracted from experiment at the reference scale μ_0^2 without subtracting quarkonic QED corrections.

The asymptotic behaviour for $x \rightarrow 0$ can be checked analytically. The singular behaviour of distributions $\propto x^{-\eta}$ for $x \rightarrow 0$ remains unchanged by the GLAP equations if $\eta > 1$. Thus the $\mathcal{O}(\alpha)$ corrected distributions have the same power behaviour as the uncorrected ones, the ratio consequently reaching a constant value for $x \rightarrow 0$. The valence parts of $U(x)$ and $D(x)$, however, which vanish at $x = 0$, receive positive corrections at small x , thus producing the well-known physical picture: radiation of gluons as well as of photons leads to a depletion at large x and an enhancement at small x , *i.e.* partons are shifted to smaller x .

Other input distribution functions lead to differences of QED corrections at the per-mille level which are again irrelevant when compared with the expected experimental precision of structure-function measurements.

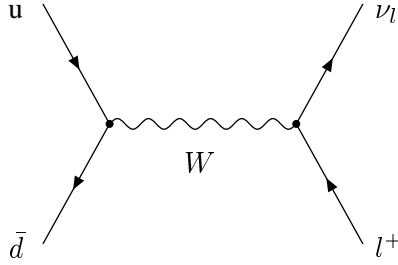


Fig. 4: Lowest-order diagram for $u\bar{d} \rightarrow W^+ \rightarrow \nu_l l^+ (+\gamma)$.

2.2 Electroweak corrections to W production

2.2.1 Physical goals of single W production

The Drell-Yan-like production of W bosons represents one of the cleanest processes with a large cross section at the LHC. This reaction is not only well suited for a precise determination of the W boson mass M_W , it also yields valuable information on the parton structure of the proton. Specifically, the target accuracy of the order of 15 MeV [53] in the M_W measurement exceeds the precision of roughly 30 MeV achieved at LEP2 [51] and Tevatron Run II [52], and thus competes with the one of a future e^+e^- collider [54]. Concerning quark distributions, precise measurements of rapidity distributions provide information over a wide range in x [50]; a measurement of the d/u ratio would, in particular, be complementary to HERA results. The more direct determination of parton-parton luminosities instead of single parton distributions is even more precise [55]; extracting the corresponding luminosities from Drell-Yan-like processes allows us to predict related $q\bar{q}$ processes at the per-cent level.

Owing to the high experimental precision outlined above, the predictions for the processes $pp \rightarrow W \rightarrow l\nu_l$ should attain per-cent accuracy. To this end, radiative corrections have to be included. In the following some basic features of this processes and recent progress [56, 57, 58, 59, 60] on electroweak corrections are summarised; a discussion of QCD corrections can be found in the QCD chapter of this report.

2.2.2 Lowest-order cross section and preliminaries

We consider the parton process $u\bar{d} \rightarrow \nu_l l^+ (+\gamma)$, where u and d generically denote the light up- and down-type quarks, $u = u, c$ and $d = d, s$. The lepton l represents $l = e, \mu, \tau$. In lowest order, only the Feynman diagram shown in Figure 4 contributes to the scattering amplitude, and the Born amplitude reads

$$\mathcal{M}_0 = \frac{e^2 V_{ud}^*}{2s_W^2} [\bar{v}_d \gamma^\mu \omega_- u_u] \frac{1}{\hat{s} - M_W^2 + iM_W \Gamma_W(\hat{s})} [\bar{u}_{\nu_l} \gamma_\mu \omega_- v_l], \quad (6)$$

with \hat{s} being the squared centre-of-mass (CM) energy of the parton system. The notation for the Dirac spinors \bar{v}_d , etc., is obvious, and $\omega_- = \frac{1}{2}(1 - \gamma_5)$ is the left-handed chirality projector. The electric unit charge is denoted by e , the weak mixing angle is fixed by the ratio $c_W^2 = 1 - s_W^2 = M_W^2/M_Z^2$ of the W and Z boson masses M_W and M_Z , and V_{ud} is the CKM matrix element for the ud transition.

Strictly speaking, Equation (6) already goes beyond lowest order, since the W boson width $\Gamma_W(\hat{s})$ results from the Dyson summation of all insertions of the (imaginary parts of the) W self-energy. Defining the mass M_W and the width Γ_W of the W boson in the on-shell scheme (see e.g. [61, 62]), the Dyson summation directly leads to a *running width*, i.e. $\Gamma_W(\hat{s})|_{\text{run}} = \Gamma_W \times (\hat{s}/M_W^2)$. On the other hand, a description of the resonance by an expansion about the complex pole in the complex \hat{s} plane corresponds to a *constant width*, i.e. $\Gamma_W(\hat{s})|_{\text{const}} = \Gamma_W$. In lowest order these two parametrisations of the resonance region are fully equivalent, but the corresponding values of the line-shape parameters M_W and Γ_W differ in higher orders [56, 63, 64]. The numerical difference is given by $M_W|_{\text{run}} - M_W|_{\text{const}} \approx 26$ MeV so

that it is necessary to state explicitly which parametrisation is used in a precision determination of the W boson mass from the W line shape.

The differential lowest-order cross section is easily obtained by squaring the lowest-order matrix element \mathcal{M}_0 of (6),

$$\left(\frac{d\hat{\sigma}_0}{d\hat{\Omega}}\right) = \frac{1}{12} \frac{1}{64\pi^2 \hat{s}} |\mathcal{M}_0|^2 = \frac{\alpha^2 |V_{ud}|^2}{192 s_W^4 \hat{s}} \frac{\hat{u}^2}{|\hat{s} - M_W^2 + iM_W \Gamma_W(\hat{s})|^2}, \quad (7)$$

where $\hat{u} = (p_u - p_l)^2$ is the squared momentum difference between the up-type quark and the lepton. The explicit factor $1/12$ results from the average over the quark spins and colours, and $\hat{\Omega}$ is the solid angle of the outgoing l^+ in the parton CM frame. The electromagnetic coupling $\alpha = e^2/(4\pi)$ can be set to different values according to different renormalisation schemes. It can be directly identified with the fine-structure constant $\alpha(0)$ or the running electromagnetic coupling $\alpha(Q^2)$ at a high energy scale Q . For instance, it is possible to make use of the value of $\alpha(M_Z^2)$ that is obtained by analysing the experimental ratio $R = \sigma(e^+e^- \rightarrow \text{hadrons})/(e^+e^- \rightarrow \mu^+\mu^-)$. These choices are called $\alpha(0)$ -*scheme* and $\alpha(M_Z^2)$ -*scheme*, respectively, in the following. Another value for α can be deduced from the Fermi constant G_μ , yielding $\alpha_{G_\mu} = \sqrt{2}G_\mu M_W^2 s_W^2/\pi$; this choice is referred to as G_μ -*scheme*.

2.23 Electroweak corrections

The electroweak $\mathcal{O}(\alpha)$ corrections consist of virtual one-loop corrections and real-photonic bremsstrahlung. The corrections to resonant W production have already been studied in [56, 57]; detailed discussions of the full calculation, including non-resonant corrections, can be found in [59, 60]. Since in $\mathcal{O}(\alpha^2)$ only two-photon bremsstrahlung [58] has been studied so far, the following discussion is restricted to $\mathcal{O}(\alpha)$ corrections.

The algebraic structure of the virtual corrections allows for a factorisation of the one-loop amplitude \mathcal{M}_1 into the Born amplitude \mathcal{M}_0 and a relative correction factor δ^{virt} . Thus, in $\mathcal{O}(\alpha)$ the correction to the squared amplitude reads

$$|\mathcal{M}_0 + \mathcal{M}_1|^2 = (1 + 2 \text{Re}\{\delta^{\text{virt}}\})|\mathcal{M}_0|^2 + \dots \quad (8)$$

Since only the real part of δ^{virt} appears, there is no double-counting of the $\mathcal{O}(\alpha)$ correction that is already included in \mathcal{M}_0 by the $iM_W \Gamma_W$ term. Moreover, the factorisation trivially avoids potential problems with gauge-invariance after the introduction of the W decay width in the resonant terms. Besides the Breit-Wigner factor in $|\mathcal{M}_0|^2$, there are logarithmic terms $\ln(\hat{s} - M_W^2)$ in δ^{virt} which are singular on resonance. The consistent replacement $\ln(\hat{s} - M_W^2) \rightarrow \ln(\hat{s} - M_W^2 + i\Gamma_W M_W)$ accounts for a Dyson summation of resonant W propagators in loop diagrams, without introducing problems with gauge-invariance.

The real corrections are included by adding the lowest-order cross section for the process $u\bar{d} \rightarrow \nu_l l^+ + \gamma$. The only non-trivial condition induced by gauge-invariance is the Ward identity for the external photon, *i.e.* electromagnetic current conservation. If the W width is zero, this identity is trivially fulfilled. This remains true even for a constant width, since the W boson mass appears only in the W propagator denominators, *i.e.* the substitution $M_W^2 \rightarrow M_W^2 - iM_W \Gamma_W$ is a consistent reparametrisation of the amplitude in this case. However, if a running W width is introduced naively, *i.e.* in the W propagators only, the Ward identity is violated. The identity can be restored by taking into account those part of the fermion-loop correction to the γWW vertex that corresponds to the fermion loops in the W self-energy leading to the width in the propagator [64, 65, 66]. For an external photon, this modification simply amounts to the multiplication of the γWW vertex by the factor $f_{\gamma WW}|_{\text{run}} = 1 + i\Gamma_W/M_W$.

Adding virtual and real corrections, all IR divergences cancel. Mass singularities of the form $\alpha \ln m_l$ related to a final-state lepton drop out for all observables in which photons within a collinear cone around the lepton are treated inclusively, in accordance with the KLN theorem. As already discussed in

Section 2.1 (see also [57]), mass singularities to the initial-state quarks are absorbed into renormalised quark distribution functions.

As long as one is interested in observables that are dominated by resonant W boson production, the radiative corrections can be approximated by the corrections to the production and decay subprocesses to resonant W bosons. Formally such an approximation can be carried out by a systematic expansion of all amplitudes about the resonance pole and is, therefore, called *pole approximation* (PA). In PA, the virtual correction consists of two parts. The first contribution is provided by the (constant) correction factors to the $W f \bar{f}'$ vertex for stable (on-shell) W bosons and is called *factorisable*. The second contribution, which is called *non-factorisable*, comprises all remaining resonant corrections. It is entirely due to photonic effects and includes, in particular, the $\ln(\hat{s} - M_W^2 + i\Gamma_W M_W)$ terms. The difference between PA and the exact result can be estimated by $\delta_{\text{PA}}^{\text{virt}} - \delta^{\text{virt}} \sim (\alpha/\pi) \ln(\hat{s}/M_W^2) \ln(\dots)$, where $\ln(\dots)$ indicates any logarithmic enhancements. In principle, also the real corrections can be treated in PA. However, since a reliable error estimate is not obvious, they are usually calculated exactly. More details about PA can be found in [56, 60].

2.24 Numerical results

The following numerical results have been obtained with the input parameters of [60] and a constant W width; in particular, we have $M_W = 80.35 \text{ GeV}$ and $\Gamma_W = 2.08 \text{ GeV}$. The QED factorisation is performed in the $\overline{\text{MS}}$ scheme with M_W being the factorisation scale, and the CTEQ4L [67] quark distributions are used in the evaluation of the pp cross section. For the partonic cross section, the CKM matrix element V_{ud} is set to 1; for the pp cross section a non-trivial CKM matrix is included in the parton luminosities (see [60]).

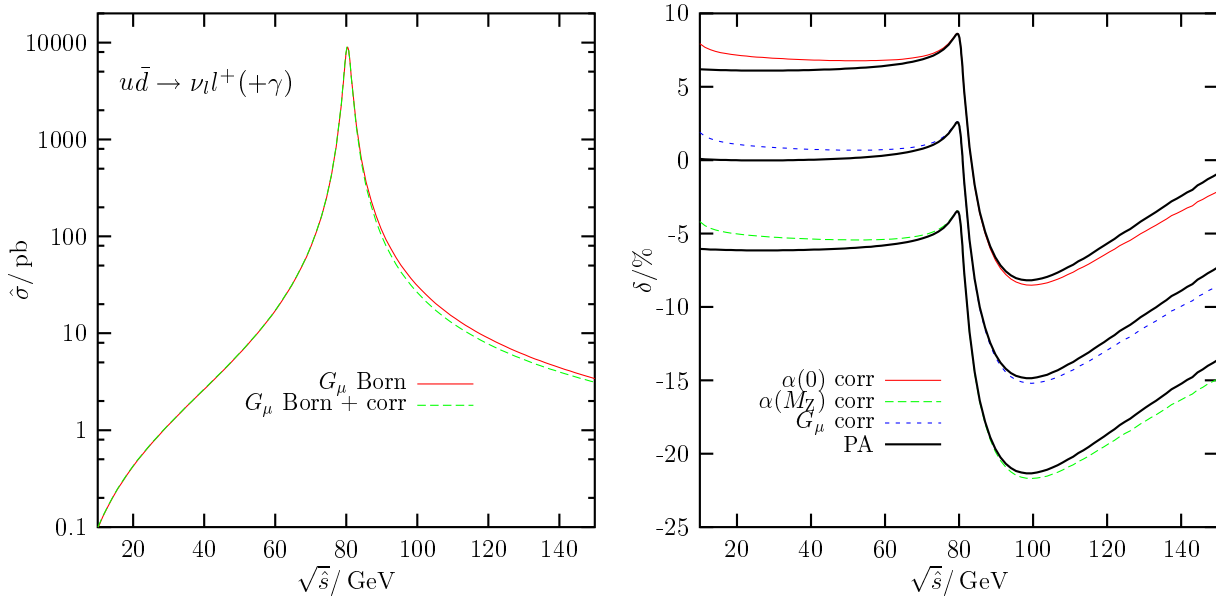


Fig. 5: Total parton cross section $\hat{\sigma}$ in G_μ parametrisation and relative corrections δ for different parametrisations (results based on [60]).

Figure 5 shows the total partonic cross section $\hat{\sigma}$ and the corresponding relative correction δ for intermediate energies. Note that the total cross section and its correction is the same for all final-state leptons $l = e, \mu, \tau$ in the limit of vanishing lepton masses. As expected, the G_μ parametrisation of the Born cross section minimises the correction at low energies, since the universal corrections induced by the running of α and by the ρ parameter are absorbed in the lowest-order cross section. Moreover, the naive error estimate for the PA taken from above turns out to be realistic. The PA describes the correction in the resonance region within a few per mille. Table 1 contains some results on the partonic

Table 1: Total lowest-order parton cross section $\hat{\sigma}_0$ in G_μ parametrisation and corresponding relative correction δ , exact and in PA (results based on [60]).

$\sqrt{\hat{s}}$ (GeV)	40	80	120	200	500	1000	2000
$\hat{\sigma}_0$ (pb)	2.646	7991.4	8.906	1.388	0.165	0.0396	0.00979
δ (%)	0.7	2.42	-12.9	-3.3	12	19	23
δ_{PA} (%)	0.0	2.40	-12.3	-0.7	18	31	43

cross section and its correction up to energies in the TeV range. Far above resonance, the PA cannot follow the exact correction anymore, since non-resonant corrections become more and more important. The leading corrections are due to Sudakov logarithms of the form $\alpha \ln^2(\hat{s}/M_W^2)$.

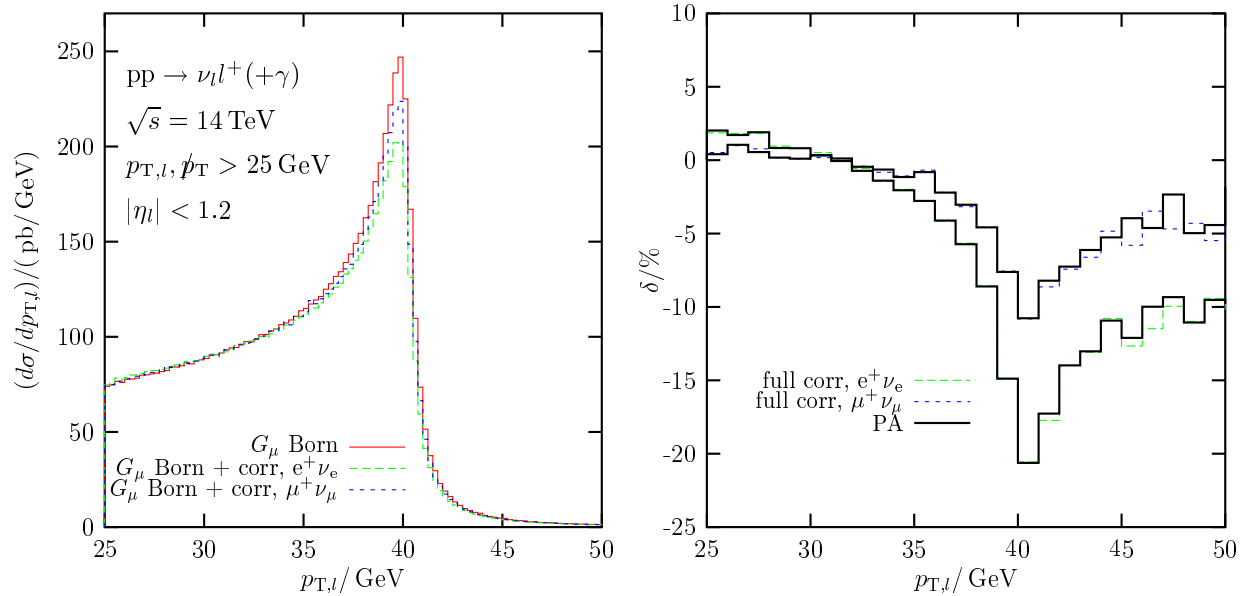


Fig. 6: Transverse-momentum distribution ($d\sigma/dp_{T,l}$) and relative corrections δ (results based on [60]).

Figure 6 shows the transverse-momentum distribution for the lepton l^+ produced in $pp \rightarrow W^+ \rightarrow \nu_l l^+ (+\gamma)$ for the pp CM energy $\sqrt{s} = 14$ TeV of the LHC. The transverse momenta p_T and the lepton pseudorapidity η_l are restricted by $p_{T,l}, \not{p}_T > 25$ GeV and $|\eta_l| < 1.2$. Since we do not recombine collinear photons and leptons, the corrections for different leptons do not coincide, but differ by corrections of the form $\ln(m_l/M_W)$. In the total cross section without any cuts these logarithms cancel, and the correction is again universal for all leptons in the massless limit. Since the $\ln m_l$ corrections are strongest for electrons, and since collinear photon emission reduces the momentum of the produced lepton, the correction δ for electrons is more negative (positive) for large (small) momenta than in the case of the muon. In particular, Figure 6 demonstrates the reliability of the PA for transverse lepton momenta $p_{T,l} \lesssim M_W/2$, where resonant W bosons dominate. However, high $p_{T,l}$ values may also be interesting in searches for new physics. Table 2 shows the contributions to the total cross section divided by different ranges in $p_{T,l}$. From the above discussion of the parton cross section it is clear that the PA is not applicable for very large $p_{T,l}$, where the W boson is far off shell.

The above results underline the importance of electroweak radiative corrections in a precise description for the W boson cross section at the LHC. Although the corrections of $\mathcal{O}(\alpha)$ are well under control now, there are still some topics to be studied, such as the impact of realistic detector cuts and photon recombination procedures or the inclusion of higher-order effects.

Table 2: Integrated lowest-order pp cross sections σ_0 for different ranges in $p_{T,l}$ and corresponding relative corrections δ , exact and in PA (results based on [60]).

$p_{T,l}$ (GeV)	25– ∞	25–45	45– ∞	50– ∞	80– ∞	200– ∞
σ_0 (pb)	1933.3(2)	1909.9(2)	23.52(5)	11.47(2)	1.682(3)	0.1014(1)
$\delta_{e+\nu_e}$ (%)	-5.51(5)	-5.45(7)	-11.8(5)	-9.7(4)	-11.7(3)	-17.7(2)
$\delta_{e+\nu_e,PA}$ (%)	-5.51(5)	-5.45(7)	-10.9(5)	-8.2(3)	-8.3(3)	-9.0(2)
$\delta_{\mu+\nu_\mu}$ (%)	-2.98(5)	-2.94(7)	-6.3(6)	-5.7(4)	-8.1(3)	-14.2(3)
$\delta_{\mu+\nu_\mu,PA}$ (%)	-2.97(5)	-2.94(7)	-5.7(6)	-4.6(4)	-4.9(3)	-5.6(2)

The impact of final state photon radiation on W observables strongly depends on the lepton identification requirements imposed by the experiment. In addition to the lepton p_T , \not{p}_T and pseudorapidity cuts, one usually imposes requirements on the separation of the charged lepton and the photon. For muons, the energy of the photon is required to be less than a critical value, E_c^γ , in a cone of radius R_c^μ around the muon. For electrons, the finite resolution of the electromagnetic calorimeter makes it difficult to separate electrons and photons for small opening angles between the particles. Their four momentum vectors are therefore recombined if their separation is smaller than a critical value R_c^e . Finally, uncertainties in the energy and momentum measurements of the charged lepton and the missing transverse energy need to be taken into account. They can be simulated by Gaussian smearing of the particle four-momentum vectors with standard deviation σ which depends on the particle type and the detector.

To illustrate how finite detector resolution affects the size of the electroweak corrections, we show in Figure 7 the ratio of the NLO and lowest-order cross sections as a function of the p_T of the electron in $pp \rightarrow \nu_e e^+(\gamma)$ obtained with the Monte Carlo generator WGRAD [57]. The solid histogram shows the cross section ratio taking only transverse-momentum and pseudorapidity cuts into account. The dashed histogram displays the result obtained when, in addition, the four-momentum vectors are smeared according to the ATLAS specifications [53], and electron and photon momenta are combined if $\Delta R(e, \gamma) < 0.07$ [53]. Recombining the electron and photon four-momentum vectors eliminates the mass-singular logarithmic terms of the form $\alpha \ln m_e$, and strongly reduces the size of the electroweak corrections.

2.3 Electroweak corrections to Z production and continuum neutral-current processes

2.3.1 QED corrections

The mass-singular universal QED corrections from initial-state radiation from quarks have already been discussed in Section 2.1. They are part of the quark distribution functions. The residual QED initial-state corrections, together with final-state corrections and interference of initial-final radiation are treated separately by an explicit diagrammatic computation.

A complete calculation of the QED $\mathcal{O}(\alpha)$ radiative corrections to $pp \rightarrow Z, \gamma \rightarrow l^+ l^-$ has been carried out in [68]. The calculation is based on an explicit diagrammatic approach. The collinear singularities associated with initial-state photon radiation are factorised into the parton distribution functions (see Section 2.1). Absorbing the initial-state mass singularities into the pdf's introduces a QED factorisation-scale dependence. The results presented here are obtained within the QED DIS scheme which is defined analogously to the QCD DIS factorisation scheme. The MRS(A) parton distributions are used, with a factorisation scale M_Z . Due to mass-singular logarithmic terms associated with photons emitted collinear with one of the final-state leptons, QED radiative corrections strongly affect the

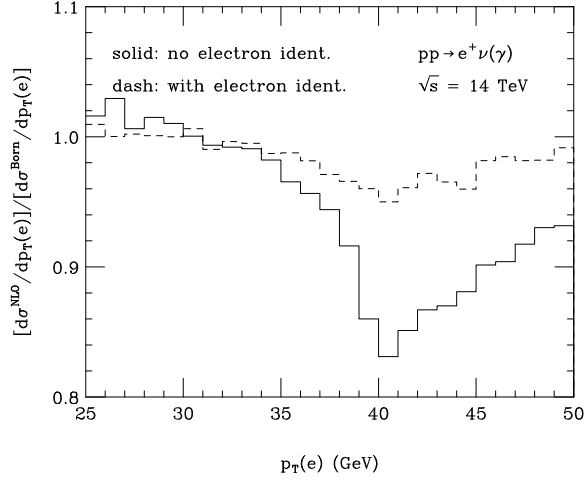


Fig. 7: Ratio of the $\mathcal{O}(\alpha^3)$ and lowest order differential cross sections as a function of the transverse momentum of the electron with and without lepton identification requirements (results based on [57]). The cuts imposed are described in the text.

shape of the di-lepton invariant mass distribution, the lepton transverse momentum spectrum, and the forward-backward asymmetry, A_{FB} .

The effect of the QED corrections on the di-muon invariant mass distribution in the region $45 \text{ GeV} < m(\mu^+\mu^-) < 105 \text{ GeV}$ is shown in Figure 8a where we plot the ratio of the $\mathcal{O}(\alpha^3)$ and lowest-order differential cross sections as a function of $m(\mu^+\mu^-)$. The lowest-order cross section has been evaluated in the effective Born approximation (EBA) which already takes into account those higher-order corrections which can be absorbed into a redefinition of the coupling constants and the effective weak mixing angle. More details on the EBA can be found in Section 2.32. In the region shown in the figure, the cross-section ratio is seen to vary rapidly. Below the Z peak, QED corrections significantly enhance the cross section. At the Z pole, the differential cross section is reduced by about 20%. Photon radiation from one of the leptons lowers the di-lepton invariant mass. Therefore, events from the Z peak region are shifted towards smaller values of $m(\mu^+\mu^-)$, thus reducing the cross section in and above the peak region, and increasing the rate below the Z pole. Final-state radiative corrections completely dominate over the entire mass range considered. They are responsible for the strong modification of the di-lepton invariant mass distribution. In contrast, initial-state corrections are uniform and small ($\approx +0.4\%$ in the QED DIS scheme).

As pointed out earlier, at the LHC a precise measurement of the effective mixing angle $\sin^2 \theta_{\text{eff}}^{\text{lept}}$ using the forward-backward asymmetry may be possible. In Figure 8b, the forward-backward asymmetry is shown in the EBA (dashed line), and including QED corrections (solid line) for $pp \rightarrow \mu^+\mu^-(\gamma)$ in the di-muon invariant mass range from 45 GeV to 105 GeV. Here, A_{FB} is defined by [68]

$$A_{\text{FB}} = \frac{F - B}{F + B} \quad (9)$$

where

$$F = \int_0^1 \frac{d\sigma}{d \cos \theta^*} d \cos \theta^*, \quad B = \int_{-1}^0 \frac{d\sigma}{d \cos \theta^*} d \cos \theta^*. \quad (10)$$

$\cos \theta^*$ is given by

$$\cos \theta^* = \frac{|p_z(\mu^+\mu^-)|}{p_z(\mu^+\mu^-)} \frac{2}{m(\mu^+\mu^-) \sqrt{m^2(\mu^+\mu^-) + p_T^2(\mu^+\mu^-)}} [p^+(\mu^-)p^-(\mu^+) - p^-(\mu^-)p^+(\mu^+)] \quad (11)$$

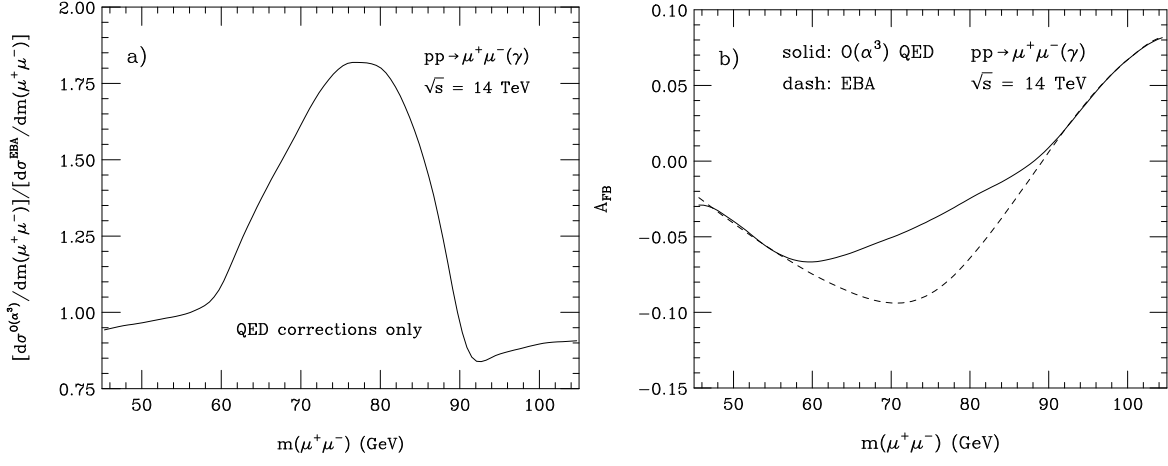


Fig. 8: Ratio of the $\mathcal{O}(\alpha^3)$ and lowest-order differential cross sections, and the forward-backward asymmetry, A_{FB} , as a function of the $\mu^+\mu^-$ invariant mass. The cuts imposed are described in the text.

in the Collins-Soper frame [69], with

$$p^\pm = \frac{1}{\sqrt{2}} (E \pm p_z), \quad (12)$$

where E is the energy and p_z is the longitudinal component of the momentum vector. As expected, the $\mathcal{O}(\alpha)$ QED corrections to A_{FB} are large in the region below the Z peak. Since events from the Z peak, where A_{FB} is positive and small, are shifted towards smaller values of $m(\mu^+\mu^-)$ by photon radiation, the forward-backward asymmetry is significantly reduced in magnitude by radiative corrections for $55 \text{ GeV} < m(\mu^+\mu^-) < 90 \text{ GeV}$. It should be noted that the forward-backward asymmetry is rather sensitive to the rapidity cuts imposed on the leptons. More details on A_{FB} and the measurement of the effective weak mixing angle can be found in Section 3.24.

The mass singular terms arising from final-state photon radiation are proportional to $\alpha \log(\hat{s}/m_l^2)$, where m_l is the lepton mass. Thus, the corrections to the Z line shape and A_{FB} for electrons in the final state are considerably larger than those in the muon case [68].

To simulate detector acceptances, we have imposed a $p_T(\mu) > 20 \text{ GeV}$ and a $|\eta(\mu)| < 3.2$ cut in Figure 8. Except for the threshold region, the effects of the lepton acceptance cuts approximately cancel in the cross section ratio. In a more realistic simulation of how QED corrections affect observables in Drell-Yan production, lepton and photon identification requirements need to be taken into account in addition to the lepton acceptance cuts. Muons are identified in a hadron collider detector by hits in the muon chambers. In addition to a hit in the muon chambers, one requires that the associated track is consistent with a minimum ionising particle. This limits the energy of a photon which traverses the same calorimeter cell as the muon to be smaller than a critical value E_c^γ . For electrons, the finite resolution of the electromagnetic calorimeter makes it difficult to separate electrons and photons for small opening angles between their momentum vectors. Therefore, electron and photon four-momentum vectors are recombined if their separation in the azimuthal angle–pseudorapidity plane is smaller than a critical value, R_c . This eliminates the mass-singular terms associated with final-state photon radiation (KLN theorem) and thus may reduce significantly the effect QED corrections have on physical observables in $pp \rightarrow e^+e^-(\gamma)$ [68]. Specific results sensitively depend on the value of R_c , which is detector dependent.

2.32 Non-QED corrections and effective Born description

The amplitude for the parton process $q(p) + \bar{q}(\bar{p}) \rightarrow l^+(k_+) + l^-(k_-)$ of quark-antiquark annihilation into charged-lepton pairs is in lowest order described by photon and Z boson exchange. In the kinematical

variables for the parton system

$$\hat{s} = (k_+ + k_-)^2, \quad t = (p - k_-)^2, \quad u = (p - k_+)^2 \quad (13)$$

the differential parton cross section can be written as follows (θ denotes the scattering angle in the parton CMS):

$$64\pi^2 \hat{s} \frac{d\hat{\sigma}}{d\Omega} = 2\mathcal{A}_0 \frac{u^2 + t^2}{\hat{s}^2} + \mathcal{A}_1 \frac{u^2 - t^2}{\hat{s}^2} = \mathcal{A}_0 (1 + \cos^2 \theta) + \mathcal{A}_1 \cos \theta \quad (14)$$

with

$$\begin{aligned} \mathcal{A}_0 &= Q_q^2 Q_l^2 e(\hat{s})^4 + 2v_q v_l Q_q Q_l e(\hat{s})^2 \operatorname{Re} \chi(\hat{s}) + (v_q^2 + a_q^2)(v_l^2 + a_l^2) |\chi(\hat{s})|^2, \\ \mathcal{A}_1 &= 4Q_q Q_l a_q a_l e(\hat{s})^2 \operatorname{Re} \chi(\hat{s}) + 8v_q a_q v_l a_l |\chi(\hat{s})|^2. \end{aligned} \quad (15)$$

This expression is an effective Born approximation, which incorporates several entries from higher-order calculations: the effective (running) electromagnetic charge containing the photon vacuum polarisation (real part)

$$e(\hat{s})^2 = \frac{4\pi\alpha}{1 - \Delta\alpha(\hat{s})}; \quad (16)$$

the Z propagator, together with the overall normalisation factor of the neutral-current couplings in terms of the Fermi constant G_μ ,

$$\chi(\hat{s}) = (G_\mu M_Z^2 \sqrt{2})^2 \frac{\hat{s}}{\hat{s} - M_Z^2 + i\hat{s}\Gamma_Z/M_Z}, \quad (17)$$

containing the Z width as measured from the Z resonance at LEP; the vector and axial-vector coupling constants for $f = l, q$

$$v_f = I_3^f - 2Q_f \sin^2 \theta_{\text{eff}}, \quad a_f = I_3^f, \quad (18)$$

which contain the effective (leptonic) mixing angle at the Z peak, which is measured at LEP and SLC. Taking Γ_Z and $\sin^2 \theta_{\text{eff}}$ from higher-order calculations, the formulae above yield a good description in the region around the Z resonance.

From the cross section (14) a forward-backward asymmetry for the produced l^+l^- system can be derived, which at the parton level is given by

$$\hat{A}_{\text{FB}} = \frac{\hat{\sigma}_{\text{F}} - \hat{\sigma}_{\text{B}}}{\hat{\sigma}_{\text{F}} + \hat{\sigma}_{\text{B}}} = \frac{3}{8} \frac{\mathcal{A}_1}{\mathcal{A}_0}. \quad (19)$$

Around the Z peak, this quantity depends sensitively on $\sin^2 \theta_{\text{eff}}$. Using a parametrisation of the Born-like expressions in Equation 15, a measurement of \hat{A}_{FB} allows a determination of the mixing angle (see Section 3.). Below we give a quantitative evaluation of the higher-order electroweak effects in the integrated cross section and in \hat{A}_{FB} to demonstrate the quality of the approximation around the Z pole and to point out deviations at higher invariant masses of the lepton pairs.

Besides the universal and non-universal QED corrections, the following IR-finite next-order electroweak terms contribute, which are schematically depicted in Figure 9: self-energy contributions to the photon and Z propagators, vertex corrections to the γ/Z - ll and γ/Z - $q\bar{q}$ 3-point couplings, and box diagrams with two massive boson exchanges. Details of the treatment of the resonance region at higher order is equivalent to that in e^+e^- annihilation in fermion pairs and can be found *e.g.* in [4]. Around the Z pole, the box graphs are negligible, but they increase strongly with the energy and hence contribute sizeably at high invariant masses of the lepton pair. A description in terms of an effective-Born cross section far away from the Z pole becomes insufficient for two reasons: the effective couplings (based on self-energies and vertex corrections only) are not static but grow as functions of \hat{s} , and the presence of the box contributions, which cannot be absorbed in effective vector and axial-vector couplings in a Born-like structure.

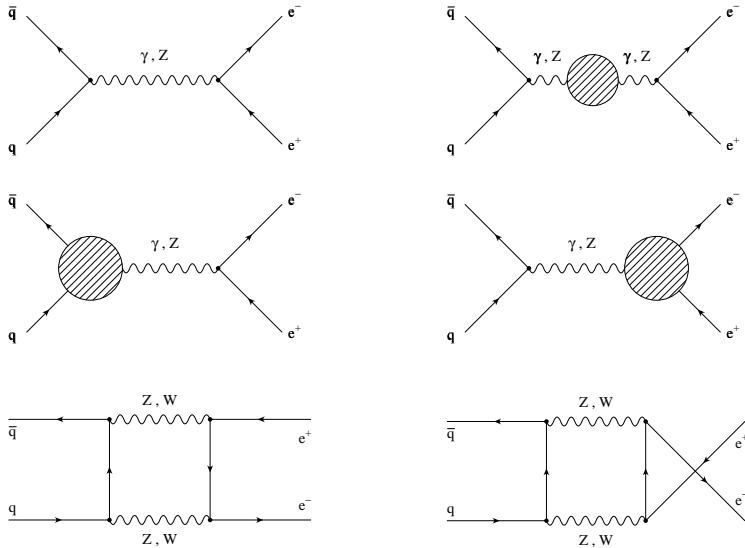


Fig. 9: Born and higher-order electroweak contributions to $q\bar{q} \rightarrow e^+e^-$ in symbolic notation.

In Figures 10 and 11 we compare the integrated cross section $\hat{\sigma}$ and the asymmetry A_{FB} at the parton level in the approximation corresponding to Equations 14 and 15 with results obtained by a complete one-loop calculation with proper treatment of higher-order terms around the Z resonance. For demonstrational purpose, the effect of the box diagrams is displayed separately. As one can see, the region where the effective Born description starts to become unsatisfactory is at rather high values of the parton energy.

In order to give an idea of the effects remaining in the hadronic cross section after convolution with the quark distribution functions, Table 3 contains the relative deviations of the cross section based on the higher-order parton results from those based on the Born approximation Equation 15. Also listed are the estimated experimental accuracies with which the cross section in the various bins can be measured. The comparison shows that at high invariant masses the radiative corrections remain sizeable and should be taken into account for studies at high \hat{s} , for example in the search for new physics effects originating from a heavy extra gauge-boson Z' .

2.33 The full electroweak $\mathcal{O}(\alpha)$ corrections: Monte Carlo simulations with ZGRAD2

The QED corrections described in Section 2.31 have been combined with the weak corrections summarised in the previous section in a new Monte Carlo program called ZGRAD2 [71]. In Figure 12a we show the ratio of the full $\mathcal{O}(\alpha^3)$ electroweak and the $\mathcal{O}(\alpha^3)$ QED differential cross sections for $pp \rightarrow \mu^+\mu^-(\gamma)$ obtained with ZGRAD2 as a function of the $\mu^+\mu^-$ invariant mass. As in Section 2.31, we have imposed a $p_T(\mu) > 20$ GeV and a $|\eta(\mu)| < 3.2$ cut, and used the EBA to evaluate the lowest-order contribution to the $\mathcal{O}(\alpha^3)$ QED cross section. Thus, the ratio directly displays the effect of the weak box-diagrams and the energy dependence of the weak coupling form factors. While the additional weak contributions only change the differential cross section by 0.6% at most, they do modify the shape of the Z resonance curve.

Figure 12b compares the effect of the $\mathcal{O}(\alpha^3)$ QED corrections and the full $\mathcal{O}(\alpha^3)$ electroweak corrections on the di-muon invariant mass distribution for $m(\mu^+\mu^-)$ values between 200 GeV and 2 TeV. Due to the presence of logarithms of the form $\log(\hat{s}/M_Z^2)$, the weak corrections become significantly larger than the QED corrections at large values of $m(\mu^+\mu^-)$, and, eventually, may have to be resummed [70]. For $m(\mu^+\mu^-) = 2$ TeV, the full $\mathcal{O}(\alpha^3)$ electroweak corrections are found to reduce the

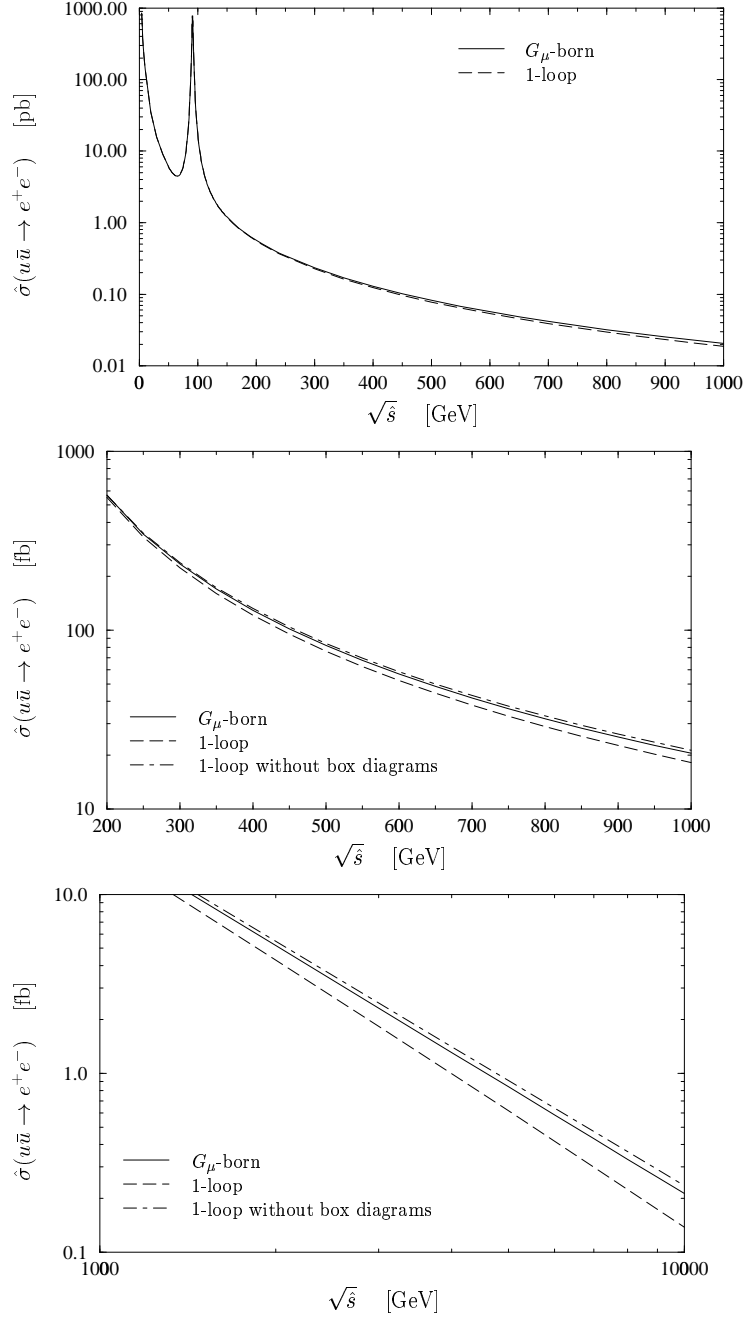


Fig. 10: $u\bar{u} \rightarrow e^+e^-$. Energy dependence of $\hat{\sigma}$ in various steps of the approximation. $M_H = 100$ GeV and $m_t = 174$ GeV.

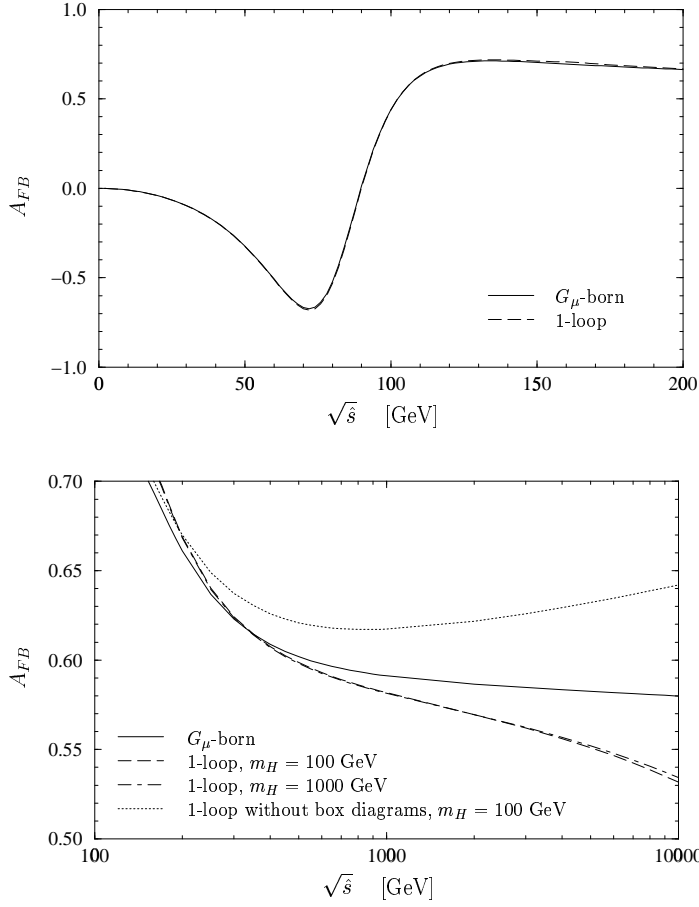


Fig. 11: $u\bar{u} \rightarrow e^+e^-$. Energy dependence of \hat{A}_{FB} at the parton level, for $m_t = 174$ GeV and different values of the Higgs mass, in various steps of the approximation.

differential cross section by more than 20%.

Finally, in Figure 13 we show how the $\mathcal{O}(\alpha^3)$ corrections affect the forward-backward asymmetry (see Equations 9 to 11). Both QED and weak corrections reduce A_{FB} , and their size increases with growing di-muon masses. For $m(\mu^+\mu^-) = 2$ TeV, the weak corrections are about twice as large as the QED corrections. Note that the electroweak corrections affect A_{FB} much less than the lepton pair invariant mass distribution. In the Z pole region, $75 \text{ GeV} < m(\mu^+\mu^-) < 105 \text{ GeV}$, the weak corrections change the forward-backward asymmetry by at most 5×10^{-4} . Results qualitatively similar to those shown in Figures 12 and 13 are obtained for $pp \rightarrow e^+e^-(\gamma)$.

ZGRAD2 includes the complete weak one-loop corrections and the full non-universal QED $\mathcal{O}(\alpha)$ corrections. The collinear singularities associated with initial-state photon radiation are factorised into the parton distribution functions. However, QED corrections to the evolution of the parton distribution functions (see Section 2.1) are not included in ZGRAD2. These corrections should be part of a complete global fit of the pdf's including all QED effect - this is beyond the scope of the calculation presented here. None of the current fits to the pdf's include QED corrections.

Table 3: Hadronic cross section for e^+e^- pairs with invariant mass in certain energy ranges. Columns two and three show the predicted cross sections in the effective Born approximation and the full one-loop calculation. Columns four and five show the relative corrections to the effective Born approximation arising from the full one-loop calculation as well as the estimated experimental errors for the cross section measurements in the various bins.

Energy range (for e^+e^- pairs) (TeV)	Born cross section (fb)	Full (non-QED) cross section (fb)	Relative correction to Born cross section (%)	Relative experimental error (%)
0.9 - 1.1	6.2299	5.6524	- 9.3	3
1.1 - 1.5	3.5205	3.1491	-10.5	4
1.5 - 1.75	0.6076	0.5317	-12.5	9.5
1.75 - 2.0	0.2681	0.2314	-13.7	14
2.0 - 2.5	0.1886	0.1590	-15.7	17
2.5 - 3.0	0.04895	0.04031	-17.7	30
3.0 - 4.0	0.01837	0.01464	-20.3	50

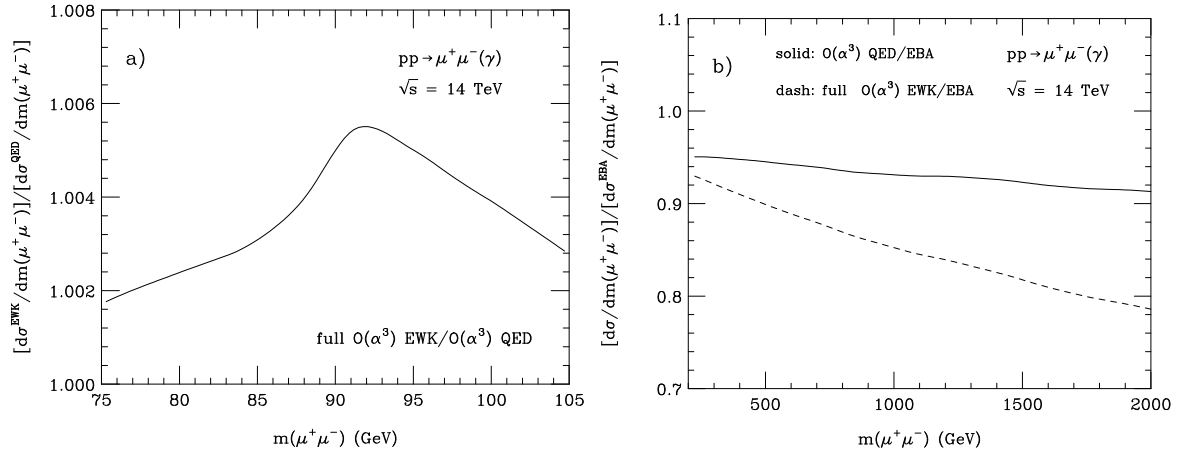


Fig. 12: a) Ratio of the full $\mathcal{O}(\alpha^3)$ electroweak and the $\mathcal{O}(\alpha^3)$ QED differential cross sections in the vicinity of the Z pole. b) Differential cross section ratios, displaying the size of the full $\mathcal{O}(\alpha^3)$ electroweak and the $\mathcal{O}(\alpha^3)$ QED corrections for large values of $m(\mu^+\mu^-)$. The cuts imposed are described in the text.

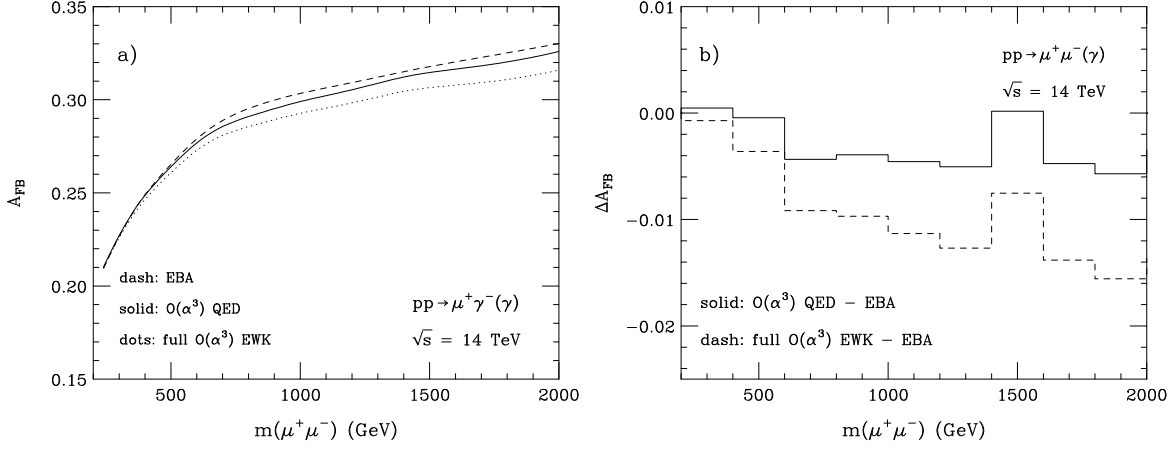


Fig. 13: ZGRAD2 predictions of a) the forward-backward asymmetry, and b) the change ΔA_{FB} due to the $\mathcal{O}(\alpha^3)$ electroweak and QED corrections. The cuts imposed are described in the text.

2.4 Z' indication from new APV data in cesium and searches at LHC

The weak charge Q_W for a heavy atom is defined in terms of the number of u, d quarks $N_u = 2Z + N$, $N_d = 2N + Z$ in the nucleus (Z, N) and the coefficients $C_{1u,d}$ in the parity-violating part of the electron-quark Hamiltonian,

$$\mathcal{H}_{PV} = -\frac{G_F}{\sqrt{2}} \bar{e} \gamma_\mu \gamma_5 e (C_{1u} \bar{u} \gamma^\mu u + C_{1d} \bar{d} \gamma^\mu d), \quad (20)$$

via the relation

$$Q_W = 2(N_u C_{1u} + N_d C_{1d}). \quad (21)$$

In the SM: $C_{1q} = I_3^q - 2Q_q \sin^2 \theta_W$.

In a recent paper [72] a new determination of the weak charge of atomic cesium has been reported. The most precise atomic parity violating (APV) experiment compares the mixing among S and P states due to neutral weak interactions to an induced Stark mixing [73]. The 1.2% uncertainty on the previous measurement of the weak charge Q_W was dominated by the theoretical calculations on the amount of Stark mixing and on the electronic parity violating matrix elements. In [72] the Stark mixing was measured and, incorporating new experimental data, the uncertainty in the electronic parity violating matrix elements was reduced. The new result $Q_W(^{133}\text{Cs}) = -72.06 \pm (0.28)_{\text{expt}} \pm (0.34)_{\text{theor}}$ represents a considerable improvement with respect to the previous determination [73, 74, 75, 76]. The discrepancy between the standard model (SM) and the experimental data is now given by $Q_W^{\text{expt}} - Q_W^{\text{SM}} = 1.18(1.28) \pm 0.46$ (for $m_t = 175$ GeV and $M_H = 100(300)$ GeV). This corresponds to 2.6(2.8) standard deviations [77], excluding the SM at 99% CL and, *a fortiori*, all the models leading to negative additional contributions to Q_W , as for example models with a sequential Z' [77]. This deviation could be explained by assuming the existence of an extra Z' from E_6 or $O(10)$ or from Z'_{LR} of left-right (LR) models [72, 77, 78]. The high-energy data at the Z resonance strongly bound the $Z - Z'$ mixing [79]; for this reason we will assume zero mixing. In this case, the new physics contribution to Q_W is due to the direct exchange of the Z' and is completely fixed by the Z' parameters, $\delta_N Q_W = 16a'_e [(2Z + N)v'_u + (Z + 2N)v'_d] M_Z^2 / M_{Z'}^2$, where a'_f, v'_f are the couplings Z' to fermions and, for ^{133}Cs , $Z = 55$ and $N = 78$. The relevant couplings of the Z' to the electron and to the up and down quarks are given in the Table 1 of [77].

In the case of the LR model considered in [77], the extra contribution to the weak charge is $\delta_N Q_W = -M_Z^2 / M_{Z'}^2 Q_W^{\text{SM}}$. For this model one has a 95% CL lower bound on $M_{Z'_{LR}}$ from the Tevatron [80] given by $M_{Z'_{LR}} \geq 630$ GeV. An LR model could then explain the APV data allowing for a mass of the Z'_{LR} varying between the intersection from the 95% CL bounds $540 \leq M_{Z'_{LR}}$ (GeV) ≤ 1470 deriving

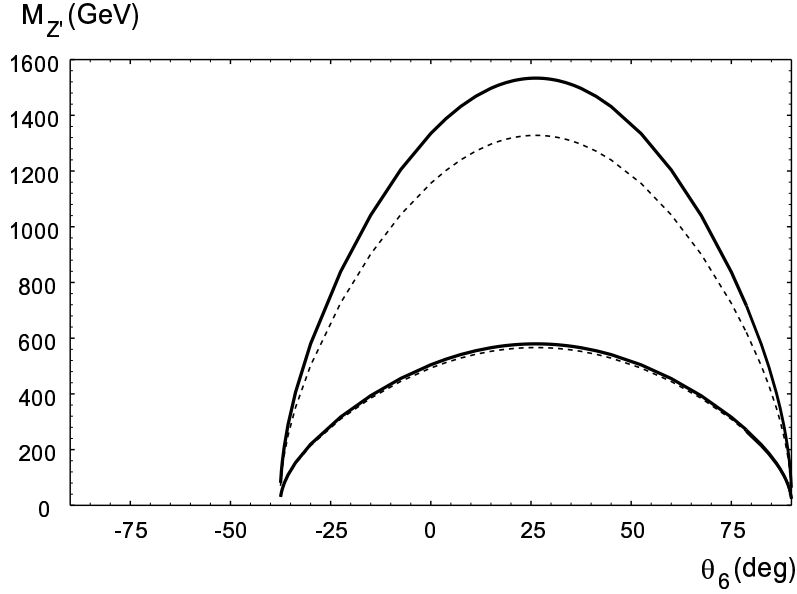


Fig. 14: The 95% CL lower and upper bounds for $M_{Z'}$ for the extra-U(1) models versus θ_6 . The solid (dash) line corresponds to $M_H = 100(300)$ GeV.

from Q_W and the lower bound of 630 GeV. In the case of the extra-U(1) models, the CDF experimental lower bounds for the masses vary according to the values of the angle θ_6 which parameterises different extra-U(1) models, but in general they are about 600 GeV at 95% CL [80]. For the particular models η , ψ , χ , corresponding to $\theta_6 = \arctan(-\sqrt{5/3})$, $\pi/2$, 0, the 95% CL lower bounds are $M_{Z'_\eta} \simeq 620$ GeV, $M_{Z'_\psi} \simeq 590$ GeV, $M_{Z'_\chi} \simeq 595$ GeV. In Figure 14, the 95% CL bounds on $M_{Z'}$ from APV are plotted versus θ_6 (the direct lower bounds from the Tevatron are about 600 GeV). We see that an extra Z' can explain the discrepancy with the SM prediction for the Q_W for a wide range of θ_6 angle. In particular, the models η and ψ are excluded, whereas the χ model is allowed for $M_{Z'_\chi}$ less than about 1.2 TeV.

In the near future, the Tevatron upgrade and LHC can confirm or disprove this indication coming from Q_W . The existing bounds for E_6 models from direct searches at the Tevatron will be upgraded by the future run with $\sqrt{s} = 2$ TeV and 1 fb^{-1} to $M_{Z'} \sim 800 - 900$ GeV and pushed to ~ 1 TeV for 10 fb^{-1} . The bounds are based on 10 events in the $e^+e^- + \mu^+\mu^-$ channels and decays to SM final-states only are assumed [81]. At the LHC with an integrated luminosity of 100 fb^{-1} , one can explore a mass range up to $4 - 4.5$ TeV depending on the θ_6 value. Concerning LR models, the 95% CL lower limits from the Tevatron run with $\sqrt{s} = 2$ TeV and $1(10) \text{ fb}^{-1}$ are $\sim 900(1000)$ GeV and extend to ~ 4.5 TeV at LHC [81]. Ratios of Z' couplings to fermions can be probed at LHC, by considering the forward-backward asymmetries, ratios of cross sections in different rapidity bins and other observables. For example, for $M_{Z'} = 1$ TeV, the LHC can determine the magnitude of normalised Z' quark and lepton couplings to around $10 - 20\%$ [81]. Therefore, if the deviation for the weak charge Q_W with respect to the SM prediction is not due to a statistical fluctuation, the new physics described by an extra gauge-boson model like Z'_χ can explain the discrepancy and the LHC will be able to verify this possible evidence.

3. PRECISION MEASUREMENTS ³

3.1 Measurement of the W mass

At the time of the LHC start-up, the W mass will be known with a precision of about 30 MeV from measurements at LEP2 [82] and Tevatron [83]. The motivation to improve on such a precision is discussed briefly below. The W mass, which is one of the fundamental parameters of the Standard Model, is related to other parameters of the theory, *i.e.* the QED fine structure constant α , the Fermi constant G_F and the Weinberg angle $\sin \theta_W$, through the relation

$$M_W = \sqrt{\frac{\pi\alpha}{G_F\sqrt{2}}} \cdot \frac{1}{\sin \theta_W \sqrt{1 - \Delta r}} \quad (22)$$

where Δr accounts for the radiative corrections which amount to about 4%. The radiative corrections depend on the top mass as $\sim m_t^2$ and on the Higgs mass as $\sim \log M_H$. Therefore, precise measurements of both the W mass and the top mass constrain the mass of the Standard Model Higgs boson or of the h boson of the MSSM. This constraint is relatively weak because of the logarithmic dependence of the radiative corrections on the Higgs mass. When it comes to making a comparison of the measurements of (M_W, m_t) with the SM predictions, it is not very useful if one measurement is much more restrictive than the other. To ensure that the two mass determinations have equal weight in a χ^2 test, the precision on the top mass and on the W mass should be related by the expression

$$\Delta M_W \approx 0.7 \times 10^{-2} \Delta m_t \quad (23)$$

Since the top mass will be measured with an accuracy of about 2 GeV at the LHC [53], the W mass should be known with a precision of about 15 MeV, so that it does not become the dominant error in the test of the radiative corrections and in the estimation of the Higgs mass. Such a precision is beyond the sensitivity of Tevatron and LEP2.

A study was performed to assess whether the LHC will be able to measure the W mass to about 15 MeV [84, 85]. The ATLAS experiment was taken as an example, but similar conclusions hold also for CMS. Such a precise measurement, which will be performed already in the initial phase at low luminosity as will the top mass measurement, would constrain the mass of the Higgs boson to better than 30%. When and if the Higgs boson will be found, such constraints would provide an important consistency check of the theory, and in particular of its scalar sector. Distinguishing between the Standard Model and the MSSM might be possible, since the radiative corrections to the W mass are expected to be a few percent larger in the latter case.

The measurement of the W mass at hadron colliders is sensitive to many subtle effects which are difficult to predict before the experiments start. However, based on the present knowledge of the LHC detector performance and on the experience from the Tevatron, it is possible to make a reasonable estimate of the total uncertainty and of the main contributions to be expected. In turn, this will lead to requirements for the detector performance and the theoretical inputs which are needed to achieve the desired precision. This is the aim of the study which is described in the next sections.

3.11 The method

The measurement of the W mass at hadron colliders is performed in the leptonic channels. Since the longitudinal momentum of the neutrino cannot be measured, the transverse mass m_T^W is used. This is calculated using the transverse momenta of the neutrino and of the charged lepton, ignoring the longitudinal momenta:

$$m_T^W = \sqrt{2p_T^l p_T^\nu (1 - \cos \Delta\phi)} \quad (24)$$

³Section coordinator: S. Haywood

where $l = e, \mu$. The lepton transverse momentum p_T^l is measured, whereas the transverse momentum of the neutrino p_T^ν is obtained from the transverse momentum of the lepton and the momentum \vec{u} of the system recoiling against the W in the transverse plane (hereafter called “the recoil”):

$$p_T^\nu = -|\vec{p}_T^l + \vec{u}| \quad (25)$$

The angle between the lepton and the neutrino in the transverse plane is denoted by $\Delta\phi$. The distribution of m_T^W , and in particular the trailing edge of the spectrum, is sensitive to the W mass. Therefore, by fitting the experimental distribution of the transverse mass with Monte Carlo samples generated with different values of M_W , it is possible to obtain the mass which best fits the data. The trailing edge is smeared by several effects, such as the W intrinsic width and the detector resolution. This is illustrated in Figure 15, which shows the distribution of the W transverse mass as obtained at particle level (no detector resolution) and by including the energy and momentum resolution as implemented in a fast particle-level simulation and reconstruction of the ATLAS detector (ATLFAST, [85]). The smearing due to the finite resolution reduces the sharpness of the end-point and therefore the sensitivity to M_W .

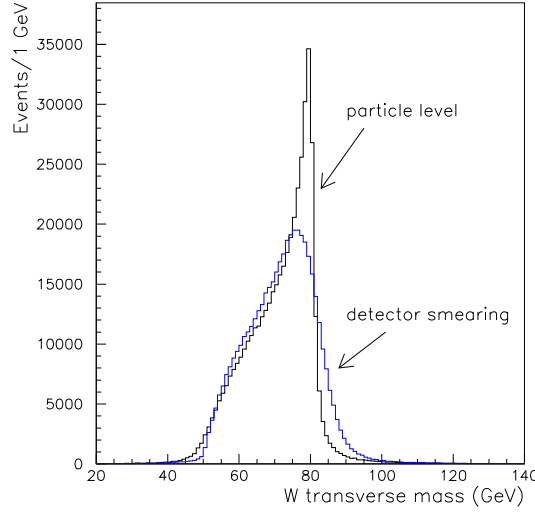


Fig. 15: Distribution of the W transverse mass as obtained at particle level and by including the expected ATLAS detector resolution.

When running at high luminosity, the pile-up will smear significantly the transverse mass distribution, therefore the use of the transverse-mass method will probably be limited to the initial phase at low luminosity. Alternative methods are mentioned in Section 3.14.

3.12 W production and selection

At the LHC, the cross-section for the process $pp \rightarrow W + X$ with $W \rightarrow l\nu$ and $l = e, \mu$ is 30 nb. Therefore, about 300 million events are expected to be produced in each experiment in one year of operation at low luminosity (integrated luminosity 10 fb^{-1}). Such a cross-section is a factor of ten larger than at the Tevatron ($\sqrt{s} = 1.8 \text{ TeV}$).

To extract a clean W signal, one should require:

- An isolated charged lepton (e or μ) with $p_T > 25 \text{ GeV}$ inside the pseudorapidity region devoted to precision physics $|\eta| < 2.4$.
- Missing transverse energy $E_T^{\text{miss}} > 25 \text{ GeV}$.
- No jets in the event with $p_T > 30 \text{ GeV}$.
- The recoil should satisfy $|\vec{u}| < 20 \text{ GeV}$.

The last two cuts are applied to reject W 's produced with high p_T , since for large p_T^W the transverse mass resolution deteriorates and the QCD background increases. The acceptance of the above cuts is about 25%. By assuming a lepton reconstruction efficiency of 90% and an identification efficiency of 80% [86], a total selection efficiency of about 20% should be achieved. Therefore, after all cuts about 60 million W 's are expected in one year of data taking at low luminosity in each experiment, which is a factor of about 50 larger than the statistics expected from the Tevatron Run 2.

3.13 Expected uncertainties

Due to the large event sample, the statistical uncertainty on the W mass should be smaller than 2 MeV for an integrated luminosity of 10 fb^{-1} .

Since the W mass is obtained by fitting the experimental distribution of the transverse mass with Monte Carlo samples, the systematic uncertainty will come mainly from the Monte Carlo modelling of the data, *i.e.* the physics and the detector performance. Uncertainties related to the physics include the knowledge of: the W p_T spectrum and angular distribution, the parton distribution functions, the W width, the radiative decays and the background. Uncertainties related to the detector include the knowledge of: the lepton energy and momentum scale, the energy and momentum resolution, the detector response to the recoil and the effect of the lepton identification cuts. At the LHC, as now at the Tevatron, most of these uncertainties will be constrained *in situ* by using data samples such as $Z \rightarrow ll$ decays. The latter will be used to determine the lepton energy scale, to measure the detector resolution, to model the detector response to the W recoil and the p_T spectrum of the W , *etc.*

The advantages of the LHC with respect to the Tevatron experiments are:

- The large number of W events mentioned above.
- The large size of the 'control samples'. About six million $Z \rightarrow ll$ decays, where $l = e, \mu$, are expected in each experiment in one year of data taking at low luminosity after all selection cuts. This is a factor of about 50 larger than the event sample from the Tevatron Run 2.
- ATLAS and CMS are in general more powerful than CDF and D0 are, in terms of energy resolution, particle identification capability, geometrical acceptance and granularity. What may be more important for this measurement is the fact that ATLAS and CMS will benefit from extensive and detailed simulations and test-beam studies of the detector performance, undertaken even before the start of data-taking

Nevertheless, the LHC experiments have complex detectors, which will require a great deal of study before their behaviour is well understood.

To evaluate the systematic uncertainty on the W mass to be expected in ATLAS, $W \rightarrow l\nu$ decays were generated with PYTHIA 5.7 and processed with ATLFAST. After applying the selection cuts discussed above, a transverse mass spectrum was produced for a reference mass value (80.300 GeV). All sources of systematic uncertainty affecting the measurement of the W mass from CDF Run 1 [87, 88] were then considered as an example⁴. Their magnitude was evaluated in most cases by extrapolating from the Tevatron results, on the basis of the expected ATLAS detector performance. The resulting error on the W mass was determined by generating new W samples, each one including one source of uncertainty, and by comparing the resulting transverse mass distributions with the one obtained for the reference mass. A Kolmogorov test [90] was used to evaluate the compatibility between distributions.

Since the goal is a total error of ~ 20 MeV per experiment, the individual contributions should be much smaller than 10 MeV. A large number of events was needed to achieve such a sensitivity. With three million events after all cuts, corresponding to twelve million events at the generation level, a sensitivity at the level of 8 MeV was obtained.

⁴Similar results have been obtained by the D0 experiment [88, 89].

The main sources of uncertainty and their impact on the W mass measurement are discussed one by one in the remainder of this section. The total error and some concluding remarks are presented in Section 3.14.

Lepton energy and momentum scale This is the dominant source of uncertainty on the measurement of the W mass from Tevatron Run 1, where the absolute lepton scale is known with a precision of about 0.1% [87, 88, 89]. Most likely, this will be the dominant error also at the LHC. In order to measure the W mass with a precision of better than 20 MeV, the lepton scale has to be known to 0.02%. The latter is the most stringent requirement on the energy and momentum scale from LHC physics. It should be noted that a very high precision (0.04%) must be achieved also by the Tevatron experiments in Run 2, in order to measure the W mass to 40 MeV [83]. If such a precision will indeed be demonstrated at the Tevatron, it would represent a good benchmark for the LHC experiments.

The lepton energy and momentum scale will be calibrated *in situ* at the LHC by using physics samples, which will complement the information coming from the hardware calibration, from the magnetic field mapping of solenoids and toroids, and from test-beam measurements. The muon scale will be calibrated by using mainly $Z \rightarrow \mu\mu$ events, and the electromagnetic calorimeter scale will be calibrated by using mainly $Z \rightarrow ee$ events or E/p measurements for isolated electrons, where E and p are the electron energy and momentum as measured in the electromagnetic calorimeter and in the inner detector respectively. Leptonic decays of other resonances (Υ , J/ψ) should provide additional constraints which minimise the extrapolation error to lower masses than the Z boson mass.

Similar methods are used today at the Tevatron, where the uncertainty on the absolute lepton scale is dominated by the statistical error due to the limited Z data sample. The main advantage of the LHC compared to the Tevatron is the large sample of $Z \rightarrow ll$ decays. The Z boson is close in mass to the W boson, therefore the extrapolation error from the point where the scale is determined to the point where the measurement is performed is small.

A preliminary study of the error on the absolute electron scale to be expected in ATLAS was performed by using a sample of 500000 $Z \rightarrow ee$ decays processed through a full GEANT-based simulation of the ATLAS detector [86]. Several possible sources of uncertainties were considered: the knowledge of the amount of material in the inner detector, which affects the electromagnetic calorimeter scale because of photon bremsstrahlung; radiative Z decays, which distort the reconstructed mass spectrum; the modelling of the underlying event and of the pile-up at low and high luminosity. Table 4 shows that the impact of these uncertainties on the electron scale in the calorimeter can most likely be kept below 0.02%. The most stringent requirement to achieve this goal is the knowledge of the material in the inner detector to 1%, which will require scrutiny during construction plus *in situ* measurements with photon conversions and E/p for isolated electrons. More details can be found in [86].

Table 4: Expected contributions to the uncertainty on the electron energy scale of the ATLAS electromagnetic calorimeter, as determined using a fully-simulated sample of $Z \rightarrow ee$ decays (from [86]).

Source	Requirement	Uncertainty on scale
Material in inner detector	Known to 1%	< 0.01%
Radiative decays	Known to 10%	< 0.01%
Underlying event	Calibrate and subtract	\ll 0.03%
Pile-up at low luminosity	Calibrate and subtract	\ll 0.01%
Pile-up at high luminosity	Calibrate and subtract	\ll 0.01%

Several experimental constraints will be needed to achieve a 0.02% uncertainty on the inner detector muon scale: the solenoidal magnetic field in the inner cavity must be known locally to better than 0.1%, the alignment must be understood locally to $\sim 1 \mu\text{m}$ in the bending plane, *etc.*. A detailed discussion on how to meet these goals can be found in [86, 91].

The scale calibration of the external muon spectrometer depends on the knowledge of the magnetic field, on the chamber alignment and on the knowledge of the muon energy losses in the calorimeters. The latter must be understood to a precision of 0.25% in order to achieve the goal uncertainty of 0.02% on the absolute scale. A preliminary study based on a full GEANT simulation of the ATLAS detector demonstrated that with a sample of only 10000 $Z \rightarrow \mu\mu$ decays a scale uncertainty of 0.1% should be attained in the muon spectrometer. More details can be found in [86, 92].

In conclusion, to achieve the needed precision on the lepton scale, several experimental constraints will have to be satisfied. In addition, cross-checks and combined fits between different sub-detectors (inner detector and electromagnetic calorimeter for the electron scale, inner detector and muon system for the muon scale) will be needed. Indeed, only in an over-constrained situation will it be possible to disentangle the various contributions to the detector response, and therefore to derive a reliable systematic error.

Lepton energy and momentum resolution To keep the uncertainty on the W mass from the lepton resolution to less than 10 MeV, the energy resolution of the electromagnetic calorimeter and the momentum resolution of the inner detector and muon system have to be known with a precision of better than 1.5%.

The lepton energy and momentum resolutions will be determined at the LHC by using information from test-beam data and from Monte Carlo simulations of the detector, as well as *in situ* measurements of the Z width in $Z \rightarrow ll$ final states. The E/p distribution for electrons from W decays provides an additional tool. These methods are used presently at the Tevatron. As an example, the statistical error on the momentum resolution obtained by CDF in Run 1A is 10%, whereas the systematic error is only 1% and is dominated by the uncertainty on the radiative decays of the Z [87]. Since the ATLAS performance in terms of momentum resolution is expected to be similar to that of CDF in the momentum range relevant to W production and decays, and since the statistical error at the LHC will be negligible, a total error of much less than 1.5% should be achieved. This uncertainty might further be decreased if improved theoretical calculations of radiative Z decays will become available.

Recoil modelling The transverse momentum of the system recoiling against the W , together with the lepton transverse momentum, is used to determine the p_T of the neutrino (see Equation 25). The recoil is mainly composed of soft hadrons from the underlying event, for which neither the physics nor the detector response are known with enough accuracy. Therefore, in order to get a reliable recoil distribution in the Monte Carlo, information from data is used at the Tevatron. By exploiting the similar production mechanisms of W and Z bosons, in each Monte Carlo event with a given p_T^W (determined from the truth information) the recoil is replaced by the recoil measured in the data for Z events characterised by a p_T^Z (measured by the leptons) similar to p_T^W . The resulting error on the W mass from CDF Run 1A is 60 MeV per channel, and is dominated by the limited statistics of Z data. The result obtained from Run 1B (about 30 MeV) shows that this uncertainty scales with \sqrt{N} , where N is the number of events. Extrapolating to the LHC data sample, an error of smaller than 10 MeV per channel should be achieved. It should be noted that the recoil includes the contribution of the pile-up expected at low luminosity (two minimum-bias events per bunch crossing on average).

W p_T spectrum The modelling of p_T^W in the Monte Carlo is affected by both theoretical and experimental uncertainties. Theoretical uncertainties arise from the difficulty in predicting the non-perturbative

regime of soft-gluon emission, as well as from missing higher-order QCD corrections. Experimental uncertainties are mainly related to the difficulty of simulating the detector response to low-energy particles.

Therefore, the method used at the Tevatron to obtain a reliable estimate of p_T^W consists of measuring the p_T distribution of the Z boson from $Z \rightarrow ll$ events in the data, exploiting the fact that both gauge-bosons have similar p_T distributions, and using the theoretical prediction for the ratio p_T^W/p_T^Z (in this ratio several uncertainties cancel) to convert the measured p_T^Z into p_T^W . The resulting error on the W mass obtained by CDF is 20 MeV, dominated by the limited Z statistics.

At the LHC, the average transverse momentum of the W (Z) is 12 GeV (14 GeV), as given by PYTHIA 5.7. Over the range $p_T(W, Z) < 20$ GeV, both gauge-bosons have p_T spectra which agree to within $\pm 10\%$. By assuming a negligible statistical error on the knowledge of p_T^Z , which will be measured with high-statistics data samples, and by using the p_T^Z spectrum instead of the p_T^W distribution, an error on the W mass of about 10 MeV per channel was obtained without any further tuning. Although the leading-order parton shower approach of PYTHIA is only an approximation to reality, this result is encouraging. Furthermore, improved theoretical calculations for the ratio of the W and Z p_T distributions should become available at the time of the LHC, so that the final uncertainty will most likely be smaller than 10 MeV.

Parton distribution functions Parton momentum distributions inside the protons determine the W longitudinal momentum, and therefore affect the transverse mass distribution through lepton acceptance effects. At the Tevatron, parton distribution functions (pdf), in particular the u/d ratio, are constrained by measuring the forward-backward charge asymmetry of the W rapidity distribution. Such an asymmetry, which is typical of $p\bar{p}$ collisions, is not present in pp collisions and therefore cannot be used at the LHC. However, it has been shown [55] that pdf can be constrained to a few percent at the LHC by using mainly the pseudorapidity distributions of leptons produced in W and Z decays. The resulting uncertainty on the W mass should be smaller than 10 MeV.

W width At hadron colliders, the W width can be obtained from the measurement of R , the ratio between the rate of leptonically decaying W 's and leptonically decaying Z 's:

$$R = \frac{\sigma_W}{\sigma_Z} \times \frac{BR(W \rightarrow l\nu)}{BR(Z \rightarrow ll)} \quad (26)$$

where the Z branching ratio (BR) is obtained from LEP measurements, and the ratio between the W and the Z cross-sections is obtained from theory. By measuring R , the leptonic branching ratio of the W can be extracted from the above formula, and therefore Γ_W can be deduced assuming Standard Model couplings for $W \rightarrow l\nu$. The precision achievable with this method is limited by the theoretical knowledge of the ratio of the W to the Z cross-sections. Another method consists of fitting the high-mass tails of the transverse mass distribution, which are sensitive to the W width.

By using these methods, the W width was measured with a precision of about 60 MeV by CDF in Run 1, which translates into an error of 10 MeV per channel on the W mass measurement.

In Run 2, the W width should be measured with a precision of 30 MeV [83], which contributes an error of 7 MeV per channel on the W mass. This is however a conservative estimate for the LHC, where the W width should be measured with higher precision than at Tevatron by using the high-mass tails of the transverse mass distribution. The measurement of R , on the other hand, in addition to being model-dependent would require very precise theoretical inputs. It should be noted that one could also use the value of the W width predicted by the Standard Model.

Radiative decays Radiative $W \rightarrow l\nu\gamma$ decays produce a shift in the reconstructed transverse mass, which must be precisely modelled in the Monte Carlo. Uncertainties arise from missing higher-order

corrections, which translate into an error of 20 MeV on the W mass as measured by CDF in Run 1. Improved theoretical calculations have become recently available [93]. Furthermore, the excellent granularity of the ATLAS electromagnetic calorimeter, and the large statistics of radiative Z decays, should provide useful additional information. Therefore, a W mass error of 10 MeV per channel was assumed in this study. This is a conservative estimate, since the D0 error from Run 1 is smaller than 10 MeV [88].

Background Backgrounds distort the W transverse mass distribution, contributing mainly to the low-mass region. Therefore, uncertainties on the background normalisation and shape translate into an error on the W mass. This error is at the level of 5 MeV (25 MeV) in the electron (muon) channel for the measurement performed by CDF in Run 1, where the background is known with a precision of about 10%.

A study was made of the main backgrounds to $W \rightarrow l\nu$ final states to be expected in ATLAS. The contribution from $W \rightarrow \tau\nu$ decays should be of order 1.3% in both the electron and the muon channel. The background from $Z \rightarrow ee$ decays to the $W \rightarrow e\nu$ channel is expected to be negligible, whereas the contribution of $Z \rightarrow \mu\mu$ decays to the $W \rightarrow \mu\nu$ channel should amount to 4%. The difference between these two channels is due to the fact that the calorimetry coverage extends up to $|\eta| \sim 5$, whereas the coverage of the muon spectrometer is limited to $|\eta| < 2.7$. Therefore, muons from Z decays which are produced with $|\eta| > 2.7$ escape detection and thus give rise to a relatively large missing transverse momentum. On the other hand, electrons from Z decays produced with $|\eta| > 2.4$ are not efficiently identified, because of the absence of tracking devices and of fine-grained calorimetry, however their energy can be measured up to $|\eta| \sim 5$. Therefore these events do not pass the E_T^{miss} cut described in Section 3.12. Finally, $t\bar{t}$ production and QCD processes are expected to give negligible contributions.

In order to limit the error on the W mass to less than 10 MeV, the background to the electron channel should be known with a precision of 30%, which is easily achievable, and the background to the muon channel should be known with a precision of 7%. The latter could be monitored by using $Z \rightarrow ee$ decays.

3.14 Results

The expected contributions to the uncertainty on the W mass measurement, of which some are discussed in the previous sections, are summarised in Table 5. For comparison, the errors obtained by CDF in Run 1A (integrated luminosity $\sim 20 \text{ pb}^{-1}$) and Run 1B (integrated luminosity $\sim 90 \text{ pb}^{-1}$) are also shown separately. The evolution of the uncertainty between Run 1A and Run 1B shows the effect of the increased statistics and of the improved knowledge of the detector performance and of the physics, and provides a solid basis for the LHC results presented here.

With an integrated luminosity of 10 fb^{-1} , which should be collected in one year of LHC operation, and by considering only one lepton species (e or μ), a total uncertainty of smaller than 25 MeV should be achieved by each LHC experiment. By combining both lepton channels, which should also provide useful cross-checks since some of the systematic uncertainties are different for the electron and the muon sample, and taking into account common uncertainties, the total error should decrease to less than 20 MeV per experiment. Finally, the total LHC uncertainty could be reduced to about 15 MeV by combining ATLAS and CMS together. Such a precision would allow the LHC to compete with the expected precision at a Next Linear Collider [94].

The most serious experimental challenge in this measurement is the determination of the lepton absolute energy and momentum scale to 0.02%. All other uncertainties are expected to be of the order of (or smaller than) 10 MeV. However, to achieve such a goal, improved theoretical calculations of radiative decays, of the W and $Z p_T$ spectra, and of higher-order QCD corrections will be needed.

The results presented here have to be considered as preliminary and far from being complete. It may be possible that, by applying stronger selection cuts, for instance on the maximum transverse

Table 5: Expected contributions to the uncertainty on the W mass measurement in ATLAS for each lepton family and for an integrated luminosity of 10 fb^{-1} (fourth column). The corresponding uncertainties of the CDF measurement in the electron channel, as obtained in Run 1A [87] and Run 1B [88], are also shown for comparison (second and third column).

Source	ΔM_W (CDF Run 1A) (MeV)	ΔM_W (CDF Run 1B) (MeV)	ΔM_W (ATLAS) (MeV)
Statistics	145	65	< 2
$E - p$ scale	120	75	15
Energy resolution	80	25	5
Recoil model	60	33	5
Lepton identification	25	–	5
p_T^W	45	20	5
Parton distribution functions	50	15	10
W width	20	10	7
Radiative decays	20	20	< 10
Background	10	5	5
TOTAL	230	113	< 25

momentum of the W , the systematic uncertainties may be reduced further. Moreover, two alternative methods to measure the W mass can be envisaged. The first one uses the p_T distribution of the charged lepton in the final state. Such a distribution features a Jacobian peak at $p_T^l \sim M_W/2$ and has the advantage of being affected very little by the pile-up, therefore it could be used at high luminosity. However, the lepton momentum is very sensitive to the p_T of the W boson, whereas the transverse mass is not, and hence a very precise theoretical knowledge of the W p_T spectrum would be needed to use this method. Another possibility is to use the ratio of the transverse masses of the W and Z bosons [95]. The Z transverse mass can be reconstructed by using the p_T of one of the charged leptons, while the second lepton is treated like a neutrino whose p_T is measured by the first lepton and the recoil. By shifting the m_T^Z distribution until it fits the m_T^W distribution, it is possible to obtain a scaling factor between the W and the Z masses and therefore the W mass. The advantage of this method is that common systematic uncertainties cancel in the ratio. The main disadvantage is the loss of a factor of ten in statistics, since the $Z \rightarrow ll$ sample is a factor of ten smaller than the $W \rightarrow l\nu$ sample (and only events near to the Jacobian peak contribute significantly to the mass determination). Furthermore, differences in the production mechanism between the W and the Z (p_T , angular distribution, *etc.*), and possible biases coming from the Z selection cuts, will give rise to a non-negligible systematic error.

The final measurement will require using all the methods discussed above, in order to cross-check the systematic uncertainties and to achieve the highest precision.

3.15 Conclusions

Preliminary studies indicate that measuring the W mass at the LHC with a precision of about 15 MeV should be possible, although very challenging. The biggest single advantage of the LHC is the large statistics, which will result in small statistical errors and good control of the systematics. To achieve such unprecedented precision, improved theoretical calculations in many areas will be needed (*e.g.* radiative decays, pdf's, p_T^W), and many stringent experimental requirements will have to be satisfied.

3.2 Drell-Yan production of lepton pairs

3.21 Introduction

Parton level: In the Standard Model (SM), the production of lepton pairs in hadron-hadron collisions (the Drell-Yan process) is described by s -channel exchange of photons or Z bosons. The parton cross section in the centre-of-mass system has the form:

$$\frac{d\hat{\sigma}}{d\Omega} = \frac{\alpha^2}{4s} [A_0(1 + \cos^2 \theta) + A_1 \cos \theta] \quad (27)$$

where $\hat{\sigma} = \frac{4\pi\alpha^2}{3s} A_0$ and $A_{FB} = \frac{3}{8} \frac{A_1}{A_0}$ give the total cross section and the forward-backward asymmetry, respectively. The terms A_0 and A_1 are fully determined by the electroweak couplings of the initial- and final-state fermions. At the Z peak, the Z exchange dominates while the interference term is vanishing. At higher energies, both photon and Z exchange contribute and the large value of the forward-backward asymmetry arises from the interference between the neutral currents.

Fermion-pair production above the Z pole is a rich search field for new phenomena at present and future high-energy colliders [96]. The differential cross section is given by

$$\frac{d\hat{\sigma}}{d\Omega} \sim |\gamma_s + Z_s + \text{New Physics ?!}|^2 \quad (28)$$

where many proposed types of new physics can lead to observable effects by adding new amplitudes or through their interference with the neutral currents of the SM.

At hadron colliders: The parton cross sections are folded with the parton distribution functions (pdf's):

$$\frac{d^2\sigma}{dM_{ll}dy}(pp \rightarrow l_1 l_2) \sim \sum_{ij} (f_{i/p}(x_1) f_{j/p}(x_2) + (i \leftrightarrow j)) \hat{\sigma} \quad (29)$$

where $\hat{\sigma}$ is the cross section for the partonic subprocess $ij \rightarrow l_1 l_2$, $M_{ll} = \sqrt{\tau s} = \sqrt{\hat{s}}$ and y are the invariant mass and rapidity of the lepton pair, $x_1 = \sqrt{\tau} e^y$ and $x_2 = \sqrt{\tau} e^{-y}$ are the parton momentum fractions, and $f_{i/p(\bar{p})}(x_i)$ is the probability to find a parton i with momentum fraction x_i in the (anti)proton.

$$\sigma_{F\pm B}(y, M) = \left[\int_0^1 \pm \int_{-1}^0 \right] \sigma_{ll} d(\cos \theta^*) \quad (30)$$

$$A_{FB}(y, M) = \frac{\sigma_{F-B}(y, M)}{\sigma_{F+B}(y, M)} \quad (31)$$

The total cross section and the forward-backward asymmetry are functions of observables which are well measured experimentally: the invariant mass and the rapidity of the final state lepton-pair. For a pair of partons ($x_1 \geq x_2$), there are four combinations of quarks initiating Drell-Yan production: $u\bar{u}, \bar{u}u, d\bar{d}, \bar{d}d$. In pp collisions, the antiquarks come always from the sea while the quarks can have valence or sea origin. The x -range probed depends on the mass and rapidity of the lepton-pair as shown in Table 6. Going to higher rapidities increases the difference between x_1 and x_2 and hence the probability that the first quark is a valence one.

3.22 Event rates

The expected numbers of events for the Tevatron Run 2 (TEV2) and the LHC are shown in Table 7 and Figure 16. The estimation is based on simulations with PYTHIA 5.7 [97] by applying the following cuts:

1. For LHC: both leptons $|\eta| < 2.5$; for TEV2: one lepton $|\eta| < 1$, the other $|\eta| < 2.5$.

Table 6: x_1 and x_2 for different masses and rapidities.

M (GeV)	91.2			200			1000		
y	0	2	4	0	2	4	0	2	4
x_1	0.0065	0.0481	0.3557	0.0143	0.1056	0.7800	0.0714	0.5278	-
x_2	0.0065	0.0009	0.0001	0.0143	0.0019	0.0003	0.0714	0.0097	-

2. For both leptons, $p_T > 20$ GeV.

The data sample can be divided into three classes:

Events near the Z pole:

- There will be a huge sample of Z events at the LHC. These will allow study of the interplay between $\sin^2 \theta_{\text{eff}}^{\text{lept}}(M_Z^2)$ and the pdf's.

High mass pairs (110-400 GeV):

- LEP2 will study this region up to 200 GeV.
- TEV2 will collect a sizeable sample of events in this region.
- LHC will be able to do precision studies.

Very high mass pairs (400-4000 GeV):

- TEV2 will have a first glance.
- LHC will collect a sizeable sample for tests of the SM at the highest momentum transfers (Q^2) and for searches of new phenomena at the TeV scale.

Table 7: PYTHIA estimate: expected number of events for one experiment in the e^+e^- and $\mu^+\mu^-$ channels. For LEP2 and CDF the observed number of events is shown.

Pair Mass	LEP2	CDF	TEV2	LHC
	600 pb ⁻¹	110 pb ⁻¹	10 fb ⁻¹	100 fb ⁻¹
	SM / Data	Data	PYTHIA	PYTHIA
Z pole	-	-	$\sim 1.5 \times 10^6$	$\sim 134 \times 10^6$
> 110 GeV	12500	148 (> 150 GeV)	46000	2.6×10^6
> 400 GeV	-	1	250	33000

3.23 Measurements of σ and A_{FB}

The experimental signature for Drell-Yan events is distinctive: a pair of well isolated leptons with opposite charge. This should be straight forward for the ATLAS and CMS detectors to identify. The backgrounds are low: W^+W^- , $\tau^+\tau^-$, $c\bar{c}$, $b\bar{b}$, $t\bar{t}$; fakes, cosmics *etc.*. If the need arises, they can be further suppressed by acoplanarity and isolation cuts. The selection cuts used in this study have already been described in the section on simulations.

An important ingredient in the cross section measurement is the precise determination of the luminosity. A promising possibility is to go directly to the parton luminosity [55] by using the W^\pm (Z) production of single (pair) leptons:

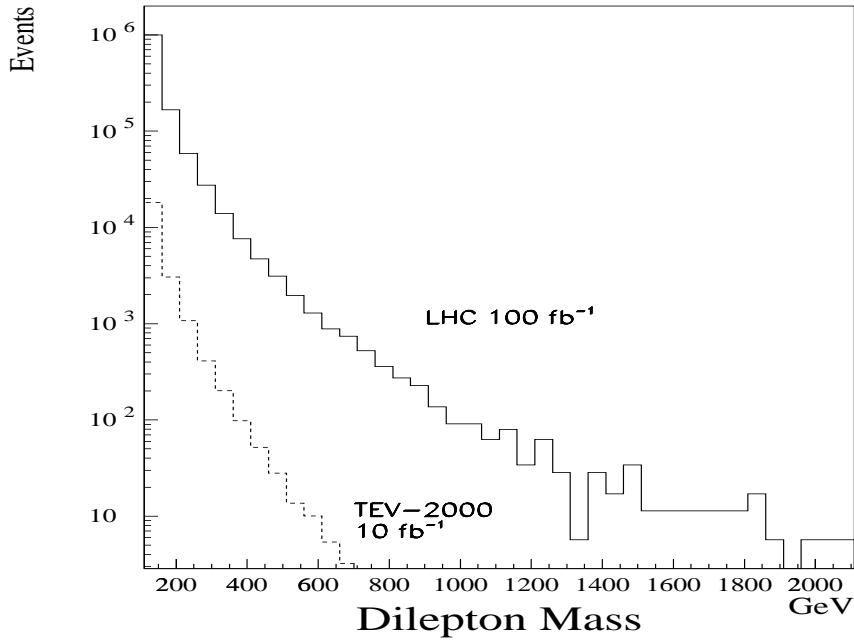


Fig. 16: Expected number of events for TEV-2000 and LHC in one channel/experiment as a function of the dilepton mass.

- Constrain the pdf's.
- Measure directly the parton-parton luminosity.

In this way, the systematic error on $\sigma_{DY}^{\text{high } Q^2}$ relative to σ_Z can be reduced to $\sim 1\%$.

In order to measure the forward-backward asymmetry, it is necessary to tag the directions of the incoming quark and antiquark. At the Tevatron, the $p\bar{p}$ collisions provide a natural label for the valence (anti)quark. In contrast at the LHC, the pp initial state is symmetric. But in the reaction $q\bar{q} \rightarrow l^+l^-$ only q can be a valence quark, carrying on average a higher momentum compared to the sea antiquarks. Therefore at the LHC, A_{FB} will be signed according to the sign of the rapidity of the lepton pair $y(ll)$. Consequently, A_{FB} increases as a function of $y(ll)$ [98, 99] (see Figure 18).

A precise measurement of σ and A_{FB} at large \hat{s} requires good knowledge of the different types of electroweak radiative corrections to the DY process: vertex, propagator, EW boxes. A complete one-loop parton cross section calculation has been performed [71]. The size of these corrections after folding with the pdf's and the expected experimental precision on the cross section measurement are compared in Figure 17. The LHC experiments can probe these corrections up to ~ 2 TeV.

3.24 Determination of $\sin^2 \theta_{\text{eff}}^{\text{lept}}(M_Z^2)$

A very precise determination of $\sin^2 \theta_{\text{eff}}^{\text{lept}}(M_Z^2)$ will constrain the Higgs mass or, if the Higgs boson is discovered, will check the consistency of the SM [100]. The latest result of the LEP Electroweak Working Group from the summer of 1999 is:

$$\sin^2 \theta_{\text{eff}}^{\text{lept}}(M_Z^2) = 0.23151 \pm 0.00017 \quad (32)$$

Event selection A careful study [101] of the precision which can be obtained from the $Z \rightarrow ee$ decay by ATLAS and CMS has been made using PYTHIA 5.7 and JETSET 7.2. Background processes

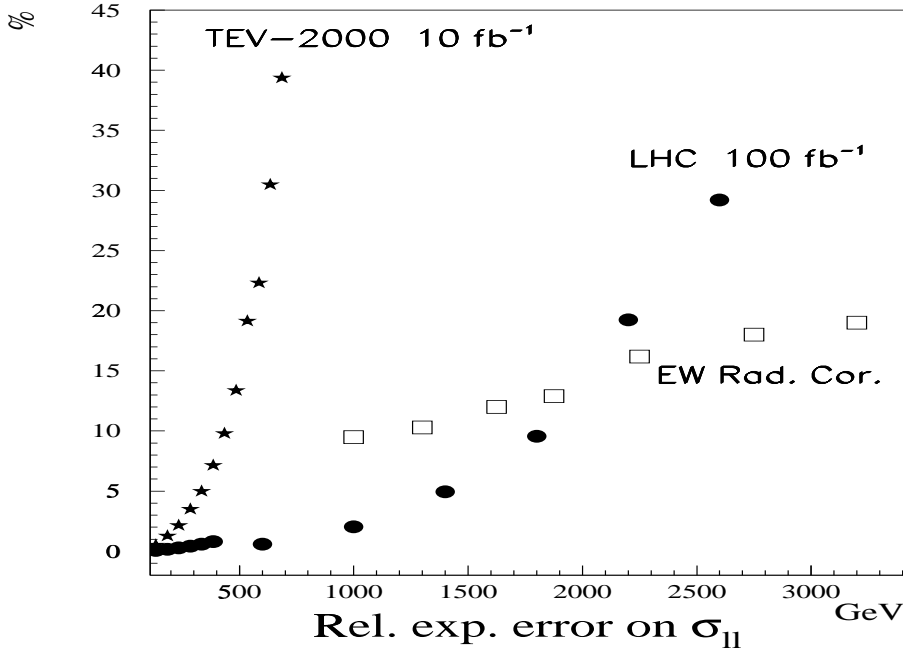


Fig. 17: Size of the electroweak radiative corrections and the expected relative experimental precision on the cross section measurement for e^+e^- and $\mu^+\mu^-$ from one experiment in % as a function of the dilepton mass.

from $pp \rightarrow 2 \text{ jets}$ and $pp \rightarrow t\bar{t} \rightarrow e^+e^-$ have been included. In the regions of precision measurements ($|\eta| \leq 2.5$), the precision which can be obtained from $Z \rightarrow \mu\mu$ decays should be comparable to that from the electron channel. In addition, the detectors have calorimetry extending to $|\eta| \sim 5$ and hence, if it is possible to tag very forward electrons, albeit with significantly lower quality, it may be possible to improve dramatically the measurement of $\sin^2 \theta_{\text{eff}}^{\text{lept}}(M_Z^2)$.

The following cuts were made:

1. $p_T^{\text{electron}} > 20 \text{ GeV}/c$
2. $85.2 \text{ GeV}/c^2 < M(e^+e^-) < 97.2 \text{ GeV}/c^2$

In all cases, one electron was required in the precision calorimetry $|\eta| \leq 2.5$. Efficiencies after typical electron identification cuts were taken from detailed studies reported in [86]. These are typically around 70%, with corresponding jet rejections of $> 10^4$ (there was no advantage for this measurement of larger rejection factors). For the second electron, the possibility for it to be identified in the forward calorimetry $2.5 < |\eta| \leq 4.9$ was considered. In this region, there is no magnetic tracking. An electron identification efficiency of 50% was assumed with a corresponding jet rejection of ρ . Extending the pseudorapidity coverage for the second electron increases the range of lepton pair rapidity from $|y(e^+e^-)| \leq \sim 2$ to $|y(e^+e^-)| \leq \sim 3$. Figure 18 shows how the asymmetry varies as a function of $|y(e^+e^-)|$.

Statistical sensitivity The sensitivity of A_{FB} to $\sin^2 \theta_{\text{eff}}^{\text{lept}}(M_Z^2)$ can be parametrised as follows:

$$\begin{aligned}
 A_{FB} &= b(a - \sin^2 \theta_{\text{eff}}^{\text{lept}}(M_Z^2)) \\
 a^{O(\alpha^3)} &= a^{\text{Born}} + \Delta a^{\text{QED}} + \Delta a^{\text{QCD}} \\
 b^{O(\alpha^3)} &= b^{\text{Born}} + \Delta b^{\text{QED}} + \Delta b^{\text{QCD}}
 \end{aligned} \tag{33}$$

Values of a and b were calculated in [68] and have been re-evaluated by Baur corresponding to the above cuts - see Table 8.

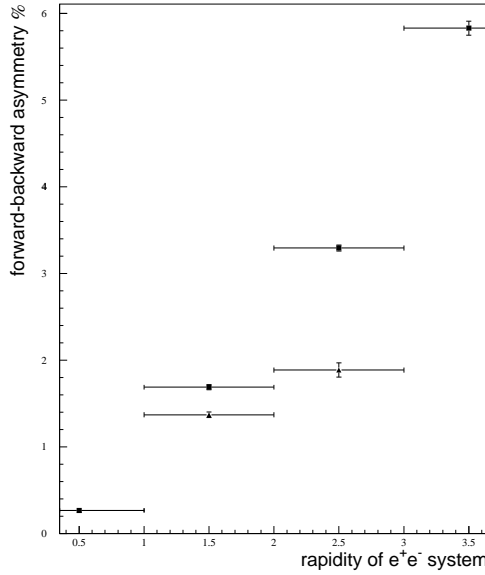


Fig. 18: Forward-backward asymmetry vs rapidity for e^+e^- pairs from Z decays satisfying the selection cuts described in Section 3.24. The asymmetry is shown where both electrons have $|\eta| < 2.5$ (triangles) and where one electron is allowed to have $|\eta| < 4.9$ (squares). The results are the same for both sets of cuts in the first bin.

A summary of the statistical errors which can be obtained with 100 fb^{-1} are indicated in Table 9. With the best rejection factors shown in the table, the effect of the background is negligible. If no jet rejection is possible in the forward calorimetry, the statistical precisions which can be obtained on $\sin^2 \theta_{\text{eff}}^{\text{lept}}(M_Z^2)$ are 3.4×10^{-4} and 4.1×10^{-4} for no y cut and $|y(e^+e^-)| > 1.0$ respectively. While the sensitivity to $\sin^2 \theta_{\text{eff}}^{\text{lept}}(M_Z^2)$ is increased by cutting on $|y(e^+e^-)|$ (see Table 8), the gain is reduced by the loss of acceptance and increased significance of the background when the forward calorimetry is used. It is probable that greater sensitivity could be obtained by fitting A_{FB} as a function of $|y(e^+e^-)|$.

From Table 9, it can be seen that for a single lepton species from one LHC experiment, using leptons measured in $|\eta| < 2.5$, a statistical precision of 4.0×10^{-4} on $\sin^2 \theta_{\text{eff}}^{\text{lept}}(M_Z^2)$ could be obtained. With the combination of electrons and muons in two experiments, 2.0×10^{-4} could be obtained.

The table shows that for moderate jet rejection ($\geq \sim 10^2$) in the forward calorimetry, a statistical precision of 1.4×10^{-4} could be reached by a single experiment using just the electron channel (cannot include the muons). Even a poor rejection ~ 10 , would provide a useful measurement. While no studies with full detector simulation have been done, it seems likely that both the ATLAS and CMS forward calorimetry will be able to provide useful electron identification because of moderate longitudinal and transverse segmentation. Combining both experiments will permit a further $\sqrt{2}$ reduction in the statistical uncertainty.

Systematic uncertainties In order to be able to exploit the possibility of measuring $\sin^2 \theta_{\text{eff}}^{\text{lept}}(M_Z^2)$ with such high precision, the systematic errors have to be comparably small. Quick estimates indicate that the following factors are the most important ones:

1. *pdf's*: affect both the lepton acceptance as well as the results of radiative correction calculations.
2. *Lepton acceptance and reconstruction efficiency as a function of lepton rapidity*: while there is some cancellation in the determination of the asymmetry, the product will need to be known to better than 0.1%. CDF [102] has shown that it is possible to achieve a precision of about 1%, with

Table 8: Parameters a and b in Equation 33.

Cuts	a^{Born}	Δa^{QED}	Δa^{QCD}	$a^{O(\alpha^3)}$	b^{Born}	Δb^{QED}	Δb^{QCD}	$b^{O(\alpha^3)}$
$ \eta < 2.5$ both e^\pm	.2481	.0025	-.0026	.2480	0.48	-0.01	-0.16	0.31
$ \eta < 2.5$ both e^\pm								
$ y(e^+e^-) > 1.0$.2503	-.0009	-.0069	.2425	0.74	0.05	-0.03	0.76
$ \eta < 2.5$ one e^\pm								
$ \eta < 4.9$ the other e^\pm	.2483	-.0005	-.0015	.2463	1.18	0.15	-0.10	1.23
$ \eta < 2.5$ one e^\pm								
$ \eta < 4.9$ the other e^\pm								
$ y(e^+e^-) > 1.0$.2486	.0011	-.0028	.2469	1.66	0.01	-0.04	1.63

the largest contribution being due to the uncertainty in the pdf's.

3. *Effects of higher order QCD (and electroweak) corrections:* can be estimated by varying the errors on the parameters a and b .
4. *Mass Scale:* A_{FB} varies as a function of the invariant mass of the lepton pair. Since the measured asymmetry corresponds to an integration over the Z resonance, it is important to understand the mass scale. It is expected that this will be known to $\sim 0.02\%$ (see 3.13) by direct comparison of the Z peak with the measured LEP parameters.

The most important systematic contribution is that coming from the uncertainties in the pdf's. A study using several "modern" pdf's (MRST, CTEQ3 and CTEQ4) gave agreement between the resulting values of A_{FB} within the 1% statistical errors of the study (5×10^5 events were generated for each pdf set). This uncertainty must be reduced by a factor of 10 if it is to be smaller than the expected statistical precision on A_{FB} shown in Table 9. It remains to be seen whether (a) the differences arising from the various pdf's will shrink with increased statistical sensitivity of the study and (b) whether the current pdf's actually describe the measured data sufficiently well (since the pdf's are fitted to common data, variations are not necessarily indicative of the actual uncertainties). New measurements from the Tevatron (and ultimately the LHC itself) will improve the understanding of the pdf's, but it is unclear at this stage whether this will be sufficient. It may be possible to fit simultaneously $\sin^2 \theta_{\text{eff}}^{\text{lept}}(M_Z^2)$ and the pdf's, or alternatively, it may be necessary to reverse the strategy and use the measurement of A_{FB} combined with existing measurements of $\sin^2 \theta_{\text{eff}}^{\text{lept}}(M_Z^2)$ to constrain the pdf's.

3.25 Search for new phenomena

Contact interactions Contact interactions offer a general framework for a new interaction with coupling g and typical energy scale $\Lambda \gg \sqrt{s}$. At LEP2, the current limits [96, 103] for quark-lepton compositeness at 95% CL vary between 3 and 8 TeV, depending on the model. At the LHC scales up to 25-30 TeV are reachable, as illustrated in Figure 19.

Search for resonances The other extreme is the search for resonances like Z' or $\tilde{\nu}$, which produce peaks in the mass distributions. A neutral heavy gauge-boson Z' is characterised by its mass $m_{Z'}$, by its couplings and by its mixing angle θ_M with the standard Z boson. If $\theta_M = 0$ and the Z' has SM couplings, the current limit is $m_{Z'} > 1050$ GeV [104]. For other coupling scenarios the lower limits

Table 9: Statistical precision which can be obtained on $\sin^2 \theta_{\text{eff}}^{\text{lept}}(M_Z^2)$ from measurements of A_{FB} in $Z \rightarrow ee$ from one LHC experiment with 100 fb^{-1} . Results are given for different jet rejection factors ρ for the forward calorimetry $2.5 < |\eta| < 4.9$.

Cuts	ρ	A_{FB} (%)	ΔA_{FB} (%)	$\Delta \sin^2 \theta_{\text{eff}}^{\text{lept}}(M_Z^2)$
$ \eta < 2.5$ both e^\pm	-	0.774	0.020	6.6×10^{-4}
$ \eta < 2.5$ both e^\pm $ y(e^+e^-) > 1.0$	-	1.66	0.030	4.0×10^{-4}
$ \eta < 2.5$ one e^\pm	10^4	2.02	0.017	1.4×10^{-4}
$ \eta < 4.9$ the other e^\pm	10^2	1.98	0.018	1.4×10^{-4}
	10^1	1.68	0.021	1.7×10^{-4}
$ \eta < 2.5$ one e^\pm	10^4	3.04	0.022	1.35×10^{-4}
$ \eta < 4.9$ the other e^\pm	10^2	2.94	0.023	1.41×10^{-4}
$ y(e^+e^-) > 1.0$	10^1	2.31	0.030	1.83×10^{-4}

are model dependent and typically of the order of several hundred GeV. Resonances with masses up to $\sim 4\text{-}5$ TeV can be probed at LHC, as shown in Figure 19.

R-parity violation In SUSY theories with R-parity violation, it is possible to couple sleptons to pairs of SM leptons or quarks through new independent Yukawa couplings (9 λ couplings for the slepton-lepton sector and 27 λ' couplings for the slepton-quark sector). This makes the resonance formation of single scalar neutrino $\tilde{\nu}$ in $d\bar{d}$ scattering possible. It can be observed through the decay of the $\tilde{\nu}$ to lepton pairs, if a suitable combination of two couplings (e.g. $\lambda'_{311}\lambda_{131}$) is present [105]. The K-factor for slepton production is not calculated yet, leading to an uncertainty $\sim 10\%$ in the estimate of the $\lambda\lambda'$ sensitivity.

Low-scale gravity An exciting possibility is the search for low-scale gravity effects in theories with extra spatial dimensions, leading to virtual graviton exchange. The best limits at LEP2 come from combined analysis of Bhabha scattering [106]:

$$\Lambda_T = 1.412(1.077) \text{ TeV for } \lambda = +1(-1) \text{ at } 95\% \text{ CL}$$

In the Drell-Yan process there is a unique contribution from s -channel graviton exchange [107], which modifies the form of the differential cross section and gives a distinct signature:

$$gg \longrightarrow l^+l^- \quad (34)$$

$$\frac{d\sigma}{d\cos\theta} = \frac{\lambda_s^2 s^3}{64\pi M_s^8} (1 - \cos^4\theta) \quad (35)$$

The large parton luminosity for gluons at LHC may also compensate the M_s^{-8} suppression. Scales up to ~ 5 TeV can be probed with luminosity 100 fb^{-1} .

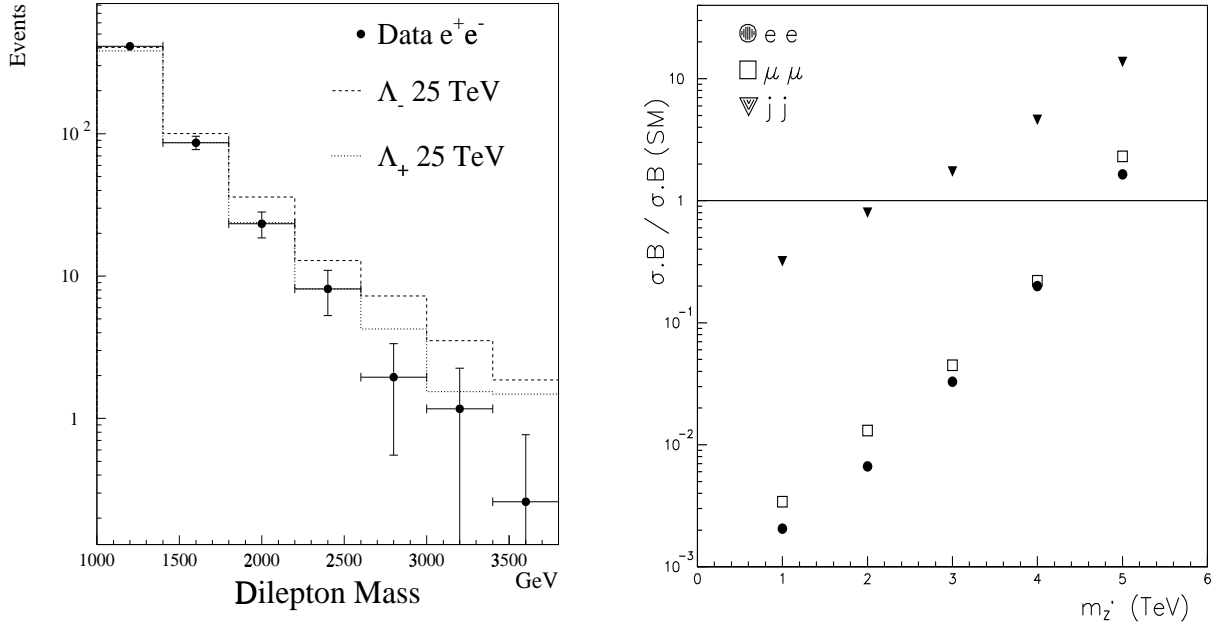


Fig. 19: Left: Contact interaction sensitivity (CMS study). Error bars show SM spectrum; histograms show effect of contact term with $\Lambda = 25$ TeV, the sign corresponds to the sign of the amplitude. Right: Z' mass reach for 100 fb^{-1} (ATLAS study) [53].

3.26 Summary

The main results of this study are:

- A competitive measurement of $\sin^2 \theta_{\text{eff}}^{\text{lept}}(M_Z^2)$ is hard due to the central acceptance of the experiments and the difficulty of controlling the pdf's (parton distribution functions) with the required precision. However, a detector with extended forward acceptance for one of the leptons offers the possibility to measure $\sin^2 \theta_{\text{eff}}^{\text{lept}}(M_Z^2)$ with a statistical precision of 1.4×10^{-4} .
- The total cross-section can be measured with systematic error $\frac{\sigma_{\text{DY}}^{\text{high } Q^2}}{\sigma_Z} < 1\%$.
- A non-zero forward-backward asymmetry A_{FB} can be measured up to 2 TeV with statistical precision $> 3 \sigma$.
- The Drell-Yan process can probe electroweak radiative corrections up to 1.5 TeV with statistical precision at the 2σ level as a function of Q^2 .
- The high energy and luminosity of LHC offers a rich search field at the TeV scale in the Drell-Yan channel: contact interactions, resonance formation (Z' , scalar neutrinos), low-scale gravity, *etc.*

Further studies will refine the following points:

- The effect of higher order QED corrections (initial- and final-state radiation and their interference).
- The effect of experimental cuts on the electroweak corrections.
- The careful separation of the $\sigma_{u\bar{u}}$ and $\sigma_{d\bar{d}}$ contributions.

3.3 Tau physics

The τ lepton is a member of the third generation which decays into particles belonging to the first and second ones. Thus, τ physics could provide some clues to the puzzle of the recurring families of leptons and quarks. One naïvely expects the heavier fermions to be more sensitive to whatever dynamics is responsible for the fermion-mass generation. The pure leptonic or semileptonic character of τ decays

provides a clean laboratory to test the structure of the weak currents and the universality of their couplings to the gauge-bosons.

The last few years have witnessed a substantial change in our knowledge of the τ properties [108, 109]. The large (and clean) data samples collected by the most recent experiments have improved considerably the statistical accuracy and, moreover, have brought a new level of systematic understanding.

A high-energy hadron collider does not provide a very good environment to perform precision τ physics. Nevertheless, there are a few topics where LHC could contribute in a relevant and unique way. Moreover, since the τ is the heaviest known lepton, it can play a very important role in searches for new particles (for example, as in Section 6.1).

3.31 Charged-current universality

Table 10: Present constraints on charged-current lepton universality [109].

	$ g_\mu/g_e $	$ g_\tau/g_\mu $	$ g_\tau/g_e $
$B_{\tau \rightarrow \mu}/B_{\tau \rightarrow e}$	1.0009 ± 0.0022	—	—
$B_{\tau \rightarrow e} \tau_\mu/\tau_\tau$	—	0.9993 ± 0.0023	—
$B_{\tau \rightarrow \mu} \tau_\mu/\tau_\tau$	—	—	1.0002 ± 0.0023
$B_{\pi \rightarrow e}/B_{\pi \rightarrow \mu}$	1.0017 ± 0.0015	—	—
$\Gamma_{\tau \rightarrow \pi}/\Gamma_{\pi \rightarrow \mu}$	—	1.005 ± 0.005	—
$\Gamma_{\tau \rightarrow K}/\Gamma_{K \rightarrow \mu}$	—	0.981 ± 0.018	—
$B_{W \rightarrow l}/B_{W \rightarrow \nu'} (p\bar{p})$	0.98 ± 0.03	—	0.987 ± 0.025
$B_{W \rightarrow l}/B_{W \rightarrow \nu'} (\text{LEP2})$	1.002 ± 0.016	1.008 ± 0.019	1.010 ± 0.019

Table 10 shows the present experimental tests on the universality of the leptonic charged-current couplings. The leptonic τ branching ratios are already known with a quite impressive precision of 0.3%; this translates into a test of g_μ/g_e universality at the 0.22% level. However, in order to test the ratios g_τ/g_μ and g_τ/g_e , one needs precise measurements of the τ mass and lifetime, in addition. At present, these quantities are known with a precision of 0.016% ($m_\tau = 1777.05^{+0.29}_{-0.26}$ MeV) and 0.34% ($\tau_\tau = 290.77 \pm 0.99$ fs), respectively [109], which leads to a sensitivity of 0.23% for the three $g_l/g_{l'}$ ratios.

Future high-luminosity e^+e^- colliders running near the $\tau^+\tau^-$ production threshold could perform more precise measurements of the leptonic τ branching fractions and the τ mass. However, one needs a high-energy machine to measure the τ lifetime. Clearly, the future tests of lepton universality will be limited by the τ_τ accuracy. It is not clear whether the B -factories would be able to improve the present τ_τ measurement in a significant way. Thus, it is important to know how well τ_τ can be determined at LHC.

A less precise but more direct test on the universality of the leptonic W^\pm couplings is provided by the comparison of the different $W^+ \rightarrow l^+\nu_l$ branching fractions. LEP2 has already achieved a better sensitivity than the Tevatron collider, and a further improvement is expected when the full LEP2 statistics will be available. It is an open question whether LHC could be competitive at this level ($\sim 1\%$) of precision.

3.32 *Tau lifetime*

The current world average for the τ lifetime is 290.8 ± 1.0 fs ($c\tau = 87\mu\text{m}$) [109]. Improvements in this measurement would be welcome in order to give better tests of the Standard Model, in particular lepton universality and electroweak calculations. In this section, the results of a preliminary study to examine the LHC potential are given.

In LEP experiments, τ pairs are produced back-to-back with well defined momenta - this will not be the case at the LHC. The first feature allows valuable correlations to be made between the two τ decays, while the second provides the boost required to obtain proper lifetime estimates. At the LHC, $Z \rightarrow \tau\tau$ events will be triggered by requiring one τ to decay to an electron or muon, while the lifetime is estimated from the other τ which is required to decay to three charged particles.

Tau reconstruction A study was made using fully simulated events in the ATLAS detector (see [86] for more details). When the Z has some transverse momentum, the momenta of the τ 's can be deduced by projecting the recoil momentum vector measured by the calorimetry along the lines of flight of the two τ 's (determined from the direction of the lepton and the hadronic jet, respectively). Due to resolution effects, this procedure works best when the τ 's are not back-to-back. The following cuts were made:

- The lepton should have $p_T > 24$ GeV, $|\eta| < 2.5$.
- The identified hadronic jet should contain three charged tracks and satisfy $E_T > 30$ GeV, $|\eta| < 2.5$.
- Transverse mass of lepton and missing energy should be < 50 GeV.
- The angle $\Delta\phi$ between the τ 's in the transverse plane should satisfy: $1.8 < \Delta\phi < 2.7$ or $3.6 < \Delta\phi < 4.5$.
- The invariant mass of the τ pair should satisfy: $60 < m_{\tau\tau} < 120$ GeV.

These cuts result in an efficiency of 1.5%. For these events, the τ momenta could be estimated with a resolution of 15%.

A vertex was formed from the charged tracks in the hadronic jet. It was required that the vertex should be within 2 cm of the interaction point and the invariant mass of the particles should be between 0.4 and 1.78 GeV. The efficiency for this was 70% and resulted in a resolution on the vertex position in the transverse plane of $490\mu\text{m}$, corresponding to a resolution on the proper decay length of $17\mu\text{m}$.

Lifetime estimate The statistical resolution on the proper decay length from the combination of the vertexing and the estimate of the tau momentum is of the order of $21\mu\text{m}$ (corresponding to 55 fs). A simple Monte Carlo study was made to estimate the statistical uncertainty on the τ lifetime (τ_τ) which could be achieved with N hadronic τ decays. Since the resolution of the lifetime for a single event (55 fs) is a fair bit smaller than the τ lifetime (291 fs), the statistical error which can be obtained is dominated by the number of events: $\sigma(\tau_\tau) \approx \tau_\tau/\sqrt{N}$.

At the LHC, the cross section for $Z \rightarrow \tau\tau$ will be 1.5 nb, with a branching ratio of 11% for a lepton and a three-prong hadronic decay. The reconstruction and selection described above results in an efficiency of 0.54%. If 30 fb^{-1} were collected in a low luminosity run, then 26,000 reconstructed τ 's could be used, leading to a statistical error on the lifetime of 1.8 fs. To make this competitive would require increased efficiency for selecting the τ decays - this is probably a low luminosity measurement and so cannot benefit from the statistics of a high luminosity run.

Increasing the efficiency may not be simple, since the cuts were designed to control the background. W +jet events will be removed by the mass cuts, and apart from a small amount of gluon splitting to heavy flavour, the jets should not contain significant lifetime information, hence this background should not be a problem. The B lifetime is a factor of five larger than that of the τ , and hence more care will be required with $b\bar{b}$ events.

Concerning systematic errors coming from the determination of the decay length in the silicon tracking, the average radial position of the detectors in the vertexing layer will need to be understood to better than $10 \mu\text{m}$. This will be challenging but studies suggest this may be feasible [91]. It should be possible to control the systematics on the measurement of recoil momentum of the Z by comparison with $Z \rightarrow ee$ or $Z \rightarrow \mu\mu$ events, where the recoil can be measured accurately by the leptons.

The use of $W \rightarrow \tau\nu$ It may be possible to use the decays $W \rightarrow \tau\nu$ which have a higher cross section than $Z \rightarrow \tau\tau$. In ATLAS, such events could be triggered by a special τ -jet and missing E_T trigger [86]. Information about the τ momentum can be deduced by comparing the energy and direction of the hadronic jet with the direction of the τ and using the τ mass constraint, where the τ direction can be determined from the reconstructed decay vertex. In principle, it is possible to solve completely for the τ momentum, although resolution effects on the vertex position and complications arising from π^0 's in the hadronic jet mean that sometimes solutions are not physical. Alternatively, an approximate estimator can be formed which does not employ the mass constraint [110]. This uses the τ -jet energy, mass and p_T relative to the τ direction - all three quantities being determined from the charged tracks alone. This is more robust but its behaviour is sensitive to the selection cuts. It is yet to be proved that a $W \rightarrow \tau\nu$ signal can be identified with sufficient efficiency above the huge QCD (and in particular, $b\bar{b}$) background.

3.33 Rare decays

Owing to the huge backgrounds, it will not be possible to make a general search for rare decay modes of the τ . However, the lepton-number violating decay $\tau^- \rightarrow \mu^+ \mu^- \mu^-$ has a clean signature, which is well suited for the LHC detectors. The present experimental bound [111] is

$$BR(\tau^- \rightarrow \mu^+ \mu^- \mu^-) < 1.9 \times 10^{-6} \quad (90\% \text{ CL})$$

This limit reflects the size of the existing τ data samples. LHC will produce a huge statistics, several orders of magnitude larger than the present one. The achievable limit will then be set by systematics and backgrounds, which need to be properly estimated. A sensitivity at the level of 10^{-8} does not seem out of reach. This could open a very interesting window into new physics phenomena, since many extensions of the Standard Model framework can lead to signals in the 10^{-6} to 10^{-8} range.

Although more difficult to detect, other lepton-number violating decays such as $\tau \rightarrow \mu\mu e, \mu ee, eee, \mu\gamma$ are worth studying.

4. VECTOR-BOSON PAIR PRODUCTION ⁵

4.1 $W^+W^-, W^\pm Z, ZZ$ production

4.11 Recent numerical implementations

As already is noted in the introduction, for the description of $W^+W^-, W^\pm Z, ZZ$ production with their subsequent decays into lepton pairs two new numerical parton-level Monte Carlo programs have recently become available [18](MCFM), [19](DKS). These packages consider the production of four leptons in the double resonance approximation with complete $\mathcal{O}(\alpha_s)$ corrections. They can be used to compute any infra-red safe quantity with arbitrary experimental cuts on the leptonic decay products. These packages have already been used for updating and cross-checking previous results. The DKS program is available in fortran90 and fortran77 versions and includes anomalous triple gauge-boson couplings. The MCFM program is more complete in the sense that single resonance background diagrams are also added and finite width effects are included in some approximation which respects gauge-invariance. However, it does not include anomalous triple gauge-boson couplings. The results of the MCFM and DKS programs agree with each other within the integration error of $\leq 0.5\%$. Similar agreement is found with the spin

⁵Section coordinator: Z. Kunszt

averaged cross section indicated in [22, 24, 26]. In the past years the majority of the experimental studies used the programs described in [29, 31, 30] (BHO). A recent comparison between the DKS and BHO programs finds agreement at the level of 1% for WZ production and 3-4% for WW production (further details see Section 5.5). This confirms the assumptions of [29] that the spin correlations effects coming from virtual corrections are small. Note that recently a new $\mathcal{O}(\alpha_s)$ package has been written also for $W\gamma$ and $Z\gamma$ production with anomalous couplings [20] and for the first time the complete one loop QCD corrections are available also for these processes (see Section 4.2).

4.12 Input parameters and bench mark cross sections

In using these packages, one should be careful with input parameters. The QCD input is standard: the latest next-to-leading order parton number densities have to be used with the corresponding running coupling constant at some physical scale defined in terms of the kinematics of the outgoing particles.

The helicity amplitudes coded into these programs are calculated in $\mathcal{O}(\alpha_s)$ but they are leading order in the electroweak theory. However, the one loop electroweak radiative corrections are not completely negligible. The dominant corrections are given by light fermion loops and large custodial symmetry violating contributions of the top quark. Fortunately, they are universal and can be taken into account in the spirit of the ‘‘improved Born approximation’’ [112, 113]. Universality means that their contributions can modify only the leading order relation between M_Z , M_W and $\sin^2 \theta_W$ which can be taken into account with the use of the effective coupling

$$\sin^2 \theta_W \equiv \frac{\pi \alpha(M_Z)}{\sqrt{2} G_F M_W^2}, \quad (36)$$

where $G_F = 1.16639 \times 10^{-5} \text{ GeV}^{-2}$ is the Fermi constant and $\alpha(\mu)$ is the running QED coupling. With the values of the gauge-bosons masses of $M_Z = 91.187 \text{ GeV}$ and $M_W = 80.41 \text{ GeV}$, one obtains $\alpha = \alpha(M_Z) = 1/128$ and $\sin^2 \theta_W = 0.230$. Ignoring this correlation may lead to about 5-6% discrepancy in the cross section values. The remaining electroweak corrections are estimated to be less than 2% as long the parton sub-energy is below $0.5 - 1 \text{ TeV}$. However, above the 1 TeV scale double logarithmic corrections of $\mathcal{O}(\alpha_W \log^2 \hat{s}/M_W^2)$ become non-negligible. The origin of these large contributions is the incomplete cancellation of the soft singularities of massless gauge-boson emission (the Bloch-Nordsieck theorem is not valid for non-Abelian theories [115]). Since the physical cross section decreases strongly with the increase of the invariant mass of the gauge-boson pairs, these corrections are not important at the LHC. The validity of the improved Born approximation and the presence of the double logarithmic corrections has been tested for W pair production at LEP2 where the full next-to-leading order corrections are available [112, 113].

Additional electroweak input parameters are the matrix elements of the CKM mixing matrix. In the light quark sector, one should use the best experimental values [116]. In the case of the heavy quark contributions, the calculation is approximate since the $\mathcal{O}(\alpha_s)$ helicity amplitudes have been calculated assuming massless quarks [17]. This assumption is clearly not valid for the top contributions. WW pair production receives contributions from diagrams with the t -channel exchange of the top quark (with $|V_{td}| = |V_{ts}| = 0$ and $|V_{tb}| = 1$). However, it is suppressed due to the large top mass and small b -quark parton densities; therefore, it is reasonable to use $|V_{tb}| = 0$. The contribution of the subprocess $b\bar{b} \rightarrow W^+W^-$ (treating the top as massless) is of the order of 2% for the LHC [17] giving an upper limit on the theoretical ambiguity coming from this source. In the case of $W^\pm Z$ production, one can neglect the subprocess $bg \rightarrow W^- Z t$. It is present at next-to-leading order but again it is strongly suppressed by the large top quark mass, as well as the small b -quark distribution function. For the numerical results presented here, values $|V_{ud}| = |V_{cs}| = 0.975$; $|V_{us}| = |V_{cd}| = 0.222$ and $|V_{ub}| = |V_{cb}| = |V_{td}| = |V_{ts}| = |V_{tb}| = 0$ are used. We present cross-section values without including the branching ratios. To get event signals, they have to be multiplied with the leptonic branching ratios of the vector-bosons. We

use

$$BR(Z \rightarrow e^+e^- \text{ or } \mu^+\mu^-) = 3.37\% \quad BR(Z \rightarrow \sum_{i=e,\mu,\tau} \nu_i\bar{\nu}_i) = 20.1\%$$

$$BR(W^+ \rightarrow e^+\nu_e \text{ or } \mu^+\nu_\mu^-) = 10.8\%$$

These ratios implicitly incorporate QCD corrections to the hadronic decay widths of the W and Z .

Most of the results are obtained with some “standard cuts” defined as follows: a transverse momentum cut of $p_T > 20$ GeV and pseudorapidity cut of $|\eta| \leq 2.5$ is applied for all charged leptons and $p_T^{\text{miss}} \geq 20$ GeV is required for WZ production while $p_T^{\text{miss}} \geq 25$ GeV for W pair production. We use two different parton distributions, MRST [114] with $M_W = 80.41$ GeV and CTEQ(4M) [67] with $M_W = 80.33$ GeV which we refer to simply as MRST and CTEQ. $\alpha_s(M_Z) = 0.1175$ is used for MRST and $\alpha_s(M_Z) = 0.116$ is used for CTEQ. In all computations, we set the renormalisation and factorisation scales equal to each other.

In Table 11, we present the total cross section values for the various processes at the LHC, for the MRST and CTEQ parton distributions. We tabulated the results for σ^{tot} (the cross sections without any cuts applied) as well as σ^{cut} (the cross sections with the standard cuts defined above). The cross section values are given for the scale

$$\mu = (M_{V_1} + M_{V_2})/2, \quad (37)$$

where M_{V_i} are the masses of the two produced vector bosons.

Table 11: Cross sections in pb for pp collisions at $\sqrt{s} = 14$ TeV. The statistical errors are ± 1 on the last digit.

	ZZ		W^+W^-		W^-Z		W^+Z	
	LO	NLO	LO	NLO	LO	NLO	LO	NLO
$\sigma^{\text{tot}}(\text{MRST})$	11.6	15.5	78.7	117	11.2	19.3	17.8	30.6
$\sigma^{\text{tot}}(\text{CTEQ})$	11.8	15.8	81.3	120	11.4	19.6	18.6	31.9
$\sigma^{\text{cut}}(\text{MRST})$	4.07	5.47	25.0	40.18	3.49	6.58	5.20	9.68
$\sigma^{\text{cut}}(\text{CTEQ})$	4.09	5.51	25.6	42.0	3.59	6.72	5.32	9.83

In previous publications [22, 24, 26, 29, 31, 30, 18, 19] a number of phenomenologically interesting questions have been considered. Here we restrict ourselves to recall two interesting and typical features: the scale dependence of the radiative corrections for WW production and radiation zeros for WZ production.

4.13 Scale dependence

The one-loop corrections to the total cross sections are of the order 50% of the leading order term and they can be much larger for the kinematical range of larger transverse momenta or invariant mass of the vector-boson pair. For differential distributions where p_T is not integrated out completely, the scale choice

$$\mu^2 = \mu_{\text{st}}^2 \equiv \frac{1}{2}(p_T^2(V_1) + p_T^2(V_2) + M_{V_1}^2 + M_{V_2}^2) \quad (38)$$

appears to be appropriate. For the total cross section, the difference between the two scale choices expressed in Equations 37 and 38 is very small since it is dominated by low- p_T vector-bosons. However, for more exclusive quantities, the differences can be substantial. At the LHC, the huge one-loop corrections in the tails of the distributions are dominated by the bremsstrahlung contributions; therefore it

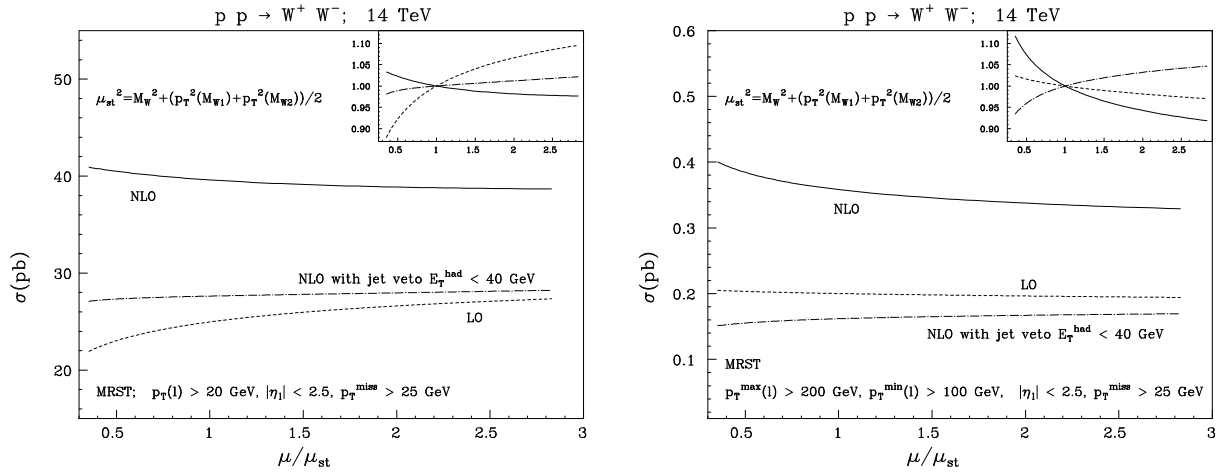


Fig. 20: Scale dependence of the cross section for W -pair production at the LHC with standard cuts. The scale is given in units of μ_{st} as defined in Equation 38. We show the LO, NLO and NLO with jet veto curves without additional cuts (left) and with an additional cut $p_T^{\max}(l) > 200$ GeV and $p_T^{\min}(l) > 100$ GeV (right). The insets show the curves normalised to 1 at $\mu = \mu_{st}$.

is natural to consider the cross sections with and without the jet veto (that is, with or without the cut $E_T^{\text{jet}} < 40$ GeV).

In Figure 20, the scale dependence of σ^{cut} is shown for standard cuts, with a jet veto and with stronger cuts on the transverse momenta of the charged leptons. We can see that the corrections are large and increase with the additional cuts applied. The scale dependence at LO is reduced at NLO and it is reduced further when a jet veto is applied. In particular, the size of the correction is strongly reduced when applying the jet veto - an important feature for background studies.

4.14 Approximate radiation zeros in WZ production

In leading order, the angular distribution of WZ production exhibits an approximate radiation zero for $\cos \theta = (g_1 + g_2)/(g_1 - g_2)$ [31] where g_1, g_2 denote the Z boson couplings to the left handed up and down quarks, respectively. Since the precise flight direction of the W boson is not known (due to the uncertainty in the longitudinal momentum carried by the neutrino) it is convenient to plot a distribution in the (true) rapidity difference between the Z boson and the charged lepton coming from the decay of the W : $\Delta y_{Zl} \equiv y_Z - y_l$. This quantity is similar to the rapidity difference $\Delta y_{WZ} \equiv |y_W - y_Z|$ studied in [24], but uses only the observable charged-lepton variables. It is the direct analogue of the variable $y_\gamma - y_{l^+}$ considered in [117] for the case of $W\gamma$ production. It is possible to determine $\cos \theta$ in the $W\gamma$ or WZ rest frame, by solving for the neutrino longitudinal momentum using the W mass as a constraint, up to a two-fold discrete ambiguity for each event [118, 119, 120]. However, it has been found [117] that the ambiguity degrades the radiation zero - at least if each solution is given a weight of 50% - so that the rapidity difference $y_\gamma - y_{l^+}$ is more discriminating than $\cos \theta$. As one can see from Figure 21, there is a residual dip in the Δy_{Zl} distribution, even at order α_s . This dip can be enhanced easily by requiring a minimal energy for the decay lepton from the W and by cutting on the rapidity of the Z boson. In Figure 21, we have chosen $E(l) > 100$ GeV with and without $y_Z < 0$. Note that the latter two curves are scaled up by a factor of 5. At the LHC, for the first time, we shall have enough statistics to test experimentally for the presence of approximate radiation zeros.

New physics contributions can modify the self-interactions of vector-bosons, in particular the triple gauge-boson vertices. If new physics occurs at an energy scale well above that being probed experimentally, it can be integrated out, and the result expressed as a set of anomalous (non-Standard Model) interaction vertices. (The physics of anomalous coupling will be considered in detail in Section 5.

W⁺Z production at LHC

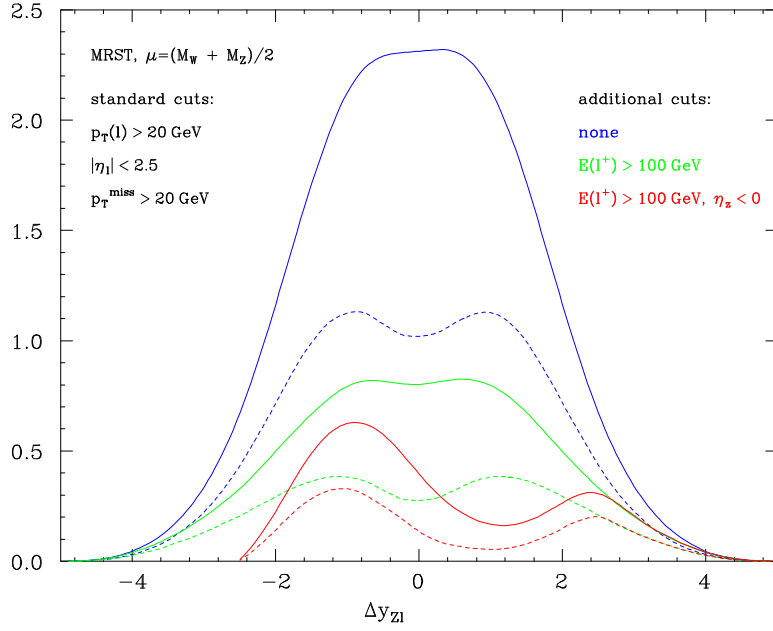


Fig. 21: WZ production followed by leptonic decays of both the W and Z bosons. We plot the distribution, in picobarns, in the rapidity difference between the Z and the charged lepton l from the decay of the W , $\Delta y_{Zl} \equiv y_Z - y_l$. Leptonic branching ratios are not included and the scale has been set to $\mu = (M_W + M_Z)/2$. The basic cuts used are $p_T(l) > 20$ GeV and $|\eta(l)| < 2$ for all three charged leptons, and a missing transverse momentum cut of $p_T^{\text{miss}} > 20$ GeV. We plot the Δy_{Zl} distribution with these cuts (blue, upper pair), with an additional cut on the W decay lepton, $E(l) > 100$ GeV (green, middle pair) and with a further cut on the rapidity of the Z boson $y_Z < 0$ (red, lower pair); the latter curves have been scaled up by a factor of 5. The dashed curves are Born-level results; the solid curves include the $\mathcal{O}(\alpha_s)$ corrections.

and our standard notation for the anomalous triple gauge-boson couplings is given there.) It is interesting to know what is the effect of the anomalous W^+W^-Z couplings on the approximate radiation zero of WZ production [121]. In Figure 22, the Δy_{Zl} distribution is plotted for two different sets of anomalous couplings at vanishing q^2 ($\Delta g_1 = -0.013$, $\lambda^Z = 0.02$, $\Delta \kappa^Z = -0.028$) and ($\Delta g_1 = 0.065$, $\lambda^Z = 0.04$, $\Delta \kappa^Z = 0.071$). For the q^2 dependence we assumed dipole form factors of the generic form

$$\hat{a}(q^2) = \frac{a}{\left(1 + \frac{q^2}{\Lambda^2}\right)^2} \quad (39)$$

with $\Lambda = 2$ TeV. As one can see in Figure 22, the contributions of anomalous couplings have the tendency to make the dip less pronounced.

4.15 Future improvements

The present state of art of the description of gauge-boson pair production is not completely satisfactory yet. Of the various issues, there are three which require further theoretical studies. First, the double resonant approximation is expected to be correct only up to a few percent accuracy - it is important to go beyond this approximation. A first attempt has been made by Campbell and Ellis [18] where, as already mentioned above, the singly-resonant diagrams have also been included. These additions are obviously relevant in the off-resonant regions. The inclusion of finite width effect is not completely straightforward because of possible conflict with gauge-invariance. This issue requires further theoretical study. Secondly, we need NLO results also for the semi-leptonic channels when one of the gauge-bosons decays hadronically. This requires the inclusion of the contributions of diagrams describing the gluonic

W⁺Z production at LHC

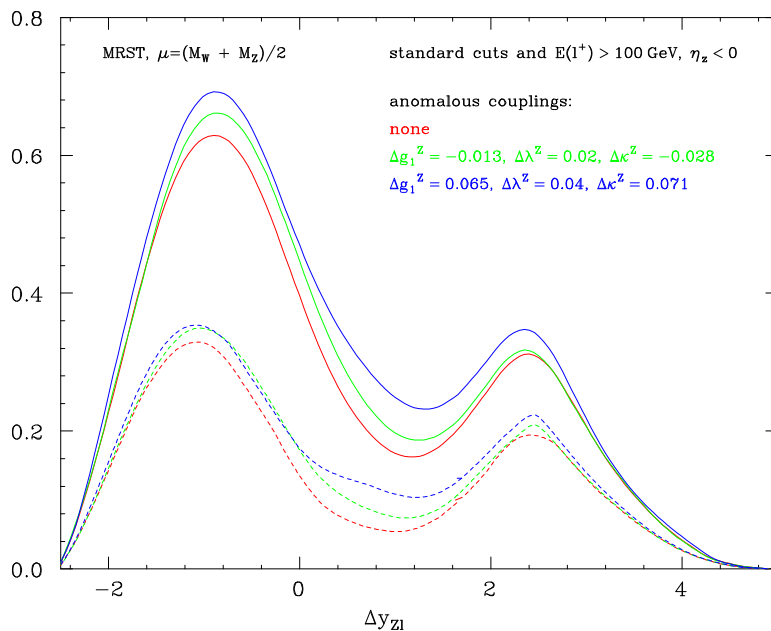


Fig. 22: WZ production followed by leptonic decays of both the W and Z bosons. We plot the NLO distribution, in picobarns, in the rapidity difference between the Z and the charged lepton l from the decay of the W : $\Delta y_{Zl} \equiv y_Z - y_l$. Leptonic branching ratios are not included and the scale has been set to $\mu = (M_W + M_Z)/2$. The standard cuts $p_T(l) > 20$ GeV, $|\eta(l)| < 2.5$ for all three charged leptons and a missing transverse momentum cut of $p_T^{\text{miss}} > 20$ GeV are applied. We plot the Δy_{Zl} distribution without anomalous couplings (red, lower pair) and with two sets of anomalous couplings ($\Delta g_1 = -0.013$, $\lambda^Z = 0.02$, $\Delta \kappa^Z = -0.028$) (green, middle pair) and ($\Delta g_1 = 0.065$, $\lambda^Z = 0.04$, $\Delta \kappa^Z = 0.071$) (blue, upper pair). The q^2 dependence of the couplings is given by the dipole form of Equation 39 with $\Lambda = 2$ TeV. Also we plot the same quantities supplementing the standard cuts with the additional cut on the the W decay lepton, $E(l) > 100$ GeV and with the rapidity cut $y_Z < 0$; the latter curves have been scaled up by a factor of 5. The dashed curves are Born-level results; the solid curves include the $\mathcal{O}(\alpha_s)$ corrections.

corrections to the final-state quarks. Thirdly, fixed order perturbative QCD description is not applicable for the description of the low- p_T behaviour of the gauge-boson pair. The technique for the resummation of the low- p_T contributions is well known and it can be applied also to the case of gauge-boson pair production. For example, one calculation for the ZZ has been carried out [122].

4.16 Comparison with PYTHIA

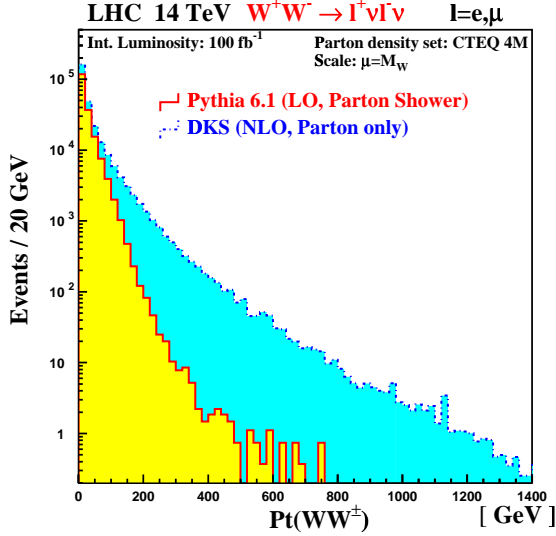


Fig. 23: Transverse momentum of the WW bosons pairs simulated with PYTHIA and DKS Monte Carlo generators and using the CTEQ 4M structure function.

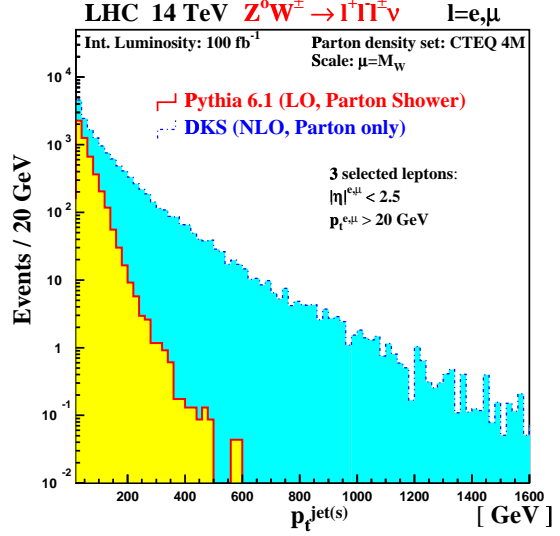


Fig. 24: Transverse momentum of the jets in the case of the WZ production. The 3 leptons fall within the detector acceptance.

In most of the studies carried out so far for the LHC, where the production of vector boson pairs played an important role, the usual Monte Carlo simulation tool has been PYTHIA [123] based on LO matrix elements [124] with parton shower. In particular, it is expected that for some optimisation cuts, where the large corrections provided by NLO diagrams (for example by choosing high- $p_T(V)$ or high- M_{VV} regions) its predictions are not acceptable. By making comparison between the predictions of PYTHIA and the the DKS parton level NLO Monte Carlo [19], we investigate here how accurate does PYTHIA simulate the di-boson cross sections at the LHC, especially in some kinematic regions. We relate our analysis to the special case of the CMS detector [125].

In all results presented in this analysis, we assume that the vector-bosons always decay leptonically. We use the CTEQ(4M) parton distribution [67] in both Monte Carols and the cross section values are for the scale $\mu = (M_{V_1} + M_{V_2})/2$, where M_{V_i} are the masses of the two produced vector-bosons. If the DKS Monte Carlo is run at Born-level, we obtain very good agreement with the total cross sections given by PYTHIA.

Figure 23 shows the transverse momentum of the WW pairs. The comparison between PYTHIA and DKS indicates the large difference in cross section observables at high- p_T^{WW} values. This is related to the fact that at NLO, the sub-processes $qg \rightarrow V_1V_2q$ have to be taken into account [26, 30]. This is also reported in Table 12. The leptons are selected following the CMS criteria, where a p_T larger than 20 GeV and a pseudorapidity $|\eta| < 2.5$ are required. Jets are selected by: $p_T > 20$ GeV and $|\eta| < 3$. The K-factor increases then from 1.5 for the total cross sections up to values of about 60 if the jets are required to have a p_T larger than 150 GeV. The same effect is shown in figure 24 for the WZ production, where the p_T of the jets is shown (the jet balances the p_T^{VV}). For this process the K-factors at large p_T -values are even larger than in the WW case (as shown in the table). The transverse momentum

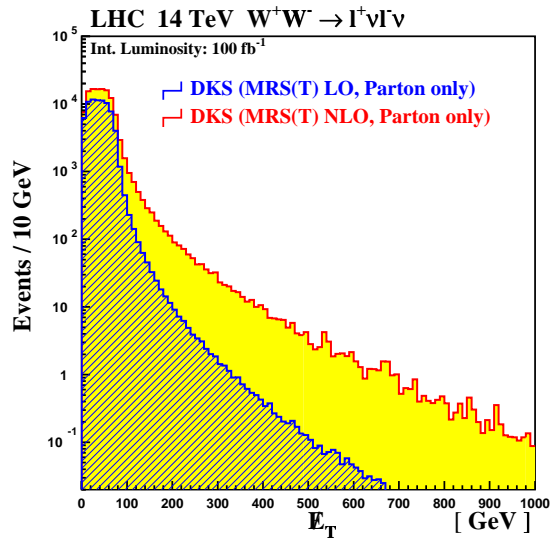


Fig. 25: Missing transverse energy in the WW production. The events are obtained by running the DKS generator with and without including the NLO corrections.

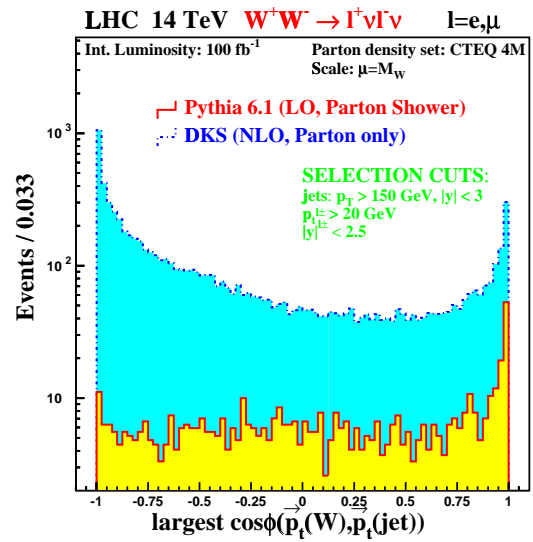


Fig. 26: Smallest angle between one of the W 's and the jet in WW pair production. The two leptons are required to be within the detector acceptance and the jet to have a p_T larger than 150 GeV.

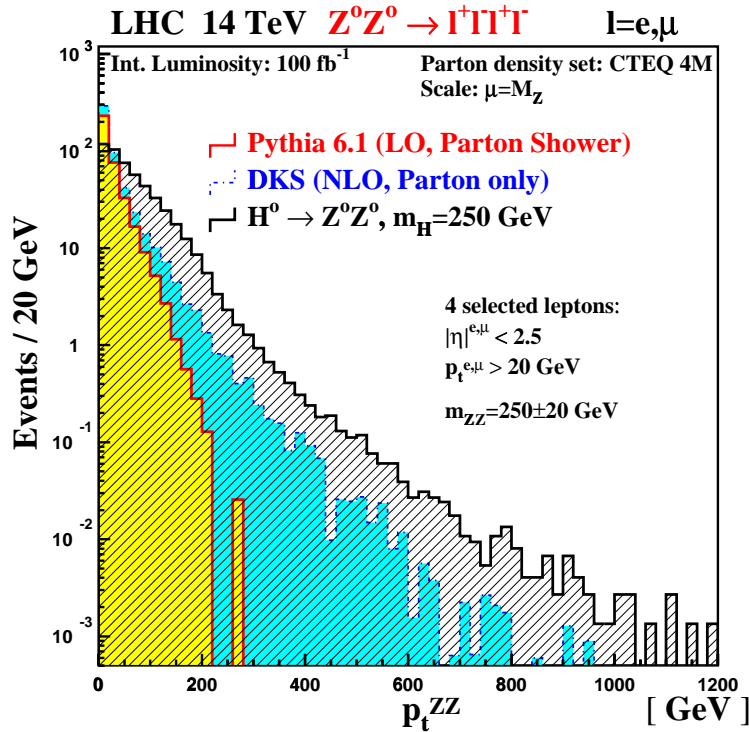


Fig. 27: Transverse momentum of ZZ pairs originating from a Higgs ($M_H = 250$ GeV), where the two leptons fall into the detector acceptance and the M_{ZZ} is consistent with the Higgs mass. The non-resonant ZZ background is simulated with (DKS) and without (PYTHIA) NLO corrections.

of the di-boson system (or of the jet(s)) are not the only variables affected by large NLO corrections. Other variables can show significant differences within their distributions: for example the lepton p_T , the invariant mass of the lepton pair M_{ll} , the missing transverse energy \cancel{E}_T (as shown in Figure 25), the maximal transverse momentum of the two charged leptons p_T^{max} , the lepton pseudorapidities η^l , their difference $\Delta\eta^l = \eta^{l^-} - \eta^{l^+}$, the angle between leptons $\cos\theta_{ll}$, the transverse angle between leptons $\cos\phi_{ll}$ and so on.

Therefore, it is extremely important to take into account the possible influence of NLO corrections for the vector-boson production at the LHC energy. Every time one is performing an optimisation of signal selection, one should be aware of the possible deviations due to the use of a LO generator like PYTHIA. This is especially true for complicated cuts, where it is difficult to judge whether the effects are large or not. An example is shown for WW events in Figure 26, where the smallest angle between one of the W 's and the jet is shown for events with a high- p_T jet. Not only is the cross section clearly smaller in PYTHIA but also the shape of the distribution is quite different, changing the result of a possible cut. Another good example is the Higgs search through the decay channel $H \rightarrow ZZ \rightarrow 4l$ (see Figure 27). The idea of using p_T -cuts to improve the signal-to-background ratio may not be as effective as one would expect from using only PYTHIA. The figure shows indeed that, if the NLO corrections are included, the p_T distribution of the non-resonant background follows much more closely those of the signal, reducing the gain considerably.

Table 12: Cross sections in pb for pp collision at $\sqrt{s}=14$ TeV. The leptons are selected by requiring a p_T larger than 20 GeV and a pseudorapidity $|\eta| < 2.5$. The jets should have a $p_T > 20$ GeV and $|\eta| < 3$.

(pb)	$\sigma^{tot} \times BR$	Selected	Jet	p_T^{jet} selection (in GeV):		
		leptons	veto	20-150	150-400	>400
$\sigma_{PYTHIA}^{W^+W^- \rightarrow l^+\nu l^-\bar{\nu}}$	3.704	1.704	1.125	0.568	2×10^{-3}	2.8×10^{-4}
$\sigma_{DKS, LO}^{W^+W^- \rightarrow l^+\nu l^-\bar{\nu}}$	3.79	1.71	-	-	-	-
$\sigma_{DKS, NLO}^{W^+W^- \rightarrow l^+\nu l^-\bar{\nu}}$	5.56	2.58	1.49	0.942	0.135	1.69×10^{-2}
K-factor	1.5	1.54	1.32	1.66	67	~ 60
$\sigma_{PYTHIA}^{W^\pm Z \rightarrow l^+\nu l^+l^-}$	4.35×10^{-1}	1.45×10^{-1}	9.47×10^{-2}	4.91×10^{-2}	9.33×10^{-4}	6.5×10^{-6}
$\sigma_{DKS, LO}^{W^\pm Z \rightarrow l^+\nu l^+l^-}$	4.34×10^{-1}	1.48×10^{-1}	-	-	-	-
$\sigma_{DKS, NLO}^{W^\pm Z \rightarrow l^+\nu l^+l^-}$	7.42×10^{-1}	2.77×10^{-1}	1.31×10^{-1}	1.27×10^{-1}	2.8×10^{-2}	4.63×10^{-3}
K-factor	1.71	1.91	1.39	2.3	30	~ 700
$\sigma_{PYTHIA}^{ZZ \rightarrow l^+l^-l^+l^-}$	5.13×10^{-2}	1.79×10^{-2}	1.15×10^{-2}	6.26×10^{-3}	1.33×10^{-4}	1.5×10^{-6}
$\sigma_{DKS, LO}^{ZZ \rightarrow l^+l^-l^+l^-}$	5.31×10^{-2}	1.84×10^{-2}	-	-	-	-
$\sigma_{DKS, NLO}^{ZZ \rightarrow l^+l^-l^+l^-}$	7.07×10^{-2}	2.55×10^{-2}	1.58×10^{-2}	8.79×10^{-3}	8.23×10^{-4}	7.78×10^{-5}
K-factor	1.38	1.42	1.38	1.4	6	~ 50

4.2 $W\gamma$ and $Z\gamma$ production at NLO

In this section, we present order α_s results for $W\gamma$ and $Z\gamma$ production at the LHC, including the *full* leptonic correlations and anomalous couplings in the narrow-width approximation [126]. Previous analyses [32, 127, 33] included decay correlations only in the bremsstrahlung amplitudes implementing, as an approximation, the finite part of the *spin-summed* one-loop amplitudes.

To perform the calculation, we use the helicity amplitudes presented in [17]. The amplitudes relevant for the inclusion of anomalous couplings are given in [126]. In order to cancel analytically the soft and collinear singularities coming from the bremsstrahlung and one loop parts, we have used the version of the subtraction method presented in [128]. Therefore, the amplitudes are implemented into a numerical Monte Carlo style program which allows calculation of any infrared-safe physical quantity with arbitrary cuts.

The results presented in this section correspond to pp scattering at $\sqrt{s} = 14$ TeV using the following cuts: a transverse momentum cut of $p_T^\perp > 25$ GeV for the charged leptons is imposed and the pseudorapidity is limited to $|\eta| < 2.4$ for all detected particles. The photon transverse momentum cut is $p_T^\gamma > 50(100)$ GeV for $W\gamma$ ($Z\gamma$) production. For the $W\gamma$ case, we require a minimum missing transverse momentum carried by the neutrinos $p_T^{\text{miss}} > 50$ GeV. Additionally, charged leptons and the photons must be separated in the pseudorapidity-azimuthal angle by $\Delta R_{l\gamma} = \sqrt{(\eta_\gamma - \eta_l)^2 + (\phi_\gamma - \phi_l)^2} > 0.7$. In order to suppress the contribution from the off-resonant diagrams, we require the transverse mass $M_T > 90$ GeV for $W\gamma$ production and the invariant mass of the $ll\gamma$ system $M_{ll\gamma} > 100$ GeV for the $Z\gamma$ case.

Finally, in order to suppress the contribution from the fragmentation of partons into photons, computed only to LO accuracy, the photons are required to be isolated from hadrons: the transverse hadronic momentum in a cone of size $R_0 = 0.7$ around the photon should be smaller than a fraction of the transverse momentum of the photon

$$\sum_{\Delta R < R_0} p_T^{\text{had}} < 0.15 p_T^\gamma \quad (40)$$

This completes the definition of the ‘‘standard’’ cuts.

In the results presented here, the branching ratios of the vector-bosons into leptons are not included. For both the LO and NLO results, we use the latest set of parton distributions of MRST(cor01) [114] and the two loop expression for the strong coupling constant. For the fragmentation component, we use the fragmentation functions from [129].

The ‘‘standard’’ scale for both the factorisation and renormalisation scales is

$$\mu^2 = \mu_{\text{st}}^2 \equiv M_V^2 + \frac{1}{2} \left[(p_T^V)^2 + (p_T^\gamma)^2 \right]. \quad (41)$$

The masses of the vector-bosons have been set to $M_Z = 91.187$ GeV and $M_W = 80.41$ GeV and the following values have been used for the Cabibbo-Kobayashi-Maskawa (CKM) matrix elements: $|V_{ud}| = |V_{cs}| = 0.975$ and $|V_{us}| = |V_{cd}| = 0.222$. We do not include any QED or electroweak corrections but choose the coupling constants α and $\sin^2 \theta_W$ in the spirit of the ‘‘improved Born approximation’’ [112, 113], with $\sin^2 \theta_W = 0.230$. Notice that the observable is order α^2 ; within the same spirit, we use the running $\alpha = \alpha(M_Z) = 1/128$ for the coupling between the vector-boson and the quarks (to take into account effectively the EW corrections) whereas we keep $\alpha = 1/137$ for the photon coupling. It is worth noticing that this modification results already in more than a 6% change in the normalisation of the cross section with respect to the standard approach of using both running coupling constants.

4.21 Results at NLO

For future checks, and for an estimate of the number of events to be observed at the LHC, some benchmark total cross section numbers are presented in Table 13. The first ones were obtained by imposing only the cut on the transverse momentum of the photon $p_T^\gamma > 50(100)$ GeV for $W\gamma$ ($Z\gamma$) production. The importance of the NLO corrections, as well as the size of the fragmentation contribution before applying the isolation cut prescription, can be seen from the table. Furthermore, we also include the result for the total cross section obtained after the implementation of the standard cuts.

σ (pb)	LO*	Frag.	NLO
$W^+\gamma$ ($p_T^\gamma > 50$ GeV)	4.79	3.02	13.89
$W^-\gamma$ ($p_T^\gamma > 50$ GeV)	3.08	3.55	10.15
$Z\gamma$ ($p_T^\gamma > 100$ GeV)	1.29	0.412	2.37
$W^+\gamma$ (std. cuts)	0.436	0.094	1.71
$W^-\gamma$ (std. cuts)	0.310	0.095	1.20
$Z\gamma$ (std. cuts)	0.524	0.041	0.877

Table 13: Cross sections for pp collisions at $\sqrt{s} = 14$ TeV. The statistical errors are ± 1 within the last digit. LO* corresponds to the direct component only.

In what follows, we will estimate the theoretical uncertainty of the results by analysing the changes on different distributions when varying the scale by a factor of two in both directions $\frac{\mu_{\text{st}}}{2} < \mu < 2\mu_{\text{st}}$.

In Figure 28, we show the scale dependence of the p_T distribution of the photon in $W^+\gamma$ production with the standard cuts (upper curves) and also with the additional requirement of a jet-veto. As can be observed, the scale dependence is still large ($\pm 10\%$) but is considerably reduced when the jet-veto is applied. The situation is similar to what has been observed in the case of WW production [19] and is caused by the suppression of the contribution from the qg initial state appearing for the first time at NLO. Since this initial state dominates the cross section, the NLO result behaves effectively like a LO one, as far as the scale dependence is concerned.

In the inset plot, we present the ratio between the NLO and LO results (with the standard scale), which remains larger than 3 and increases with the photon transverse momentum. This clearly shows that the LO calculation is not even sufficient for an understanding of the shape of the distribution, since the NLO effect goes beyond a simple normalisation. As is well known [28], the relevance of the NLO corrections for this process is mainly due to the breaking of the radiation amplitude zero appearing at LO and to the large qg initial state parton luminosity at the LHC. It is worth mentioning that the scale dependence of the LO result turns out to be very small. This is an artificial effect and illustrates that a small scale dependence is by no means a guarantee for small NLO corrections. Furthermore, we present the ratio of the NLO jet-veto and the LO result. As expected, this ratio is closer to 1, again due to the fact that most of the contributions coming from the new subprocesses appearing at NLO are suppressed by the jet-veto.

In Figure 29, we study the lepton correlation in the azimuthal angle for $Z\gamma$ production $\Delta\phi_{ll} = |\phi_{l-} - \phi_{l+}|$. Notice that this observable can be studied at NLO since the spin correlations between the leptons are fully taken into account in the implementation of the one-loop corrections. In this case, we observe that the NLO corrections are rather sizeable and increase the cross section by 50% for small $\Delta\phi_{ll}$. The region $\Delta\phi_{ll} > 2$ (with the standard cuts) is kinematically forbidden unless a jet with a high transverse momentum is produced; therefore, the cross section vanishes at LO and it is strongly suppressed for the NLO calculation with jet-veto. In this region, the full NLO calculation is effectively LO and its scale dependence becomes larger, as expected.

Because there is no radiation amplitude zero appearing at LO for $Z\gamma$ production, the NLO corrections are under better control in the kinematical region where the LO cross section does not vanish. Nevertheless, for large transverse momentum, the qg initial state again dominates the NLO contribution and the corrections increase considerably.

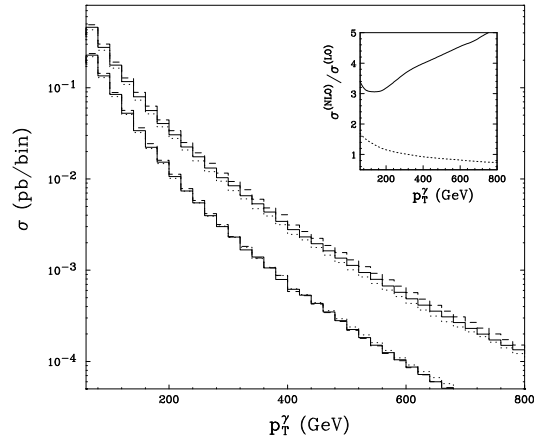


Fig. 28: Scale dependence of σ^{NLO} without (upper curves) and with (lower curves) jet-veto. The scale has been varied according to $\frac{\mu_{st}}{2}$ (dashes) $< \mu < 2\mu_{st}$ (dots). The inset plot shows the ratio σ^{NLO}/σ^{LO} , again without (solid) and with (dots) jet-veto.

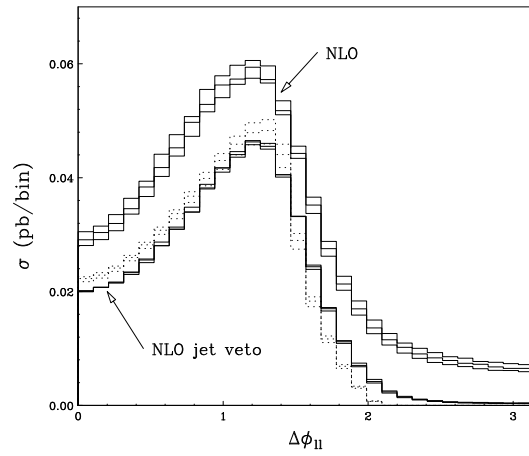


Fig. 29: Scale dependence of σ^{NLO} without jet-veto (upper solid curves), σ^{NLO} with jet-veto (lower solid curves) and σ^{LO} (dotted curves). The scale has been varied according to $\frac{\mu_{st}}{2} < \mu < 2\mu_{st}$.

4.22 Anomalous couplings without form factors

The study of triple vector-boson couplings is motivated by the hope that some physics beyond the Standard Model leads to a modification of these couplings which eventually could be detected. In order to quantify the effects of the new physics, an effective Lagrangian is introduced which contains all Lorentz invariant terms, in principle. The new terms spoil the gauge-cancellation in the high energy limit and, therefore, will lead to violation of unitarity for increasing partonic centre of mass energy \hat{s} . Usually, in an analysis of anomalous couplings from experimental data in hadronic collisions, this problem is circumvented by supplementing the anomalous couplings α_{AC} with form factors. A common choice for the form factor is

$$\alpha_{AC} \rightarrow \frac{\alpha_{AC}}{\left(1 + \frac{\hat{s}}{\Lambda^2}\right)^n} \quad (42)$$

where n has to be large enough to ensure unitarity and Λ is interpreted as the scale for new physics. Obviously, this procedure is rather *ad hoc* and introduces some arbitrariness. Therefore, it would be very convenient to avoid it in an analysis of anomalous couplings at hadron colliders. This would bring these analyses more into line with those at e^+e^- colliders. In order to do so, one should analyse the data at fixed values of \hat{s} , as it is done at LEP. This results in limits for the anomalous parameters which are a function of \hat{s} .

Clearly, it is possible to do such analysis for the production of $Z\gamma$ when both leptons are detected [130], since the partonic centre of mass energy can be reconstructed from the kinematics of the final state particles and therefore the cross section can be measured for different bins of fixed \hat{s} .

The situation is more complicated for $W\gamma$ production since the neutrino is not observed. Nevertheless, by identifying the transverse momentum of the neutrino with the missing transverse momentum, and assuming the W boson to be on shell, it is possible to reconstruct the neutrino kinematics (particularly the longitudinal momentum) with a two-fold ambiguity. In the case of the Tevatron, since it is a $p\bar{p}$ collider, it is possible to choose the ‘‘correct’’ neutrino kinematics 73% of the times by selecting the maximum (minimum) of the two reconstructed values for the longitudinal momentum of the neutrino for $W^+\gamma(W^-\gamma)$.

This is not true at the LHC where, due to the symmetry of the colliding beams, both reconstructed kinematics have equal chances to be correct. Fortunately, in the case of anomalous couplings, we are interested in a efficient way to reconstruct the \hat{s} rather than the full kinematics. Again there are two possible values of \hat{s} . It turns out that there is a simple method to choose the ‘‘correct’’ one 66% of the times at the LHC (73% of the times at Tevatron) by selecting the minimum \hat{s} , \hat{s}_{\min} , of the two reconstructed values (for both $W^+\gamma$ and $W^-\gamma$). Furthermore, we checked that the selected value \hat{s}_{\min} differs in almost 90% of the events by less than 10% from the exact value \hat{s} . This is likely to be enough precision, since the data will be collected in sizeable bins of \hat{s} and the anomalous parameters are not expected to change very rapidly with the energy in any case.

To quantify the advantage of the method, we show in Figure 30 the correlations of $\sqrt{\hat{s}_{\min}}$ with $\sqrt{\hat{s}}$. The left plot corresponds to the case of pure Standard Model, whereas the right plot presents results for (already experimentally ruled out) huge values of anomalous couplings $\Delta\kappa = 0.8$ and $\lambda = 0.2$ with an ordinary form factor ($n = 2$, $\Lambda = 1$ TeV).

The cross section drops very rapidly for increasing $\sqrt{\hat{s}} - \sqrt{\hat{s}_{\min}}$. This correlation clearly holds in the particularly interesting large $\sqrt{\hat{s}}$ region and for both Standard Model and anomalous contribution.

As a result of this investigation, we conclude that even in the case of $W\gamma$ production, reliable bounds for anomalous couplings as a function of \hat{s} (using \hat{s}_{\min}) can be obtained. Such a procedure would certainly allow a comparison of various bounds from different experiments.

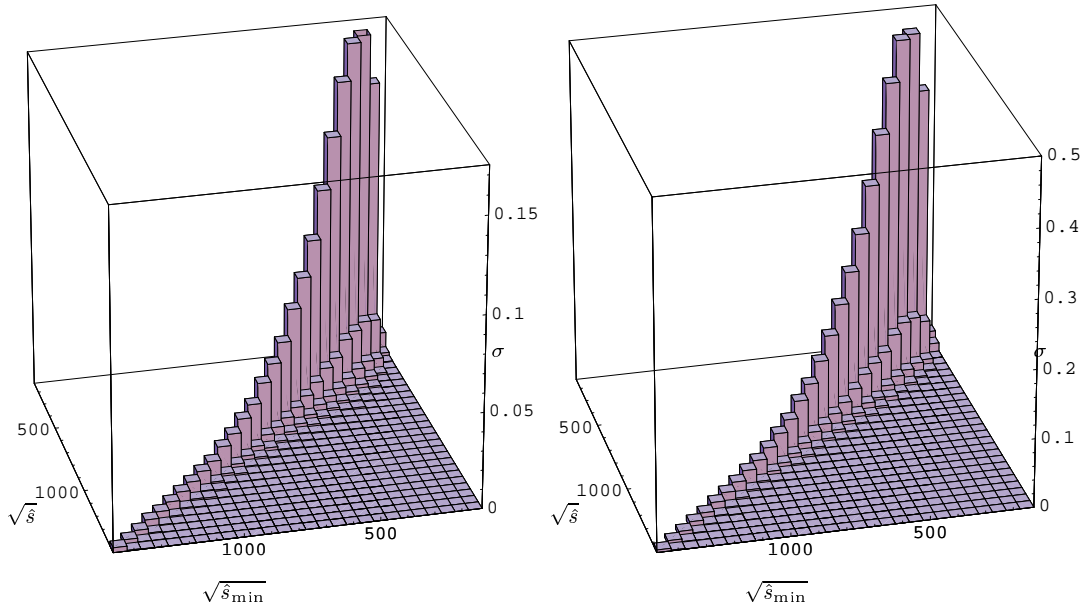


Fig. 30: The cross section for $W^+\gamma$ production (in pb/bin) as a function of \sqrt{s} and $\sqrt{s_{\min}}$ (in GeV) in order to illustrate the steep fall of σ for increasing $|\sqrt{s} - \sqrt{s_{\min}}|$. The left plot corresponds to the Standard Model, whereas the right plot includes anomalous couplings (see text).

5. ANOMALOUS VECTOR-BOSON COUPLINGS ⁶

The principle of gauge-invariance is used as the basis for the Standard Model. The non-Abelian gauge-group structure of the theory of electroweak interactions predicts very specific couplings between the electroweak gauge-bosons. Measurements of these triple gauge-boson couplings (TGCs) of the W , Z and γ gauge-bosons therefore provide powerful tests of the Standard Model.

In the most general Lorentz invariant parametrisation, the three gauge-boson vertices, $WW\gamma$ and WWZ , can be described by fourteen independent couplings [131], seven for each vertex. The possible four quadruple gauge-boson vertices: $\gamma\gamma WW$, $Z\gamma WW$, $ZZWW$ and $WWWW$ require 36, 54, 81 and 81 couplings, respectively for a general description. Assuming electromagnetic gauge-invariance, C- and P-conservation, the set of 14 couplings for the three gauge-boson vertices is reduced to 5: g_1^Z , κ_γ , κ_Z , λ_γ and λ_Z [132], where their Standard Model values are equal to $g_1^Z = \kappa_\gamma = \kappa_Z = 1$ and $\lambda_\gamma = \lambda_Z = 0$ at tree level.

The TGCs related to the $WW\gamma$ vertex determine properties of the W , such as its magnetic dipole moment μ_W and electric quadrupole moment q_W :

$$\mu_W = \frac{e}{2M_W}(g_1^Z + \kappa_\gamma + \lambda_\gamma) \quad (43)$$

$$q_W = \frac{e}{M_W^2}(\kappa_\gamma - \lambda_\gamma) \quad (44)$$

In the following, the anomalous TGCs are denoted by Δg_1^Z , $\Delta\kappa_\gamma$, $\Delta\kappa_Z$, λ_γ and λ_Z , where the Δ denotes the deviations of the respective quantity from its Standard Model value.

5.1 Introduction

The Standard Model is well established by the experiments at LEP and the Tevatron. Any deviations of the Standard Model can therefore be introduced only with care. Changes to the Standard Model come

⁶Section coordinators: P.R. Hobson, W. Hollik

with different forms of severity. In order to see at what level anomalous vector-boson couplings can be reasonably discussed, one has to consider these cases separately. Changes to the gauge-structure of the theory, that do not violate the renormalisability of the theory, *i.e.* the introduction of extra fermions or possible extensions of the gauge-group are the least severe. They will typically generate small corrections to vector-boson couplings via loop effects. In this case also, radiative effects will be generated at lower energies. For the LHC, the important thing in this case is not to measure the anomalous couplings precisely, but to look for the extra particles. However, this is beyond the scope of this chapter. In the other case, a more fundamental role is expected for the anomalous couplings, implying strong interactions. In this case, one has to ask oneself whether one should study a model with or without a fundamental Higgs boson.

Simply removing the Higgs boson from the Standard Model is a relatively mild change. The model becomes non-renormalisable, but the radiative effects grow only logarithmically with the cut-off at the one-loop level. The question is whether this scenario is ruled out by the LEP1 precision data. The LEP1 data appear to be in agreement with the Standard Model, preferring a low Higgs mass. One is sensitive to the Higgs mass in three parameters, labelled S , T , U or ϵ_1 , ϵ_2 , ϵ_3 . These receive corrections of the form $g^2(\log(M_H/M_W) + \text{constant})$, where the constants are of order one. The logarithmic enhancement is universal and would also appear in models without a Higgs as $\log(\Lambda)$, where Λ is the cut-off at which new interactions should appear. Only when one can determine the three different constants independently, can one say that one has established the Standard Model. At present, the data do not provide sufficient precision to do this.

A much more severe change to the Standard Model is the introduction of vector-boson couplings not of the gauge-interaction type. These new couplings violate renormalisability much more severely than simply removing the Higgs boson. Typically, quadratically and quartically divergent corrections would appear to physical observables. Therefore, it is questionable as to whether one should study models with a fundamental Higgs boson, but with extra anomalous vector-boson couplings. It is hard to imagine a form of dynamics that could do this. If the vector-bosons become strongly interacting, the Higgs probably would exist at most in an “effective” way. Therefore, the most natural way is to study anomalous vector-boson couplings in models without a fundamental Higgs. Actually when one removes the Higgs boson, the Standard Model becomes a gauged non-linear sigma-model. It is well known that the nonlinear sigma-model describes low-energy pion physics. The “pions” correspond to the longitudinal degrees of freedom of the vector-bosons and f_π corresponds to the vacuum expectation value of the Higgs field. Within this description, the Standard Model corresponds to the lowest-order term quadratic in the momenta, anomalous couplings to higher derivative terms. The systematic expansion in terms of momenta is known as chiral perturbation theory and is extensively used in meson physics.

Writing down the most general non-linear chiral Lagrangian containing up to four derivatives gives rise to a large number of terms, which are too general to be studied effectively. One therefore has to look for dynamical principles that can limit the number of terms. Of particular importance are approximate symmetry principles. In the first place one, expects CP-violation to be small. We limit ourselves therefore to CP-preserving terms. In order to see what this means in practice, it is advantageous to describe the couplings in a manifestly gauge-invariant way, using the Stückelberg formalism [133, 37]. One needs the following definitions:

$$F_{\mu\nu} = \frac{i\tau_i}{2}(\partial_\mu W_\nu^i - \partial_\nu W_\mu^i + g\epsilon^{ijk}W_\mu^j W_\nu^k) \quad (45)$$

is the $SU(2)$ field strength with the $SU(2)$ gauge-coupling g ;

$$D_\mu U = \partial_\mu U + \frac{ig}{2}\tau_i W_\mu^i U + ig \tan \theta_W U \tau_3 B_\mu \quad (46)$$

is the gauge-covariant derivative of the $SU(2)$ -valued field U , which describes the longitudinal degrees

of freedom of the vector fields in a gauge-invariant way;

$$B_{\mu\nu} = \partial_\mu B_\nu - \partial_\nu B_\mu \quad (47)$$

is the hypercharge field strength. In addition,

$$V_\mu = (D_\mu U)U^\dagger/g, \quad (48)$$

$$T = U\tau_3 U^\dagger/g \quad (49)$$

are auxiliary quantities having simple transformation properties. Excluding CP violation, the non-standard three and four vector-boson couplings are described in this formalism by the following set of operators:

$$\mathcal{L}_1 = \text{Tr}(F_{\mu\nu}[V_\mu, V_\nu]) \quad (50)$$

$$\mathcal{L}_2 = i\frac{B_{\mu\nu}}{2}\text{Tr}(T[V_\mu, V_\nu]) \quad (51)$$

$$\mathcal{L}_3 = \text{Tr}(TF_{\mu\nu})\text{Tr}(T[V_\mu, V_\nu]) \quad (52)$$

$$\mathcal{L}_4 = (\text{Tr}[V_\mu V_\nu])^2 \quad (53)$$

$$\mathcal{L}_5 = (\text{Tr}[V_\mu V_\mu])^2 \quad (54)$$

$$\mathcal{L}_6 = \text{Tr}(V_\mu V_\nu)\text{Tr}(TV_\mu)\text{Tr}(TV_\nu) \quad (55)$$

$$\mathcal{L}_7 = \text{Tr}(V_\mu V_\mu)(\text{Tr}[TV_\nu])^2 \quad (56)$$

$$\mathcal{L}_8 = \frac{1}{2}[(\text{Tr}[TV_\mu])(\text{Tr}[TV_\nu])]^2 \quad (57)$$

In the unitary gauge $U = 1$, one has (with $c_W = \cos \theta_W$, $s_W = \sin \theta_W$)

$$\mathcal{L}_1 = i(c_W Z_{\mu\nu} + s_W F_{\mu\nu})W_\mu^+ W_\nu^- + Z_\nu/c_W(W_{\mu\nu}^+ W_\mu^- - W_{\mu\nu}^- W_\mu^+) \quad (58)$$

+ gauge-induced four boson vertices,

$$\mathcal{L}_2 = i(c_W F_{\mu\nu} - s_W Z_{\mu\nu})W_\mu^+ W_\nu^-, \quad (59)$$

$$\mathcal{L}_3 = i(c_W Z_{\mu\nu} + s_W F_{\mu\nu})W_\mu^+ W_\nu^-. \quad (60)$$

where $Z_{\mu\nu} = \partial_\mu Z_\nu - \partial_\nu Z_\mu$ and $W_{\mu\nu}^{+,-} = \partial_\mu W_\nu^{+,-} - \partial_\nu W_\mu^{+,-}$. The Standard Model without a Higgs corresponds to

$$\mathcal{L}_{EW} = \frac{1}{2}\text{Tr}(F_{\mu\nu}F^{\mu\nu}) - \frac{1}{4}B_{\mu\nu}B^{\mu\nu} + \frac{g^2 v^2}{4}\text{Tr}(V_\mu V^\mu). \quad (61)$$

5.2 Dynamical constraints

The list given in the previous section contains terms that give rise to vertices with minimally three or four vector-bosons. Already with the present data a number of constraints and/or consistency conditions can be put on the vertices. The most important of these come from the limits on the breaking of the so-called custodial symmetry. If the hypercharge is put to zero, the effective Lagrangian has a larger symmetry than $SU_L(2) \times U_Y(1)$, *i.e.* it has the symmetry $SU_L(2) \times SU_R(2)$. The $SU_R(2)$ invariance is a global invariance. Within the Standard Model this invariance is an invariance of the Higgs potential, but not of the full Lagrangian. It is ultimately this invariance that is responsible for the fact that the ρ parameter, which is the ratio of charged to neutral current strength, is equal to one at the tree level. Some terms in the Lagrangian, *i.e.* the ones containing the hypercharge field explicitly or the terms with T , that project out the third isospin component violate this symmetry explicitly. These terms, when inserted in a loop graph, give rise to quartically divergent contributions to the ρ parameter. Given the measurements, this means that the coefficients of these terms must be extremely small. It is therefore reasonable to limit oneself to a Lagrangian, where hypercharge appears only indirectly via a minimal coupling, so without explicit T . This assumption means physically that the ultimate dynamics that is

responsible for the strong interactions among the vector-bosons acts in the non-Abelian sector. Indeed one would not normally expect the hypercharge alone to become strong. However, we know that there is a strong violation of the custodial symmetry in the form of the top-quark mass. Actually the top-mass almost saturates the existing corrections to the ρ parameter, leaving no room for violations of the custodial symmetry in the anomalous vector-boson couplings. Therefore, we conclude: *If there really are strong vector-boson interactions, the mechanism for mass generation is unlikely to be the same for bosons and fermions.*

Eliminating the custodial symmetry violating interactions, we are left with the simplified Lagrangian, containing $\mathcal{L}_1, \mathcal{L}_4, \mathcal{L}_5$. Besides the vertices, there are also propagator corrections, in principle. We take the two-point functions without explicit T . Specifically, we add to the theory [134]

$$\mathcal{L}_{hc,tr} = -\frac{1}{2\Lambda_W^2} \text{Tr}[(D_\alpha F_{\mu\nu})(D^\alpha F^{\mu\nu})] + \frac{1}{2\Lambda_B^2} \text{Tr}[(\partial_\alpha B_{\mu\nu})(\partial^\alpha B^{\mu\nu})] \quad (62)$$

for the transverse degrees of freedom of the gauge-fields, and

$$\mathcal{L}_{hc,lg} = -\frac{g^2 v^2}{4\Lambda_V^2} \text{Tr}[(D^\alpha V^\mu)(D_\alpha V_\mu)] \quad (63)$$

for the longitudinal ones, where the Λ_X parametrise the quadratic divergences and are expected to represent the scales where new physics comes in. In phenomenological applications, these contributions give rise to form factors in the propagators [134, 139]. Introducing such cut-off dependent propagators in the analysis of the vector-boson pair production is similar to having s -dependent triple vector-boson couplings, which is the way the data are usually analysed.

This effective Lagrangian is very similar to the one in pion-physics. Indeed, if one takes the limit vacuum expectation value (vev) fixed and gauge-couplings to zero, one finds the standard pion Lagrangian. As it stands, one can use the LEP1 data to put a limit on the terms in the two point vertices. Using a naive analysis one finds [134] $1/\Lambda_B^2 = 0$. For the other two cut-offs one has:

- | | |
|--|---|
| A. The case $\Lambda_V^2 > 0, \Lambda_W^2 < 0$: | $\Lambda_V > 0.49 \text{ TeV}, \Lambda_W > 1.3 \text{ TeV}$. |
| B. The case $\Lambda_V^2 < 0, \Lambda_W^2 > 0$: | $ \Lambda_V > 0.74 \text{ TeV}, \Lambda_W > 1.5 \text{ TeV}$. |

This information is important for further limits at high-energy colliders, as it tells us, how one has to cut off off-shell propagators. We notice that the limits on the form factors are different for the transverse, longitudinal and hypercharge form factors. The precise limits are somewhat qualitative and should be taken as such. The current data show that $\Lambda = 0.5 \text{ TeV}$, which thus has to be considered as a minimal possible value as long as a dipole form factor is used. Further information comes from the direct measurements of the three-point couplings at LEP2, which tell us that they are small. Similar limits at the Tevatron have to be taken with some care, as there is a cut-off dependence. As there is no known model that can give large three-point interactions, we assume for the further analysis of the four-point vertices, that the three-point anomalous couplings are absent. Two more constraints can be put on the remaining two four-point vertices. The first comes from consistency of chiral perturbation theory [135]. Not every effective chiral Lagrangian can be generated from a physical underlying theory.

A second condition comes from the ρ parameter. Even the existing violation of the custodial symmetry, though indirect via the minimal coupling to hypercharge, gives a contribution to the ρ parameter. It constrains the combination $5g_4 + 2g_5$. The remaining combination $2\mathcal{L}_4 - 5\mathcal{L}_5$ is fully unconstrained by experiment and in principle gives a possibility for very strong interactions to be present. However, this particular combination does not seem to have any natural interpretation from underlying dynamics. Therefore, one can conclude presumably that both couplings g_4, g_5 are small. There is a loophole to this conclusion, namely when the anomalous couplings are so large that the one-loop approximation, used to arrive at the limits, is not consistent and resummation has to be performed everywhere. This is a somewhat exotic possibility that could lead to very low-lying resonances and which ought to be easy to discover at the LHC [41].

5.3 LHC processes

Given the situation described above, one has to ask oneself, what the LHC can do and in which way the data should be analysed. There are essentially three processes that can be used to study vector-boson vertices: vector-boson pair production, vector-boson scattering, triple vector-boson production. About the first two we have only a few remarks to make. They are discussed more fully in other contributions to the workshop.

5.31 *Vector-boson pair production*

Vector-boson pair production can be studied in a relatively straightforward way. The reason is that here the Higgs boson does not play a role in the Standard Model, as we take the incoming quarks to be massless. Therefore naive violations of unitarity can be compensated by the introduction of smooth form-factors.

One produces two vector-bosons via normal Standard Model processes with an anomalous vertex added. The extra anomalous coupling leads to unitarity-violating cross sections at high energy. As a total energy of 14 TeV is available this is a serious problem, in principle. It is cured by introducing a form factor for the incoming off-shell line connected to the anomalous vertex. Naively this leads to a form-factor dependent limit on the anomalous coupling in question. The LEP1 data gives a lower limit on the cut-off to be used inside the propagator. When one wants an overall limit on the anomalous coupling, one should use this value. This is particularly relevant for the Tevatron. Here one typically takes a cut-off of 2 TeV. This might give too strict a limit, as the LEP1 data indicate that the cut-off can be as low as 500 GeV. For practical purposes the analysis at the Tevatron should give limits on anomalous couplings for different values of the cut-off form factors, including low values of the cut-off. For the analysis at the LHC, one has much larger statistics. This means that one can do better and measure limits on the anomalous couplings as a function of the invariant mass of the produced system. This way one measures the anomalous form factor completely.

5.32 *Vector-boson scattering*

Here the situation is more complicated than in vector-boson pair production. The reason is that within the Standard Model the process cannot be considered without intermediate Higgs contribution. This would violate unitarity. However the incoming vector-bosons are basically on-shell and this allows the use of unitarisation methods, as are commonly used in chiral perturbation theory in pion physics. These methods tend to give rise to resonances in longitudinal vector-boson scattering. The precise details depend on the coupling constants. The unitarisation methods are not unique, but generically give rise to large $I = J = 0$ and/or $I = J = 1$ cross section enhancements. The literature is quite extensive: a good introduction is [136]; a recent review is [137].

5.33 *Triple vector-boson production*

In this case it is not clear how one should consistently approach an analysis of anomalous vector-boson couplings. Within the Standard Model the presence of the Higgs boson is essential in this channel. Leaving it out, one has to study the unitarisation. This unitarisation has to take place not only on the two-to-two scattering subgraphs, as in vector-boson scattering, but also on the incoming off-shell vector-boson, decaying into three real ones. The analysis here becomes too arbitrary to derive very meaningful results. One cannot calculate confidently anything here without a fully known underlying model of new strong interactions. Also measurable cross sections tend to be small, so that the triple vector-boson production is best used as corroboration of results in vector-boson scattering. Deviations of Standard Model cross sections could be seen, but the vector-boson scattering would be needed for interpretation.

One therefore needs the Standard Model results. The total number of events with three vector-bosons in the final state is given in Table 14. We used an integrated luminosity of 100 fb^{-1} and an

energy of 14 TeV throughout.

Table 14: Number of events: before cuts and all decays ($\sqrt{s} = 14$ TeV, 100 fb^{-1}).

M_{Higgs} (GeV)	200	400	600	800
$W^+W^-W^-$	11675	5084	4780	4800
$W^+W^+W^-$	20250	9243	8684	8768
W^+W^-Z	20915	11167	10638	10685
W^-ZZ	2294	1181	1113	1113
W^+ZZ	4084	2243	2108	2165
ZZZ	4883	1332	1087	1085

One sees from this table that a large part of the events comes from associated Higgs production, when the Higgs is light. However for the study of anomalous vector-boson couplings, the heavier Higgs results are arguably more relevant. Not all the events can be used for the analysis. If we limit ourselves to events, containing only electrons, muons and neutrinos, assuming just acceptance cuts we find the results shown in Table 15.

Table 15: Number of events containing only leptonic decays. Cuts on leptons: $|\eta| < 3$, $p_T > 20$ GeV; no cuts on missing energy ($\sqrt{s} = 14$ TeV, 100 fb^{-1}).

M_{Higgs} (GeV)	200	400	600	800
$W^+W^-W^-$	68	28	25	25
$W^+W^+W^-$	112	49	44	44
W^+W^-Z	32	17	15	15
W^-ZZ	1.0	0.51	0.46	0.45
W^+ZZ	1.7	0.88	0.79	0.79
ZZZ	0.62	0.18	0.13	0.12

We see that very little is left, in particular in the processes with at least two Z bosons, where the events can be fully reconstructed. In order to see how sensitive we are to anomalous couplings, we assumed a $4Z$ coupling with a form factor cut-off at 2 TeV. We make here no correction for efficiencies *etc.*. Using the triple Z boson production, assuming no events are seen in 100 fb^{-1} , we find a limit $|g_4 + g_5| < 0.09$ at the 95% CL, where g_4 and g_5 are the coefficients multiplying the operators \mathcal{L}_4 and \mathcal{L}_5 . This is to be compared with $-0.15 < 5g_4 + 2g_5 < 0.14$ [138] or $-0.066 < (5g_4 + 2g_5)\Lambda^2(\text{TeV}) < 0.026$ [134, 139]. So the sensitivity is not better than present indirect limits. Better limits exist in vector-boson scattering [140] or at a linear collider [141, 142, 143].

In the following tables we present numbers for observable cross sections in different decay modes of the vector-bosons. We used the following cuts.

$$\begin{aligned}
|\eta|_{\text{lepton}} < 3, \quad & |\eta|_{\text{jet}} < 2.5, \\
|p_T|_{\text{lepton}} > 20 \text{ GeV}, \quad & |p_T|_{\text{jet}} > 40 \text{ GeV}, \quad |p_T|_{2\nu} > 50 \text{ GeV}, \\
\Delta R_{\text{jet,lepton}} > 0.3, \quad & \Delta R_{\text{jet,jet}} > 0.5.
\end{aligned}$$

States with more than two neutrinos are not very useful because of the background from two vector-boson production. We did not consider final states containing τ -leptons.

With the given cuts, the total number of events to be expected is rather small. In particular, this is the case because we did not consider the reduction in events due to experimental inefficiencies, which may be relatively large because of the large number of particles in the final state. For the processes containing jets in the final state, there will be large backgrounds due to QCD processes. A final conclusion on the significance of the triple vector-boson production for constraining the four vector-boson couplings will need more work, involving detector Monte Carlo calculations.

However it is probably fair to say from the above results, that no very strong constraints will be found from this process at the LHC, but it is useful as a cross-check with other processes. It may provide complementary information if non-zero anomalous couplings are found.

Table 16: Number of events from ZZZ production in different decay modes ($\sqrt{s} = 14$ TeV, 100 fb^{-1}).

M_{Higgs} (GeV)	200	300	400	500	600
$6l$	0.62	0.29	0.18	0.14	0.13
$4l, 2\nu$	5.1	2.5	1.5	1.2	1.1
$4l, 2j$	6.6	3.8	2.2	1.7	1.4
$2l, 2j, 2\nu$	34	20	12	9.0	7.7
$2l, 4j$	24	19	11	7.6	6.0
$2\nu, 4j$	37	34	21	15	11
$6j$	25	31	19	12	8.7

Table 17: Number of events from WWZ production in different decay modes ($\sqrt{s} = 14$ TeV, 100 fb^{-1}).

M_{Higgs} (GeV)	200	300	400	500	600
$4l, 2\nu$	31	20	17	16	15
$3l, 2j, 1\nu$	51	40	31	28	26
$2l, 4j$	19	22	17	14	13
$2\nu, 4j$	63	74	60	51	48
$2l, 2j, 2\nu$	102	68	54	49	48
$1l, 4j, 1\nu$	262	196	140	127	127
$6j$	86	104	78	62	56

5.4 Unitarity limits and form factors

Unitarity in the Standard Model depends directly on its gauge-structure. Departure from this structure can violate unitarity at relatively low energies and so protection is provided in the effective Lagrangian for triple gauge-boson vertices by expressing the anomalous couplings as energy dependent form factors. For experimental results at a given subprocess energy \hat{s} (*i.e.* e^+e^- colliders), the choice of form

Table 18: Number of events from ZZW^- (upper) and ZZW^+ (lower) production in different decay modes ($\sqrt{s} = 14$ TeV, 100 fb^{-1}).

M_{Higgs} (GeV)	200	300	400	500	600
$5l, 1\nu$	0.45	1.04	0.63	0.52	0.47
	0.80	1.69	1.08	0.91	0.81
$3l, 2j, 1\nu$	3.37	6.89	5.36	4.18	3.73
	5.9	11.5	9.3	7.4	6.5
$1l, 4j, 1\nu$	7.6	11.5	12.4	10.0	8.4
	13.3	20.0	21.6	18	15
$4l, 2j$	0.29	1.0	0.54	0.38	0.32
	0.49	1.6	0.91	0.65	0.54
$2l, 2j, 2\nu$	2.0	6.5	3.5	2.5	2.2
	3.4	10.7	6.1	4.4	3.7
$2l, 4j$	2.5	7.4	5.4	3.6	2.9
	4.7	9.5	9.5	6.9	5.6
$4j, 2\nu$	8.9	27	18	12.6	10.4
	195.	54	38	28	23
$6j$	5.3	12.3	13.3	8.8	7.4
	9.1	20.7	23	16	12.5

factor parametrisation is not important since one can unambiguously translate between parametrisations. However, when results are integrated over a range of \hat{s} as they will be at the LHC, no simple translation is possible and results depend crucially on the choice of the form factors. The form factor behaviour of anomalous couplings should not be neglected, particularly in regions of \hat{s} near to unitarity limits. Any measurement of anomalous couplings over integrated energies carries with it *assumptions on the parametrisation of the form factor*.

This section outlines the considerations which influence the choice of form factor and suggests a method for measuring energy dependent anomalous couplings.

5.41 Form factor parametrisation

Triple gauge-boson vertices in di-boson production arise in the $J = 1$ partial wave amplitude only (s -channel exchange of a gauge-boson coupled to massless fermions). S -matrix unitarity implies a constant bound to any partial wave amplitude. This means unitarity is violated at asymptotically high energies if constant anomalous couplings are assumed. Unambiguous and model-independent constant unitarity constraints for WV production have been derived⁷ [144].

To conserve unitarity at arbitrary energies, anomalous couplings must be introduced as form factors. Thus, an arbitrary anomalous coupling $\tilde{A} = \tilde{A}_0 \times \mathcal{F}(q_1^2, q_2^2, P^2)$ vanishes when q_1^2 , q_2^2 , or P^2 becomes large, where q_1^2 and q_2^2 are the invariant masses squared of the production bosons and $P^2 = \hat{s}$ is

⁷Cancellations may occur if more than one anomalous coupling is allowed non-zero at a time, which weakens the unitarity limits somewhat.

Table 19: Number of events from $W^-W^+W^+$ production in different decay modes ($\sqrt{s} = 14$ TeV, 100 fb^{-1}).

M_{Higgs} (GeV)	200	300	400	500	600
$3l, 3\nu$	66	44	37	35	33
$l^+l^+, 2j, 2\nu$	57	43	31	26	24
$l^+l^-, 2j, 2\nu$	13	7.9	5.3	4.4	4.0
$l^+, 4j, 1\nu$	148	129	86	66	58
$l^-, 4j, 1\nu$	99	61	36	26	23
$6j$	50	74	46	32	25

Table 20: Number of events from $W^+W^-W^-$ production in different decay modes ($\sqrt{s} = 14$ TeV, 100 fb^{-1}).

M_{Higgs} (GeV)	200	300	400	500	600
$3l, 3\nu$	40	26	22	21	20
$l^-l^-, 2j, 2\nu$	34	25	17	14	13
$l^+l^-, 2j, 2\nu$	78	45	30	25	23
$l^-, 4j, 1\nu$	90	76	49	37	33
$l^+, 4j, 1\nu$	59	35	20	15	13
$6j$	29	43	26	18	14

the virtual exchange boson invariant mass squared. We refer to \tilde{A}_0 as the ‘‘bare coupling’’ and \tilde{A} as the form factor ($\tilde{A} \in \lambda^V, \Delta\kappa^V, h_i^V, \dots$). For di-boson production, the final state bosons are nearly on-shell $q_1^2, q_2^2 \simeq M_V^2$ even when finite width effects are taken into account, though large virtual exchange boson masses $\sqrt{\hat{s}}$ will be probed at the LHC.

The choice of parametrisation for the form factors is arbitrary provided unitarity is conserved at all energies for a sufficiently small value of anomalous coupling. A step function operating at a cutoff scale Λ_{FF} is sufficient⁸ though discontinuous and thus unphysical. More common in the literature is a generalised dipole form factor which is motivated by the well known nucleon form factors and has further appeal because it enters the Lagrangian in a form similar to that of a propagator of mass Λ_{FF} . The parametrisation is

$$\tilde{A} = \frac{\tilde{A}_0}{\left(1 + \frac{\hat{s}}{\Lambda_{\text{FF}}^2}\right)^n} \quad (64)$$

where $n > 1/2$ ($n > 1$) is sufficient for the WWV vertex anomalous couplings $\Delta\kappa^V$ ($\lambda^V, \Delta g_1^V$) which grow like $\hat{s}^{1/2}$, (\hat{s}). For the $ZV\gamma$ vertex $n > 3/2$ ($n > 5/2$) is sufficient for anomalous couplings $h_{1,3}^V, (h_{2,4}^V)$ which grow like $\hat{s}^{3/2}$, ($\hat{s}^{5/2}$). The usual assumptions are $n = 2$ for $g_1^V, \lambda^V, \kappa^V$ [31, 32, 30] and $n = 3$ ($n = 4$) for $h_{1,3}^V, (h_{2,4}^V)$ [145]. Unitarity limits for generalised dipole form factors have been enumerated [146, Equations 22-26].

The form factor scale Λ_{FF} can be regarded as a regularisation scale. It is related to (but not neces-

⁸*i.e.* assuming a step function form factor operating at 2 TeV, the λ^γ coupling conserves unitarity for $\lambda^\gamma < 0.99$ [144, Equation 23].

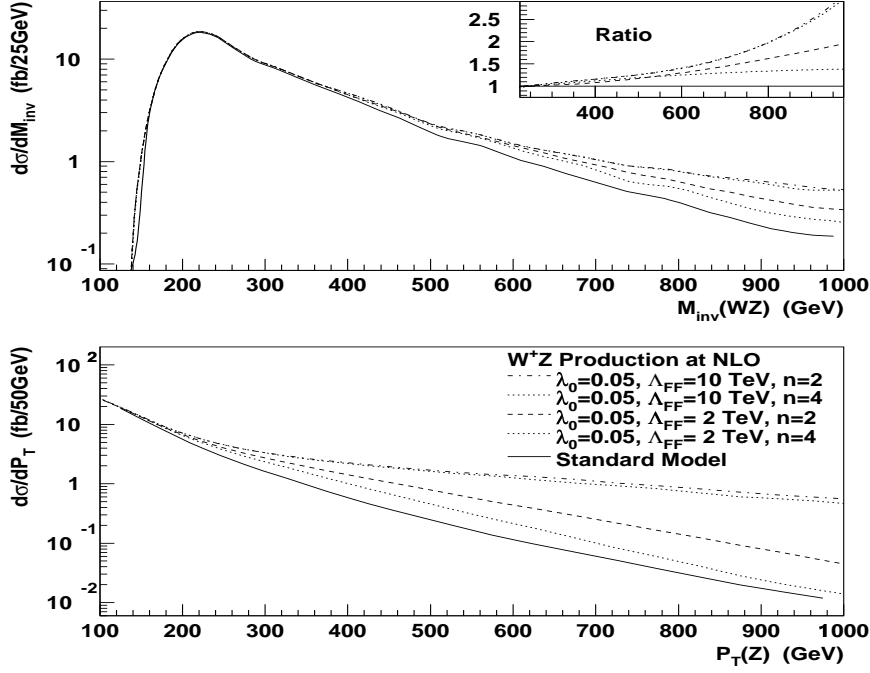


Fig. 31: Reconstructed $M_{\text{inv}}(WZ)$ and $p_T(Z)$ spectra are plotted for LHC W^+Z production with leptonic decays at $O(\alpha_s)$ for the Standard Model and various choices of the generalised dipole form factor parametrisation with bare coupling $\lambda_0 = 0.05$.

sarily identical to) the energy scale at which new physics becomes important in the weak boson sector.

5.42 Impact of form factor on \hat{s} dependent distributions

The impact of the form factor parametrisation on \hat{s} dependent distributions is illustrated in Figure 31 where the reconstructed ⁹ $M_{\text{inv}}(WZ)$ and $p_T(Z)$ spectra are plotted for LHC W^+Z production with leptonic decays at $O(\alpha_s)$. The Standard Model expectation is compared to scenarios with a modest $\lambda_0^Z = 0.05$ coupling for various generalised dipole form factor parametrisations.

For the region of low invariant mass where $\sqrt{\hat{s}} \ll \Lambda_{\text{FF}}$, the form factors remain essentially constant and distributions with the same bare coupling agree well. As the form factor scale Λ_{FF} is approached, the distributions begin to be pushed back to the SM expectation (visible at about $M_{\text{inv}}(WZ) = 500$ GeV for the $\Lambda_{\text{FF}}=2$ TeV case). For $\sqrt{\hat{s}} > \Lambda_{\text{FF}}$ the distribution returns to the SM expectation. The exponent of the form factor n dictates how fast the “pushing” occurs as Λ_{FF} is approached. Thus distributions sensitive to the $ZV\gamma$ vertex (for which $n = 3$ or 4 is the usual choice) exhibit a more pronounced form factor behaviour than distributions sensitive to the WWV vertex (for which $n = 2$ is usual).

Since distributions are constrained to the SM expectation at invariant masses above the form factor scale, great care should be taken when fitting to a form factor parametrised model in a region with data where $\sqrt{\hat{s}} \geq \Lambda_{\text{FF}}$. Effectively, since the anomalous couplings are constrained near zero above Λ_{FF} by the parametrisation model, *there are no free parameters for the fit* in this \hat{s} region. For the case of observable non-zero anomalous couplings, an analysis assuming a parametrisation of the form factor with fixed Λ_{FF} smaller than that provided by nature but within the \hat{s} accessible by the machine would overestimate the

⁹Reconstructing $M_{\text{inv}}(WZ)$ requires knowledge of the neutrino longitudinal momentum which is obtained up to a two-fold ambiguity using the W mass constraint. Each solution is given half weight in the $M_{\text{inv}}(WZ)$ spectrum.

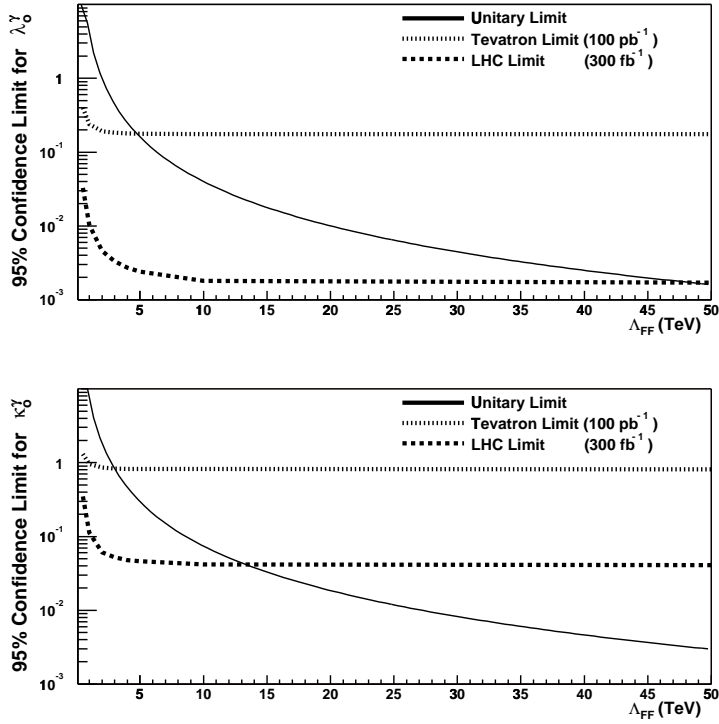


Fig. 32: Limits for $WW\gamma$ vertex anomalous couplings at the 95% confidence level as a function of Λ_{FF} for a $n = 2$ dipole form factor parametrisation are presented. The limits are derived at NLO generator level for the $W\gamma \rightarrow e\nu_e\gamma, \mu\nu_\mu\gamma$ channel using a binned maximum likelihood fit to the $p_T(\gamma)$ distribution. The limits are for illustrative purposes only. Further details are provided in the text.

anomalous coupling. This is because large bare coupling fit values are necessary in the $\sqrt{\hat{s}} \geq \Lambda_{\text{FF}}$ region to counter the (artificially imposed) form factor behaviour.

5.43 Impact of form factor scale on sensitivity limits

If triple gauge-coupling (TGC) measurements are consistent with the SM and confidence limits are to be derived, it is impossible to avoid form factor parametrisation assumptions.

The dependence of anomalous coupling limits on the form factor scale Λ_{FF} is illustrated in Figure 32 where the 95% confidence limits for $WW\gamma$ vertex anomalous $\lambda_0^\gamma, \Delta\kappa_0^\gamma$ couplings in $W\gamma$ production with $W \rightarrow e\nu_e, \mu\nu_\mu$ are presented as a function of Λ_{FF} for a dipole form factor with $n = 2$. The limits are for illustrative purposes only and have been derived at NLO generator level using a binned maximum likelihood fit to the $p_T(\gamma)$ distribution. No detector simulation has been applied and the specific choice of cuts are unimportant.

The unitarity limit curve is superimposed. The region above this is non-physical (violates unitarity). The curve is independent of experiment and analysis but depends on the form factor parametrisation. It goes asymptotically to zero for large Λ_{FF} indicating TGC couplings are restricted to SM values at extreme energies.

Simulated experimental limits for the Tevatron (2 TeV $p\bar{p}$ collisions, $\mathcal{L} = 100 \text{ pb}^{-1}$) and the LHC (14 TeV pp collisions, $\mathcal{L} = 300 \text{ fb}^{-1}$) are presented. The limits depend on the analysis and machine parameters. The restricted \hat{s} accessible by the machines result in an asymptotic behaviour wherein an optimal limit for anomalous couplings is reached. We refer to the scale at which this occurs as Λ_{machine} .

A measurement with this scale reflects the maximal discovery potential for anomalous couplings for a given machine (since the full spectra in \hat{s} contributes to the limit). It occurs at about 2 TeV for the Tevatron and about 5-10 TeV for the LHC for λ^γ , $\Delta\kappa^\gamma$ and lies below the unitarity limit in both cases. The experimental limits are not sensitive to changes in Λ_{FF} for $\Lambda_{\text{FF}} \geq \Lambda_{\text{machine}}$. Indeed, in this region the distributions behave exactly as if the form factors were constants $\tilde{A} \equiv \tilde{A}_0$. There is no contradiction with unitarity in approximating them as such, provided we consider sufficiently small anomalous couplings so as to remain far from the unitarity limit *at the energy regimes accessible by the machines*. This is consistent with the basic assumption ($\Lambda \gg \sqrt{\hat{s}}$) which allows for the effective Lagrangian parametrisation of the TGC vertex keeping only the lowest dimensions: it is sufficient to assume the form factor behaviour commences above the observable scale so as to regulate the distributions before the unitarity limit.

There is also a region on the extreme left side of the plots in Figure 32 (although not indicated) which is excluded by direct experimental searches. This is the region where physics is believed to be well described by the SM.

Experimentally it is desirable to report confidence limits as a function of Λ_{FF} . A result using $\Lambda_{\text{FF}} = \Lambda_{\text{machine}}$ should be included (so long as Λ_{machine} lies below the unitarity limit) as it is motivated by machine parameters and provides a reasonable point of reference for comparisons between different experiments. Other scales (particularly those of theoretical interest) should not be neglected¹⁰.

5.44 Measuring form factors

For a machine of sufficient luminosity such as the LHC, it is possible to measure the energy dependence of anomalous couplings¹¹ by grouping the data into bins of invariant mass and extracting constant anomalous couplings within these restricted domains. Such a measurement does not carry any assumptions about the form factor (until a fit to a given parametrisation is performed). It is a viable method for measuring form factors, but due to the restricted number of events in each bin, will not produce competitive limits. The method is best employed in the case where non-zero anomalous couplings have been observed.

The method is illustrated in Figure 33 for the case of the $W\gamma$ channel with $W \rightarrow e\nu_e, \mu\nu_\mu$ assuming nature provides an anomalous $\lambda_0^\gamma = 0.025$ coupling described by an $n = 2$ dipole form factor with $\Lambda_{\text{FF}} = 2$ TeV. Three years of high luminosity (300 fb^{-1}) LHC events generated at NLO are binned according to the reconstructed $M_{\text{inv}}(W\gamma)$. The corresponding points derived using the generated (unobservable) $M_{\text{inv}}(W\gamma)$ are superimposed for comparison. Bin widths (denoted by arrows along the x-axis) are chosen so as to ensure sufficient data in each $M_{\text{inv}}(W\gamma)$ domain. A measurement of the anomalous coupling (assumed constant) is performed within each domain using a binned maximum likelihood fit to the $p_T(\gamma)$ distribution. No detector simulation has been applied and the specific choice of cuts is unimportant for this illustration. The results of the likelihood fits are plotted as a function of $M_{\text{inv}}(W\gamma)$ and a fit to an $n = 2$ dipole form factor is performed. With this simple illustration, the bare coupling and form factor scale are reconstructed as $\lambda_0^\gamma = 0.029$ and $\Lambda_{\text{FF}} = 1.67$ TeV. Sensitivity to the anomalous coupling increases in the larger invariant mass domains, reflecting the \hat{s} growth of the λ_0^γ coupling (indeed the measurement in the first bin is consistent with zero). Systematic effects related to the fit method (such as the non-uniform distribution of events within the bins) have not been accounted for in this illustration.

5.5 Partonic simulation tools for di-boson production

Several Monte Carlo programs for hadronic di-boson event simulation are in common use. General purpose programs such as PYTHIA [123] evaluate the matrix element at leading order (LO) with no spin correlations for boson decay products. Limited or no anomalous couplings are included. In the past

¹⁰It should be noted that particularly for small choices of Λ_{FF} , a change in the analysis strategy may be necessary to increase sensitivity to the relevant regions of \hat{s} .

¹¹The suggestion of making such a measurement is not new [130] but has received little attention in the literature.

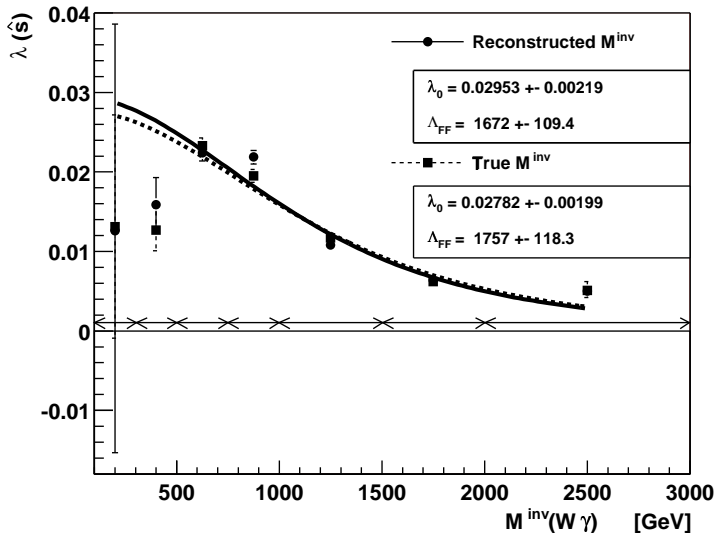


Fig. 33: The λ^γ form factor is extracted in restricted invariant mass domains for 300 fb^{-1} of LHC data in the $W\gamma$ channel with $W \rightarrow e\nu_e, \mu\nu_\mu$ assuming nature provides an anomalous $\lambda_0^\gamma = 0.025$ coupling described by an $n = 2$ dipole form factor with $\Lambda_{\text{FF}} = 2 \text{ TeV}$. A fit to a $n = 2$ dipole form factor is performed to reconstruct the bare coupling and form factor scale. Arrows along the x -axis denote bin widths. Further details are provided in the text.

decade, programs have been implemented to calculate di-boson production with leptonic decays to next-to-leading order (NLO) in QCD. The diagrams contributing to $O(\alpha_s)$ are: the squared Born (LO) graphs, the interference of the Born with the virtual one-loop graphs, and the squared real emission graphs.

The NLO generators by Baur, Han, and Ohnemus [32, 31, 30, 33] (BHO) have been available for several years. They employ the phase space slicing method [147] and the calculation is performed in the narrow width approximation for the leptonically decaying gauge-bosons. Non-standard TGC couplings are included. Spin correlations in the leptonic decays are included everywhere except in the virtual contribution. The authors expect a negligible overall effect from neglecting the spin correlations in the virtual corrections as compared to the uncertainty from parton distribution functions and the choice of factorisation scale. More recently Dixon, Kunszt, and Signer [19] (DKS) have implemented a program with full lepton decay spin correlations (helicity amplitudes are presented in [17]). The subtraction method [128, 149] is employed in the narrow width approximation including non-standard TGC couplings. A third Monte Carlo program, MCFM, by Campbell and Ellis [18] exists. It does not assume the narrow width approximation and includes singly resonant diagrams but does not allow for non-standard TGC couplings. The effects of these improvements in MCFM are largest in off-resonant regions - such as near di-boson production thresholds. The regions are of importance to studies of SM backgrounds to new physics but contribute negligibly to the cross section in TGC studies for typical choices of kinematic cuts [30].

A common feature of the NLO generators is the inability to produce unweighted events. Both the phase space slicing and subtraction methods produce events for which the weight may be either positive or negative - thus it is only the integrated cross section over a region of phase space (*i.e.* histogram bin) which is physical. This makes traditional Monte Carlo techniques for unweighting events (such as hit-and-miss) difficult to apply, and we are aware of no universally satisfactory technique for producing unweighted events using the NLO generators¹². Computationally this can render analyses very slow, since a large fraction of CPU time can be spent processing events with near-vanishing cross sections.

¹²One method involves reweighting events from a LO generator using a “look-up table” constructed at NLO.

5.51 Comparison of NLO particle level generators

In this section, we present a comparison of the predictions from the BHO and DKS generators, for which no published consistency check exists, restricting ourselves to W^+Z and WW production for simplicity. The DKS and MCFM packages have been found to be in good agreement [19].

The comparison is performed at LHC energy (14 TeV pp collisions) using CTEQ4M [67] structure functions¹³. Input parameters are taken as $\alpha_{EM} = \frac{1}{128}$, $\sin^2 \theta_W = 0.23$, $\alpha_s(M_Z) = 0.116$, $M_W = 80.396$ GeV, $M_Z = 91.187$ GeV, factorisation scale $Q^2 = M_W^2$, and Cabibbo angle $\cos \theta_C = 0.975$ with no 3rd generation mixing. Branching ratios are taken as $BR(Z \rightarrow l^+l^-) = 3.36\%$, $BR(W^\pm \rightarrow l^\pm \nu) = 10.8\%$. The b quark contribution to parton distributions has been taken as zero ($b\bar{b} \rightarrow W^+W^-$ contributes $\mathcal{O}(2\%)$ at LHC [19]). Kinematic cuts motivated by TGC analyses are chosen. The transverse momentum of all leptons must exceed 25 GeV and the rapidity of all leptons must be less than 3. Missing transverse momentum must be greater than 25 GeV. A jet is defined when the transverse momentum of a parton exceeds 30 GeV in the pseudorapidity interval $|\eta| < 3$.

For W^+Z production, the transverse momentum distribution of the Z boson $p_T(Z)$, the distribution of rapidity separation between the W^+ decay lepton and the Z boson $y(l) - y(Z)$, and total cross section are compared at LO, inclusive NLO, and NLO with a jet veto. Branching ratios to e, μ -type leptons are applied. For WW production, the transverse momentum distribution of the lepton pair from the W^\pm decays $|\vec{p}_T(e^-) + \vec{p}_T(e^+)|$, the distribution of rapidity separation between the W decay leptons $y(e^-) - y(e^+)$, the angle between the W decay leptons in the transverse plane $\cos \Phi(e^-, e^+)$, and the total cross section are compared at LO, inclusive NLO, and NLO with a jet veto. Branching ratios to one lepton flavour are applied.

The cross section results are presented in Table 21 and the distributions in Figure 34. Consistency between generators is at the 1% level for WZ production and 3-4% level for WW production. Qualitative agreement is observed in the distribution shapes.

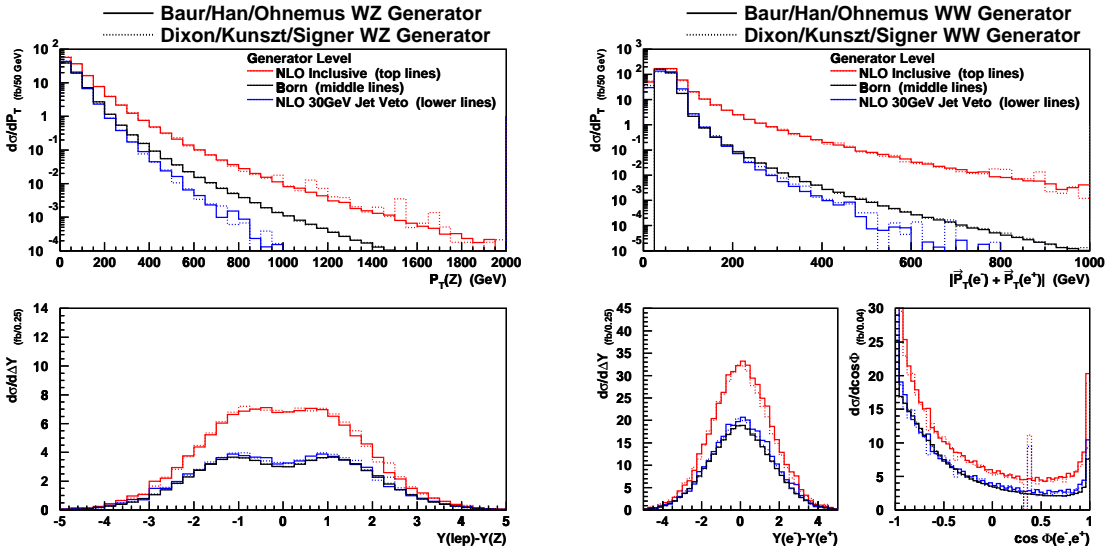


Fig. 34: Distributions for W^+Z production (left) and WW production (right) from the Baur/Han/Ohnemus and Dixon/Kunszt/Signer generators are superimposed at Born level, inclusive NLO, and NLO with a jet veto (defined as $p_T(\text{jet}) > 30$ GeV, $|\eta(\text{jet})| < 3$).

¹³The choice of parton distribution function has an $\mathcal{O}(5\%)$ effect on the cross section.

Table 21: W^+Z and WW cross section predictions are tabulated for the BHO and DKS generators at LO, inclusive NLO, and NLO with a jet veto. A jet is defined for $p_T(\text{jet}) > 30$ GeV, $\eta(\text{jet}) < 3$. Statistical precision is $\mathcal{O}(1$ fb).

W^+Z Production			
	Baur/Han/Ohnemus	Dixon/Kunszt/Signer	% diff.
Standard Model			
$\sigma_{\text{NLO inclusive}}$	127.9 fb	129.8 fb	1.4%
$\sigma_{\text{NLO 0jet}}$	74.7 fb	75.1 fb	0.5%
σ_{Born}	70.5 fb	70.9 fb	0.5%
$\Delta g_Z^1 = 0, \Delta \kappa_Z = 0.5, \lambda_Z = 0.1$ ($\Lambda = 2$ TeV)			
$\sigma_{\text{NLO inclusive}}$	198.5 fb	199.9 fb	0.7%
$\sigma_{\text{NLO 0jet}}$	107.5 fb	106.8 fb	0.7%
σ_{Born}	119.7 fb	119.9 fb	0.2%
WW Production			
	Baur/Han/Ohnemus	Dixon/Kunszt/Signer	% diff.
Standard Model			
$\sigma_{\text{NLO inclusive}}$	500.5 fb	483.2 fb	3.5%
$\sigma_{\text{NLO 0jet}}$	321.0 fb	309.6 fb	3.6%
σ_{Born}	294.0 fb	295.5 fb	0.5%
$\Delta g_Z^1 = 0.25, \Delta \kappa_Z = \Delta \kappa_\gamma = 0.1, \lambda_Z = \lambda_\gamma = 0.1$ ($\Lambda = 2$ TeV)			
$\sigma_{\text{NLO inclusive}}$	594.2 fb	575.0 fb	3.3%
$\sigma_{\text{NLO 0jet}}$	363.0 fb	349.6 fb	3.8%
σ_{Born}	351.6 fb	353.7 fb	0.6%

5.52 Effects of NLO corrections

NLO corrections in hadronic di-boson production are large at LHC energies, particularly in the region of high transverse momentum and small rapidity separation (see Figure 34) which is the same region of maximum sensitivity to anomalous TGCs. The corrections can amount to more than an order of magnitude. The high quark-gluon luminosity at the LHC and a logarithmic enhancement at high transverse momentum in the qg and $\bar{q}g$ real emissions subprocesses are primarily responsible [32, 31, 30]. In the channels which exhibit radiation zero behaviour (*i.e.* $W\gamma$ and WZ), the Born contribution is suppressed and NLO corrections are even larger [32, 31]. Since the $O(\alpha_s)$ subprocesses responsible for the enhancement at large transverse momentum do not involve TGCs, the overall effect of NLO corrections is a spoiling of sensitivity to anomalous TGCs.

Jet veto Distributions obtained by vetoing hard jets in the central rapidity region for one possible choice of jet definition ($p_T(\text{jet}) > 30$ GeV, $|\eta(\text{jet})| < 3$) are shown in Figure 34. The jet veto is effective in recovering the qualitative shape of the LO distributions including the approximate radiation zero in WZ production (Figure 34, bottom left). The jet veto serves to recover anomalous TGC sensitivity which is otherwise lost when introducing NLO corrections. A 10-30% improvement in anomalous TGC coupling sensitivity limits in WZ production can be achieved [31] when a jet veto is applied as compared to the inclusive NLO case. These limits are often close to those obtained at LO. In general results derived at LO can be considered approximate zero jet results and their conclusions remain interesting. A jet veto also reduces the scale dependence of NLO results [32, 31, 30, 19].

5.6 Determination of TGCs

At the LHC the measurement of TGCs will benefit from both the large statistics and the high centre-of-mass energy. The large available statistics will allow the use of multi-dimensional distributions to increase the sensitivity to the TGCs.

This section discusses the experimental observables sensitive to TGCs and describes the analysis methods employed to measure the TGCs.

5.61 Experimental observables

The experimental sensitivity to the TGCs comes from the increase of the production cross section and the modification of differential distributions with non-standard TGCs. The sensitivity is enhanced at high centre-of-mass energies of the hard scattering process, more significantly for λ -type TGCs than for κ -type TGCs in the case of $W\gamma$ and WZ production. As an example, the increase in the number of events with large di-boson invariant masses is a clear signature of non-standard TGCs as illustrated in Figure 35, where the invariant mass of the hard scattering is shown for $W\gamma$ events, simulated with a parametric description of the ATLAS detector, for the Standard Model and non-standard TGCs. A form factor of 10 TeV was used.

For the event generation employing non-standard values of the TGCs, leading order (LO) [150] as well as next to leading order (NLO) [32, 33] calculations have been used (see Section 5.5). Limits on the TGCs can be obtained from event counting in the high invariant mass region. The disadvantage of such an approach alone is that the behaviour of the cross section as function of the TGCs makes it difficult to disentangle the contributions from different TGCs and even their sign (with respect to SM). It is therefore advantageous to combine it with information from angular distributions of the bosons and possibly their decay angles; this improves the sensitivity and improves the separation of contributions from different non-standard TGCs.

In general it is possible experimentally to reconstruct up to four (six) angular variables in the di-boson rest-frame describing an $W\gamma$ or $Z\gamma$ (WZ) event:

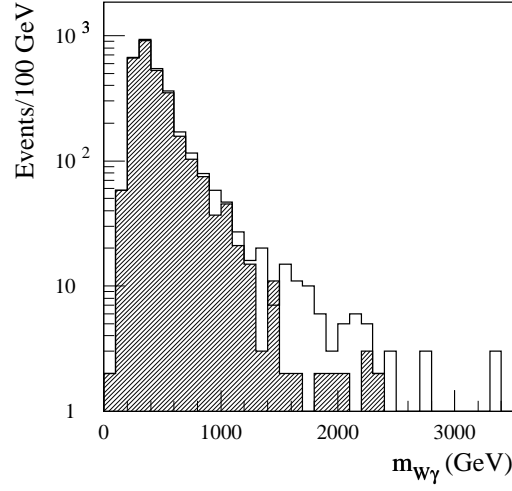


Fig. 35: The distribution of the invariant mass of the $W\gamma$ system from $pp \rightarrow W\gamma$. Standard Model data (shaded histogram) and a non-standard value of 0.01 for λ_γ (white histogram) are shown. Both charges of W were generated using a parameterised Monte Carlo and summed. The number of events corresponds to an integrated luminosity of 30 fb^{-1} .

- Boson production angles, Θ and Φ , of the di-boson system with respect to the beam-axis in the di-boson rest-frame.
- Decay angles of bosons, $\theta_{1(2)}^*$ and $\phi_{1(2)}^*$, in the rest-frame of the decaying bosons.

The azimuthal boson production angle, Φ , has no sensitivity to the TGCs. In case of $W\gamma/WZ$, Θ is the most sensitive kinematical variable. The enhanced sensitivity to the TGCs in WV production is due to the vanishing of helicity amplitudes in the Standard Model prediction at $\cos \Theta \sim 1/3$, affecting the small $|\eta|$ region [150]. Non-standard TGCs may partially eliminate the radiation zero, although the zero radiation prediction is less significant when including NLO corrections [32]. In $Z\gamma$ production, no radiation amplitude zero is present.

In contrast, the sensitivity to the TGCs from the decay angles is weak; the decay angles primarily serve as projectors of different helicity components, enhancing the sensitivity of other variables.

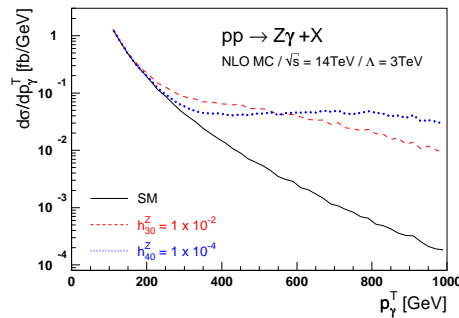


Fig. 36: Differential cross section for $Z\gamma$ production versus p_T^γ for Standard Model (solid line) and two different non-standard couplings (dashed and dotted lines) at LHC.

In the study presented here, several experimentally derived observables and combinations thereof have been studied to assess the possible sensitivity to the TGCs. For both $(W\gamma, WZ)$ and $(Z\gamma, ZZ)$ events the observables are very similar; for WZ , the Z takes the role of the γ . The actual behaviour of

the observables as function of the couplings and the energy is different between the processes, due to the different masses of the involved bosons.

One observable, the transverse momentum, p_T , of the γ or Z (depending on the di-boson process), which has traditionally been used at hadron colliders, has sensitivity from a combination of high mass event counting and the Θ angular distribution. Figure 36 shows the enhancement of di-boson production cross section for large values of the photon transverse momentum in presence of non-standard couplings.

The distribution of $p_T^{\gamma, Z}$ assuming an integrated luminosity of 30 fb^{-1} is shown in Figure 37 for $W\gamma$ and WZ events, simulated with a parametric detector simulation program, for the Standard Model and non-standard TGCs. The enhancement for non-standard TGCs at high $p_T^{\gamma, Z}$ is clearly visible and, furthermore, the qualitative behaviour is the same for different TGCs.

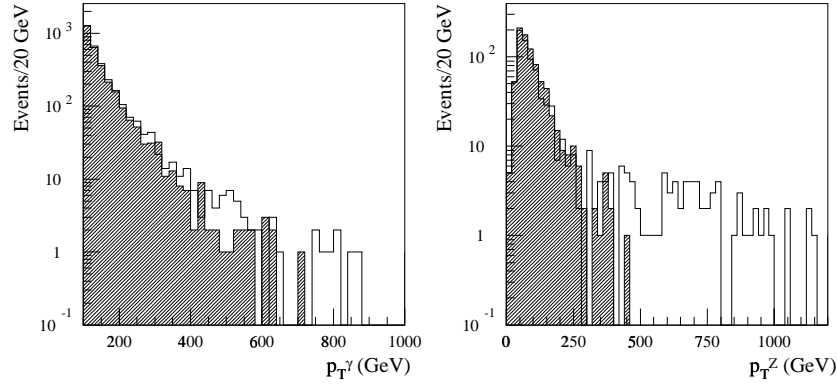


Fig. 37: Distribution of $p_T^{\gamma, Z}$ for $W\gamma$ (left) and WZ (right) events for an integrated luminosity of 30 fb^{-1} . Distributions are shown for the Standard Model (shaded histograms) and for non-standard values $\lambda_\gamma = 0.01$ (left) and $\Delta g_1^Z = 0.05$ (right).

For the statistics expected at the LHC, even after 3 years running at low luminosity, one may enhance the experimental sensitivity further by separating the different types of information in multi-dimensional distributions. For $W\gamma$ and WZ di-boson production, two sets of variables have been studied (and the equivalent set for WZ): $(m_{W\gamma}, |\eta_\gamma^*|)$, and $(p_T^{\gamma, Z}, \theta^*)$, where $|\eta_\gamma^*|$ is the rapidity of γ with respect to the beam direction in the $W\gamma$ system (equivalent to Θ), and θ^* is the polar decay angle of the charged lepton in the W rest-frame. Both sets consist of one variable sensitive to the energy behaviour and one sensitive to the angular information. For $|\eta_\gamma^*|$ and θ^* , a complete reconstruction of the W is necessary. The momentum of the W can be reconstructed by using the W mass as a constraint and assuming that the missing transverse energy is carried away by the neutrino. This leads to a two-fold ambiguity in the reconstruction. Alternatively, $|\eta_\gamma^*|$ may be approximated by the rapidity difference between the lepton from the W and the γ . Distributions of $|\eta_\gamma^*|$ and θ^* are shown in Figure 38, for both the standard model expectation and different non-standard TGCs. The high sensitivity to the TGCs from $|\eta_\gamma^*|$ is due to the characteristic “zero radiation” gap. In contrast, the sensitivity to the TGCs from the decay polar angle, θ^* , is weak.

5.62 Analysis techniques for TGC determination

Depending on the available statistics and the dimensionality of the experimental distributions, different extraction techniques can be used in the determination of the TGCs.

One approach employed in this study determines the couplings by a binned maximum-likelihood fit to distributions of the observables, combined with the total cross section information. The likelihood

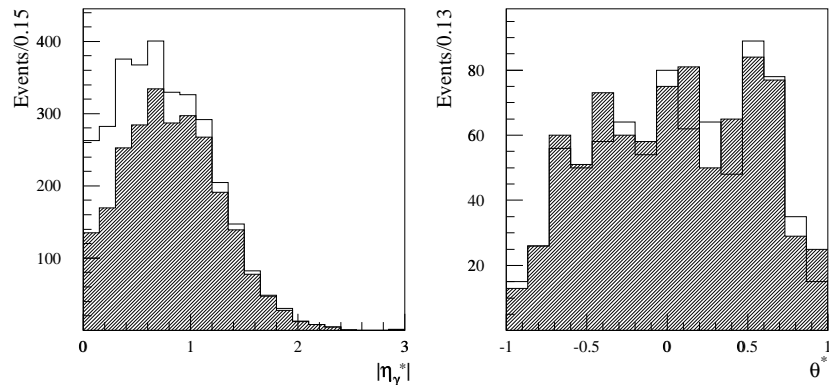


Fig. 38: Distribution of $|\eta_\gamma^*|$ (left) and θ^* (right) from $W\gamma$ and WZ events, respectively, for an integrated luminosity of 30 fb^{-1} . Distributions are shown for the Standard Model (shaded histograms) and for non-standard values (white histograms) $\Delta\kappa_\gamma = 0.2$ (left) and $\Delta\kappa_Z = 0.2$ (right).

function is constructed by comparing the fitted histogram with a reference histogram using Poisson probabilities. The reference distributions can be obtained for different values of the couplings by reweighting Monte Carlo events at generator level or equivalently using several Monte Carlo event samples generated for different values of the TGCs.

Although the expected number of events at the LHC will allow binning in two dimensions, a general multidimensional binned fit using all the TGC sensitive information will not be possible. In the latter case, an unbinned maximum likelihood fit to the observed information can be used, where the probability distribution functions can be constructed by Monte Carlo techniques. In the case of many dimensions, this approach can be time-consuming, but it may be advantageously combined with the reweighting technique. The information from the absolute prediction of the cross section can be included by the so-called “extended maximum likelihood” method [151].

5.7 Sensitivities at LHC

Sensitivity limits have been derived for the triple gauge-couplings $WW\gamma$ (ATLAS, CMS), WWZ (ATLAS) and $ZZ\gamma$ (CMS). The analysis techniques used by ATLAS and CMS are described in Section 5.6. The ATLAS studies assume an integrated luminosity of $\int \mathcal{L} dt = 30 \text{ fb}^{-1}$, corresponding to three years of LHC low luminosity operation. CMS assumes 100 fb^{-1} , which is the expectation for one year of LHC high luminosity running.

CMS has performed its studies for a range of different form factor scales Λ_{FF} , as motivated in Section 5.4. The plots in Figure 39 show the expected 95% CL limits on the anomalous $WW\gamma$ and $ZZ\gamma$ coupling parameters together with the corresponding unitarity limits. Only the displayed coupling is considered to deviate from the Standard Model. The points where the experimental curves turn asymptotic with respect to Λ_{FF} - or are crossed by the unitarity limit - give an indication on the range of form factor scales accessible by the experiments. While the current Tevatron measurements probe the triple gauge-couplings up to form factors of $\Lambda_{FF} = 0.75 \text{ TeV}$ and around 2 TeV for $ZZ\gamma$ and $(WW\gamma, WWZ)$, respectively [16], the LHC experiments will be able to study far smaller structures with scales up to 10 TeV , assuming an integrated luminosity of 100 fb^{-1} .

Multi-dimensional fits where several couplings are allowed to vary have also been performed [152]. Here, the sensitivity limits extracted from the log likelihood curves form an ellipse for a particular confidence level. Figure 40 shows the typical $WW\gamma$ sensitivity contours in the two-dimensional CP-conserving $(\kappa \times \lambda)$ coupling space for a form factor scale of 10 TeV .

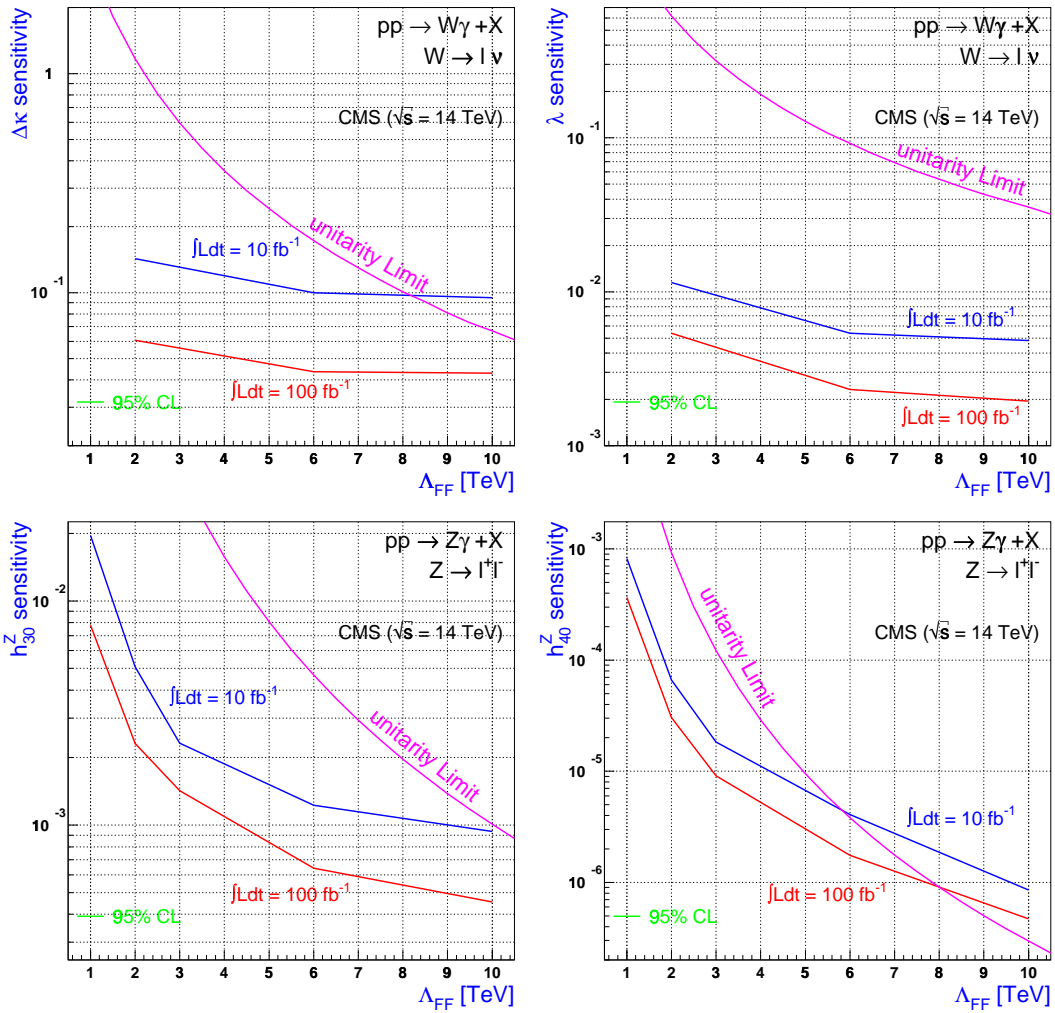


Fig. 39: Sensitivity limits on the $WW\gamma$ (top) and $ZZ\gamma$ (bottom) coupling parameters from a two-dimensional likelihood fit as a function of the form factor scale Λ_{FF} .

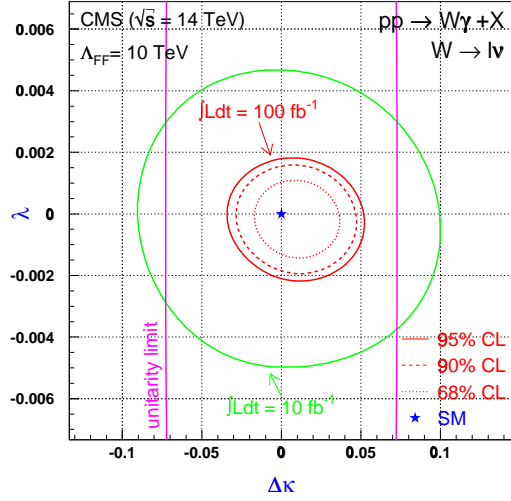


Fig. 40: Sensitivity contours in the CP-conserving $W\gamma$ coupling space for integrated luminosities of 10 fb^{-1} and 100 fb^{-1} .

Table 22: Sensitivity limits (95% CL), assuming integrated luminosities of 30 fb^{-1} and 100 fb^{-1} , respectively. The form factor scale is $\Lambda_{FF} = 10 \text{ TeV}$ for $WW\gamma$, WWZ and 6 TeV for $ZZ\gamma$.

Vertex	Coupling	$(m_{W\gamma}, \eta^*)$	(p_T^γ, θ^*)	p_T^γ
$WW\gamma$	$\Delta\kappa_\gamma$	0.035	0.046	0.043
$\Lambda_{FF} = 10 \text{ TeV}$	λ_γ	0.0025	0.0027	0.0020
WWZ	Δg_1^Z	0.0078	0.0089	—
	$\Delta\kappa_Z$	0.069	0.100	—
$\Lambda_{FF} = 10 \text{ TeV}$	λ_Z	0.0058	0.0071	—
$ZZ\gamma$	h_{30}^Z	—	—	6.4×10^{-4}
$\Lambda_{FF} = 6 \text{ TeV}$	h_{40}^Z	—	—	1.8×10^{-6}

Table 22 summarises the sensitivity limits obtained by ATLAS and CMS as reported in [53, 152]. In addition, ATLAS has performed a fit using the complete generator level phase space information [53]. The results for this *ideal case* show that, as the high energy tails of the p_T^γ distributions exhibit a very strong sensitivity to the λ -like anomalous couplings, the additional information does not improve the limits on this type of couplings considerably. However, the κ -type couplings may profit from a more sophisticated data analysis.

From the numbers in Table 22, we expect an improvement in sensitivity by up to two (four) orders of magnitude for anomalous $WW\gamma/WWZ$ ($ZZ\gamma$) couplings, with respect to the current Tevatron limits. The strong increase in sensitivity is due to the pronounced high \hat{s} enhancement at the LHC, most prominently for $ZZ\gamma$ (see Section 5.42). A smaller choice of the form factor scale would cut off this enhancement and diminish the sensitivity considerably, as shown in the lower plots in Figure 39.

5.8 Backgrounds to $W\gamma$

The $W\gamma$ signal has a very small cross section, compared to W +jet production for example, and can contain a significant amount of background. The dominant background to the $W\gamma$ signal is from W +jet production where the jet is misidentified as a photon, resulting in a fake signal. Radiative W decay also contributes when the electron from the W decay radiates a photon, and both $t\bar{t}\gamma$ and $b\bar{b}\gamma$ quark-gluon fusion processes can also produce a fake signal contributing to the background. $Z\gamma$ production and $W(\tau\nu)\gamma$ also make a small contribution to the backgrounds.

Previous studies [153, 154, 155, 156] have shown that the $W\gamma$ signal will be observable at the LHC provided that the backgrounds can be suppressed. All the backgrounds were generated with PYTHIA 5.7 [123] in conjunction with the CMSJET [157] fast detector simulation for the CMS experiment.

5.8.1 W +jet and $W \rightarrow l\nu\gamma$ backgrounds

The dominant background to the process $pp \rightarrow W(e\nu)\gamma$ arises from W +jet events where the jet decays electromagnetically and is reconstructed in the calorimeter as a photon. The probability for the jet to fluctuate into an isolated electromagnetic shower is small, but the large number of jets above 10 GeV in the W sample guarantees that some jets will look identical to photons. Even if the jet is not misidentified as a photon, it is possible for a radiative decay of the W to produce the same signature as the signal. If the lepton from the W decay radiates a photon, an event signature of γ, l, ν may be observed. Cuts must therefore be applied to reduce this background.

W +jet Figure 41 shows the $p_T(\gamma)$ spectrum for misidentified photon from the W +jet background and the real photon from the $W\gamma$ signal. A photon isolation cut has been applied to both data sets. A rejection power of nearly 7 can be obtained with an efficiency loss of less than 5%, by using an isolation area of $\Delta R = 0.25$ and a p_T threshold of 2 GeV [158]. A greater rejection power with a much smaller efficiency loss is available at low luminosity. Therefore an event is selected if the photon meets the isolation criteria and if it is within $\eta = \pm 2.5$. The isolation cut clearly makes it possible to observe the signal, especially at high p_T , however a cut at $p_T(\gamma) = 100$ GeV further reduces the background. This would not harm the sensitivity to anomalous couplings greatly as the anomalies only manifest themselves at high p_T .

Radiative W One method of reducing the background of radiative W decays is to make a cut on the invariant mass of the $\gamma l\nu$ system. For the $W\gamma$ signal, $M(\gamma l\nu)$ is always larger than M_W if finite W width effects are ignored.

However, the $M(\gamma l\nu)$ cannot be determined unambiguously as the four-momentum of the neutrino is unknown: even if the transverse momentum is correctly determined from the missing momentum in the event, there is no measurement of the missing longitudinal momentum. Therefore the cluster transverse mass, or minimum invariant mass, may be used instead [159]. The transverse mass is independent of the longitudinal momenta of the parent particle and its decay products.

For $W \rightarrow \gamma l\nu$ the cluster transverse mass sharply peaks at M_W [160] and drops rapidly above the W mass. Thus $\gamma l\nu$ events originating from $W\gamma$ production and radiative W decays can be distinguished if $M_T(\gamma l\nu)$ is cut slightly above M_W [161]. Hence a cut at $M_T(\gamma l\nu) > 90$ GeV should take into account the finite width of the W whilst not significantly affecting the signal.

The $W\gamma$ signal produces the lepton and photon almost back-to-back. Ensuring that they are well separated will further reduce the radiative W background. This can be done using the quantity $\Delta R = \sqrt{(\Delta\phi^2 + \Delta\eta^2)}$. Leading order analysis of the signal and radiative background enabled a study of the optimum value of ΔR to use for separation. Typically a cut at $\Delta R > 0.5$ is used to ensure separation, but increasing the separation to $\Delta R > 0.7$ makes little difference to the signal whilst greatly reducing the background.

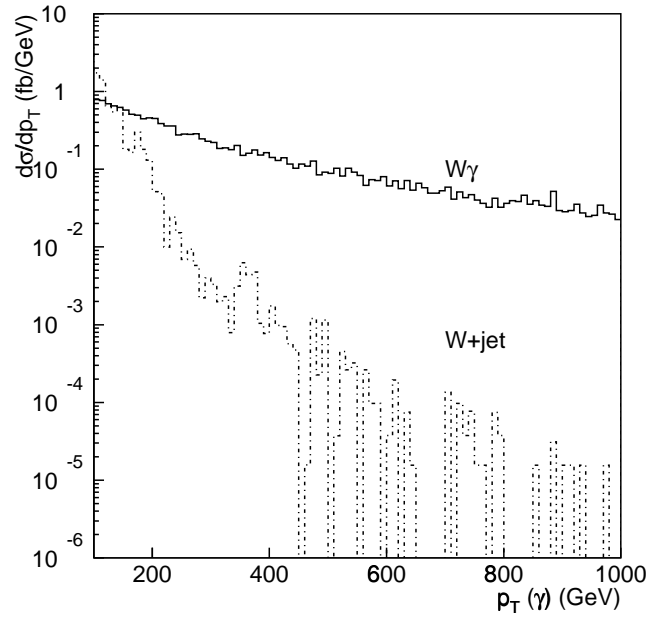


Fig. 41: $p_T(\gamma)$ distribution for the $W\gamma$ signal and the W +jet background where the jet is misidentified as a photon.

In order to suppress the radiative W background events, cuts of $\Delta R(\gamma, l) > 0.7$ and $M_T(\gamma l\nu) > 90$ GeV are used.

5.82 Quark-Gluon fusion background

Quark-gluon fusion is important at the LHC because the rate is extremely high. There are lots of available gluons in the proton at relatively high x , and because the $WW\gamma$ reaction is suppressed in some regions of phase space.

$b\bar{b}\gamma$ At the LHC 10^{12} $b\bar{b}$ events [162] are expected for a years running at high luminosity. Although the $b\bar{b}\gamma$ events are not kinematically similar to the signal, the expected number of events is so large that the background will be a problem unless it is reduced by cuts.

The $b\bar{b}\gamma$ background was generated using the processes: $q\bar{q} \rightarrow g\gamma$, and $q\bar{q} \rightarrow Z\gamma$. Events were generated from $\hat{p}_T = 500$ GeV with a cross section of 1.055 pb. This parton-level requirement was for computational efficiency as only the very highest p_T events contribute to the background. A cut on missing p_T can be made at 50 GeV in order to reduce the $b\bar{b}\gamma$ background.

$t\bar{t}\gamma$ Since the $M_t > M_W + M_b$, $t\bar{t}$ events represent an irreducible background to $W\gamma$ pair production. $t\bar{t}\gamma$ production is a copious source of high p_T photons in association with hard leptons and without cuts has a cross section, $\sigma \sim 300$ pb, of at least 3 orders of magnitude more than the $W\gamma$ signal [163]. The subsequent decay of top quarks into a W boson and a b quark and also the W decay into a $f\bar{f}$ pair provide the same event signature as the $W\gamma$ signal. Therefore, due to the very large top quark production cross section at LHC energies, the process $pp \rightarrow t\bar{t}\gamma \rightarrow W\gamma + X$ represents a potentially significant background.

Events were generated by the process $q\bar{q} \rightarrow g\gamma$ and looking for $t\bar{t}$ production. This method is very inefficient, 4 million events were generated and 489 $t\bar{t}\gamma$ events were produced, with 10 events passing

all of the cuts. The $t\bar{t}\gamma$ events were generated from $\hat{p}_T = 500$ GeV (for the same reasons as $b\bar{b}$), with a cross section of 1.049 pb. The large cross section means that although only a few events pass the cuts, this background is a potential problem.

Studies for the SSC [164] showed that the background can be reduced to a manageable level by requiring the photon to be isolated from the hadrons in the event, and by imposing a jet veto (*i.e.* by considering the exclusive reaction $pp \rightarrow W\gamma + 0$ jets).

Since the top quark decays predominantly into a Wb final state, $t\bar{t}\gamma$ events are characterised by a large hadronic activity which frequently results in one or several high- p_T jets. If the second W boson decays hadronically, up to four jets are possible. This observation suggests that the $t\bar{t}\gamma$ background may be suppressed by vetoing high- p_T jets. Such a “zero jets” requirement has been demonstrated to be very useful in reducing the size of the NLO QCD corrections in $pp \rightarrow W\gamma + X$ at SSC energies [32]. If the second W in the $t\bar{t}\gamma$ events decays hadronically, the number of jets in $pp \rightarrow t\bar{t}\gamma \rightarrow W\gamma + X$ is generally larger than for leptonic W decays, and the jet veto is more efficient.

Unfortunately the jet veto also drastically reduces the number of signal events. Only 10% of the signal survives the jet veto cut alone and only 4% survive all the cuts and the jet veto. This suggests that an alternative method for reducing this background needs to be found for the LHC.

ATLAS [154] studied the possibility of exploiting the number of jets in the $t\bar{t}\gamma$ events by imposing a cut on the second jet in the event. The $W\gamma$ signal will not have a 2nd jet, or if it does, it is a misidentified jet and will be of very low p_T . The $t\bar{t}\gamma$ events will have up to four high p_T jets in each event. By cutting all events where the p_T of the second jet is greater than 25 GeV, the majority of the $t\bar{t}\gamma$ events will be eliminated without greatly affecting the signal.

5.83 $Z\gamma$ background

There is a small background to $e\nu\gamma$ that comes from $Z(ee)\gamma$ events in which one of the electrons gives rise to significant missing energy (generally by entering a gap in the detector). As CMS is hermetic and the crystals of the ECAL are off-pointing with respect to the interaction point, this background is very small. ATLAS [154] calculate this background to be ~ 25 times smaller than the signal before any cuts are imposed. Thus the $Z\gamma$ background is assumed to be negligible.

5.84 $W(\tau\nu)\gamma$ background

The final background to $pp \rightarrow W(e\nu, \mu\nu)\gamma$ is $pp \rightarrow W(\tau\nu)\gamma$ where the τ lepton decays into an electron or muon. The background is very small because the decay of the tau lepton results in electrons or muons with significantly reduced p_T and the kinematical threshold for an electron is 25 GeV. Previous studies at Fermilab have shown this background to be negligible [165].

5.85 Summary of backgrounds

Table 23 shows a list of all the cuts proposed to reduce the backgrounds to the $W\gamma$ signal. Having chosen each cut to reduce an individual background, it is important to understand how each cut effects both the signal and the other backgrounds.

Table 24 shows the efficiency of the individual cuts on the signal and the backgrounds. The W +jet and radiative W backgrounds are treated together. See Figure 42.

5.86 Conclusion

The backgrounds to the $W\gamma$ signal have been studied and cuts have been made in order to reduce the backgrounds to at least an order of magnitude less than the signal for $p_T(\gamma) > 200$ GeV. The W +jet

Table 23: Proposed cuts to reduce the backgrounds to the $W\gamma$ signal.

Quantity	$ \eta(\gamma, l, jet) $	$p_T(\gamma)$ (GeV)	$p_T(l)$ (GeV)	$M_T(\gamma, l, \nu)$ (GeV)	$\Delta R(\gamma, l)$	$p_T(\nu)$ (GeV)	2nd jet (GeV)
Cut value	< 2.5	> 100	> 25	> 90	> 0.7	> 50	< 25

Table 24: Efficiency of individual cuts on the signal and backgrounds, errors are statistical.

Cut	Signal (%)	Background (%)		
		$W+\text{jet}/\text{Rad.}W$	$t\bar{t}\gamma$	$b\bar{b}\gamma$
$p_T(\gamma)$	67 ± 0.49	0.06 ± 0.008	72 ± 5.33	84 ± 0.22
$p_T(l)$	84 ± 0.52	62 ± 0.25	5 ± 1.02	0.2 ± 0.001
$M_T(\gamma, l, \nu)$	85 ± 0.52	19 ± 0.14	87 ± 4.2	0.3 ± 0.0115
$\Delta R(\gamma, l)$	95 ± 0.55	94 ± 0.3	95 ± 4.4	94 ± 0.23
$p_T(\nu)$	86 ± 0.53	60 ± 0.25	43 ± 2.9	28 ± 0.124
2nd jet	89 ± 0.54	42 ± 0.2	0 ± 0.2	34 ± 0.14
All Cuts	55 ± 0.42	0.033 ± 0.018	0 ± 0.2	0.006 ± 0.0019

and radiative W backgrounds have been well studied and understood and the cuts made reduce these significantly. The quark-gluon fusion backgrounds are not so well understood in this work since a less than optimal generator for $t\bar{t}\gamma$ was used. However, the cuts studied for this channel work well for the low statistic samples presented here. Further study of this background would be interesting.

Backgrounds to WZ production have been studied briefly and are similar, within statistical errors, to those in the $W\gamma$ channel presented here.

6. VECTOR-BOSON FUSION AND SCATTERING ¹⁴

6.1 Searching for $VV \rightarrow H \rightarrow \tau\tau$

6.11 Introduction

The search for the Higgs boson and, hence, for the origin of electroweak symmetry breaking and fermion mass generation, remains one of the premier tasks of present and future high energy physics experiments. Fits to precision electroweak (EW) data have for some time suggested a relatively small Higgs boson mass, of order 100 GeV [166, 167], hence we have studied an intermediate-mass Higgs, with mass in the 110 – 150 GeV range, beyond the reach of LEP at CERN and perhaps of the Fermilab Tevatron. Observation of the $H \rightarrow \tau\tau$ decay channel in weak boson fusion events at the Large Hadron Collider (LHC) is quite promising, both in the Standard Model (SM) and Minimal Supersymmetric Standard Model (MSSM). This channel has lower QCD backgrounds compared to the dominant $H \rightarrow b\bar{b}$ mode, thus offering the best prospects for a direct measurement of a $Hf\bar{f}$ coupling.

At the LHC, despite the fact that the cross section for Higgs production by weak-boson fusion is significantly lower than that from gluon fusion (by almost one order of magnitude), it has the advantage

¹⁴Section coordinators: Z. Kunszt, R. Mazini, D. Rainwater

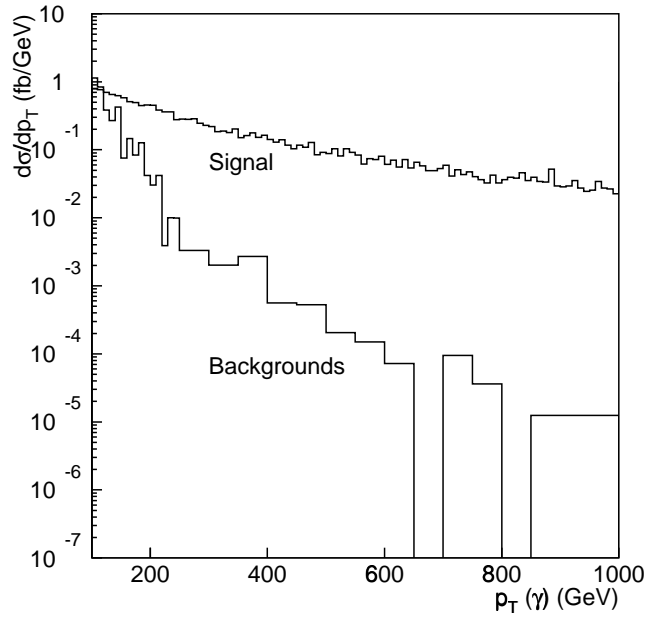


Fig. 42: $p_T(\gamma)$ distribution for the $W\gamma$ signal and the backgrounds.

of additional information in the event other than the decay products' transverse momentum and their invariant mass resonance: namely, the observable quark jets. Thus one can exploit techniques like forward jet tagging [168, 169, 170, 171, 172, 173, 174, 175, 176] to reduce the backgrounds. Another advantage is the different colour structure of the signal vs the background. Additional soft jet activity (minijets) in the central region, which occurs much more frequently for the colour-exchange processes of the QCD backgrounds [177, 178], are suppressed via a central jet veto.

We have performed first analyses of intermediate-mass SM $H \rightarrow \tau\tau$ and of the main physics and reducible backgrounds at the LHC, considering separately the decay modes $\tau\tau \rightarrow h^\pm l^\mp \not{p}_T, e^\pm \mu^\mp \not{p}_T$. These modes demonstrate the feasibility of Higgs boson detection in this channel with modest luminosity [179, 180]. We demonstrated that forward jet tagging, τ identification and reconstruction criteria alone yield a signal-to-background (S/B) ratio of approximately 1/1 or better. Additional large background suppression factors can be obtained with the minijet veto, achieving final S/B ratios as good as 6/1, depending on the Higgs mass.

In the MSSM, strategies to identify the structure of the Higgs sector are much less clear. For large $\tan\beta$, the light neutral Higgs bosons may couple much more strongly to the $T_3 = -1/2$ members of the weak isospin doublets than its SM analogue. As a result, the total width can increase significantly compared to a SM Higgs of the same mass. This comes at the expense of the branching ratio $BR(h \rightarrow \gamma\gamma)$, the cleanest Higgs discovery mode, possibly rendering it unobservable over much of MSSM parameter space and forcing consideration of other observational channels. Instead, since $BR(h \rightarrow \tau\tau)$ is enhanced slightly, we have examined the τ mode as an alternative [180, 181].

6.12 Simulations of signal and backgrounds

The analyses used full tree-level matrix elements for the weak boson fusion Higgs signal and the various backgrounds. Extra minijet activity was simulated by adding the emission of one extra parton to the basic signal and background processes, with the soft singularities regulated via a truncated shower approximation (TSA) [182, 183].

We simulated pp collisions at the LHC, $\sqrt{s} = 14$ TeV. For all QCD effects, the running of the strong-coupling constant was evaluated at one-loop order, with $\alpha_s(M_Z) = 0.118$. We employed CTEQ4L parton distribution functions [67] throughout. The factorisation scale was chosen as $\mu_f = \min(p_T)$ of the defined jets, and the renormalisation scale μ_r was fixed by $(\alpha_s)^n = \prod_{i=1}^n \alpha_s(p_{T_i})$. Detector effects were considered by including Gaussian smearing for partons and leptons according to ATLAS expectations [153, 125].

At lowest order, the signal is described by two single-Feynman-diagram processes, $qq \rightarrow qq(WW, ZZ) \rightarrow qqH$, *i.e.* WW and ZZ fusion where the weak bosons are emitted from the incoming quarks [184]. From a previous study of $H \rightarrow \gamma\gamma$ decays in weak boson fusion [185], we know several features of the signal which we could exploit directly here: the centrally produced Higgs boson tends to yield central decay products (in this case $\tau^+\tau^-$), and the two quarks enter the detector at large rapidity compared to the τ 's and with transverse momenta in the 20-80 GeV range, thus leading to two observable forward tagging jets.

We considered separately the cases of one τ decaying leptonically (e, μ) and the other decaying hadronically (with a combined branching fraction of 45%), and both decaying leptonically but with different flavour ($e\mu$ or μe , with a combined branching fraction of 6.3%). Our analyses critically employed transverse momentum cuts on the charged τ -decay products and, hence, some care was taken to ensure realistic momentum distributions. Because of its small mass, we simulated τ decays in the collinear and narrow-width approximations and with decay distributions to π, ρ, a_1 [186], adding the various hadronic decay modes according to their branching ratios. We took into account the anti-correlation of the τ^\pm polarisations in the decay of the Higgs.

Lepton-hadron mode Positive identification of the hadronic $\tau^\pm \rightarrow h^\pm X$ decay requires severe cuts on the charged hadron isolation. We based our simulations on the possible strategies analysed by Cavalli *et al.* [187]. Considering hadronic jets of $E_T > 40$ GeV in the ATLAS detector, they found non-tau rejection factors of 400 or more while true hadronic τ decays are retained with an identification efficiency of 26%.

Given the H decay signature, the main physics background to the $\tau^+\tau^-jj$ events of the signal arises from real emission QCD corrections to the Drell-Yan process $q\bar{q} \rightarrow (Z, \gamma) \rightarrow \tau^+\tau^-$, dominated by t -channel gluon exchange. All interference effects between virtual photon and Z -exchange were included, as was the correlation of τ^\pm polarisations. The Z component dominates, so we call these processes collectively the ‘‘QCD Zjj ’’ background.

An additional physics ‘‘EW Zjj ’’ background arises from Z and γ bremsstrahlung in (anti)quark scattering via t -channel electroweak boson exchange, with subsequent decay $Z, \gamma \rightarrow \tau^+\tau^-$. Naively, this EW background may be thought of as suppressed compared to the analogous QCD process. However, the EW background includes electroweak boson fusion, $VV \rightarrow \tau^+\tau^-$, which has a momentum and colour structure identical to the signal and thus cannot easily be suppressed via cuts.

Finally, we considered reducible backgrounds, *i.e.* any event that can mimic the Hjj signature of a hard, isolated lepton and missing p_T , a hard, narrow τ -like jet, and two forward tagging jets. Thus we examined $W + jets$, where the W decays leptonically (e, μ) and one jet fakes a hadronic τ , and $b\bar{b} + jets$, where one b decays leptonically and either a light quark or b jet fakes a hadronic τ . We neglected other sources like $t\bar{t}$ events which had previously been shown to give substantially smaller backgrounds [187].

Fluctuations of a parton into a narrow τ -like jet are considered with probability 0.25% for gluons and light-quark jets and 0.15% for b jets (which may be considered an upper bound) [187].

In the case of $b\bar{b} + jj$, we simulated the semileptonic decay $b \rightarrow l\nu c$ by multiplying the $b\bar{b}jj$ cross section by a branching factor of 0.395 and implementing a three-body phase space distribution for the decay momenta to estimate the effects of lepton isolation cuts. We normalised our resulting cross section to reproduce the same factor 100 reduction found in [187].

Dual lepton mode For the dilepton mode, we consider decay only to e, μ pairs to completely eliminate the backgrounds from real Z production decaying directly to ee or $\mu\mu$. Tau decays were performed in the same manner as in the lepton-hadron channel. We again considered QCD and EW Zjj ; $Z \rightarrow \tau\tau$ production as the physics backgrounds.

We calculated the primary contributions from reducible backgrounds by considering all significant sources of two W 's, which decay leptonically to form the signature e, μ , and two forward jets. This consists of $t\bar{t} + jets$, as well as both QCD and EW $WWjj$ production. As with the EW Zjj case, EW $WWjj$ processes contain an electroweak boson fusion component kinematically similar to the signal, and so cannot be ignored.

We also considered $b\bar{b}jj$ production, with each b decaying semileptonically simulated by implementing the $V - A$ decay distributions of the b -quarks in the collinear limit, and multiplying the resultant cross section by a branching fraction 0.0218 (for the e, μ or μ, e final states).

Finally, we considered the overlapping contribution from the signal itself in the decay mode $H \rightarrow WW \rightarrow e\mu p_T$, which can be significant above $M_H \geq \sim 130$ GeV.

6.13 Standard Model analysis

The basic acceptance requirements must ensure that the two jets and two τ 's are observed inside the detector (within the hadronic and electromagnetic calorimeters, respectively), and are well-separated from each other:

$$\begin{aligned} p_{T_j} &\geq 20 \text{ GeV}, & |\eta_j| &\leq 5.0, & \Delta R_{jj} &\geq 0.7, \\ |\eta_\tau| &\leq 2.5, & \Delta R_{j\tau} &\geq 0.7. \end{aligned} \quad (65)$$

Tau-tau separation and tau decay product p_T requirements are slightly different for the two signatures and are discussed separately below.

The Hjj signal is characterised by two forward jets with large invariant mass, and central τ decay products. The QCD backgrounds have a large gluon-initiated component and thus prefer lower invariant tagging jet masses. Also, their τ and W decay products tend to be less central. Thus, to reduce the backgrounds to the level of the signal, we required tagging jets with a combination of large invariant mass, far forward rapidity, and high p_T , as well as τ decay products central with respect to the tagging jets [185]:

$$\begin{aligned} \eta_{j,min} + 0.7 &< \eta_{\tau_{1,2}} < \eta_{j,max} - 0.7, & \eta_{j_1} \cdot \eta_{j_2} &< 0, \\ \Delta\eta_{tags} = |\eta_{j_1} - \eta_{j_2}| &\geq 4.4, & m_{jj} &> m_{jjmin}, \end{aligned} \quad (66)$$

where m_{jjmin} is chosen slightly differently for the two scenarios, as discussed below.

Lepton-hadron mode Here we required two additional cuts to form the tagging jet signature:

$$p_{T_j} > 40, 20 \text{ GeV}, \quad \Delta R_{\tau\tau} \geq 0.7. \quad (67)$$

That is, the p_T requirement on the tagging jets is staggered, and as one tau decay is hadronic, it must have a large separation from the leptonic tau.

Triggering the event via the isolated τ -decay lepton and identifying the hadronic τ decay as discussed in [187] requires sizable transverse momenta for the observable τ decay products: $p_{T_{\tau,lep}} > 20$ GeV and $p_{T_{\tau,had}} > 40$ GeV. It is possible to reconstruct the τ -pair invariant mass from the observable τ decay products and the missing transverse momentum vector of the event [188]. The τ mass was

neglected and collinear decays assumed, a condition easily satisfied because of the high τ transverse momenta required. The τ momenta were reconstructed from the charged decay products' p_T and missing p_T vectors. We imposed a cut on the angle between the τ decay products to satisfy the collinear decay assumption, $\cos\theta_{lh} > -0.9$, and demanded a physicality condition for the reconstructed τ momenta (unphysical solutions arise from smearing effects); that is, the fractional momentum x_τ a charged decay observable takes from its parent τ cannot be negative. Additionally, the x_{τ_l} distribution of the leptonically decaying τ -candidate is softer for real τ 's than for the reducible backgrounds, because the charged lepton shares the parent τ energy with two neutrinos. Cuts $x_{\tau_l} < 0.75$ and $x_{\tau_h} < 1$ proved very effective in suppressing the reducible backgrounds.

Our Monte Carlo predicted a τ -pair mass resolution of 10 GeV or better, so we chose ± 10 GeV mass bins for analysing the cross sections. To further reduce the QCD backgrounds, which prefer low invariant masses for the tagging jets, we required $m_{jj} > 1$ TeV. Additionally, the $Wj + jj$ background exhibits a Jacobian peak in its m_T distribution [187]; hence a cut $m_T(l, \not{p}_T) < 30$ GeV largely eliminates this background.

Finally, to compensate for overall rate loss based on ATLAS and CMS expected detector ID efficiencies, we apply a factor 0.86 to the cross section for each tagging jet, and a factor 0.95 for the charged lepton.

Using all these cuts together, although not in a highly optimised combination, we expect already a signal to background ratio of 2/1 with a signal cross section of 0.4 fb for $M_H = 120$ GeV.

A probability for vetoing additional central hadronic radiation was obtained by measuring the fraction of events that have additional radiation in the central region, between the tagging jets, with p_T above 20 GeV, using the matrix elements for additional parton emission. This minijet veto reduces the signal by about 15%, but eliminates typically 70% of the QCD backgrounds; the EW Zjj background is reduced by about 20%, indicating the presence of both boson bremsstrahlung and weak boson fusion effects. Because the veto probability for QCD backgrounds is found to be process independent, we applied the same value to the $bb + jj$ background.

Table 25 summarises the signal and various background cross sections at progressive levels of the cuts, ID efficiencies and minijet veto as described above, for the case $M_H = 120$ GeV. Table 26 gives the expected numbers of events for 60 fb^{-1} integrated luminosity (low luminosity running) at the LHC.

Table 25: Signal and background cross sections $\sigma \cdot BR$ (fb) for $M_H = 120$ GeV Hjj events in the lepton-hadron channel. Results are given for successive cuts, as discussed in the text. The last column gives the ratio of the signal to the background cross sections listed in the previous columns.

Cuts	Hjj	QCD Zjj	EW Zjj	$Wj + jj$	$b\bar{b} + jj$	S/B
forward tagging	68.4	1680	91			
τ identification	1.99	20.0	1.45	26.4	7.6	1/28
$110 < m_{\tau\tau} < 130 \text{ GeV}$	1.31	0.95	0.07	1.77	0.59	1/2.6
$m_{jj} > 1 \text{ TeV}, m_T(l, \not{p}_T) < 30 \text{ GeV}$	0.69	0.16	0.04	0.11	0.15	1.5/1
$x_{\tau_l} < 0.75, x_{\tau_h} < 1.0$	0.54	0.15	0.03	0.03	0.05	2.1/1
ID efficiency ($\epsilon = 0.70$)	0.38	0.10	0.03	0.03	0.05	2.1/1
$P_{surv,20}$	$\times 0.87$	$\times 0.28$	$\times 0.80$	$\times 0.28$	$\times 0.28$	-
minijet veto	0.33	0.03	0.02	0.004	0.011	5.2/1

Table 26: Number of expected events in the lepton-hadron channel for the signal and backgrounds, for 60 fb^{-1} at low luminosity running; cuts, ID efficiency ($\epsilon = 0.70$) and minijet veto as in the last line of Table 25; for a range of Higgs boson masses. Mass bins of $\pm 10 \text{ GeV}$ around a given central value are assumed. As a measure of the Poisson probability of the background to fluctuate up to the signal level, the last row gives σ_{Gauss} , the number of Gaussian equivalent standard deviations.

M_H (GeV)	110	120	130	140	150
$\epsilon \cdot \sigma_{sig}$ (fb)	0.38	0.33	0.25	0.16	0.08
N_S	22.9	19.6	15.2	9.5	4.6
N_B	10.2	3.8	2.4	1.8	1.5
S/B	2.2	5.2	6.4	5.2	3.1
σ_{Gauss}	5.6	6.6	6.3	4.7	2.6

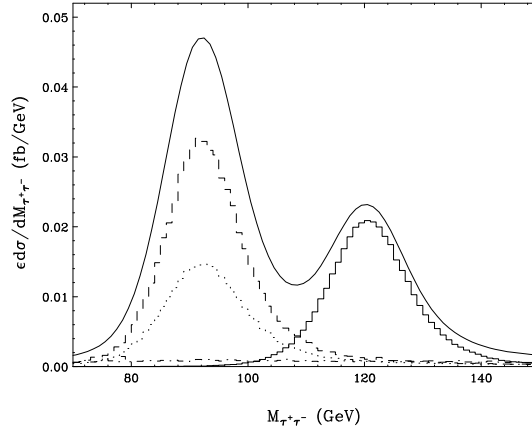


Fig. 43: Reconstructed τ pair invariant mass distribution for the signal (lepton-hadron channel) and backgrounds after all cuts and multiplication by the expected survival probabilities. The solid line represents the sum of the signal and all backgrounds. Individual components are shown as histograms: the Hjj signal (solid), the irreducible QCD Zjj background (dashed), the irreducible EW Zjj background (dotted), and the combined $Wj + jj$ and $b\bar{b}jj$ reducible backgrounds (dash-dotted).

It is possible to isolate a virtually background-free $qq \rightarrow qqH \rightarrow jj\tau\tau$ signal at the LHC, leading to a 5σ observation of a SM Higgs boson with a mere 60 fb^{-1} of data. The expected purity of the signal is demonstrated in Figure 43 showing the reconstructed $\tau\tau$ invariant mass for a SM Higgs of 120 GeV after all cuts, particle ID efficiency factors and a minijet veto have been applied. While the reducible $Wj + jj$ and $b\bar{b} + jj$ backgrounds are the most complicated and do require further study, they appear to be easily manageable.

Dual lepton mode For this signature, we simulated tau decays as before, but with both decaying to final-state leptons. As this would form a different final state in experiment, to form the basic tagging jet signature we require the cuts of Equations 65 and 66 as before, but additionally a minimum separation of the charged leptons somewhat less than for the lepton-hadron scenario, $\Delta R_{\tau\tau} \geq 0.4$. To be able to trigger on the leptons, we require them to have minimum transverse momentum $p_{T_l} > 10 \text{ GeV}$. In the LHC experiments, this may be slightly higher for electrons and slightly lower for muons, but we do not make the distinction here.

Both the $t\bar{t} + jets$ and $b\bar{b}jj$ backgrounds are about three orders of magnitude larger than the signal,

but the contribution from $b\bar{b}jj$ may be reduced by a cut on missing transverse energy, $\cancel{p}_T > 30$ GeV, and that from $t\bar{t} + jets$ may be severely restricted by vetoing additional jets in the central region between the tagging jets, which even before considering additional gluon radiation (minijets) may come from the decays of central final-state b -quarks. We veto all events with a central b with $p_T > 20$ GeV. This provides approximately a factor 17 in reduction of the top quark background, which may be substantially improved to even lower p_T threshold via a b -tag, which we cannot simulate.

As the dual lepton final state has a lower overall branching ratio than the lepton-hadron case, we retained more overall rate by making a looser cut on the tagging jet invariant mass, $m_{jj} > 800$ GeV. This cut was still necessary to reduce the QCD backgrounds.

Our Monte Carlo again predicted an excellent τ -pair mass resolution, so we retain the mass binning of ± 10 GeV. We also rejected non-tau's as in the lepton-hadron case, although our exact cut was somewhat differently defined:

$$x_{\tau_1}, x_{\tau_2} > 0, \quad x_{\tau_1}^2 + x_{\tau_2}^2 < 1.$$

Finally, we found that a cut on the maximal separation of the two charged leptons is very useful in reducing the heavy quark backgrounds: $\Delta R_{e\mu} < 2.6$.

Efficiency factors for detection are the same as in the previous case, although with two final-state leptons an extra factor 0.95 was taken into account. A minijet veto was applied as before, although other analyses we have performed suggest the survival probabilities change slightly due to the lower hardness of the event, which is strongly correlated with m_{jj} (see Table 27).

Table 27 outlines the cross sections of signal and background for progressive levels of cuts as described above, for the case $M_H = 120$ GeV. Table 28 gives the expected numbers of events for 60 fb^{-1} integrated luminosity (low luminosity running) at the LHC.

Table 27: Signal rates $\sigma \cdot BR(H \rightarrow \tau\tau \rightarrow e^\pm \mu^\mp \cancel{p}_T)$ for a SM Higgs of $M_H = 120$ GeV and progressive levels of cuts as discussed in the text. All rates are given in fb. Note: the fifth line, non-tau rejection, also includes a cut $90 \text{ GeV} < m_{\tau\tau} < 160 \text{ GeV}$.

Cuts	$H \rightarrow \tau\tau$	$H \rightarrow WW$	QCD	EW	$t\bar{t} + jets$	$b\bar{b}jj$	QCD	EW	S/B
	signal	bkgd	$\tau\tau jj$	$\tau\tau jj$			$WW jj$	$WW jj$	
forward tags	2.2		57	2.3	1230	1050	4.9	3.3	1/1100
b veto					72				1/550
$\cancel{p}_T > 30$ GeV	1.73		29	1.57	62	29	4.1	2.9	1/74
$M_{jj} > 800$ GeV	1.34		10.3	1.35	16.3	10.4	1.60	2.6	1/32
non- τ reject.	1.15		5.2	0.63	0.31	0.42	0.032	0.042	1/5.8
± 10 GeV mass bins	0.87		0.58	0.10	0.09	0.10	0.009	0.012	1/1
$\Delta R_{e\mu} < 2.6$	0.84	0.023	0.52	0.086	0.087	0.028	0.009	0.011	1.1/1
ID effic. ($\times 0.67$)	0.56	0.015	0.34	0.058	0.058	0.019	0.006	0.008	1.1/1
$P_{surv,20}$	$\times 0.89$	$\times 0.89$	$\times 0.29$	$\times 0.75$	$\times 0.29$	$\times 0.29$	$\times 0.29$	$\times 0.75$	-
minijet veto	0.50	0.014	0.100	0.043	0.017	0.006	0.002	0.006	2.7/1

Although the dual lepton channel does not appear to be able to achieve quite as high an S/B ratio as the lepton-hadron channel, it is still better than 1/1 over much of the mass range of interest, which is also clearly evident in the tau pair invariant mass plot of Figure 44. Furthermore, the independent statistical significance of this channel is as good as that found for the lepton-hadron case.

Table 28: Number of expected events for a SM Hjj signal in the $H \rightarrow \tau\tau \rightarrow e^\pm \mu^\mp \not{p}_T$ channel, for a range of Higgs boson masses. Results are given for 60 fb^{-1} of data at low luminosity running, and application of all efficiency factors and cuts, including a minijet veto. As a measure of the Poisson probability of the background to fluctuate up to the signal level, the last line gives σ_{Gauss} , the number of Gaussian equivalent standard deviations.

M_H	100	105	110	115	120	125	130	135	140	145	150
$\epsilon \cdot \sigma_{sig}$ (fb)	0.62	0.61	0.58	0.55	0.50	0.44	0.37	0.30	0.23	0.16	0.11
N_S	37.4	36.5	35.0	32.8	30.0	26.3	22.3	18.0	13.7	9.9	6.5
N_B	67.7	45.4	27.4	16.8	11.2	8.4	7.1	6.4	6.1	5.9	5.7
S/B	0.6	0.8	1.3	2.0	2.7	3.2	3.1	2.8	2.2	1.7	1.1
σ_{Gauss}	4.1	4.8	5.6	6.4	6.8	6.7	6.1	5.3	4.3	3.2	2.2

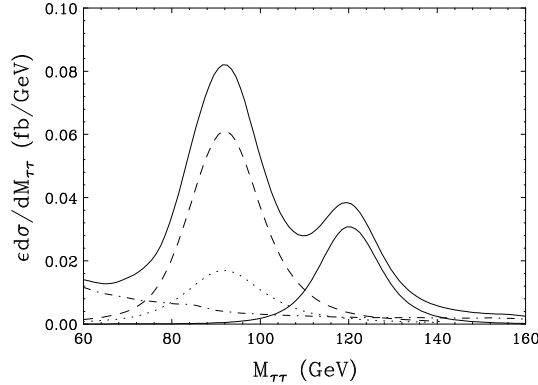


Fig. 44: Reconstructed τ pair invariant mass distribution for a SM $H \rightarrow \tau\tau \rightarrow e^\pm \mu^\mp \not{p}_T$ ($M_H = 120 \text{ GeV}$) signal and backgrounds after all cuts, particle ID efficiencies and minijet veto. The double-peaked solid line represents the sum of the signal and all backgrounds. Individual components are: the Hjj signal (solid), the irreducible QCD Zjj background (dashed), the irreducible EW Zjj background (dotted), and the combined reducible backgrounds from QCD + EW + Higgs $WWjj$ events and $t\bar{t} + jets$ and $b\bar{b}jj$ production (dash-dotted).

6.14 MSSM analysis

The production of CP even Higgs bosons in weak boson fusion is governed by the hWW, HWW couplings, which are suppressed by factors $\sin(\beta - \alpha), \cos(\beta - \alpha)$, respectively [189], compared to the SM case. Their branching ratios are modified with slightly more complicated factors. One can simply multiply SM cross section results from our analysis by these factors to determine the observability of $H \rightarrow \tau\tau$ in MSSM parameter space. We used a renormalisation group improved next-to-leading order calculation, which allows a light Higgs mass up to $\sim 125 \text{ GeV}$, and examined two trilinear term mixing cases, no mixing and maximal mixing [180, 181].

Varying the pseudoscalar Higgs boson mass M_A , one finds that M_h, M_H each approach a plateau for the case $M_A \rightarrow \infty, 0$, respectively. Below $M_A \sim 120 \text{ GeV}$, the light Higgs mass will fall off linearly with M_A , while the heavy Higgs will approach $M_H \sim 125 \text{ GeV}$, whereas above $M_A \sim 120 \text{ GeV}$, the light Higgs will approach $M_h \sim 125 \text{ GeV}$ and the heavy Higgs mass will rise linearly with M_A . The transition region behaviour is very abrupt for large $\tan \beta$, such that the plateau state will go to $\sim 125 \text{ GeV}$ almost immediately, while for small $\tan \beta$ the transition is much softer and the plateau state reaches the limiting value via a more gradual asymptotic approach.

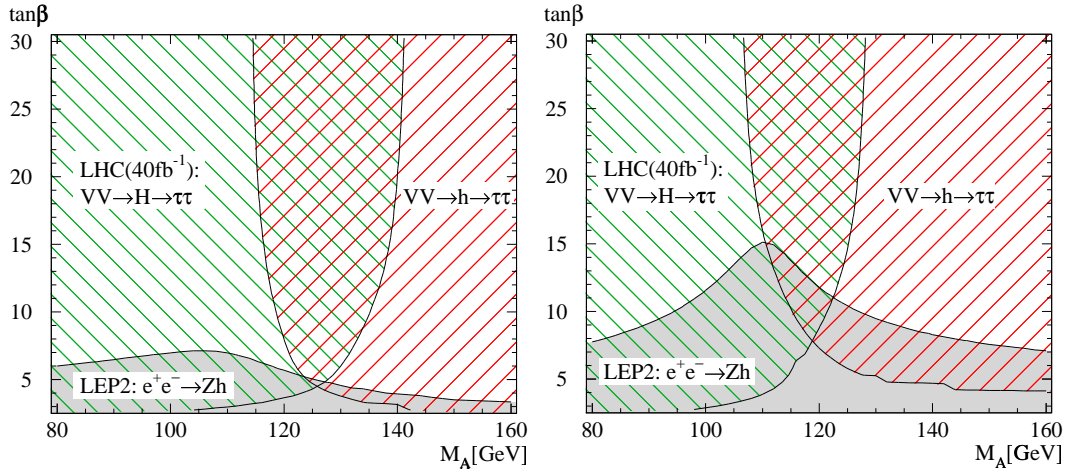


Fig. 45: 5σ discovery contours for $h \rightarrow \tau\tau$ and $H \rightarrow \tau\tau$ in weak boson fusion at the LHC, with 40 fb^{-1} . Also shown are the projected LEP2 exclusion limits. Results are shown for maximal mixing (left) and no mixing (right). From [180, 181].

With reasonable integrated luminosity and combination of the lepton-hadron and dual-lepton channels, 40 fb^{-1} in the worst case, it will be possible to observe at the 5σ level either h or H decays to τ pairs when they are in their respective plateau region, with the possibility of some overlap in a small region of M_A , as shown in Figure 45. Very low values of $\tan\beta$ would be unobservable, but already excluded by LEP2; there should be considerable overlap between this mode at the LHC and the LEP2 excluded region. Furthermore, a parton shower Monte Carlo with full detector simulation should be able to optimise the analysis so that much less data is required to observe or exclude the MSSM Higgs.

6.15 Conclusions

The production of a neutral, CP even Higgs via weak boson fusion and decay $H \rightarrow \tau\tau$ at the LHC has been studied for the Standard Model and MSSM, utilising parton level Monte Carlo analyses. Each of the decay channels $\tau\tau \rightarrow h^\pm l^\mp \cancel{p}_T, e^\pm \mu^\mp \cancel{p}_T$ independently allows a 5σ observation of a Standard Model Higgs with an integrated luminosity of about 60 fb^{-1} or less, and provides a direct measurement of the $H\tau\tau$ coupling. For the MSSM case, a highly significant signal for at least one of the Higgs bosons with reasonable luminosity is possible over the entire physical parameter space which will be left unexplored by LEP2. Only 40 fb^{-1} of data is required after combining the two channels. We conclude that this mode provides a **no-lose strategy** for seeing at least one of the CP even neutral MSSM Higgs bosons.

6.2 Searching for $VV \rightarrow H \rightarrow WW$

In the previous section, vector-boson fusion forming a Higgs which then decays to two τ 's was identified as a valuable process by which to find a Higgs boson in the mass range 110 to 150 GeV. Rainwater and Zeppenfeld have shown that a heavier Higgs in the range 130 to 200 GeV could be found by looking for the process $VV \rightarrow H \rightarrow WW \rightarrow e^\pm \mu^\mp \cancel{p}_T$ [190]. As for the lighter Higgs, the forward jet tagging is a powerful tool for removing background (W pairs, $t\bar{t}$ and $Z \rightarrow \tau\tau$ accompanied by jets). This approach appears more promising than the a search for an inclusive $H \rightarrow WW \rightarrow e^\pm \mu^\mp \cancel{p}_T$ signal, yielding a significant result with $\sim 5 \text{ fb}^{-1}$.

Work has started in the context of the Workshop to investigate this with fast detector simulation, but has not yet been completed.

6.3 The strongly interacting symmetry breaking sector

One possible scenario for the spontaneous breaking of the electroweak (EW) symmetry is a strongly interacting symmetry breaking sector (SBS), which generically is formed by new particles with strong interactions at the TeV scale. This sector should provide a global $SU(2)_L \times SU(2)_R$ spontaneous symmetry breaking down to the custodial $SU(2)_{L+R}$ subgroup, thus triggering the Standard Model spontaneous breaking from the $SU(2)_L \times U(1)_Y$ gauge-symmetry down to $U(1)_{\text{em}}$. This is the minimal symmetry pattern ensuring that $\rho \simeq 1 + O(g^2)$.

By assuming that the new states appear at the TeV scale, we are only left, at low energies, with the three massless Goldstone Bosons (GB) associated to the global symmetry breaking. We will refer to this scenario as the minimal strongly interacting symmetry breaking sector (MSISBS). In this case, the low-energy EW interactions can be well described with the Electroweak Chiral Lagrangian (EChL) [36, 37], which is an $SU(2) \times U(1)$ gauge-invariant effective field theory that couples the GB to the gauge-bosons and fermions, without any further assumptions than those just described. The EChL, inspired in Chiral Perturbation Theory [191], is organised as a derivative (momentum) expansion, with a set of effective operators of increasing dimension. Although the lowest-order Lagrangian is common to all models satisfying the minimal assumptions, at higher orders each effective operator has a coefficient, whose different values will account for different underlying symmetry breaking mechanisms. Within this approach it is possible, not only to calculate at tree level, but to include loops whose divergences will be absorbed in the coefficients of operators of higher dimension, thus yielding finite results order by order in the calculations. The values of these renormalised parameters are expected in the 10^{-3} to 10^{-2} range.

As far as physics at the LHC is concerned, the most characteristic feature of a strong SBS is the enhanced production of longitudinal gauge-boson pairs. We will review the EChL amplitudes for these processes. However, the EChL perturbative predictions can only describe EW physics at low energies, well below the mass of the heavy states. Indeed, any amplitude calculated with the EChL is obtained as a truncated series in powers of the external momenta. Hence, it will always violate unitarity bounds at high enough energies. In addition, it cannot reproduce any pole associated to new resonant states. Consequently, in order to apply this formalism to study strong SBS phenomenology at the LHC, we have several ways to proceed:

1. Perform studies strictly within the EChL, but restricted to subprocess energies below 1.5 TeV and to very small chiral parameters.
2. Enlarge the EChL introducing explicitly the heavy resonances of each particular model, but this adds new unknown parameters, namely the mass and the width of each resonance.
3. Follow a more model-independent approach, by unitarising the EChL amplitudes and generating heavy resonances from the information contained in the chiral coefficients.

In the last approach, it is possible to describe the different resonant scenarios with just two chiral parameters. Finally we present a study of the LHC sensitivity reach within this parameter space, using the signal of the cleanest leptonic decays of ZZ and WZ pairs.

6.31 Effective Chiral Lagrangian description of electroweak interactions

The EChL [36, 37] provides a phenomenological description of EW interactions when the SBS is strongly-interacting. The only degrees of freedom at low energies are the GBs associated to the $SU(2)_L \times SU(2)_R \rightarrow SU(2)_{L+R}$ global symmetry breaking, which are coupled to the EW gauge and fermion fields in an $SU(2)_L \times U(1)_Y$ invariant way. Customarily, the GBs, ω^a with $a = 1, 2, 3$, are gathered in an $SU(2)$ matrix $U = \exp(i\omega^a \tau^a / v)$, where τ^a are the Pauli matrices and $v = 246$ GeV. The C and P invariant effective bosonic operators up to dimension four are (see the appendix for other notations)

$$\mathcal{L}_{\text{EChL}} = \frac{v^2}{4} \text{Tr}(D_\mu U (D^\mu U)^\dagger) + a_0 \frac{g'^2 v^2}{4} [\text{Tr}(TV_\nu)]^2 + a_1 \frac{igg'}{2} \mathcal{B}_{\mu\nu} \text{Tr}(T\mathcal{W}^{\mu\nu})$$

$$\begin{aligned}
& + a_2 \frac{ig'}{2} \mathcal{B}_{\mu\nu} \text{Tr}(T[V^\mu, V^\nu]) + a_3 g \text{Tr}(\mathcal{W}_{\mu\nu}[V^\mu, V^\nu]) + a_4 [\text{Tr}(V_\mu V_\nu)]^2 \\
& + a_5 [\text{Tr}(V_\mu V^\mu)]^2 + a_6 \text{Tr}(V_\mu V_\nu) \text{Tr}(TV^\mu) \text{Tr}(TV^\nu) + a_7 \text{Tr}(V_\mu V^\mu) [\text{Tr}(TV^\nu)]^2 \\
& + a_8 \frac{g^2}{4} [\text{Tr}(T\mathcal{W}_{\mu\nu})]^2 + a_9 \frac{g}{2} \text{Tr}(T\mathcal{W}_{\mu\nu}) \text{Tr}(T[V^\mu, V^\nu]) + a_{10} [\text{Tr}(TV_\mu) \text{Tr}(TV_\nu)]^2 \\
& + \text{e.o.m. terms} + \text{standard YM terms}
\end{aligned} \tag{68}$$

where we have defined $T \equiv U\tau^3 U^\dagger$ and $V_\mu \equiv (D_\mu U)U^\dagger$, as well as

$$\begin{aligned}
D_\mu U & \equiv \partial_\mu U - g\mathcal{W}_\mu U + g'U\mathcal{B}_\mu, & \mathcal{W}_\mu & \equiv \frac{-i}{2} \vec{W}_\mu \cdot \vec{\tau}, & \mathcal{B}_\mu & \equiv \frac{-i}{2} B_\mu \tau^3, \\
\mathcal{W}_{\mu\nu} & \equiv \partial_\mu \mathcal{W}_\nu - \partial_\nu \mathcal{W}_\mu - g[\mathcal{W}_\mu, \mathcal{W}_\nu], & \mathcal{B}_{\mu\nu} & \equiv \partial_\mu \mathcal{B}_\nu - \partial_\nu \mathcal{B}_\mu.
\end{aligned} \tag{69}$$

The ‘‘e.o.m.’’ terms refer to operators that can be removed using the equations of motion and the ‘‘standard YM terms’’ are the usual Yang Mills Lagrangian together with the gauge-fixing and Faddeev-Popov terms.

The first operator in Equation 68, which provides the W and Z masses, has dimension two and has the form of a gauged non-linear sigma model (NL σ M). Note that it is universal, since it only depends on v - that is why its predictions for longitudinal gauge-boson scattering amplitudes are called ‘‘Low Energy Theorems’’. In contrast, the a_i couplings will have different values depending on the underlying theory.

The gauge-boson observables are obtained from $\mathcal{L}_{\text{EChL}}$ as a double expansion in $p^n/(4\pi v)^n$, p being an external momentum, and in the gauge-couplings g and g' . The lowest-order predictions are given by the tree level NL σ M, whereas the next order corrections are obtained with a one-loop calculation using the NL σ M vertices plus the tree level contributions of the other operators. The a_i coefficients not only provide a model independent parametrisation of the unknown dynamics, but also some of them are used to absorb all the one-loop NL σ M divergences. This procedure could be carried out to any desired order, adding higher dimensional operators, thus yielding finite results order by order in the expansion.

In principle, the a_i values for a particular scenario can be obtained by integrating out the heavy degrees of freedom. In fact, they have been determined for the particular cases of the SM with a heavy Higgs [192, 193] and for technicolor theories in the large N_{TC} limit [194]. In both cases, these couplings lie in the range 10^{-2} to 10^{-3} , with either sign. They all have a constant contribution, but those needed in the renormalisation also have a logarithmic term.

6.32 Present bounds on the chiral parameters

Let us now look at the present experimental constraints on the EChL parameters a_i from low energy EW data. The best constraints come from the oblique radiative corrections, giving bounds on the a_0 , a_1 and a_8 parameters that contribute to the gauge-bosons two-point functions up to order q^2 . The EChL calculation of the S , T and U [195] self-energy combinations give [196]

$$\begin{aligned}
S & = 16\pi [-a_1(\mu) + \text{EChL loops}(\mu)], & T & = \frac{8\pi}{c_W^2} [a_0(\mu) + \text{EChL loops}(\mu)], \\
U & = 16\pi [a_8(\mu) + \text{EChL loops}(\mu)]
\end{aligned}$$

Note that the a_i have been renormalised to absorb the one-loop divergences from the NL σ M chiral loops, so that S , T and U are scale independent. Using the a_i values for a heavy Higgs boson [192, 193], the deviations of EW observables from the SM predictions at a reference value of the Higgs mass M_H are

$$\begin{aligned}
\Delta S & \equiv S - S_{\text{SM}}(M_H) = 16\pi \left[-a_1(\mu) + \frac{1}{12} \frac{5/6 - \log M_H^2/\mu^2}{16\pi^2} \right], \\
\Delta T & \equiv T - T_{\text{SM}}(M_H) = \frac{8\pi}{c_W^2} \left[a_0(\mu) - \frac{3}{8} \frac{5/6 - \log M_H^2/\mu^2}{16\pi^2} \right], & \Delta U & \equiv U - U_{\text{SM}}(M_H) = 16\pi a_8.
\end{aligned}$$

A global fit with $M_H = 300$ GeV and $m_t = 175$ GeV to the low energy EW data gives [197]

$$\Delta S = -0.26 \pm 0.14 \quad , \quad \Delta T = -0.11 \pm 0.16 \quad , \quad \Delta U = 0.26 \pm 0.24$$

which imply the following bounds for the three chiral couplings

$$a_1(1\text{TeV}) = (6.8 \pm 2.8) \times 10^{-3}, a_0(1\text{TeV}) = (4.3 \pm 4.9) \times 10^{-3}, a_8(1\text{TeV}) = (4.9 \pm 4.7) \times 10^{-3}.$$

Other studies agree with these values [198]. These data already disfavour the SM with a heavy Higgs boson and set strong constraints in models with a dominance of vector resonances [195] (like technicolor). With further assumptions on the underlying SBS dynamics, the latter give a negative contribution to a_1 . However, the precision EW measurements leave room for a strong SBS [198].

Further constraints come from the three-point functions, whose anomalous electroweak effective couplings were traditionally parametrised in terms of $g_1^\gamma, g_1^Z, \kappa_\gamma, \kappa_Z, \lambda_\gamma$ and λ_Z . A one-loop EChL calculation of these vertices [199] gives

$$\begin{aligned} g_1^\gamma - 1 &= 0 + \text{EChL loops}, & g_1^Z - 1 &= \frac{-g^2}{c_W^2} a_3 + \text{EChL loops}(\mu) \\ \kappa_\gamma - 1 &= g^2(a_2 - a_3 - a_1 + a_8 - a_9) + \text{EChL loops}, & \lambda_\gamma &= 0 \\ \kappa_Z - 1 &= g^2(a_8 - a_3 - a_9) + g'^2(a_1 - a_2) + \text{EChL loops}(\mu), & \lambda_Z &= 0 \end{aligned}$$

There are several analyses [200, 41] that constrain these chiral couplings from LEP and Tevatron data. Ignoring the loops from the NL σ M, we get the following values from present LEP data (the Tevatron precision is comparable) $\lambda_\gamma = -0.037^{+0.035}_{-0.036}$,

$$\begin{aligned} \kappa_\gamma - 1 &= 0.038^{+0.079}_{-0.075}, & \longrightarrow & a_2 - a_3 - a_1 + a_8 - a_9 = 0.088^{+0.184}_{-0.174}, \\ g_1^Z - 1 &= -0.010 \pm 0.033 & \longrightarrow & a_3 = 0.018 \pm 0.059. \end{aligned}$$

Finally, some indirect bounds on quartic couplings have also been found [201, 202]. These indirect estimates come from loops containing a_i vertices, but do not include 2-loop diagrams from the NL σ M. They find bounds on a_i for $i = 4, 5, 6, 7, 10$ ranging from 10^{-1} to 10^{-2} .

In summary, the present data on the oblique EW corrections already sets significant bounds on the a_0, a_1 and a_8 chiral parameters, but there is not much sensitivity yet to those chiral parameters that contribute to the three or four-point functions. We will see next how, at the LHC, the situation will improve significantly.

6.33 The Effective Chiral description at the LHC

At the next generation of colliders, we will be probing the W and Z interactions at TeV energies. As long as we are only considering the GBs and no other fundamental fields up to the TeV scale, we expect the self-interactions of longitudinal gauge-bosons, V_L , to become strong at LHC energies. This can be easily understood since, intuitively, longitudinal gauge-bosons are nothing but the GBs, which interact strongly. This intuitive statement is rigorously given in terms of on-shell amplitudes and is known as the Equivalence Theorem (ET),

$$A(V_L^a, V_L^b, V_L^c \dots \text{Other fields}) \simeq A(\omega^a \omega^b \omega^c \dots \text{Other fields}) + O\left(M_W^2/\sqrt{s}\right), \quad (70)$$

which holds for any spontaneously broken non-Abelian theory. Indeed, it was first derived for the SM [203, 204, 205]. Its usefulness is twofold: it relates the pure SBS fields with the observables, but also the calculations can now be performed in terms of scalars instead of gauge-bosons, at least in the high energy limit $s \gg M_W^2$. At first sight it may seem that the ET is incompatible with the use of the EChL,

since an effective theory is a low energy limit. Nevertheless, the ET can still be applied with the EChL, *only at leading order in g and g'* , if we only consider energies below 1.5 TeV and small chiral parameters [206, 207, 208].

Hence, in a first approximation, we will simplify the high energy description of the strong SBS by neglecting EW corrections. Thus, due to our assumption that $SU(2)_{L+R}$ is preserved in the SBS, only the operators that respect custodial symmetry once the gauge-symmetries are switched off will be relevant in this regime. These are the universal term and the operators with a_i couplings for $i = 3, 4, 5$.

At the LHC, the two most relevant processes of $V_L V_L$ production are the scattering of two longitudinal vector-bosons in fusion reactions and the V_L pair production from $q\bar{q}$ annihilation. Through the ET, they are identified with GB elastic scattering and $q\bar{q} \rightarrow \omega\omega$, respectively. Customarily, GB elastic scattering is described in terms of partial wave amplitudes of definite angular momentum, J , and isospin, I , associated to the custodial $SU(2)_{L+R}$ group. With the EChL, these partial waves, t_{IJ} are obtained as

$$t_{IJ}(s) = t_{IJ}^{(2)}(s) + t_{IJ}^{(4)}(s) + \dots, \quad (71)$$

where the superscript refers to the corresponding power of momenta. They are given by [191, 209, 210]

$$\begin{aligned} t_{00}^{(2)} &= \frac{s}{16 \pi v^2}, & t_{00}^{(4)} &= \frac{s^2}{64 \pi v^4} \left[\frac{16(11a_5 + 7a_4)}{3} + \frac{101/9 - 50 \log(s/\mu^2)/9 + 4 i \pi}{16 \pi^2} \right], \\ t_{11}^{(2)} &= \frac{s}{96 \pi v^2}, & t_{11}^{(4)} &= \frac{s^2}{96 \pi v^4} \left[4(a_4 - 2a_5) + \frac{1}{16 \pi^2} \left(\frac{1}{9} + \frac{i \pi}{6} \right) \right], \\ t_{20}^{(2)} &= \frac{-s}{32 \pi v^2}, & t_{20}^{(4)} &= \frac{s^2}{64 \pi v^4} \left[\frac{32(a_5 + 2a_4)}{3} + \frac{273/54 - 20 \log(s/\mu^2)/9 + i \pi}{16 \pi^2} \right]. \end{aligned} \quad (72)$$

Note that, within our approximations, the above amplitudes only depend on a_4 and a_5 . The projection in angular momentum has been defined, from the definite I amplitude T_I , as

$$t_{IJ} = \frac{1}{64 \pi} \int_{-1}^1 d(\cos \theta) P_J(\cos \theta) T_I(s, t). \quad (73)$$

The $V_L V_L$ production from $q\bar{q}$ annihilation, is very important since vector resonances can also couple to this channel. By means of the ET, we are thus interested in $q\bar{q} \rightarrow \omega\omega$. As far as GBs couple to quarks proportionally to their mass, the only relevant contribution comes from the s -channel annihilation through a vector-boson. In practice, for the WZ final state, the $W \rightarrow \omega z$ interaction is described as $g F_V(s)$, by means of a vector form factor, $F_V(s)$, which is obtained from the EChL as

$$F_V(s) = 1 + F_V^{(2)}(s) + \dots \quad \text{with} \quad F_V^{(2)}(s) = \frac{s}{(4 \pi v)^2} \left[64 \pi^2 a_3(\mu) - \frac{1}{6} \log \frac{s}{\mu^2} + \frac{4}{9} + i \frac{\pi}{6} \right] \quad (74)$$

Let us then review the studies of the LHC sensitivity to the chiral parameters via these two processes.

6.34 Non-resonant studies for LHC

The EChL formalism has been applied to study the LHC sensitivity to different non-resonant SBS sectors in [211, 212, 125, 213, 214, 215]. We summarise in Table 29 the results from [125, 213, 214] where the expected number of gold-plated ZZ and WZ from VV -fusion and $q\bar{q}$ -annihilation was calculated for values of the custodial preserving a_3 , a_4 and a_5 parameters in the 10^{-2} to 10^{-3} range. Since for values of a_4 or $a_5 \geq 5 \times 10^{-3}$ *unitarity violations cannot be ignored at energies beyond 1.5 TeV*, these studies only include events in the region of low invariant mass $V_L V_L$ pair, *i.e.* $M_{VV} \leq 1.5$ TeV. The rest of kinematical cuts are similar to those given in Equation 81. To illustrate the agreement between these kinds of studies, we give in Table 29 other estimates [215] of the a_i bounds attainable at the LHC.

Table 29: Expected number of signal and total (signal+background) gold-plated WZ and ZZ events [125, 213, 214]. The statistical significance is defined as $r = (N(a_i) - N(0))/\sqrt{N(0)}$ where $N(a_i)$ is the expected number of events for a given a_i . On the bottom right, expected limits on the chiral parameters attainable at the LHC [215] are shown.

$\mathcal{L} = 100 \text{ fb}^{-1}$	a_4				a_5			
	10^{-2}	-10^{-2}	5×10^{-3}	-5×10^{-3}	10^{-2}	-10^{-2}	5×10^{-3}	-5×10^{-3}
$W^\pm Z \rightarrow W^\pm Z$	36	80	27	47	22	58	23	41
total $W^\pm Z$	118	162	109	129	104	139	105	122
r_{WZ}	0.7	4.8	0.2	1.7	0.7	2.6	0.6	1.0
$r_{WZ \text{ tagging}}$	1.0	7.5	0.3	2.7	1.0	4.2	0.9	1.7
$W^+W^- \rightarrow ZZ$	12	7	9	7	21	7	13	6
$ZZ \rightarrow ZZ$	6	6	1	1	6	6	1	1
total ZZ	37	32	30	27	46	32	33	26
r_{ZZ}	1.9	0.9	0.5	$\simeq 0$	3.8	0.9	1.2	0.1
$r_{ZZ \text{ tagging}}$	3.5	1.8	0.9	0.1	6.6	1.8	2.3	0.2

$\mathcal{L} = 100 \text{ fb}^{-1}$	a_3		LHC Limits (90% CL)	Process
	10^{-2}	-10^{-2}		
$qq' \rightarrow W^\pm Z$	96	139	$-0.0035 \leq a_4 \leq 0.015$	$W^\pm W^\pm, WZ, ZZ$
$r_{WZ \text{ tagging}}$	1.4	2.7	$-0.0072 \leq a_5 \leq 0.013$	$W^\pm W^\pm, WZ, ZZ$
			$-0.013 \leq a_6 \leq 0.013$	WZ, ZZ
			$-0.013 \leq a_7 \leq 0.011$	WZ, ZZ
			$-0.029 \leq a_{10} \leq 0.029$	ZZ

It will be very difficult to detect these non-resonant signals over the continuum background, since they just give small enhancements in the high energy region of the M_{VV} and p_T distributions. There is a general agreement that, although the present bounds could be significantly improved, with these non-resonant studies, the LHC would be hardly sensitive to values of the chiral parameters down to the 10^{-3} level. Like-sign $W^\pm W^\pm$ production may be better in these channels [171, 216].

Obviously, these studies do not describe one of the most characteristic features of strong interactions: resonances. Moreover, they are limited to moderate energies due to the unitarity violations mentioned already. These caveats can be overcome by means of unitarisation procedures which we explain next.

6.35 Unitarisation and resonances in the SBS

In terms of the partial waves defined in Equation 72, the elastic $V_L V_L$ scattering unitarity condition, (basically, the Optical Theorem) for physical values of s , is

$$\text{Im } t_{IJ}(s) = |t_{IJ}(s)|^2 \Rightarrow \text{Im} \frac{1}{t_{IJ}(s)} = -1, \Rightarrow t_{IJ}(s) = \frac{1}{\text{Re } t_{IJ}^{-1}(s) - i}. \quad (75)$$

Hence we only have to use the EChL to approximate

$$\text{Re } t_{IJ}^{-1} = (t_{IJ}^{(2)})^{-1} [1 - \text{Re } t_{IJ}^{(4)}/t_{IJ}^{(2)} + \dots]. \quad (76)$$

But since the EChL amplitudes satisfy elastic unitarity *perturbatively*, i.e.

$$\text{Im } t_{IJ}^{(4)}(s) = |t_{IJ}^{(2)}(s)|^2 \Rightarrow \frac{\text{Im } t_{IJ}^{(4)}(s)}{|t_{IJ}^{(2)}(s)|^2} = -1, \quad (77)$$

we find

$$t_{IJ}(s) = \frac{t_{IJ}^{(2)}}{1 - t_{IJ}^{(4)}/t_{IJ}^{(2)}} \quad (78)$$

This is the $O(p^4)$ Inverse Amplitude Method (IAM), which has given remarkable results describing meson interactions, which have a symmetry breaking pattern almost identical to our present case [217, 218, 219, 220]. Note that it respects strict elastic unitarity, while keeping the correct EChL low energy expansion. Furthermore, the extension of Equation 78 to the complex plane can be justified using dispersion theory [217, 218, 219, 220]. In particular, it has the proper analytical structure and, eventually, poles in the second Riemann sheet for certain a_4 and a_5 values, that can be interpreted as resonances. Thus, EChL+IAM formalism can describe resonances without increasing the number of parameters and respecting chiral symmetry and unitarity.

The EChL+IAM has already been applied to the SBS [221, 222] to study some specific choices of a_4 and a_5 that mimic models with vector or scalar resonances. The LHC sensitivity to resonances parametrised with a_4 and a_5 was first studied in [222] and [223], and more recently in [42]. A map of these resonances in the (a_4, a_5) space was first obtained in [224]. We show in Figure 46 the vector and scalar neutral resonances expected in the (a_4, a_5) parameter space. As far as we expect a_4 and a_5 to lie between 10^{-2} and 10^{-3} , we scan only that range. Furthermore, the poles of the IAM amplitudes will give us the positions and widths of the resonances. Note that, from Equation 72 within our approximations, the $I = J = 1$ and $I = J = 0$ channels only depend on the $a_4 - 2a_5$ and $7a_4 + 11a_5$ combinations, respectively. Thus the straight lines that keep these combinations constant have the same physics in the corresponding channel. We give several examples in the tables within the figure. The fact that each IAM amplitude depends only on one combination of a_i implies that their mass and width are related by the KSFR relation [225, 226]. In addition, we locate five points that we will use later as illustrative examples.

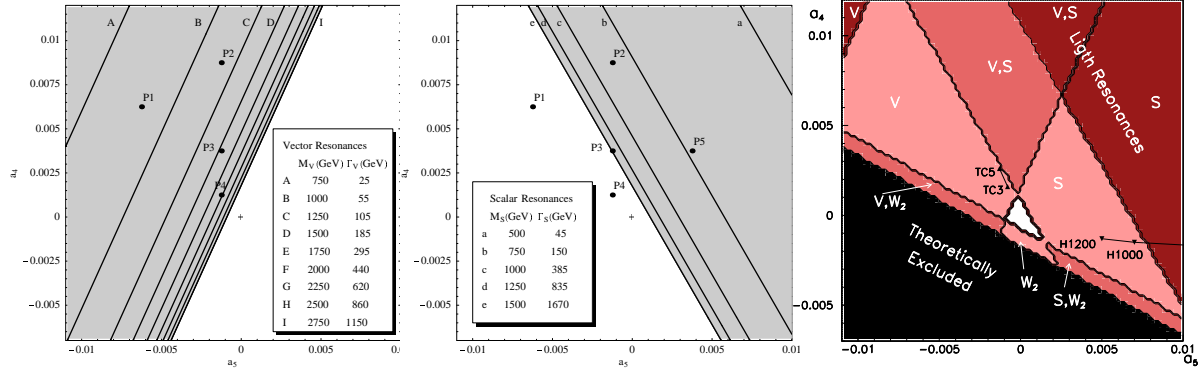


Fig. 46: Resonances in the (a_4, a_5) space [224]. In the tables we give the resonance parameters for several lines. a) Left: Vector resonances. The points with the same $a_4 - 2a_5$ have the same physics in the $I = J = 1$ channel. b) Middle: Scalar neutral neutral resonances. Those points with constant $7a_4 + 11a_5$ have the same physics in this channel. c) Right: General Resonance Spectrum of the strong SBS. V stands for vector resonances, S for neutral scalar resonances and W_2 , for wide structures that saturate the doubly charged ($I = 2$) channel. For illustration, we have also located several simple and familiar models explained in the text.

The white area means that no resonances or saturation of unitarity is reached below $4\pi v \simeq 3$ TeV, which we expect to be the region of applicability for our approach.

We do not give results for the $I = 2, J = 0$ channel since we do not expect any heavy resonance with our minimal assumptions. Intuitively this occurs because the $I = 2, J = 0$ channel is repulsive.

The general resonance spectrum of the MSISBS is gathered in the last plot of Figure 46 [224]. Depending on a_4 and a_5 , we find one scalar resonance (S), one vector resonance (V), two resonances (S, V), a resonance and a doubly charged wide saturation effect (W_2) or even no resonances below 3 TeV (white area). For illustration, we have included points for some simple and familiar scenarios: minimal technicolor models with 3 and 5 technicolors ($TC3$ and $TC5$), and the heavy Higgs SM case, with a tree level mass of 1000 and 1200 GeV ($H1000$ and $H1200$). The black region is excluded by the constraints on the $I = 2, J = 0$ wave [224]. In the dark “Light Resonances” areas (lighter than 700 GeV), our results should be interpreted cautiously. Outside these areas, we estimate that the predictions of Figure 46 are reliable within $\sim 20\%$ [42].

Once we have the general spectrum, our aim is to study to what extent the LHC is sensitive to different resonant scenarios via $V_L V_L$ production. For that purpose, we cannot forget the unitarisation of $q\bar{q} \rightarrow V_L V_L$, since we expect the final state to re-scatter strongly, in particular when there is a resonance in the $I = J = 1$ elastic channel. This effect can be parametrised in terms of a vector form factor, F_V . Again, the F_V obtained from the EChL does not satisfy exactly its unitarity condition

$$\text{Im } F_V(s) = F_V(s) t_{11}^*(s), \quad (79)$$

which implies that the phases of F_V and t_{11} should be the same (Watson’s Final State Theorem). Moreover, the poles of F_V should be those of t . Hence, we can relate the combination of a_i that appears in the perturbative expansion of F_V (Equation 74) with $a_4 - 2a_5$. All in all, it is possible to unitarise F_V using only the t_{11} EChL result, as follows [42]:

$$F_V \simeq \frac{1}{1 - t_{11}^{(4)}/t_{11}^{(2)}}. \quad (80)$$

In summary, F_V is determined just by $a_4 - 2a_5$, and we can still use the map of resonances in Figure 46.

We will restrict the study to ZZ and WZ production, assuming that their gold-plated decays, $ZZ \rightarrow 4l$ and $WZ \rightarrow l\nu ll$ (with $l = e, \mu$) can be identified and reconstructed with a 100% efficiency. We do not consider like-sign $W^\pm W^\pm$ production, since, as we have seen, we do not expect $I = 2$ resonances.

To evaluate VV fusion processes, we use the leading-order Effective- W Approximation (EWA) [227]. Non-fusion diagrams are not included since they are expected to be small in our kinematic region. We also use the CTEQ4 [229] parton distribution functions at $Q^2 = M_W^2$ for VV fusion and at $Q^2 = s$ for $q\bar{q}$ annihilation and gg fusion, with \sqrt{s} being the centre of mass energy of the parton pair. More detail can be found in [42].

Since we do not consider final W and Z decays, the cuts are set directly on the gauge-boson variables. A first criterion to enhance the strong $V_L V_L$ signal over the background is to require high invariant mass M_{VV} and small rapidities. We have applied the following set of minimal cuts:

$$500 \text{ GeV} \leq M_{V_1 V_2} \leq 10 \text{ TeV}, \quad |y_{\text{lab}}(V_1)|, |y_{\text{lab}}(V_2)| \leq 2.5, \quad p_T(V_1), p_T(V_2) \geq 200 \text{ GeV}, \quad (81)$$

which are also required by our approximations, mainly by the ET. An additional invariant mass cut around each resonance will be imposed later.

The ZZ production signal occurs through the $W_L^+ W_L^- \rightarrow Z_L Z_L$ and $Z_L Z_L \rightarrow Z_L Z_L$ fusion processes. In addition, we have included the following backgrounds

$$q\bar{q} \rightarrow ZZ, (61\%), \quad W^+ W^- \rightarrow ZZ, (18\%), \quad gg \rightarrow ZZ, (21\%)$$

where we also give their relative contribution to the total background with the minimal cuts. The continuum from $q\bar{q}$ annihilation has only tree level SM formulae, which is probably too optimistic since the NLO QCD corrections [25, 23, 24, 26] can enhance significantly the tree level cross sections. The second background is calculated in the SM at tree level, with at least one transverse weak boson. Finally, the one-loop $gg \rightarrow ZZ$ amplitude has been taken from [228].

For $W^\pm Z$ final states, two processes contribute to the signal: $W_L^\pm Z_L \rightarrow W_L^\pm Z_L$ and $q\bar{q}' \rightarrow W_L^\pm Z_L$, whereas the backgrounds, calculated at tree level within the SM, are

$$W^\pm Z \rightarrow W^\pm Z, (18\%), \quad \gamma Z \rightarrow W^\pm Z, (15\%), \quad q\bar{q}' \rightarrow W^\pm Z, (67\%).$$

The $W^\pm Z \rightarrow W^\pm Z$ amplitudes have at least one transverse boson and exclude the Higgs contribution. In the $q\bar{q}' \rightarrow W^\pm Z$ background, we have excluded the amplitude with a $V_L V_L$ pair, which is part of the signal. The QCD corrections to $q\bar{q}'$ annihilation would give an enhancement in both the signal and the background, so we expect that they will not modify considerably our estimates of the statistical significance of vector resonance searches. We have not studied the $t\bar{t}$ background since it can be efficiently suppressed after imposing kinematic constraints and isolation cuts to high- p_T leptons [153, 125, 53].

For illustrative purposes, let us first concentrate on the five representative points given in Figure 46. Points 1, 3 and 4 represent models containing a $J = I = 1$ resonance with masses in the range 900-2000 GeV. Point 5 represents a model with a scalar resonance with mass 730 GeV and a width of 140 GeV. Finally, point 2 represents both a scalar and a vector resonance. The M_{VV} distributions for these five models are shown in Figure 47, where we have plotted the signal on top of the background for gold-plated ZZ and WZ events, assuming an integrated luminosity of 100 fb^{-1} . The vector resonances in points 1 to 4 can be seen as peaks in the distribution of final WZ pairs. The scalar resonances in points 2 and 5 give small enhancements of ZZ pairs. Note that as both a_4 and a_5 tend to 0, the resonances become heavier and broader, yielding a less significant signal. It seems evident that it will be much harder to detect scalar than vector resonances. The reasons are that scalars are wider, they are not produced with a significant rate from $q\bar{q}$ annihilation, and there is a smaller rate of ZZ production from VV fusion. Furthermore, the ZZ branching ratio to leptons is smaller than that of WZ .

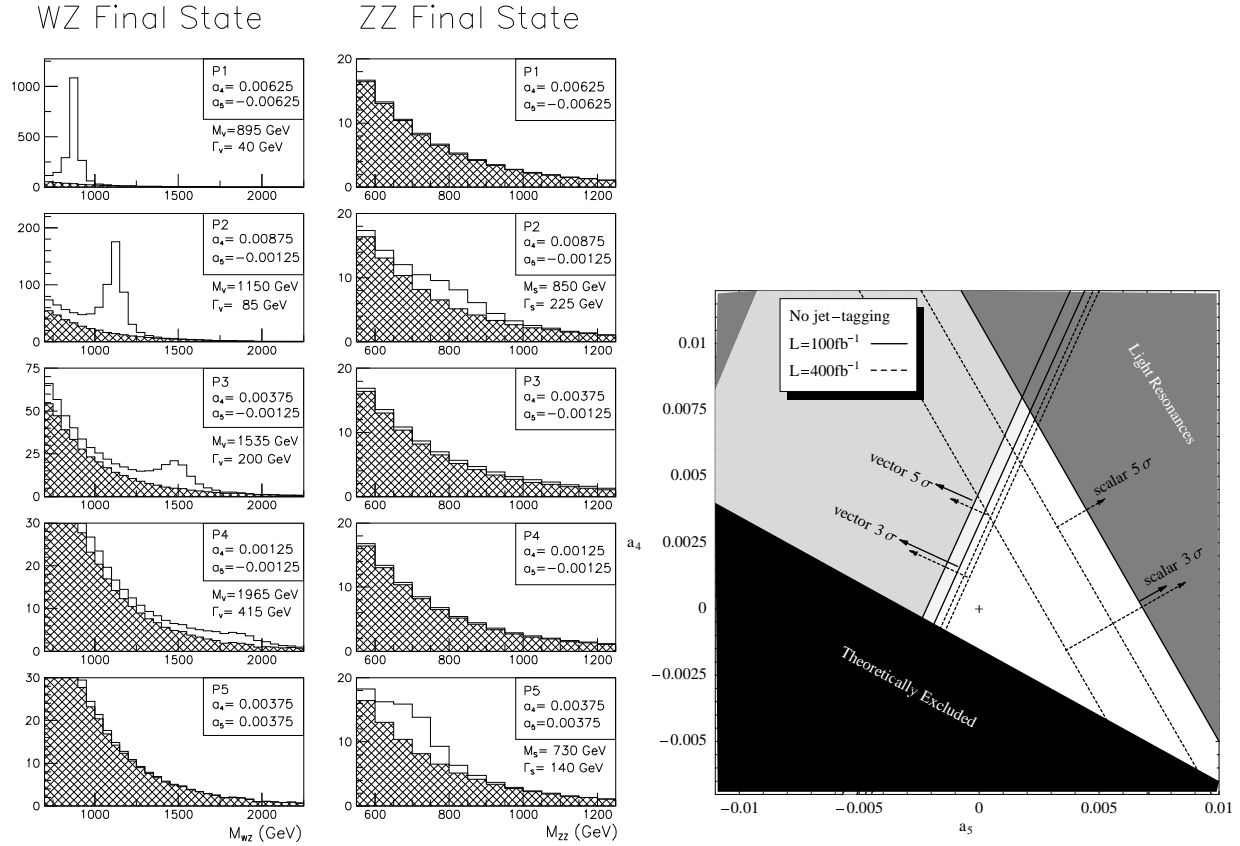


Fig. 47: a) Left: Distribution of gold-plated events from WZ and ZZ production [42]. The shaded histogram corresponds to the background as described in the text. On top of it we have plotted the signal as a white histogram. The points labelled $P1$ to $P5$ correspond to those in Figure 46 and are representative of cases which, from top to bottom, present: one narrow vector resonance, a vector and a scalar resonance, an intermediate vector resonance, a very wide vector resonance and, finally, a “narrow” scalar resonance. b) Right: Sensitivity of the LHC to the resonance spectrum of the strong SBS with WZ and ZZ gold plated events [42]. In the (a_4, a_5) parameter space, we show the 3σ and 5σ reach with an integrated luminosity of 100 fb^{-1} (solid lines limiting the shaded areas) and 400 fb^{-1} (dashed lines), both for scalar and vector resonances.

The contributions to signal and background for WZ and ZZ production at these representative points are given in Table 30. In order to enhance the signal to background ratio, we have optimised the M_{VV} cut, keeping events within approximately one resonance width around the resonance mass (see the second column of these tables). From the WZ results, it is clear that the LHC will have a very good sensitivity to light vector resonances, due to the $q\bar{q}$ -annihilation, which dominates by far the VV -fusion process. As the vector resonance mass increases, the $q\bar{q}$ contribution is damped faster than that of VV fusion, and both signals become comparable for vector masses around 2 TeV. Let us remark that, in ZZ production, there is only strong interaction signal in VV fusion, and therefore to tag forward jets is always convenient in this final state in order to reject non-fusion processes. This is not the case, however, for vector resonance searches since it is mostly due to $q\bar{q}$ annihilation. In these tables, we have also estimated the statistical significance, $\text{Signal}/\sqrt{\text{Bkgd}}$, assuming integrated luminosities of 100 and 400 fb^{-1} . In ZZ final states, we also give the significance assuming perfect forward jet-tagging.

Table 30: Expected number of signal and background gold-plated VV events at the LHC with $\mathcal{L} = 100 \text{fb}^{-1}$. a) Top: For $W^\pm Z$ final state and four different (a_4, a_5) values representing vector resonances. b) Bottom: For ZZ and two representative (a_4, a_5) values with scalar resonances. The statistical significance is also given for ideal forward jet-tagging.

M_V, Γ_V (GeV)	Cuts:	Signal	Signal	Signal	Bkgd	Bkgd	Bkgd	S/\sqrt{B}	S/\sqrt{B}
$(a_4, a_5) \times 10^3$	$(M_{VV}^{min}, M_{VV}^{max})$	Fusion	$q\bar{q}$	Total	Fusion	$q\bar{q}$	Total	100 fb^{-1}	400 fb^{-1}
$P1: 894, 39$ (-6.25,6.25)	(700,1000)	123	1630	1743	74	150	224	116	232
$P2: 1150, 85$ (-1.25,8.75)	(900, 1300)	65	369	434	50	84	134	37	75
$P3: 1535, 200$ (-1.25,3.75)	(1250, 1700)	24	56	80	21	27	48	11	23
$P4: 1963, 416$ (-1.25,1.25)	(1500, 2350)	10	12	22	14	16	30	4	8

M_S, Γ_S (GeV)	Cuts:	Signal	Bkgd	Bkgd	Bkgd	Bkgd	S/\sqrt{B}	S/\sqrt{B}	S/\sqrt{B}
$(a_4, a_5) \times 10^3$	$(M_{VV}^{min}, M_{VV}^{max})$	Fusion	Fusion	gg	$q\bar{q}$	Total	100 fb^{-1}	jet-tagging	400 fb^{-1}
$P2: 850, 225$ (-1.25,8.75)	(600, 1050)	15	10	11	34	55	2	5	4
$P5: 750, 140$ (3.25,3.75)	(550, 900)	21	10	14	39	63	3	6	5

Finally, we also show in Figure 47 the regions of the (a_4, a_5) space accessible at the LHC, giving 3 and 5σ contours and assuming integrated luminosities of 100 and 400 fb^{-1} . In terms of resonance mass reach limits, we find that with 100 fb^{-1} , scalar resonances could be discovered (5σ) in gold-plated ZZ events up to a mass of 800 GeV with forward jet-tagging. Vector resonances could be discovered using gold-plated WZ events up to a mass of 1800 GeV. These numbers are in good agreement with more realistic studies [153, 125, 53] of particular cases. We can also see that there is a central region in the (a_4, a_5) space that does not give significant signals in gold-plated ZZ and WZ events. This region corresponds to models in which either the resonances are too heavy or there are no resonances in the SBS and the scattering amplitudes are unitarised smoothly. It is a key issue as to whether this type of non-resonant $V_L V_L$ signal could be probed at the LHC. It has been argued that doubly-charged WW production could be relevant to test this non-resonant region. But non-resonant VV distributions would only have slight enhancements at high energies, and a very accurate knowledge of the backgrounds and the detector performance would be necessary in order to establish their existence.

Table 31: Relation between different notations in the literature.

Ours [192, 193]	a_0	a_1	a_2	a_3	a_4	a_5	a_6	a_7	a_8	a_9	a_{10}
App.& Longh. [36, 37]	$\frac{g^2}{g'^2}\beta_1$	$\frac{g}{g'}\alpha_1$	$\frac{g}{g'}\alpha_2$	$-\alpha_3$	α_4	α_5	α_6	α_7	$-\alpha_8$	$-\alpha_9$	$\frac{1}{2}\alpha_{10}$
S.Alam [200, 41]	$\frac{1}{g'^2}\beta_1$	α_1	α_2	$-\alpha_3$	α_4	α_5	α_6	α_7	$-\alpha_8$	$-\alpha_9$	$\frac{1}{2}\alpha_{10}$
He <i>et al.</i> [211, 212]	$\frac{l_0}{16\pi^2 g'^2}$	$\frac{l_1}{16\pi^2}$	$\frac{l_2}{16\pi^2}$	$\frac{l_3}{16\pi^2}$	$\frac{l_4}{16\pi^2}$	$\frac{l_5}{16\pi^2}$	$\frac{l_6}{16\pi^2}$	$\frac{l_7}{16\pi^2}$	$\frac{-l_8}{16\pi^2}$	$\frac{-l_9}{16\pi^2}$	$\frac{-l_{10}}{32\pi^2}$
Vertex	2	2,3	3	3,4	4	4	4	4	2,3,4	3,4	4
$SU(2)_{L+R}$	no	no	no	yes	yes	yes	no	no	no	no	no

6.4 Vector-boson scattering

The search for a fundamental scalar particle which would be responsible for electroweak symmetry breaking has so far proven unsuccessful. While the existence of a light Standard Model (SM) Higgs alone would be consistent with all precision electroweak measurements, the well known hierarchy problems [230] make the theory unsatisfactory. The model makes *ad hoc* assumptions about the shape of the potential, responsible for electroweak symmetry breaking, and provides no explanation for the values of the parameters. Although supersymmetry is an appealing alternative, no indication exists, yet, of its validity. Therefore, in the absence of a low mass Higgs particle, a strongly coupled theory must be considered. The study of electroweak symmetry breaking will require measurements of the production rate of pairs of longitudinal gauge-bosons, since they are the Goldstone bosons of the symmetry breaking process. It will also be essential to search for the presence of resonances which regularise the vector-boson scattering cross-section. Scalar resonances occur in models with a heavy SM Higgs boson, and vector resonances, in charged or neutral channels, are also predicted in dynamical theories, such as technicolor.

In this section, different channels for scattering of high energy gauge-bosons at the LHC are considered. These include heavy Higgs production and resonant WZ as well as non-resonant WZ and W^+W^+ production in the Chiral Lagrangian model. High mass gauge-boson pair production in a multi-scale technicolor model is also examined. The possibility of making such measurements at the LHC is evaluated.

6.41 Heavy Higgs signal

It is now generally believed that a SM Higgs should be light, its mass being bound by requirements of vacuum stability and by the validity of the SM to high scales in perturbative calculations [231]. The parameters of the Higgs used in this study were calculated at tree level. One should note that in NNLO, the resonance saturates [232]. Nevertheless, the search for such a resonance at the LHC can serve as a testing ground for the measurement of the production of high mass longitudinal gauge-boson pairs or for the search of a generic resonance. The $H \rightarrow WW \rightarrow l\nu jj$ channel is presented in this section as an example of a typical analysis of a heavy Higgs signal. In fact, $V_L V_L$ fusion is also detectable in the case of a heavy Higgs resonance, through the processes $H \rightarrow ZZ$, up to $M_H \sim 800$ GeV. Simultaneous detection of a heavy Higgs in other signals would not only confirm the discovery but also provide additional information on the Higgs couplings, which are essential for determining the nature of the resonance.

$H \rightarrow WW \rightarrow l\nu jj$ In the vector-boson fusion process of Higgs production, $qq \rightarrow qqH$, the rate for this channel is sufficient to be observed at low luminosity with a very distinctive signature [235, 237, 238]:

- A high- p_T central lepton ($|\eta| < 2$).
- A large E_T^{miss} .

- Two high- p_T jets from the $W \rightarrow jj$ decay in the central region and close-by in space ($\Delta R \sim 0.4$) arising from the large boost of the W boson.
- Two tag jets in the forward regions ($|\eta_j| > 2$).
- No extra jet in the central region (central jet veto).

The main backgrounds are:

- W +jet which gives the largest contribution but also suffers from significant theoretical uncertainties due to higher-order corrections [236].
- $t\bar{t} \rightarrow l\nu b jj\bar{b}$, with the presence of a real $W \rightarrow jj$ decay, but also additional hadronic activity from the b -jets in the central region.
- $WW \rightarrow l\nu jj$ continuum production, which has a much lower rate but is irreducible in the central region.

In addition to central jet veto and forward tag jets cuts, other cuts (high- p_T cuts) have been used to optimise the statistical significance of the signal. They are:

- Lepton cuts: $p_T^l, E_T^{miss} > 100$ GeV, $p_T^{W \rightarrow l\nu} > 350$ GeV.
- Jet cuts: two jets reconstructed within $\Delta R = 0.2$ with $p_T > 50$ GeV and $p_T^{W \rightarrow jj} > 350$ GeV.
- W mass window: $m_{jj} = m_W \pm 2\sigma$, where σ is the resolution on m_{jj} .

Table 32 shows the number of events resulting from this selection, for an integrated luminosity of 30 fb^{-1} , for $M_H = 1$ TeV and $M_H = 800$ GeV as evaluated with the ATLAS fast simulation program (ATLFAST, [85]). A significant signal remains above background. Variation of the E_{tag} cut provides the possibility to compare the shape and cross section of the resonance production to the expected parameters of the Higgs signal (see Figure 48).

Table 32: $H \rightarrow WW \rightarrow l\nu jj$ with $M_H = 1$ TeV and $M_H = 800$ GeV and $\mathcal{L} = 30 \text{ fb}^{-1}$. Accepted signal and background events after high- p_T cuts, central jet veto and a double forward tag with $E_{tag} > 300$ GeV.

	Higgs signal	$t\bar{t}$ ($p_T > 300$ GeV)	W +jets ($p_T > 250$ GeV)	WW ($p_T > 50$ GeV)	S/\sqrt{B}
$M_H = 1$ TeV	37.9	3.3	9.2	1.0	10.3
$M_H = 800$ GeV	43.5	3.3	9.2	1.0	11.8

The $H \rightarrow ZZ \rightarrow ll\nu\nu$ and $H \rightarrow ZZ \rightarrow lljj$ channels in ATLAS have also been studied [233, 234, 237] over most of the mass range from 300 GeV to 1 TeV. It has been shown that forward jet tagging ($2 < |\eta_j| < 5$), is a powerful method for rejecting background and selecting $qq \rightarrow qqH$ production, *i.e.* the vector-boson fusion process.

6.42 Strong vector-boson scattering

Chiral Lagrangian model In the Chiral Lagrangian model [249], the form of the Lagrangian is only constrained by symmetry considerations which are common to any strong electroweak symmetry breaking sector. Differences among underlying theories appear through the values of the parameters of the Chiral Lagrangian. Within the chiral approach, the low-energy Lagrangian is built as an expansion in derivatives of the Goldstone boson fields. There is only one possible term with two derivatives which respects $SU(2)_{L+R}$ symmetry:

$$\mathcal{L}^{(2)} = \frac{v^2}{4} \text{Tr}(D_\mu U D^\mu U^\dagger)$$

where $D_\mu U = \partial_\mu U - W_\mu U + U B_\mu$, $W_\mu = -ig\sigma^a W_\mu^a/2$, $B_\mu = ig\sigma^3 B_\mu/2$.

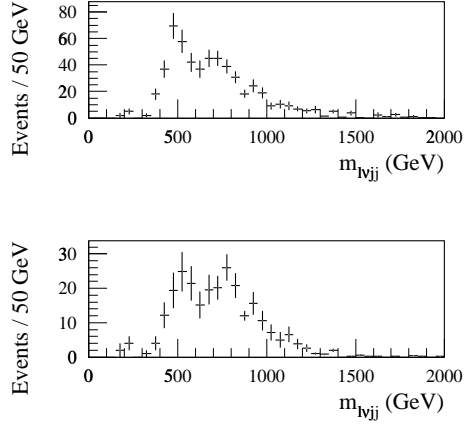


Fig. 48: m_{lwj} distribution for the summed signal+background obtained with $M_H = 800$ GeV and $\mathcal{L} = 30 \text{ fb}^{-1}$ after requiring two tag jets with $E_{tag} > 200$ GeV (top) and $E_{tag} > 400$ GeV (bottom) [238].

The dependence on the different models appears at next order through two phenomenological parameters L_1 and L_2 :

$$\mathcal{L}^{(4)} = L_1(\text{Tr}(D_\mu U D^\mu U^\dagger))^2 + L_2(\text{Tr}(D_\mu U D^\nu U^\dagger))^2$$

The $SU(2)_{L+R}$ symmetry allows us to define a weak isospin I . The $W_L W_L$ scattering can then be written in terms of isospin amplitudes, exactly as in low energy hadron physics. We assign isospin indices as follows:

$$W_L^a W_L^b \rightarrow W_L^c W_L^d$$

where W_L denotes either W_L^\pm or Z_L , where $W_L^\pm = (1/\sqrt{2})(W_L^1 \mp iW_L^2)$ and $Z_L = W_L^3$. The scattering amplitude is given by:

$$\mathcal{M}(W_L^a W_L^b \rightarrow W_L^c W_L^d) \equiv A(s, t, u)\delta^{ab}\delta^{cd} + A(t, s, u)\delta^{ac}\delta^{bd} + A(u, t, s)\delta^{ad}\delta^{bc}$$

where $a, b, c, d = 1, 2, 3$ and s, t, u are the usual Mandelstam kinematical variables.

In this approach it is possible to compute the function $A(s, t, u)$ in $\mathcal{O}(p^4)$ [250, 251]:

$$A(s, t, u) = \frac{s}{v^2} + \frac{1}{4\pi v^4}(2L_1 s^2 + L_2(t^2 + u^2)) + \frac{1}{16\pi^2 v^4} \left(-\frac{t}{6}(s+2t) \log\left(-\frac{t}{\mu^2}\right) - \frac{u}{6}(s+2u) \log\left(-\frac{u}{\mu^2}\right) - \frac{s^2}{2} \log\left(-\frac{s}{\mu^2}\right) \right)$$

The values of L_1 and L_2 depend on the model, but are expected to be in the range 10^{-2} to 10^{-3} .

The usual Chiral Lagrangian approach does not respect unitarity at high energies. The Inverse Amplitude Method (IAM) [217, 218, 249], which is based on the assumption that the inverse of the amplitude has the same analytic properties as the amplitude itself, has been very successful at describing low energy hadron scattering. The most interesting feature of this approach is that it allows us to describe different reactions by using only the two parameters L_1 and L_2 .

In analogy to $\pi\pi$ scattering, there are three possible isospin channels $I = 0, 1, 2$. At low energies, the states of lowest momentum J are the most important, and thus only the a_{00} , a_{11} and a_{20} partial waves are considered. It is possible to reproduce, with the IAM model, the broad Higgs-like resonance in the $(I, J) = (0, 0)$ channel as well as resonant and non-resonant scattering in the channel $(1, 1)$ by selecting appropriate values for L_1 and L_2 . It has been shown [224] that in the $(I = 1, J = 1)$ channel there may exist narrow resonances up to 2500 GeV and this scattering only depends on the combination of $(L_2 - 2L_1)$.

Resonant $W_L Z_L \rightarrow W_L Z_L$ channel As a reference for the IAM model, the process $W_L Z_L \rightarrow W_L Z_L$, with $Z \rightarrow ll$ ($l = e, \mu$) and $W \rightarrow jj$ is used [241]. A modified version of PYTHIA 5.7 was used to generate $V_L V_L$ scattering processes for each value of L_1 and L_2 . The simulation was done for two values of $(L_2 - 2L_1) = 0.006$ and 0.01 , which yield $\sigma \times BR$ of 1.5 fb and 2.8 fb, with mass peaks at 1.5 TeV and 1.2 TeV respectively.

Irreducible background arises from continuum WZ production and the main QCD background is from Z +jets production with two final state jets faking the W decay if their invariant mass is close to m_W . $t\bar{t}$ production is potentially dangerous but is efficiently suppressed by a cut on the invariant mass of leptons from the W decay [241]. The following cuts were used for background rejection:

- Two isolated leptons with the same flavour and opposite charges in the region $|\eta| < 2.5$ and $p_T > 100$ GeV. Their invariant mass was required to lie in the region $|m_{ll} - m_Z| < 6$ GeV.
- Jets were reconstructed in a cone of width $\Delta R = 0.2$. Only two jets with $p_T > 50$ GeV were allowed in the central region ($|\eta| < 2$) and $|m_{jj} - m_W| < 15$ GeV was required. Only W and Z with $p_T > 200$ GeV were kept.
- In the forward region ($2 < |\eta| < 5$), jets were reconstructed in a cone of width $\Delta R = 0.5$ and events were accepted only if jets with $p_T > 30$ GeV and $E_{jet} > 500$ GeV were present in each hemisphere.

The expected number of signal and background events after all cuts and for $\mathcal{L} = 100 \text{ fb}^{-1}$ are presented in Table 33. The mass spectra obtained after all cuts (Figure 49) shows a clear peak with a width of 75 GeV (100 GeV) for the 1.2 TeV (1.5 TeV) resonance and 14 (8) signal events in the window $|m_{WZ} - m_V| < 2\sigma$. The contribution from irreducible backgrounds is negligible and is below 0.05 events inside the mass window. It is clear that such a narrow resonance could be detected easily after a few years of high luminosity.

Table 33: Number of signal and background events after all cuts for $\mathcal{L} = 100 \text{ fb}^{-1}$ with $(L_2 - 2L_1) = 0.01$ and 0.006 , corresponding to $m_V = 1.2$ TeV and $m_V = 1.5$ TeV respectively.

Cuts	$M_V=1.2$ TeV		$M_V=1.5$ TeV	
	$W_L Z_L$	Z +jets	$W_L Z_L$	Z +jets
Central jets cut	284	2187	145	1781
$m_{jj} = m_W \pm 15$ GeV	101	154	46	82
Leptonic cuts	70	84	36	47
Forward jet tagging	14	3	8	1.3

Non-resonant channels If nature does not provide resonances in $V_L V_L$ scattering, the measurement of cross sections at high mass for non-resonant channels becomes the only probe for the mechanism of regularisation of the cross section. It would then be essential to understand very well the magnitude and energy dependence of backgrounds. Those channels can be particularly important since it has been shown that a complementary relationship exists between resonant and non-resonant processes [216, 171, 242]. Both $W_L Z_L$ and $W_L W_L$ scattering have been studied within the ATLAS framework.

$W_L Z_L \rightarrow W_L Z_L$ The non-resonant $W_L Z_L \rightarrow W_L Z_L$ process, with $Z \rightarrow ll$ and $W \rightarrow l\nu$ ($l = e, \mu$), was incorporated in PYTHIA and used with two values of L_1 : 0.003 and 0.01, leading to $\sigma \times BR = 0.19$ fb and 0.11 fb respectively. The main features of the signal are:

- The presence of two high- p_T leptons of same flavour and opposite charge in the barrel region, having an invariant mass consistent with the mass of the Z boson.

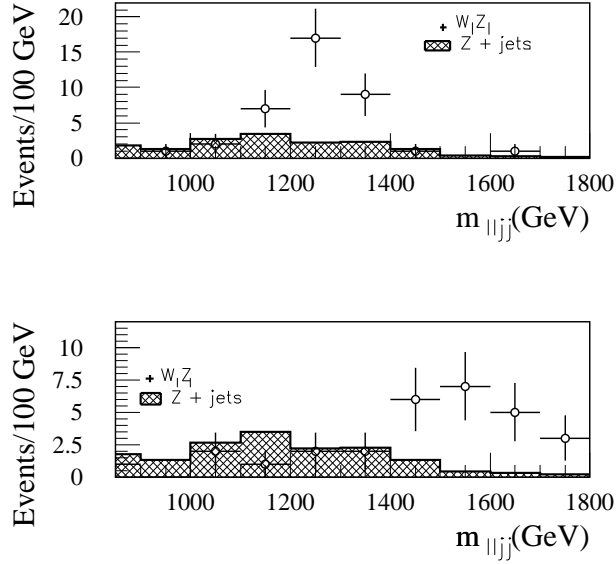


Fig. 49: Reconstructed distribution of the WZ system for 1.2 TeV and 1.5 TeV resonances and $\mathcal{L} = 300 \text{ fb}^{-1}$.

- One additional high- p_T lepton in the barrel region.
- Significant missing momentum in the event due to the presence of a neutrino.
- The presence of energetic jets in the forward region.

The main irreducible background, coming from continuum WZ production, was generated by PYTHIA with $\sigma \times BR = 13.5 \text{ fb}$. The main reducible background is the QCD process $Zt\bar{t}$ where one of the W bosons from a t -quark decays into a lepton and an anti-neutrino. The value of $\sigma \times BR$ of this process is 26.3 fb. A less important contribution comes from ZZ production with $\sigma \times BR = 1.52 \text{ fb}$. These different backgrounds were rejected with a high efficiency by using the following cuts:

- Two isolated leptons of same flavour and opposite charge were required in the central region with $p_T > 30 \text{ GeV}$ and invariant mass satisfying $|m_{ll} - m_Z| < 6 \text{ GeV}$. One additional lepton was required.
- A missing momentum of at least 75 GeV.
- At least one jet with $p_T > 40 \text{ GeV}$ and $E_{jet} > 500 \text{ GeV}$ should be present in the forward region.

In order to analyse WZ scattering in the high-mass region, the transverse mass M_T

$$M_T^2 = \left[\sqrt{M^2(lll) + p_T^2(lll) + |\not{p}_T|^2} \right]^2 - [\vec{p}_T(lll) + \vec{\not{p}}_T]^2$$

was used. $M(lll)$ and $p_T(lll)$ are the invariant mass and transverse momentum of the three charged leptons and \not{p}_T is the missing momentum in the event. The transverse mass M_T distribution for the $W_L Z_L$ scattering and for $Zt\bar{t}$ background, after the application of cuts, is shown in Figure 50. The number of signal and background events with the invariant mass of WZ system larger then 600 GeV for an integrated luminosity of $\mathcal{L} = 500 \text{ fb}^{-1}$ and applying different cuts, are shown in Table 34. The ZZ background is not shown since it is effectively removed by the requirement of missing transverse momentum.

Like-sign W pair production $W_L^+ W_L^+$ production has been extensively studied [243]. As possible scenarios for this process by $W_L^+ W_L^+$ scattering, the following are considered:

- A t -channel exchange of a Higgs with $M_H = 1 \text{ TeV}$, ($W_L W_L$ only), simulated with PYTHIA with $\sigma \times BR = 1.33 \text{ fb}$ (the same parameters of the resonance as in Section 6.41 were used).

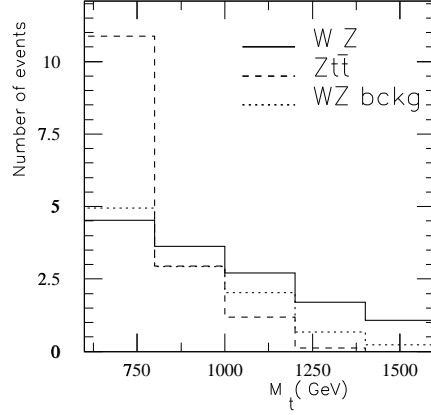


Fig. 50: The transverse mass M_T distribution for ZW system (GeV) for $W_L^\pm Z_L$ scattering and for $Zt\bar{t}$.

Table 34: Number of expected events for the WZ signal and backgrounds with an integrated luminosity of 500 fb^{-1} .

Cuts	$L_1=0.003$	$L_1=0.01$	$Zt\bar{t}$	WZ	S/\sqrt{B}	
					$L_1=0.003$	$L_1=0.01$
Leptonic cuts	33.3	18.3	223.	762		
Missing momentum	25.9	14.3	85.1	405		
$p_T(Z) > M_T/4$	22.2	12.2	67.	300		
Forward jet tagging	14	7.3	15	10.8	2.7	1.43

- The K-matrix unitarised amplitude [216, 240] $a_{IJ}^K = \frac{Re(a_{IJ})}{1 - iRe(a_{IJ})}$, where a_{IJ} is the low-energy theorem amplitude, proportional to s . This model is constructed to satisfy explicitly elastic unitarity and would yield the maximum expected signal. The $\sigma \times BR = 1.12$ fb.
- A Chiral Lagrangian model, as in the WZ resonant channel, with the same parameters: $L_1 = 0$, and $L_2 = 0.006$ or 0.01 , leading to $\sigma \times BR = 0.484$ and 0.379 fb, respectively.

Backgrounds from continuum WW bremsstrahlung produce mostly transverse W 's. Other backgrounds include processes involving non-Higgs exchange, as well as QCD processes of order α_s in amplitude, with gluon exchange and W bremsstrahlung from interacting quarks. The effects of $Wt\bar{t}$ and WZ backgrounds are also considered. The signal was generated with PYTHIA 6.2 and backgrounds were incorporated into PYTHIA from a Monte Carlo generator based on Barger's work [244], which takes into account all diagrams. The contribution from electroweak processes not involving the Higgs were estimated by assuming a low-mass Higgs ($M_H = 100$ GeV).

An analysis was performed using the fast ATLAS detector simulation (ATLFAST), with parameters set for high luminosity. The following leptonic cuts were first applied:

- L1. Two positively charged isolated leptons in the central region ($p_T > 40$ GeV and $|\eta| < 1.75$) must be identified. They will satisfy the trigger requirement.
- L2. The opening angle between the two leptons, in the transverse plane, must satisfy: $\cos \Delta\phi < -0.5$. This cut selects preferentially events with longitudinal W 's which have high p_T . The invariant mass of the two leptons was further required to satisfy $m_{ll} > 100$ GeV. This latter cut eliminates few events in the low $m_{ll\nu\nu}$ region.

At the jet level, backgrounds can be reduced by requiring that:

- J1. No jet having $p_T > 50$ GeV be present in the central region ($|\eta| < 2$). This reduces significantly the background from the $Wt\bar{t}$ process.
- J2. Two jets must be present in the forward and backward regions: $\eta > 2$ and $\eta < -2$, with energies > 300 GeV.
- J3. A lower p_T was required for the forward jets: $p_T < 150$ GeV for the first and $p_T < 90$ GeV for the second.

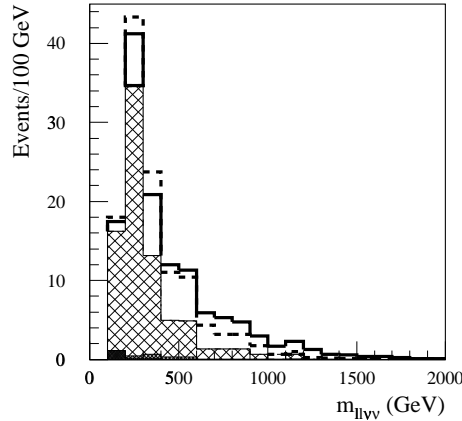


Fig. 51: Distribution of invariant transverse mass of the two leptons with E_T^{miss} in the $W_L^+ W_L^+ \rightarrow l^+ l^+ \nu\nu$ process, after three years of high luminosity running. Full line: K-matrix unitarisation; dashed line: Higgs with $M_H = 1$ TeV, at tree level; hatched area: background from transverse W 's.

Figure 51 shows expected mass distribution of the $ll\nu\nu$ system, for an integrated cross section of 300 fb^{-1} , after all cuts were applied, accounting only for transverse momentum. No correction was made for pile-up effects in jet tagging or central jet veto. If one counts only events with $m_{ll\nu\nu} > 400$ GeV,

a significant signal to background ratio is obtained (see Table 35). As expected, the K-matrix scenario gives the highest signal [216] - this could be observable after a few years of high luminosity running. By contrast, it was shown in Section 6.42 that if the ρ resonance is itself clearly observable in the resonant channel, then the signal will be very low. The major remaining background, especially at low values of $m_{ll\nu\nu}$, is from continuum transverse W pairs. Note that only a $W_L^+ W_L^+$ signal was searched for in this analysis. Combining the results with $W_L^- W_L^-$ would add approximately one-half to one-third of the signal and backgrounds. The Chiral Lagrangian model, with its parameters leading to a resonance in the WZ system, would yield a very weak signal in the $W^+ W^+$ channel, confirming the complementarity relationship between those two channels [216, 171, 242].

Table 35: Number of events expected for an integrated luminosity of 300 fb^{-1} , after successive applications of cuts. The results are for $m_{ll\nu\nu} > 400 \text{ GeV}$.

	Lepton cuts		Jet cuts		
	L1	L2	J1	J2	J3
$M_H=1 \text{ TeV}$	59	56	43	24	19.0
K-matrix	90	86	69	41	32
Chiral Lagrangian $L_2=0.006$	22	21	15.8	9.3	7.1
Chiral Lagrangian $L_2=0.01$	15.1	14.1	10.4	6.0	4.6
$W_T W_T$	350	243	68	54	14.0
gluon exchange	76	51	3.2	0	0
$W t \bar{t}$	93	71	2.0	0	0
WZ	36	35	19.1	0.5	0.3

6.43 Technicolor

Technicolor (TC) provides a framework for dynamical electroweak symmetry breaking [34, 35]. It assumes the existence of techni-fermions possessing a technicolor charge and interacting strongly at high scale. Chiral symmetry is broken by techni-quark condensates giving rise to Goldstone bosons, the techni-pions, which are the longitudinal degrees of freedom of the W and Z gauge-bosons. TC has been extended (extended TC, or ETC) to allow the generation of fermion masses [245, 246]. In order to account for the absence of FCNCs, the coupling constant is required to “walk”, rather than “run”. To achieve a walking α_{TC} , multi-scale TC models contain several representations of the fundamental family, and lead to the existence of techni-hadron resonances accessible at LHC energies. Such models [247, 248] are constrained by precision electroweak data [250, 251], but not necessarily excluded [252, 253]. However, the constraints from those data make it unnatural to have a large top quark mass. In top-colour-assisted TC (TC2) models [254, 255], the top quark arises in large part from a new strong top-colour interaction, which is a separate broken gauge-sector.

The possible observation of TC resonances using the ATLAS detector is described in [256]. In particular, the search for a ($I=1, J=1$) techni-rho resonance, a techni-pion and a techni-omega has been performed. Although certain models, with a given set of parameters, are used as reference, the signals studied can be considered generic in any model which predicts resonances. The model adopted here is that of multi-scale TC [257, 258], with the TC group $SU(N_{TC})$ where $N_{TC} = 4$ and two isotriplets of techni-pions. The longitudinal gauge-boson and the techni-pions mix

$$|\Pi_T \rangle = \sin \chi |W_L \rangle + \cos \chi |\pi_T \rangle$$

with a mixing angle which has a value $\sin \chi = 1/3$. The decay constant of the mixed state is $F_T = F_\pi \sin \chi = 82$ GeV and the charge of the up-type (down-type) techni-fermion is $Q_U = 1$ ($Q_D = 0$). This model is incorporated in PYTHIA 6.1. The decay channels of ρ_T depend on the assumed masses of the techni-particles. Some mass scenarios have been considered to be representative of what one may expect to probe at the LHC and it is also assumed that the π_T coupling to the top quark is very small, as may be expected in TC2 models. The following sections present an example showing a typical analysis for extracting TC signals. More channels and an extensive description can be found in [256].

$\rho_T^\pm \rightarrow W^\pm Z \rightarrow l^\pm \nu l^+ l^-$ This decay could be the cleanest channel for the techni-rho detection and complements the study shown in Section 6.42. The good efficiency of the ATLAS and CMS detectors for lepton detection and missing transverse energy measurement will provide good identification of the W and Z bosons. Table 36 shows the parameters for the various sets of events which were generated. For each set, 10^4 events were generated and the signal was normalised to three years of low luminosity running at the LHC (30 fb^{-1}). The branching ratios quoted include a preselection on the transverse mass ($\hat{m} > 150, 300, 600$ GeV for $m_{\rho_T^\pm} = 220, 500$ and 800 GeV respectively).

Table 36: Signal parameters for the $\rho_T^\pm \rightarrow W^\pm Z \rightarrow l^\pm \nu l^+ l^-$. The last column gives the significance (S/\sqrt{B}) for three years of low luminosity running.

m_{ρ_T} (GeV)	m_{π_T} (GeV)	Γ_{ρ_T} (GeV)	BR	$\sigma \times BR$ (pb)	S/\sqrt{B}
220	110 (a)	0.93	0.13	0.16	31.6
	110 (b)	67.1	0.014	1.0×10^{-3}	0.7
500	300 (c)	4.47	0.21	1.3×10^{-2}	14.7
	500 (d)	1.07	0.87	5.4×10^{-2}	64.2
800	110 (e)	130.2	0.013	1.5×10^{-4}	0.3
	300 (f)	52.4	0.032	3.6×10^{-4}	1.2
	500 (g)	7.6	0.22	2.5×10^{-3}	10.9

The only background which needs to be considered is the continuum production of WZ gauge-bosons, with $\sigma = 21$ pb. The cuts which were applied are:

- At least three charged leptons were required (with $E_T > 20$ GeV for electrons and $E_T > 6$ GeV for muons), two of which must have the same flavour and opposite charge.
- The invariant mass of the lepton pair with the same flavour and opposite sign should be close to that of the Z : $|m_{l^+l^-} - m_Z| < 5$ GeV.
- The longitudinal momentum of the neutrino is calculated (with a 2-fold ambiguity) from the missing transverse energy and the momentum of the unpaired lepton assuming an invariant mass $m_{l\nu} = m_W$. Once the W and Z were reconstructed, their transverse momentum was required to be larger than 40 GeV.
- Only events for which the decay angle with respect to the direction of the WZ system (ρ_T) in its rest frame was $|\cos \hat{\theta}| < 0.8$ were accepted.

The significance (S/\sqrt{B}) of the signal (S) above the background (B) is shown in Table 36. The number of signal and background events was counted in mass regions around the ρ_T peak: 210 to 240, 460 to 560 and 740 to 870 for $m_{\rho_T} = 220, 500$ and 800 GeV respectively. No evident signal can be observed for cases (b), (e) and (f) (see Figure 52), principally because the ρ_T resonance is too wide.

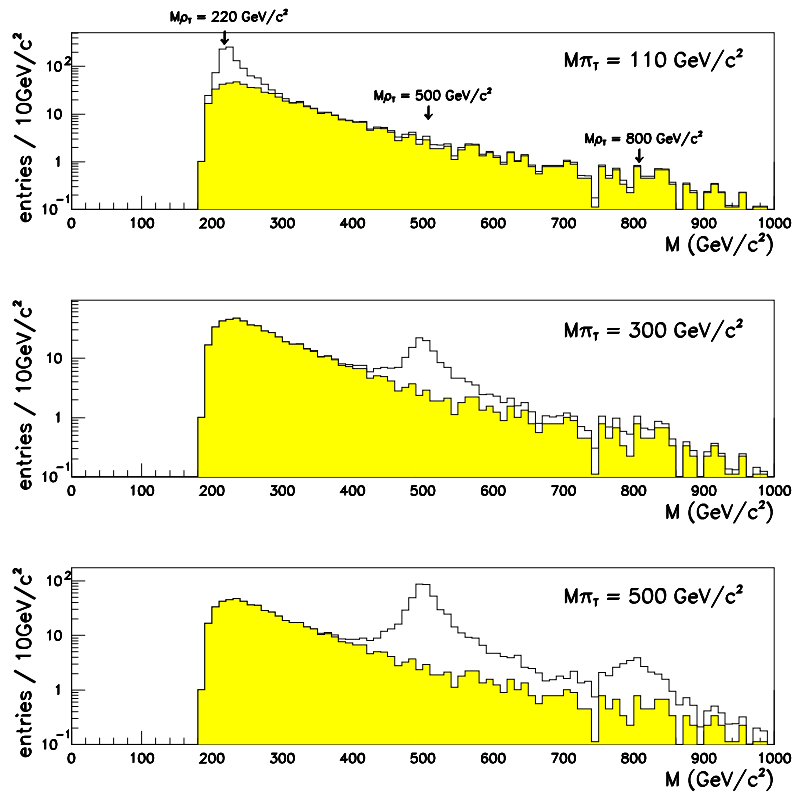


Fig. 52: Reconstructed $W^\pm Z$ invariant mass. The solid line is for the ρ_T signal and the filled area for the WZ background. The three plots, each characterised by the value of m_{π_T} , correspond to the cases (a,b,e), (c,f) and (d,g) defined in Table 36.

The Authors would like to thank M. Chanowitz, K. Lane, M. Mangano, J.R. Peláez, S.R. Slabospitsky and P. Savard for their technical help with some Monte Carlo generators and for fruitful discussions.

6.5 The degenerate BESS Model at the LHC

It is well known that naïve Dynamical Symmetry Breaking (DSB) models like standard QCD-scaled technicolor generally tend to provide large corrections to electroweak precision observables. New physics effects are naturally small if decoupling holds. In fact in this case the corrections to electroweak observables are power suppressed in the limit in which the masses of the new particles are made large. It is thus a natural question as to whether examples of DSB models with decoupling do exist.

Here we will focus on a scheme of DSB, called degenerate BESS (D-BESS) [43] in which decoupling is naturally satisfied in the low energy limit. The model predicts the existence of two triplets of new resonances corresponding to the gauge-bosons of an additional gauge-symmetry $SU(2)_L \otimes SU(2)_R$. The global symmetry group of the theory is $(SU(2)_L \otimes SU(2)_R)^3$ breaking down spontaneously to $SU(2)_D \otimes (SU(2)_L \otimes SU(2)_R)$ and giving rise to nine Goldstone bosons. Six of these give mass to the new gauge-bosons, which turn out to be degenerate. As soon as we perform the gauging of the subgroup $SU(2)_L \otimes U(1)_Y$, the three remaining Goldstone bosons disappear giving masses to the SM gauge-bosons.

What makes the model [43] so attractive is the fact that, due to the degeneracy of the masses and couplings of the extra gauge-bosons (L^\pm, L_3, R^\pm, R_3), it decouples, so all the deviations in the low-

energy parameters from their SM values are strongly suppressed. Also, the degeneracy is protected by the additional ‘‘custodial’’ symmetry ($SU(2)_L \otimes SU(2)_R$). The deviations from the SM predictions come from the mixing of ($\mathbf{L}_\mu, \mathbf{R}_\mu$) with the standard gauge-bosons. In order to compare with the experimental data, radiative corrections have to be taken into account. Since the model is an effective parametrisation of a strongly interacting symmetry breaking sector, one has to introduce a UV cut-off Λ . We neglect the new physics loop corrections and assume for D-BESS the same radiative corrections as for the SM with $M_H = \Lambda = 1$ TeV [43]. The 95% CL bounds on the parameter space of the model coming from the precision electroweak data can be expressed by the following approximated relation: $M(\text{TeV}) \geq 2.4 g/g''$, where M is the common mass of the new resonances, g and g'' are the standard $SU(2)_L$ and the new strong gauge-couplings respectively. Therefore one has a large allowed region available for the model even for the choice $M_H = \Lambda = 1$ TeV - a value highly disfavoured by the fit within the SM [259]. Also, the bounds on the D-BESS model from the direct search for new gauge bosons performed at Tevatron are very loose [43]. This allows the existence of a strong electroweak sector at relatively low energies such that it may be accessible with accelerators designed for the near future. A peculiar feature of this strong electroweak symmetry breaking model is the absence of WW enhancement due to the absence of direct couplings of the new resonances to the longitudinal weak gauge-bosons. For this reason, the gold plated channels to consider for discovering ($\mathbf{L}_\mu, \mathbf{R}_\mu$) are the fermionic ones.

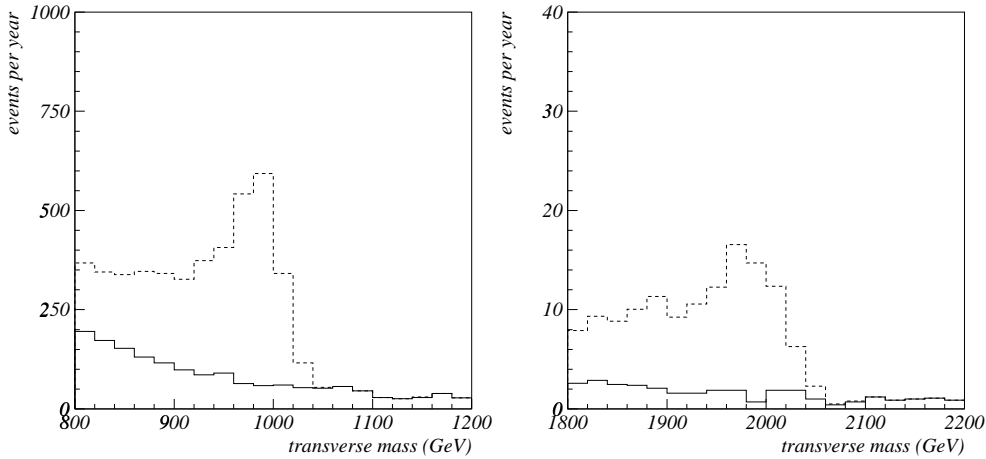


Fig. 53: Transverse mass differential distributions for $pp \rightarrow L^\pm, W^\pm \rightarrow e\nu_e$ events at the LHC within the D-BESS model (dash line) for $g/g'' = 0.1$ and $M = 1$ TeV (left), $M = 2$ TeV (right). The solid line is the SM prediction.

Here we have considered the production of these new resonances at the LHC for the following configuration $\sqrt{s} = 14$ TeV and $\mathcal{L} = 10^{34} \text{ cm}^{-2} \text{ sec}^{-1}$ and for the electron channel decay (the muon channel was studied in [260]). The events were generated using PYTHIA Monte Carlo (version 6.136) [123]. Only the Drell-Yan mechanism for production was considered since it turns out to be the dominant one. We have analysed the production of the charged resonances in $pp \rightarrow L^\pm, W^\pm \rightarrow e\nu_e$ (R^\pm are completely decoupled) and neutral ones in $pp \rightarrow L_3, R_3, Z, \gamma \rightarrow e^+e^-$. The signal events were compared with the background from SM production. We have performed a rough simulation of the detector, in particular, assuming a 2% smearing in the momenta of charged leptons and a resolution $\Delta E_T^{miss} = 0.6\sqrt{E_T^{miss}}$ in the missing transverse energy. In the neutral channel, we have assumed an error of 2% in the reconstruction of the e^+e^- invariant mass, which includes bremsstrahlung effects [261]. We have considered several choices of the model parameters, in the region allowed by the present bounds, and for each case we have selected cuts to maximise the statistical significance of the signal. In Figure 53 we show the transverse mass distributions for the signal and for the SM background for the case $M = 1$ TeV (left)

and $M = 2$ TeV (right) and $g/g'' = 0.1$. The following cuts have been applied for $M = 1$ TeV: $|p_T^e|$ and $|p_T^{miss}| > 0.3$ TeV and $M_T > 0.8$ TeV. The number of signal events per year is 3200, the corresponding background is of 1900 events. The corresponding statistical significance $S/\sqrt{S+B}$ for one year of running is 44. For $M = 2$ TeV, the applied cuts are: $|p_T^e|$ and $|p_T^{miss}| > 0.7$ TeV and $M_T > 1.8$ TeV, resulting in $S = 108$, $B = 46$ and $S/\sqrt{S+B} = 8.7$.

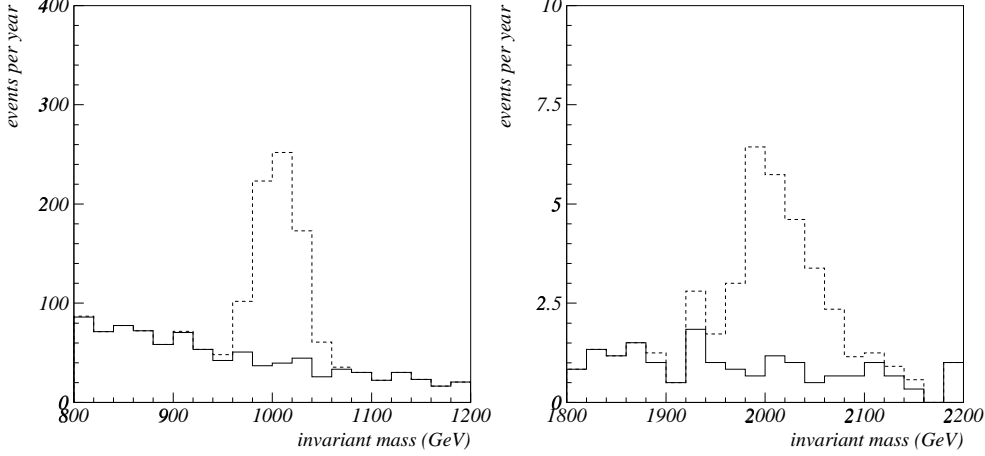


Fig. 54: Invariant mass differential distributions for $pp \rightarrow L_3, R_3, Z, \gamma \rightarrow e^+e^-$ events at the LHC within the D-BESS model (dash line) for $g/g'' = 0.1$ and $M = 1$ TeV (left), $M = 2$ TeV (right). The solid line is the SM prediction.

In Figure 54, we show the results of our simulation for the same choice of the parameters as in Figure 53 for the neutral channel. The following cuts have been applied for $M = 1$ TeV: $|p_T^{e^+}|$ and $|p_T^{e^-}| > 0.3$ TeV and $M_{e^+e^-} > 0.8$ TeV. The number of signal events per year is 620, the background is of 1200 events with a corresponding statistical significance of 15. For $M = 2$ TeV, the cuts are: $|p_T^{e^+}|$ and $|p_T^{e^-}| > 0.7$ TeV and $M_{e^+e^-} > 1.8$ TeV, resulting in $S = 24$, $B = 30$ and $S/\sqrt{S+B} = 3.3$. It turns out that the cleanest signature is in the neutral channel, but the production rate is lower than for the charged one. Also we observe that, due to the fact that the D-BESS resonances are almost degenerate ($\Delta M/M \sim (g/g'')^2$), it will be impossible to disentangle L_3 and R_3 which both contribute to the peak of the signal in Figure 54.

Our conclusion is that the LHC will be able to discover a strong electroweak resonant sector as described by the degenerate BESS model for masses up to 2 TeV - in some cases with very significant numbers of events. Furthermore, if no deviations from the SM predictions are seen within the statistical and systematic errors, the LHC with $L = 100 \text{ fb}^{-1}$ will put a 95% CL bound $g/g'' < 0.04 - 0.06$ for $0.5 < M(\text{TeV}) < 2$ [260].

References

- [1] M. Veltman, Nucl. Phys. **B123**, 89 (1977).
- [2] A. Sirlin, Phys. Rev. **D22**, 971 (1980).
- [3] W. J. Marciano and A. Sirlin, Phys. Rev. **D22**, 2695 (1980).
- [4] Reports of the Working Group on Precision Calculations at the Z Resonance, CERN 95-03 (1995), Eds. D. Bardin, W. Hollik, G. Passarino.
- [5] G. Degrassi, P. Gambino and A. Vicini, Phys. Lett. **B383**, 219 (1996) hep-ph/9603374.
- [6] G. Degrassi, P. Gambino and A. Sirlin, Phys. Lett. **B394**, 188 (1997) hep-ph/9611363.
- [7] S. Bauberger and G. Weiglein, Phys. Lett. **B419**, 333 (1998) hep-ph/9707510.

- [8] A. Freitas, S. Heinemeyer, W. Hollik, W. Walter and G. Weiglein, in preparation.
- [9] K. G. Chetyrkin, J. H. Kühn and M. Steinhauser, Phys. Rev. Lett. **75**, 3394 (1995) hep-ph/9504413.
- [10] The LEP Electroweak Working Group, CERN-EP/99-15, and update by J. Mnich, Plenary talk at the EPS Conference on High Energy Physics, Tampere (Finland) 1999.
- [11] P. H. Chankowski, A. Dabelstein, W. Hollik, W. M. Mosle, S. Pokorski and J. Rosiek, Nucl. Phys. **B417**, 101 (1994).
- [12] A. Djouadi, P. Gambino, S. Heinemeyer, W. Hollik, C. Jünger and G. Weiglein, Phys. Rev. **D57**, 4179 (1998) hep-ph/9710438.
- [13] J. Gunion, H. Haber, G. Kane, S. Dawson, ‘The Higgs Hunter’s Guide’, Addison-Wesley (1990).
- [14] S. Heinemeyer, W. Hollik and G. Weiglein, Eur. Phys. J. **C9**, 343 (1999) hep-ph/9812472.
- [15] H.T. Diehl, Proceeding of the 29th International Conference on High Energy Physics, Vancouver 1998, Eds. A. Astbury, D. Axen and J. Robinson, World Scientific, Vol. I, 520-524.
- [16] J. Ellison and J. Wudka, Ann. Rev. Nucl. Part. Sci. **48**, 33 (1998).
- [17] L. Dixon, Z. Kunszt and A. Signer, Nucl. Phys. **B531**, 3 (1998) hep-ph/9803250.
- [18] J. M. Campbell and R. K. Ellis, Phys. Rev. **D60**, 113006 (1999).
- [19] L. Dixon, Z. Kunszt and A. Signer, Phys. Rev. **D60**, 114037 (1999) hep-ph/9907305.
- [20] D. De Florian and A. Signer, hep-ph/0002138.
- [21] J. Ohnemus and J.F. Owens, Phys. Rev. **D43**, 3626 (1991).
- [22] B. Mele, P. Nason and G. Ridolfi, Nucl. Phys. **B357**, 409 (1991).
- [23] J. Ohnemus, Phys. Rev. **D44**, 3477 (1991).
- [24] S. Frixione, P. Nason and G. Ridolfi, Nucl. Phys. **B383**, 3 (1992).
- [25] J. Ohnemus, Phys. Rev. **D44**, 1403 (1991).
- [26] S. Frixione, Nucl. Phys. **B410**, 280 (1993).
- [27] J. Smith, D. Thomas and W.L. van Neerven, Z. Phys. **C44**, 267 (1989).
- [28] J. Ohnemus, Phys. Rev. **D47**, 940 (1992).
- [29] U. Baur, T. Han and J. Ohnemus, Phys. Rev. Lett. **72**, 3941 (1994).
- [30] U. Baur, T. Han and J. Ohnemus, Phys. Rev. **D53**, 1098 (1996).
- [31] U. Baur, T. Han and J. Ohnemus, Phys. Rev. **D51**, 3381 (1995).
- [32] U. Baur, T. Han and J. Ohnemus, Phys. Rev. **D48**, 5140 (1993).
- [33] U. Baur, T. Han and J. Ohnemus, Phys. Rev. **D57**, 2823 (1998).
- [34] S. Weinberg, Phys. Rev. **D13**, 974 (1976); Phys. Rev. **D19**, 1277 (1979).
- [35] L. Susskind, Phys. Rev. **D20**, 2619 (1979).
- [36] T. Appelquist and C. Bernard, Phys. Rev. **D22** 200 (1980).
- [37] A. Longhitano, Phys. Rev. **D22**, 1166 (1980); Nucl. Phys. **B188**, 118 (1981).
- [38] J. A. Bagger, A. F. Falk and M. Swartz, hep-ph/9908327.
- [39] M. Veltman, Act. Phys. Pol. **B8**, 475 (1977).
- [40] M. S. Chanowitz, 1998 Ed. D. Graudenz, PSI Proceedings 98-02, hep-ph/9812215.
- [41] J.J. van der Bij and B. Kastening, Phys. Rev. **D60**, 095003 (1999).
- [42] A. Dobado, M.J. Herrero, J.R. Pelaez, E. Ruiz Morales, hep-ph/9912224.
- [43] R. Casalbuoni, A. Deandrea, S. De Curtis, D. Dominici, R. Gatto and M. Grazzini, Phys. Rev. **D53**, 5201 (1996).
- [44] T. Appelquist, P. S. Rodrigues da Silva and F. Sannino, Phys. Rev. **D60**, 116007 (1999).
- [45] A. de Rújula, R. Petronzio and A. Savoy-Navarro, Nucl. Phys. **154**, 394 (1979).
- [46] V.N. Gribov and L.N. Lipatov, Sov. J. Nucl. Phys. **15**, 438 (1972) and *ibidem* 675 (1972).
- [47] G. Altarelli and G. Parisi, Nucl. Phys. **B126**, 298 (1977).
- [48] J. Kripfganz and H. Perl, Z. Phys. **C41**, 319 (1988).
- [49] H. Spiesberger, Phys. Rev. **D52**, 4936 (1995).
- [50] A. Martin, R.G. Roberts, J. Stirling and R. Thorne, DTP-99-64, hep-ph/9907231.
- [51] Z. Kunszt *et al.*, in ‘Physics at LEP2’, CERN 96-01 (1996), Eds. G. Altarelli, T. Sjöstrand,

- F. Zwirner, Vol. 1, p141, hep-ph/9602352.
- [52] H. Aihara *et al.*, 'Future Electroweak Physics at the Fermilab Tevatron: Report of the TEV-2000 Study Group', FERMILAB-Pub-96/082.
- [53] ATLAS Collaboration, 'Detector and Physics Performance Technical Design Report', CERN/LHCC/99-15, Vol. 2.
- [54] E. Accomando *et al.*, Phys. Rep. **299**, 1 (1998).
- [55] M. Dittmar, F. Pauss and D. Zürcher, Phys. Rev. **D56**, 7284 (1997).
- [56] W. Hollik and D. Wackerroth, Phys. Rev. **D55**, 6788 (1997).
- [57] U. Baur, S. Keller and D. Wackerroth, Phys. Rev. **D59**, 013002 (1998).
- [58] U. Baur and T. Stelzer, hep-ph/9910206.
- [59] U. Baur and D. Wackerroth, in preparation.
- [60] S. Dittmaier and M. Krämer, BI-TP 2000/04.
- [61] M. Böhm, W. Hollik and H. Spiesberger, Fortschr. Phys. **34**, 687 (1986).
- [62] A. Denner, Fortschr. Phys. **41**, 307 (1993).
- [63] D. Bardin, A. Leike, T. Riemann and M. Sachwitz, Phys. Lett. **B206**, 539 (1998).
- [64] W. Beenakker *et al.*, Nucl. Phys. **B500**, 255 (1997).
- [65] U. Baur and D. Zeppenfeld, Phys. Rev. Lett. **75**, 1002 (1995).
- [66] E.N. Argyres *et al.*, Phys. Lett. **B358**, 339 (1995).
- [67] H.L. Lai *et al.* (CTEQ Collaboration), Phys. Rev. **D55**, 1280 (1997) hep-ph/9606399.
- [68] U. Baur, S. Keller and W. K. Sakumoto, Phys. Rev. **D57**, 199 (1998) hep-ph/9707301.
- [69] J. Collins and D. Soper, Phys. Rev. **D16**, 2219 (1977).
- [70] J.H. Kühn, A.A. Penin and V.A. Smirnov, hep-ph/9912503.
- [71] U. Baur, O. Brein, W. Hollik, C. Schappacher and D. Wackerroth, in preparation.
- [72] S.C. Bennett and C.E. Wieman, Phys. Rev. Lett. **82**, 2848 (1999).
- [73] C.S. Wood *et al.*, Science **275**, 1759 (1997).
- [74] M.C. Noecker, B.P. Masterson and C.E. Wieman, Phys. Rev. Lett. **61**, 310 (1988).
- [75] S.A. Blundell, W.R. Johnson and J. Sapirstein, Phys. Rev. Lett. **65**, 1411 (1990).
- [76] V. Dzuba, V. Flambaum, P. Silvestrov and O. Sushkov, Phys. Lett. **A141**, 147 (1989).
- [77] R. Casalbuoni, S. De Curtis, D. Dominici and R. Gatto, Phys. Lett. **B460**, 135 (1999).
- [78] J.L. Rosner, hep-ph/9907524; J. Erler and P. Langacker, hep-ph/9910315.
- [79] E. Gross, Contribution to the International Europhysics Conf., Tampere, Finland, 15-21 July 1999.
- [80] F. Abe *et al.*, Phys. Rev. Lett. **79**, 2191 (1997).
- [81] T.G. Rizzo, in 'New Directions For High-Energy Physics', Eds. D.G. Cassel, L. Trindle Genari, R.H. Siemann, Stanford, CA, (1997) and references therein. M. Cvetič and S. Godfrey, in 'Electroweak Symmetry Breaking and Beyond the Standard Model', Eds. T. Barklow, S. Dawson, H. Haber and J. Seigrist, (World Scientific 1995) and references therein.
- [82] G. Altarelli, T. Sjöstrand and F. Zwirner, 'Physics at LEP2', CERN 96-01 (1996).
- [83] D. Amidei and R. Brock, 'Future electroweak physics at the Fermilab Tevatron', FERMILAB-PUB-96/082 (1996).
- [84] F. Gianotti, 'Measurement of the W mass at the LHC', ATLAS Internal Note ATL-COM-PHYS-99-063 (1999).
- [85] E. Richter-Was, D. Froidevaux and L. Poggioli, 'ATLFAST 1.0 A package for particle-level analysis', ATLAS Internal Note ATL-PHYS-96-079 (1996) and ATL-PHYS-98-131 (1998).
- [86] ATLAS Collaboration, 'Detector and Physics Performance Technical Design Report', CERN/LHCC/99-14, Vol. 1.
- [87] CDF Collaboration, Phys. Rev. **D52**, 4784 (1995).
- [88] R. Wagner, presentation in Plenary Meeting of this Workshop, 25 May 1999 - see associated web pages.
- [89] D0 Collaboration, Phys. Rev. Letters **80**, 3008 (1998).
- [90] Eadie *et al.*, 'Statistical methods in experimental physics', North-Holland, (1971).

- [91] S. Haywood, ‘Offline alignment and calibration of the Inner Detector’, ATL-INDET-2000-005 (2000).
- [92] M. Aleksa, ‘Absolute mass scale calibration using $Z \rightarrow \mu\mu$ events’, ATLAS Internal Note ATL-MUON-99-001 (1999).
- [93] U. Baur, S. Keller and D. Wakeroth, Phys. Rev. **D59**, 13002 (1999).
- [94] E. Accomando *et al.*, ‘Physics with e^+e^- Linear Colliders’, DESY 97-100 (1997) hep-ph/9705442.
- [95] S. Keller and W. Giele, Phys. Rev. **D57**, 4433 (1998); S. Rajagopalan and M. Rijssenbeek, ‘Measurement of M_W using the transverse mass ratio of W and Z ’, in Proceedings of the Workshop on New Directions in High Energy Physics, Snowmass 1996.
- [96] D. Bourilkov, LEP review talk, XXXIII Rencontres de Moriond, France, 1998; published in the proceedings, Ed. J. Trân Thanh Vân, Edition Frontiers, Paris, 1999, p139, hep-ex/9806027.
- [97] D. Bourilkov, ‘Drell-Yan Production of Lepton Pairs at LHC’, CMS Note 2000/xxx (2000).
- [98] J. Rosner, Phys. Rev. **D35**, 2244 (1987).
- [99] M. Dittmar, Phys. Rev. **D55**, 161 (1997) hep-ex/9606002.
- [100] P. Fischer, U. Becker and J. Kirkby, Phys. Lett. **B356**, 404 (1995).
- [101] K. Sliwa, S. Riley, U. Baur, ‘Effects of Possible Extensions to Rapidity Coverage of the ATLAS Detector on the Determination of $\sin^2 \theta_{\text{eff}}^{\text{lept}}(M_Z^2)$ ’, ATLAS Internal Note, ATL-COM-PHYS-2000-003 (2000).
- [102] F. Abe *et al.*, Phys. Rev. **D52** 2624 (1995).
- [103] OPAL Collaboration, CERN-EP/99-097, July 8, 1999, subm. to Eur. Phys. J. C, hep-ex/9908008.
- [104] ALEPH Collaboration, ALEPH 99-018, submitted to EPS-HEP99 # 6-694.
- [105] J. Kalinowski, R. Rückl, H. Spiesberger and P.M. Zerwas, Phys. Lett. **B414**, 297 (1997) hep-ph/9708272.
- [106] D. Bourilkov, J. High Energy Phys. **08**, 006 (1999) hep-ph/9907380.
- [107] J. Hewett, Phys. Rev. Lett. **82**, 4765 (1999) hep-ph/9811356.
- [108] A. Pich and A. Ruiz (Eds.), Proc. Fifth Workshop on Tau Lepton Physics (Santander, 14-17 September 1998), Nucl. Phys. (Proc. Suppl.) **B76** (1999).
- [109] A. Pich, ‘Tau Physics’, in Proc. 1999 Symposium on Lepton and Photon Interactions (Stanford, August 1999), hep-ph/9912294.
- [110] E653 Collaboration, Phys. Lett. **B303** 359 (1993).
- [111] CLEO Collaboration, Phys. Rev. **D57**, 5903 (1998).
- [112] S. Dittmaier, M. Böhm and A. Denner, Nucl. Phys. **B376**, 29 (1992); *erratum* **B391**, 483 (1993).
- [113] W. Beenakker *et al.*, in ‘Physics at LEP2’, Eds. G. Altarelli, T. Sjöstrand and F. Zwirner (Geneva, 1996) hep-ph/9602351.
- [114] A.D. Martin, R.G. Roberts, W.J. Stirling and R.S. Thorne, Eur. Phys. J **C4**, 463 (1998) hep-ph/9803445.
- [115] M. Ciafaloni, P. Ciafaloni and D. Comelli, hep-ph/0001142.
- [116] C. Caso *et al.*, Eur. Phys. J. **C3**, 1 (1998).
- [117] U. Baur, S. Errede and G. Landsberg, Phys. Rev. **D50**, 1917 (1994) hep-ph/9402282.
- [118] J. Gunion, Z. Kunszt and M. Soldate, Phys. Lett. **163B**, 389 (1985).
- [119] J. Gunion and M. Soldate, Phys. Rev. **D34**, 826 (1986).
- [120] W.J. Stirling *et al.*, Phys. Lett. **163B**, 261 (1985).
- [121] D. Zeppenfeld and S. Willenbrock, Phys. Rev. **D37**, 1775 (1988).
- [122] T. Han, R. Meng and J. Ohnemus, Nucl. Phys. **B384**, 59 (1992).
- [123] T. Sjöstrand, JETSET 7.4, Comput. Phys. Commun. **82**, 74 (1994). See also T. Sjöstrand, ‘Recent progress in PYTHIA,’ hep-ph/0001032.
- [124] J.F. Gunion and Z. Kunszt, Phys. Rev. **D33**, 665 (1986).
- [125] CMS Collaboration, CMS Technical Proposal, CERN/LHCC 94-38 (1994).
- [126] D. De Florian, paper in preparation.

- [127] J. Ohnemus, Phys. Rev. **D51**, 1068 (1995) hep-ph/9407370.
- [128] S. Frixione, Z. Kunszt and A. Signer, Nucl. Phys. **B467**, 399 (1996) hep-ph/9512328.
- [129] M. Glück, E. Reya and A. Vogt, Phys. Rev. **D48**, 116 (1993); *erratum*, **D51**, 1427 (1995).
- [130] G.J. Gounaris, J. Layssac and F.M. Renard, ‘Signatures of the anomalous Z gamma and ZZ production at the lepton and hadron colliders’, hep-ph/9910395.
- [131] K. Hagiwara, R. Peccei, D. Zeppenfeld and K. Hikasa, Nucl. Phys. **B282** 253, (1987).
- [132] U. Baur and D. Zeppenfeld, Nucl. Phys. **B308**, 127 (1988).
- [133] E.C.G. Stückelberg, Helv. Phys. Acta **11**, 299 (1933).
- [134] J.J. van der Bij and B. Kastening, Phys. Rev. **D57**, 2903 (1998).
- [135] J. R. Pelaez, Phys. Rev. **D55**, 4193 (1997), and contribution to this workshop (see associated web pages).
- [136] Ken-ichi Hikasa, Physics and Experiments with Linear Colliders (World Scientific), Vol. 2, 451 (1992).
- [137] D. Dominici, Riv. Nuovo Cim. **20**, 11 (1997).
- [138] S. Dawson and G. Valencia, Nucl. Phys. **B439**, 3 (1995).
- [139] J.J. van der Bij, Phys. Rev. **D35**, 1088 (1987); Phys. Lett. **B296**, 239 (1992).
- [140] A.S. Belyaev *et al.*; hep-ph/9805229.
- [141] A. Ghinculov and J.J. van der Bij, Phys. Lett. **B279**, 189 (1992).
- [142] G. Bélanger and F. Boudjema, Phys. Lett. **B288**, 201 (1992).
- [143] E. Boos *et al.*, Phys. Rev. **D57**, 1553 (1998).
- [144] U. Baur, D. Zeppenfeld, Physics Letters **B201**, 383 (1988).
- [145] U. Baur and E.L. Berger, Phys. Rev. **D47**, 4889 (1993).
- [146] H. Aihara *et al.*, ‘Anomalous gauge boson interactions’, hep-ph/9503425.
- [147] H. Baer, J. Ohnemus and J.F. Owens, Phys. Rev. **D40**, 2844 (1989).
- [148] S. Frixione, Z. Kunszt and A. Signer, Nucl. Phys. **B467**, 399 (1996).
- [149] R.K. Ellis, D.A. Ross and A.E. Terrano, Nucl. Phys. **B178**, 421 (1981).
- [150] U. Baur and D. Zeppenfeld, Nucl. Phys. **B308**, 127 (1988).
- [151] R. Barlow, ‘Statistics’ (John Wiley and Sons, Chichester, 1989), p90.
- [152] T. Müller, D. Neuberger and W. H. Thümmel, ‘Sensitivities on anomalous $WW\gamma$ and $ZZ\gamma$ couplings at CMS’, CMS Note 2000/017 (2000).
- [153] ATLAS Collaboration, ATLAS Technical Proposal, CERN/LHCC/94-43 (1994).
- [154] D. Fouchez, ‘Gauge boson pairs production study with Atlas’, ATLAS Internal Note ATL-PHYS-94-060 (1995).
- [155] C.K. Mackay, ‘The electromagnetic calorimeter for CMS and a study of the $WW\gamma$ vertex’, CMS Ph.D. Thesis, Brunel University, Uxbridge, UK (1998) CMS/1999-012 THESIS, RAL-TH-1999-001, ISSN 1362-0215.
- [156] M. Reichel, ‘Simulationsstudien zur $W\gamma$ Produktion in hadronischen Kollisionen bei CDF und CMS’, Karlsruhe Internal Report IKEP-KA-98-06 (1998).
- [157] S. Abdullin, A. Khanov, N. Stepanov, ‘CMSJET 4.3’, CMS NOTE 180 (1994).
- [158] CMS Collaboration, ‘The Electromagnetic Calorimeter Design Project, Technical Design Report’ CERN/LHCC 97-33 (1997).
- [159] E.L. Berger, D. DiBitanto, M. Jacob and W. Stirling, Phys. Lett. **B140** 259 (1984).
- [160] V. Barger, A. Martin and R. Phillips, Phys. Lett. **B125** 343 (1983).
- [161] J. Cortes, K. Hagiwara and F. Herzog, Nucl. Phys. **B278** 26 (1986).
- [162] D. Vite, ‘ B -physics prospects with ATLAS and CMS at the LHC’, CMS Technical Note 010 (1995).
- [163] E. Maina and S. Moretti, Phys. Lett. **B286** 370 (1992).
- [164] U. Baur and A. Stange, ‘The $t\bar{t}\gamma$ background to $pp \rightarrow W\gamma + X$ at the SSC’, Proc. Workshop on Physics at Current Accelerators and the Supercollider, Argonne National Lab. U.S. ANL-HEP-CP-93-92, 319 (1992).

- [165] M. Kelly, ‘Test of the standard model of electroweak interactions by measuring the anomalous $WW\gamma$ couplings at $\sqrt{s}=1.8$ TeV’, D0 Ph.D. Thesis, Notre Dame, South Bend Indiana (1996).
- [166] For recent reviews, see *e.g.* J.L. Rosner, EFI-97-18, hep-ph/9704331.
- [167] K. Hagiwara, Ann. Rev. Nucl. Part. Sci., 463 (1998) and references therein.
- [168] R.N. Cahn *et al.*, Phys. Rev. **D35**, 1626 (1987).
- [169] V. Barger, T. Han, and R.J.N. Phillips, Phys. Rev. **D37**, 2005 (1988).
- [170] R. Kleiss and W.J. Stirling, Phys. Lett. **200B**, 193 (1988).
- [171] V. Barger, K. Cheung, T. Han, and R.J.N. Phillips, Phys. Rev. **D42**, 3052 (1990).
- [172] V. Barger *et al.*, Phys. Rev. **D44**, 1426 (1991).
- [173] V. Barger, K. Cheung, T. Han, and D. Zeppenfeld, Phys. Rev. **D44**, 2701 (1991); *erratum* Phys. Rev. **D48**, 5444 (1993); Phys. Rev. **D48**, 5433 (1993).
- [174] V. Barger *et al.*, Phys. Rev. **D46**, 2028 (1992).
- [175] D. Dicus, J.F. Gunion and R. Vega, Phys. Lett. **B258**, 475 (1991).
- [176] D. Dicus, J.F. Gunion, L.H. Orr and R. Vega, Nucl. Phys. **B377**, 31 (1991).
- [177] V. Barger, R.J.N. Phillips and D. Zeppenfeld, Phys. Lett. **B346**, 106 (1995).
- [178] K. Iordanidis and D. Zeppenfeld, Phys. Rev. **D57**, 3072 (1998).
- [179] K. Hagiwara, D. Rainwater and D. Zeppenfeld, Phys. Rev. **D59**, 14037 (1999).
- [180] T. Plehn, D. Rainwater and D. Zeppenfeld, hep-ph/9911385.
- [181] T. Plehn, D. Rainwater and D. Zeppenfeld, Phys. Lett. **B454**, 297 (1999).
- [182] V. Barger and R.J.N. Phillips, Phys. Rev. Lett. **55**, 2752 (1985).
- [183] H. Baer, V. Barger, H. Goldberg and R.J.N. Phillips, Phys. Rev. **D37**, 3152 (1988).
- [184] R. Cahn and S. Dawson, Phys. Lett. **136B**, 196 (1984).
- [185] D. Rainwater and D. Zeppenfeld, Journal of High Energy Physics **12**, 005 (1997).
- [186] K. Hagiwara, A.D. Martin and D. Zeppenfeld, Phys. Lett. **B235**, 198 (1990).
- [187] D. Cavalli *et al.*, ATLAS Internal Note, PHYS-NO-051 (1994).
- [188] R.K. Ellis *et al.*, Nucl. Phys. **B297**, 221 (1988).
- [189] J.F. Gunion and H.E. Haber, Nucl. Phys. **B272**, 1 (1986); *erratum* Nucl. Phys. **B402**, 567 (1993).
- [190] D. Rainwater and D. Zeppenfeld, Phys. Rev. **D60**, 113004 (1999) hep-ph/9906218.
- [191] S. Weinberg, Physica **96A**, 327 (1979). J. Gasser and H. Leutwyler, Ann. Phys. **158**, 142 (1984).
- [192] M.J. Herrero and E. Ruiz Morales, Nucl. Phys. **B418**, 431 (1994); Nucl. Phys. **B437**, 319 (1995).
- [193] S. Dittmaier and C. Grosse-Knetter, Nucl. Phys. **B459**, 497 (1996).
- [194] T. Appelquist and G.-H. Wu, Phys. Rev. **D48**, 3235 (1993).
- [195] M.E. Peskin and T. Takeuchi, Phys. Rev. Lett. **65**, 964 (1990); Phys. Rev. **D46**, 381 (1992).
- [196] A. Dobado *et al.*, Phys. Lett. **B255**, 405 (1991).
- [197] Review of Particle Physics, Particle Data Group, Eur. Phys. J. **C3**, 1 (1998).
- [198] J.A. Bagger *et al.*, hep-ph/9908327.
- [199] D. Espriu and M. J. Herrero, Nucl. Phys. **B373**, 117 (1992).
- [200] S. Alam *et al.*, Phys. Rev. **D57**, 1577 (1998).
- [201] P. Hernández and J. Vegas, Phys. Lett. **B307**, 116 (1993).
- [202] O. Eboli *et al.*, Phys. Lett. **B339**, 119 (1994).
- [203] J.M. Cornwall *et al.*, Phys. Rev. **D10**, 1145 (1974).
- [204] B.W. Lee *et al.*, Phys. Rev. **D16**, 1519 (1977).
- [205] M.S. Chanowitz and M.K. Gaillard, Nucl. Phys. **B261**, 379 (1985).
- [206] H.J. He *et al.*, Phys. Lett. **B329**, 278 (1994).
- [207] A. Dobado and J.R. Peláez, Phys. Lett. **B329**, 469 (1994); Nucl. Phys. **B425**, 110 (1994).
- [208] A. Dobado *et al.*, Phys. Rev. **D56**, 7133 (1997).
- [209] A. Dobado and M.J. Herrero, Phys. Lett. **B228**, 425 (1989); Phys. Lett. **B233**, 505 (1989).
- [210] J. Donoghue and C. Ramirez, Phys. Lett. **B234**, 361 (1990).
- [211] J. Bagger *et al.*, Nucl. Phys. **B399**, 364 (1993).
- [212] H.J. He *et al.*, Mod. Phys. Lett **A11**, 3061 (1996); Phys. Rev. **D55**, 3038(1997).

- [213] A. Dobado and M.T. Urdiales, *Z. Phys.* **C71**, 659 (1996).
- [214] A. Dobado *et al.*, *Phys. Lett.* **B352**, 400 (1995).
- [215] A.S. Belyaev *et al.*, *Phys. Rev.* **D59**, 015022 (1999).
- [216] M. Chanowitz and W. Kilgore, *Phys. Lett.* **B322**, 147 (1994).
- [217] T.N. Truong, *Phys. Rev. Lett.* **661**, 2526 (1988); *Phys. Rev. Lett.* **67**, 2260 (1991).
- [218] A. Dobado *et al.*, *Phys. Lett.* **B235**, 134 (1990).
- [219] A. Dobado and J.R. Peláez, *Phys. Rev.* **D47**, 4883 (1993); *Phys. Rev.* **D56**, (1997) 3057.
- [220] J.A. Oller *et al.*, *Phys. Rev. Lett.* **80**, 3452 (1998); *Phys. Rev.* **D59**, 074001 (1999).
- [221] A. Dobado *et al.*, *Phys. Lett.* **B235**, 129 (1990).
- [222] A. Dobado *et al.*, *Z. Phys.* **C50**, 205 (1991); *Z. Phys.* **C50**, 465 (1991).
- [223] I. Josa *et al.*, in Proc. LHC Workshop, Vol.II, Aachen, CERN 90-10, ECFA 90-133.
- [224] J.R. Peláez, *Phys. Rev.* **D55**, 4193 (1997).
- [225] K. Kawarabayashi and M. Suzuki, *Phys. Lett.* **16B**, 225 (1966).
- [226] Riazuddin and Fayyazuddin, *Phys. Rev.* **147**, 1071 (1996).
- [227] S. Dawson, *Nucl. Phys.* **B249**, 24 (1985).
- [228] E.W.N. Glover and J.J. van der Bij, *Nucl. Phys.* **B321**, 561 (1989).
- [229] CTEQ Collaboration, MSUHEP-60426, CTEQ-604.
- [230] R.S. Chivukula, ‘NATO Advanced Study Institute on Quantum Field Theory Since 1970: Perspective and Prospective’, Les Houches, 1998, hep-ph/9803219.
- [231] M. Quirós, ‘Constraints on the Higgs boson properties from the effective potential’, Publ. in: ‘Perspective on Higgs Physics II’, Ed. G.L. Kane, World Scientific, Singapore, Advanced Series on Directions in High-Energy Physics, **17**, 148 (1997).
- [232] A. Ghinculov and T. Binoth, *Acta Phys. Polon.* **B30**, 99 (1999).
- [233] M. Bossman and M. Nessi, ‘Study of Z +jets background to $H \rightarrow ZZ \rightarrow ll\nu\nu$ signal using full simulation of ATLAS calorimetry’, ATLAS Internal Note ATL-PHYS-94-050 (1995).
- [234] H. Ruiz, ‘Discovery potential of a heavy Standard Model Higgs boson through the $H \rightarrow ZZ \rightarrow ll\nu\nu$ channel at the LHC with the ATLAS detector’, ATLAS Internal Note ATL-PHYS-99-031 (1999).
- [235] S. Zmushko *et al.*, ‘Study of $H \rightarrow WW \rightarrow l\nu jj$ and $H \rightarrow ZZ \rightarrow lljj$ decays for $M_H = 1$ TeV’, ATLAS Internal Note ATL-PHYS-92-008 (1992).
- [236] M. Cobal *et al.*, ‘VECBOS: a lowest Order Matrix Element Calculation to simulate direct QCD $W + n$ jets events’, ATLAS Internal Note ATL-PHYS-96-084 (1996).
- [237] S. Zmushko, D. Froidevaux and L. Poggioli, ‘ $H \rightarrow WW \rightarrow l\nu jj$ and $H \rightarrow ZZ \rightarrow lljj$ Particle level studies’, ATLAS Internal Note ATL-PHYS-97-103 (1997).
- [238] P. Savard and G. Azuelo, ATLAS Internal Note ATL-PHYS-98-128 (1998).
- [239] T.N. Truong *et al.*, *Phys. Rev. Lett.* **61**, 2526 (1988); *ibid* **D67**, 2260 (1991).
- [240] M.S. Chanowitz, private communication.
- [241] A. Miagkov, ‘Vector boson scattering in Chiral Lagrangian model’, ATLAS Internal Note ATL-PHYS-99-006 (1999).
- [242] V. Barger *et al.*, *Phys. Rev.* **D52**, 3878 (1995).
- [243] G. Azuelos, R. Mazini, A. Miagkov and K. Strahl, ‘Measuring the rate of non-resonant high mass longitudinal gauge boson pairs in ATLAS’, ATLAS Internal Note ATL-PHYS-99-048 (1999).
- [244] V. Barger, K. Cheung, A. Djouadi, B.A. Kniehl and P.M. Zerwas, *Phys. Rev.* **D49**, 79 (1994).
- [245] S. Dimopoulos and L. Susskind, *Nucl. Phys.* **B155**, 237 (1979).
- [246] E. Eichten and K. Lane, *Phys. Lett.* **B90**, 125 (1980).
- [247] E. Eichten, K. Lane and J. Womersley, *Phys. Lett.* **B405**, 305 (1997).
- [248] B.A. Dobrescu and J. Terning, *Phys. Lett.* **B416**, 29 (1998).
- [249] A. Dobado, M.J. Herrero, J.R. Peláez and E. Ruiz Morales, contribution to this Workshop.
- [250] M. Golden and L. Randall, *Nucl. Phys.* **B361**, 3 (1991).
- [251] R.S. Chivukula *et al.*, *Phys. Lett.* **B311**, 157 (1993) hep-ph/9305232.

- [252] K. Lane, 27th International Conference on High Energy Physics (ICHEP), Glasgow, Scotland, 1994, hep-ph/9409304.
- [253] M. Knecht and E. de Rafael, Phys. Lett. **B242**, 335 (1998).
- [254] C.T. Hill, Phys. Lett. **B266**, 419 (1991).
- [255] K. Lane and E. Eichten, Phys. Lett. **B352**, 382 (1995).
- [256] G. Azuelos, P. Depommier, R. Mazini, and K. Strahl, 'Search for Technicolor Signals with the ATLAS Detector', ATLAS Internal Note ATL-PHYS-99-020 (1999).
- [257] K. Lane, 'Electroweak and Flavor Dynamics at Hadron Colliders', hep-ph/9605257.
- [258] E. Eichten and K. Lane, Phys. Lett. **B388**, 803 (1996) hep-ph/9607213.
- [259] R. Casalbuoni, S. De Curtis, D. Dominici, R. Gatto and M. Grazzini, Phys. Lett. **B435**, 396 (1998).
- [260] R. Casalbuoni, P. Chiappetta, A. Deandrea, S. De Curtis, D. Dominici and R. Gatto, Phys. Rev. **D56**, 2812 (1997).
- [261] D. Denegri, private communication.